UNIVERSIDAD DE CHILE
FACULTAD DE CIENCIAS FÍSICAS Y MATEMÁTICAS
DEPARTAMENTO DE GEOLOGÍA

GENESIS OF THE EL ROMERAL IRON ORE: NEW CONTRIBUTIONS TO THE UNDERSTANDING OF IRON OXIDE-APATITE DEPOSITS

TESIS PARA OPTAR AL GRADO DE MAGÍSTER EN CIENCIAS, MENCIÓN GEOLOGÍA
MEMORIA PARA OPTAR AL TÍTULO DE GEÓLOGA

PAULA AMANDA ROJAS MARTÍNEZ

PROFESOR GUÍA
FERNANDO BARRA PANTOJA

MIEMBRO DE LA COMISIÓN
MARTIN REICH MORALES
DIEGO MORATA CÉSPEDES

SANTIAGO DE CHILE
2017

GENESIS OF THE EL ROMERAL IRON ORE: NEW CONTRIBUTIONS TO THE UNDERSTANDING OF IRON OXIDE-APATITE DEPOSITS

Los depósitos denominados de tipo magnetita-apatito o *iron oxide-apatite* (IOA) son una importante fuente de Fe, P y REE a nivel mundial. Sin embargo, el origen de estos depósitos sigue siendo tema de debate, en donde predominan tres teorías: una hipótesis magmática que involucra inmiscibilidad de líquidos, un origen hidrotermal por reemplazo de la roca hospedante y una teoría magmático-hidrotermal por flotación de pares magnetita-burbuja.

Con el fin de dilucidar el origen de estos depósitos, el presente trabajo se centra en el estudio del yacimiento El Romeral, principal depósito tipo IOA de la IV Región, ubicado en la Franja Ferrífera de la Cordillera de la Costa. Este depósito se emplaza en andesitas de la Formación La Liga, limitado al oeste por la Diorita Romeral. La mineralización está conformada por cuerpos subverticales de magnetita maciza con intercrecimiento de actinolita, relacionados con el sistema de Falla Romeral.

A través de estudios petrográficos, combinado con microscopio electrónico de barrido, análisis de microsonda electrónica y micro-Raman en inclusiones minerales se han definido y estudiado los distintos eventos de mineralización. Se define (i) un primer evento con magnetita (I), rica en inclusiones minerales, la cual presenta altos contenidos de V (~2500-2800 ppm) y Ti (~80-3000 ppm). A mayores profundidades se observan inclusiones de alta temperatura (e.g. Ti-pargasita, ilmenita y clinocloro) que van gradando a inclusiones de menor temperatura en zonas someras (e.g. α-cuarzo). Por otro lado, se define un (ii) segundo evento caracterizado por magnetita prístina, sin inclusiones (II), con altas concentraciones de V (~2300-2700 ppm) y menor contenido de Ti (~50-400 ppm).

Esta misma variación termal se evidencia con la química de minerales accesorios. La presencia de cristales de actinolita con bajos #Fe, asociados a la magnetita II, sugiere una cristalización a altas temperaturas (hasta 840°C), al igual que la presencia de F-apatito, los cuales se detectaron a mayores profundidades. En contraste, a menores profundidades predominan los apatitos ricos en OH, con mayor contenido de Cl. Asimismo, mayores razones de Co:Ni (>1) se midieron en sulfuros de eventos primarios, asociados a la mineralización de magnetita II, a diferencia de menores razones Co:Ni (<0.5) asociadas a sulfuros tardíos.

En vista de los resultados anteriores y de la estrecha relación temporal entre la actinolita relacionada con la mineralización (~128 Ma, $^{40}Ar/^{39}Ar$) y la Diorita Romeral (~129 Ma, U-Pb en circones) se establece un primer evento de origen magmático, posiblemente relacionado con la cristalización de este cuerpo intrusivo, que va gradando a un sistema hidrotermal en superficie, influenciado por la acción de la Falla Romeral.

"La satisfacción radica en el esfuerzo, no en el logro.
Un esfuerzo total es una victoria completa"
-Mahatma Gandhi

"Cada libro, cada tomo que ves, tiene alma.
El alma de quien lo escribió,
y el alma de quienes lo leyeron y vivieron
y soñaron con él."
La Sombra del Viento
-Carlos Ruiz Zafón

AGRADECIMIENTOS

De igual manera, quisiera agradecer a mis padres por apoyarme a lo largo de toda mi vida y sobre todo durante estos interminables años de estudio, por darme la oportunidad de poder hacer lo que me gusta, por entregarme amor y por ser un pilar fundamental en mi vida; y a mi padre por mostrarme desde pequeña el mundo de las ciencias y, en particular, lo maravilloso que es la geología. Gracias a mi madre, mis hermanas, Ale y Soso, y a mi mamí por ser las mujeres más valientes, resilientes y sabias de este mundo. Ellas son mi ejemplo a seguir y gracias a ellas he logrado llegar lejos y ser quien soy hoy en día.

También quiero agradecer a mis amigas de toda la vida, mis amigas del colegio: Dani, Aymi, Coti, Mae, Belen, Jaci, Pilito, Dani.B y Paski por estar siempre a mi lado apoyándome, por compartir penas y alegrías, por enseñarme y, a la vez, aprender juntas, y por disfrutar conmigo los mejores momentos de mi vida. Agradezco también a la gente maravillosa que he conocido en el camino y quienes han sido parte importante de mi vida durante estos casi 8 años, especialmente a Vini y a mis amigos: Pati, Tania, Nico, Maca, Mane, Andre, Martín, Dieter, Yayer, Tomi, Juancho, Gonchi, JP, Marito, Marta, Nicoso, Cristian y a todos los LC-LCH. Agradezco a los de la oficina milenio, por los buenos momentos que hemos compartido, por las tertulias milenio y por el apoyo que me han entregado durante estos últimos dos años, en especial a Salo, Rurik, Gilla, Nacho y Negro.

Finalmente, agradezco a los funcionarios del Departamento de Geología, Carlos Gómez, Quilo, y en particular a Maritza y Blanquis por su ayuda y apoyo infinito.

TABLA DE CONTENIDO

ÍNDICE DE TABLAS

ÍNDICE DE FIGURAS

CAPÍTULO 1

INTRODUCCIÓN

1.1. Presentación

La franja ferrífera chilena se encuentra entre la III y IV región, abarcando 700 km de la Cordillera de la Costa (Ruiz et al., 1965). Dentro de esta franja se emplazan depósitos tipo óxidos de hierro-cobre-oro o *iron oxide-copper-gold* (IOCG) y un conjunto de depósitos denominados de tipo Kiruna, magnetita-apatito o i*ron oxide-apatite* (IOA). Estos últimos corresponden a cuerpos irregulares de magnetita maciza con bajo contenido en titanio y enriquecidos en vanadio, con proporciones variables de actinolita, apatito y escapolita, que siguen el dominio sinestral del Sistema de Falla de Atacama. Generalmente, estos cuerpos se hospedan en rocas volcánicas y están limitados por rocas intrusivas del Cretácico Inferior (Ruiz et al., 1968; Bookstrom, 1977). Hitzman et al. (1992) y Sillitoe (2003) proponen un origen en común entre estos yacimientos y los depósitos tipo IOCG, basándose en diversas observaciones. En primer lugar, esta hipótesis se apoya en la presencia de sulfuros en ambos depósitos, principalmente de pirita y menor calcopirita para el caso de depósitos tipo IOA; por otro lado, se evidencia magnetita maciza en las etapas tempranas y profundas de algunos IOCGs, además de existir una clara semejanza en cuanto a la alteración hidrotermal asociada a ambos depósitos, generalmente de tipo calco-sódica. Más aún, hay una fuerte correlación espacial entre ambos, en donde los depósitos tipo Kiruna se asocian directamente a un ambiente extensional o transtensional a lo largo de zonas estructurales mayores, tal como la traza de la Falla Atacama, y por otro lado, los depósitos tipo IOCG se asocian a las estructuras secundarias de dirección NW, las cuales cortan la estructura principal (**Figura 1**). Sin embargo, a diferencia de los IOCGs, los depósitos ferríferos chilenos reflejan un proceso de deposición en un ambiente pobre en sulfuros (Cox y Singer, 2007) y generalmente el contenido en cobre y oro es más bien bajo.

Este trabajo de tesis consta de seis capítulos principales: una introducción general, seguido de la metodología empleada en cada etapa del trabajo, un marco geológico detallado tanto regional como local, un primer artículo científico titulado *Geology and geochronology of the El Romeral deposit, Chile: New constraints on the genesis of iron oxide-apatite deposits* en donde se integran resultados de la petrografía, dataciones e isótopos estables, y un segundo artículo titulado *New contributions to the understanding of Kiruna-type iron oxide-apatite deposits revealed by magnetite ore and gangue minerals geochemistry at the El Romeral deposit, Chile*, el cual se enfoca en los análisis químicos de elementos mayores y menores realizados en la mineralización y en los minerales de alteración. El último capítulo considera conclusiones generales de los trabajos realizados.

1
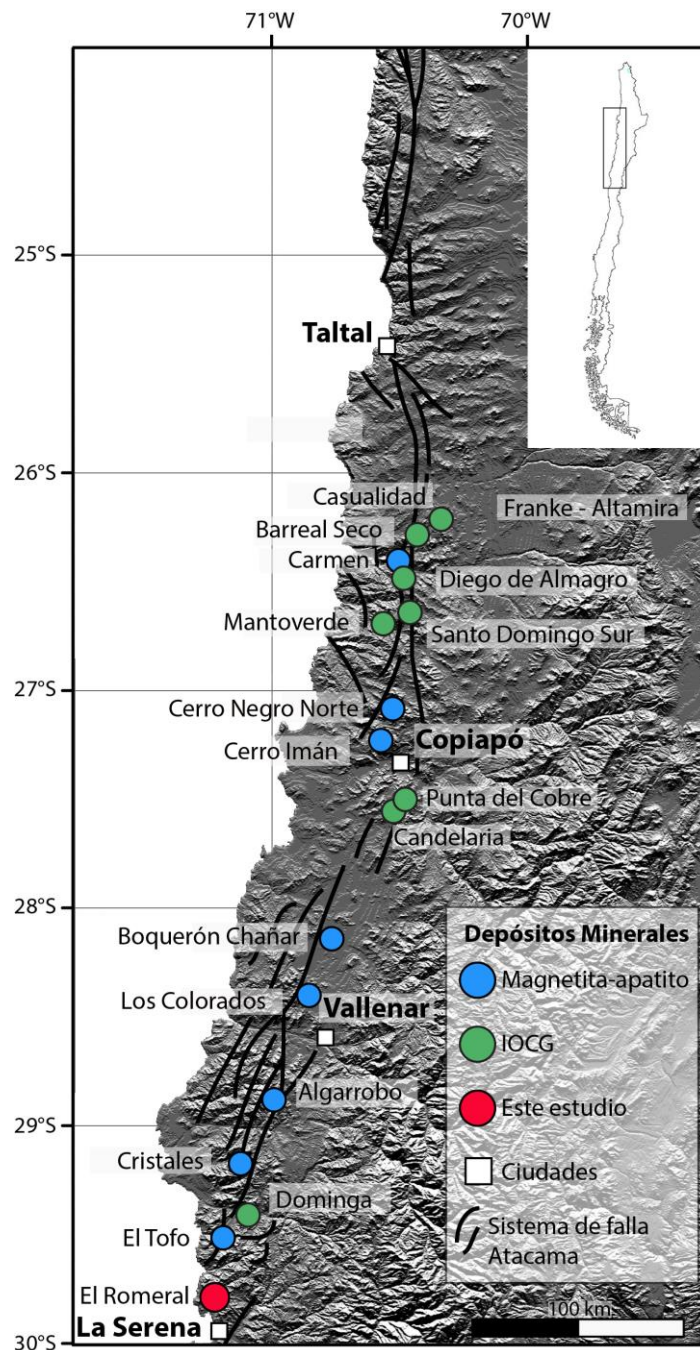
Figura 1. Mapa en donde se presentan los depósitos tipo IOCG y magnetita-apatito de la III y IV región y su fuerte relación con el Sistema de Falla Atacama (modificado de Barra et al., 2017).

La génesis de estos depósitos ha sido motivo de gran controversia. Por un lado, se considera que la magnetita tendría un origen magmático, es decir, provendría de un fundido inmiscible rico en magnetita con alta fugacidad de oxígeno y alto contenido de volátiles, el que permitiría bajar el punto de fusión conllevando al ascenso de este fundido rico en hierro, y posterior intrusión en las secuencias volcánicas hospedantes de la mineralización (Park, 1961; Henríquez y Martin, 1978; Nyström y Henríquez, 1994; Nyström y Henríquez, 1995; Travisany

et al., 1995; Espinoza, 2000; Henríquez et al., 2003). En oposición a esta teoría está la hipótesis hidrotermal, donde se explica el enriquecimiento en hierro por fluidos de origen magmático o no magmático, fluidos que permiten el transporte de magnesio, calcio y hierro, este último como complejo clorurado, hasta alcanzar rocas más frías en donde precipitaría la magnetita (Ménard, 1995) y/o donde se generaría un reemplazo metasomático de la mineralogía primaria (Bookstrom, 1977; Bookstrom, 1995; Rhodes et al., 1999; Rhodes y Oreskes, 1999; Sillitoe y Burrows, 2002; Sillitoe y Burrows, 2003). Este modelo se basa en la existencia de texturas características de un reemplazo hidrotermal, además de la concordancia entre los patrones de REE de la roca caja y la magnetita (Rhodes et al., 1999), el bajo contenido de titanio en la magnetita y en la presencia de intercalaciones volcánicas alteradas dentro del cuerpo de magnetita masiva para el caso de El Laco (Sillitoe y Burrows, 2002). Por otra parte, la hipótesis magmática se ve respaldada por evidencias texturales de flujo y rocas pegmatíticas (Nyström y Henriquez, 1994), junto con análisis químicos y la existencia de grandes cuerpos masivos de magnetita, que al ser de origen hidrotermal sólo podrían estar formados por un reemplazo total del protolito, lo cual se considera poco factible.

Recientemente, en el trabajo de Knipping et al. (2015), en el yacimiento Los Colorados, se propone una nueva hipótesis para el origen de los depósitos tipo Kiruna. Mediante isótopos estables de Fe y O y geoquímica de elementos mayores y trazas en magnetitas se determina que gran parte de las muestras se encuentran dentro del rango relacionado con magnetitas de origen magmático, sin embargo, algunos granos de magnetita presentan zonaciones, las cuales reflejan una transición desde condiciones puramente magmáticas a condiciones magmático-hidrotermales con temperatura decreciente. Esta secuencia de eventos se puede explicar mediante un nuevo modelo, propuesto por los autores, de flotación de magnetitas primarias. En este modelo se explica el ascenso de la magnetita por la nucleación de burbujas las cuales se acoplan a cristales primarios de magnetitas durante la cristalización de un magma de arco hidratado y oxidado, burbujas que posteriormente ascienden con estos cristales, coalescen y se acumulan, procesos que se pueden ver facilitados por la presencia de estructuras y por la participación de fluidos magmáticos hipersalinos. Finalmente, a niveles más someros y a medida que se va enfriando el sistema, se pueden generar las zonaciones de carácter hidrotermal mencionadas anteriormente (Knipping et al., 2015). Con esta hipótesis se puede explicar el *link* entre los depósitos tipo IOA e IOCG, donde a medida que se va enfriando el sistema y que las burbujas de magnetita van ascendiendo, los granos obtienen una signatura más hidrotermal y a temperaturas inferiores a 420°C comienza la precipitación de sulfuros de cobre, conllevando, de esta manera, a la formación de sistemas tipo IOCG.

Con el fin de determinar el origen de la mineralización, se han realizado en estudios anteriores mapeos geológicos de las zonas de interés, junto con el desarrollo de estudios petrográficos y químicos. Mediciones de isotopos de oxígeno en magnetita (Rhodes y Oreskes, 1999) y de elementos trazas, mayores o menores, tanto en inclusiones fluidas (Sheets et al., 1997;

Broman et al., 1999) como en la misma mineralogía de mena, (Nyström y Henriquez, 1994) permiten definir la fuente mineralizadora responsable de la génesis de los yacimientos tipo magnetita-apatito.

Este estudio se centra en el Distrito Ferrífero Minas El Romeral, el cual se sitúa en la región de Coquimbo, a 22 km al noreste de la ciudad de La Serena, dentro de la Franja Ferrífera de la Cordillera de la Costa. Este distrito corresponde al principal yacimiento de hierro de la zona, adquirido por la Compañía Minera del Pacífico S.A. (CMP) en 1971, Sociedad Anónima de Inversiones creada por la restructuración orgánica de la Compañía de Acero del Pacífico S.A (CAP), y anteriormente explotado por la compañía norteamericana Bethlehem Chile Iron Mines Company (CAP Minería, 2014).

Este yacimiento tipo magnetita-apatito se emplaza en la Formación La Liga, correspondiente a rocas volcánicas de composición andesítica del Jurásico tardío-Cretácico Inferior, y está limitado por un intrusivo pre-mineralización, o posiblemente syn-mineralización, de composición cuarzo-monzonita al oeste de la zona y por una falla transcurrente sinestral al este, que pone en contacto La Formación La Liga y un batolito granodiorítico emplazado posteriormente a la mineralización (Bookstrom, 1977). La mineralización se caracteriza por una zona central de magnetita maciza que está rodeada por brechas de magnetita-actinolita, seguido de un halo de alteración compuesto principalmente por actinolita y magnetita diseminada (Espinoza, 2000).

En este depósito no se han realizado estudios recientes acerca del origen de la mineralización, por lo que en el presente trabajo se busca entender la génesis de este yacimiento, realizando un análisis integrado que permita definir los controles de la mineralización, junto con el ambiente geotectónico que caracteriza la formación de estos depósitos. Este trabajo es financiado por el proyecto FONDECYT: *Metallogenesis of the mesozoic magmatic arc of northern Chile: Testing the IOCG connection using a multy-proxy geochemical approach* con el Dr. Fernando Barra como investigador principal y profesor guía de este trabajo de Tesis y se enmarca dentro del Núcleo Milenio Trazadores de Metales en Zonas de Subducción (NMTM) con el Dr. Martin Reich como director y el Dr. Fernando Barra como director alterno, núcleo financiado por la Iniciativa Científica Milenio (ICM) del Ministerio de Economía, Fomento y Turismo. Adicionalmente, este proyecto es parcialmente financiado por la Unidad de Recursos Minerales del Servicio Nacional de Geología y Minería.

1.2. Objetivos

1.2.1. Generales

El objetivo general del presente trabajo es determinar el origen de la mineralización de hierro en el Distrito El Romeral, mediante el estudio de las unidades geológicas, la química mineral de las fases de mena y ganga y la geocronología de los eventos de mineralización, alteración y magmatismo.

1.2.2. Específicos

1- Estudiar la mineralogía de mena, ganga y la alteración hidrotermal asociada por medio de muestras obtenidas en sondajes y en superficie.

2- Establecer una caracterización química detallada de la magnetita, sulfuros, apatito, actinolita y otros minerales asociados.

3- Establecer una cronología de eventos mediante dataciones radiométricas de la mineralogía de alteración y de cuerpos intrusivos.

4- Establecer un modelo genético para una mayor comprensión del origen de estos depósitos.

1.3. Hipótesis de trabajo

Los depósitos de magnetita-apatito de la Franja Ferrífera de la Cordillera de la Costa del norte de Chile tienen un origen magmático-hidrotermal. La mineralización de hierro se forma en un continuo desde un ambiente netamente magmático a un ambiente transicional magmático-hidrotermal. Además, la mineralización de hierro está temporal y genéticamente ligada a magmas dioríticos formados en respuesta a las condiciones tectónicas dominantes y bajo un fuerte control estructural.

1.4. Ubicación y accesos

El Distrito Ferrífero Minas El Romeral se ubica en la IV Región de Coquimbo, a 22 km al noreste de La Serena, en los flancos orientales del cerro La Liga, a unos 400 m.s.n.m. Las coordenadas son 29º43'19''S y 71º14'09''O, las que corresponden al punto central ubicado dentro del rajo del depósito. Se accede a la zona de estudio desde la ciudad de La Serena, por la Ruta 5 en dirección norte hasta la intersección con el camino ripiado D-165, el cual conduce directamente al rajo principal de la mina (**Figura 2**).
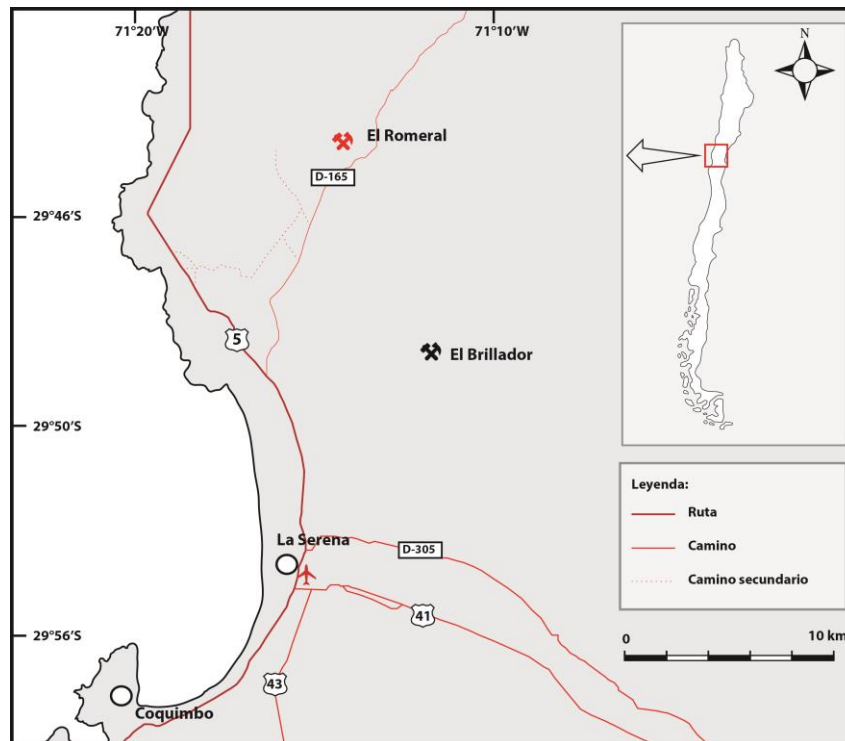
Figura 2. Ubicación y acceso a la mina El Romeral.

1.5. Trabajos anteriores

Dentro del área de interés se han realizado diversos estudios, sin embargo, en fechas recientes los trabajos son escasos y ninguno le ha dado un enfoque químico de detalle. Los siguientes trabajos son los que se utilizarán como material de apoyo para la realización de este estudio:

Bookstrom (1975) elabora un estudio detallado de la geología de El Romeral por medio de mapeo de unidades litológicas y estructuras, además de estudios petrográficos, y escasos análisis químicos de microsonda electrónica en anfíboles y rayos-X en arcillas. El autor propone un origen hidrotermal con participación de la Falla Romeral que facilitó la movilización de fluidos acuosos provenientes de un magma residual, fluidos que incorporaron el hierro para generar el depósito en cuestión.

Llaumet (1977) genera una evaluación geológica de las reservas del yacimiento e interpreta la información obtenida de sondajes definiendo dos cuerpos principales: la mena masiva de magnetita, la cual contiene mayor porcentaje de Fe y menor P y S, y el cuerpo brechoso con vetillas o cúmulos de actinolita.

Dobbs (1977) estudia la distribución de vanadio y titanio dentro del cuerpo principal del distrito, utilizando análisis de microsonda electrónica en distintas especies minerales. De este modo, se obtienen patrones norte-sur tanto para el titanio como para el vanadio, con un mayor enriquecimiento en el sector oeste para este último. Además, se determinó que el vanadio se aloja, a altas temperaturas, en la estructura de la magnetita a diferencia del titanio que se encuentra mayoritariamente en el esfeno y de manera secundaria en magnetitas, resultados insuficientes para determinar el origen de la mineralización.

Ulloa (1979) realiza una recopilación y actualización de la información geológica del yacimiento además de realizar una evaluación y distribución del azufre y fósforo que acompañan a la magnetita. De esta manera, observó un aumento de estos compuestos a profundidades mayores a 180 metros, lo cual se asocia a la mayor abundancia de inclusiones de apatito y pirita en magnetita.

Betzhold (1981) estudia la geología del Cuerpo Oeste de Baja Ley del distrito, realizando una descripción estructural, litológica y mineralógica. Mediante estudios texturales, definió la relación entre el contenido de hierro, azufre y fosfato, concluyendo que, a pesar de que probablemente los sulfuros, el apatito y la magnetita tienen un origen en común, los dos últimos son contemporáneos a diferencia de los sulfuros que se depositarían en una fase más tardía.

Romo (1981) desarrolla un estudio geológico detallado del cuerpo Cerro Norte dándole énfasis a la descripción de la mineralogía de mena, litología, alteración y estructuras, junto con realizar una evaluación geológica de las reservas del cuerpo.

Zeballos (1986) se basa en el estudio macroscópico de la zona de baja ley de hierro mediante el mapeo de sondajes y de la pared oeste del Cerro Principal para evaluar la cantidad y calidad de los recursos geológicos de baja ley, estudiar la distribución de esta mineralización y analizar las texturas de mena observadas.

Lorca (1990) caracteriza la geoquímica y cristalografía de las piritas de los yacimientos de hierro-apatito El Romeral y El Algarrobal. Determinó la presencia de oro, plata, platino, paladio, cobalto, níquel y selenio dentro de su estructura, sugiriendo un origen magmático de la mineralización de sulfuros.

Espinoza (1996) realiza un estudio petrográfico de las unidades litológicas circundantes al cuerpo de mena dentro del Cerro Principal, estudiando tanto la mineralogía de mena como de

ganga. La autora define un cuerpo de actinolita de origen hidrotermal posiblemente generado por el emplazamiento del cuerpo macizo de hierro, al cual se sobreimpone una cloritización leve. Además, observa tres cuerpos relacionados con procesos magmáticos tardíos: un cuerpo aplítico de cuarzo, microclina, albita y turmalina, filones aplíticos emplazados en la Diorita Romeral y brechas hidrotermales dentro de la roca de actinolita silicificada, los cuales representarían la resurgencia del fenómeno magmático que generó las rocas de la zona de estudio.

Espinoza (2000) realiza una caracterización del distrito gracias a la confección de perfiles E-W, descripciones petrográficas y análisis químicos de elementos mayores y menores en el cuerpo de mena (Fe, P, S, Na, K, V, Ti, Al_2O_3, Ca, MgO, Mn, Cu y SiO_2) y en ocho muestras de rocas circundantes, utilizando el método de absorción atómica.

CAPÍTULO 2

METODOLOGÍA

2.1. Investigación bibliográfica y recopilación geológica

Para lograr un conocimiento previo de la zona de estudio, se procede a la compilación de material bibliográfico sobre la geología regional y el distrito. Todo esto se complementa con la revisión de trabajos anteriores relacionados con la génesis de yacimientos tipo IOCG y Kiruna. Posterior a esto, se realiza la construcción de un proyecto GIS con toda la información preexistente, tal como la geología regional, datos geoquímicos, imágenes de sensores remotos y la base de datos sobre depósitos del distrito ya incorporados en el levantamiento del Mapa Metalogénico de la Cuarta Región, realizado por el Servicio Nacional de Geología y Minería.

2.2. Trabajo en terreno

El trabajo en terreno se divide en dos campañas donde se busca realizar una recolección de muestras para distintos fines, junto con el mapeo de sondajes y la caracterización geológica de la zona, para lo cual se eligen cinco secciones características de la zona norte, centro y sur del Cerro Principal (**Figura 3** y **Tabla 1**). Durante esta etapa se generó una plantilla de mapeo para testigos de sondajes, la cual incluye descripción de litología, mineralogía de alteración hidrotermal, vetillas, texturas cuando fue posible observar y mineralización metálica.

2.3. Trabajo en laboratorio

El trabajo en laboratorio se divide en cuatro etapas principales donde se busca estudiar las muestras recolectadas en sondajes y en superficie. En primer lugar, se realiza una caracterización de cortes petrográficos, calcográficos y de muestras de mano, mediante microscopio petrográfico y microscopio estereoscópico en el Laboratorio de Microscopía del Departamento de Geología de la Universidad de Chile. Este estudio abarca el reconocimiento mineralógico y de paragénesis minerales, la identificación de texturas de equilibrio/desequilibrio, metamórficas o ígneas y toma de microfotografías, con el propósito de comprender los patrones de alteración, las asociaciones mineralógicas presentes y la temporalidad de eventos tanto de alteración hidrotermal como de mineralización metálica.

Por otro lado, se procede a realizar estudios de isótopos estables de azufre en sulfuros, principalmente en pirita en el *Environmental Isotope Laboratory of the Department of Geosciences* de la Universidad de Arizona y a analizar químicamente mediante microsonda

electrónica muestras seleccionadas de magnetita, sulfuros, apatito, actinolita y otros silicatos, tales como biotita y piroxenos, en el *Centre for Microscopy, Characterisation and Analysis (CMCA)* de la Universidad de Western Australia, a fin de determinar el origen, ya sea hidrotermal y/o magmático de esta mineralización.

Además se realizan dataciones radiométricas mediante $^{40}Ar/^{39}Ar$ en actinolita y biotita en el laboratorio de Geología Isotópica del Servicio Nacional de Geología y Minería, y $^{238}U/^{206}Pb$ en circones de los cuerpos intrusivos circundantes en el laboratorio CEGA de Geocronología del Departamento de Geología de la Universidad de Chile, para determinar una posible relación entre ambos y para definir la temporalidad de estos eventos.

Finalmente, se analizan inclusiones seleccionadas dentro de cristales de magnetita, principalmente de cuarzo, mediante espectroscopía Micro-Raman en el Centro de Equipamiento Mayor (CEM) de la Facultad de Ciencias de la Universidad de Chile.
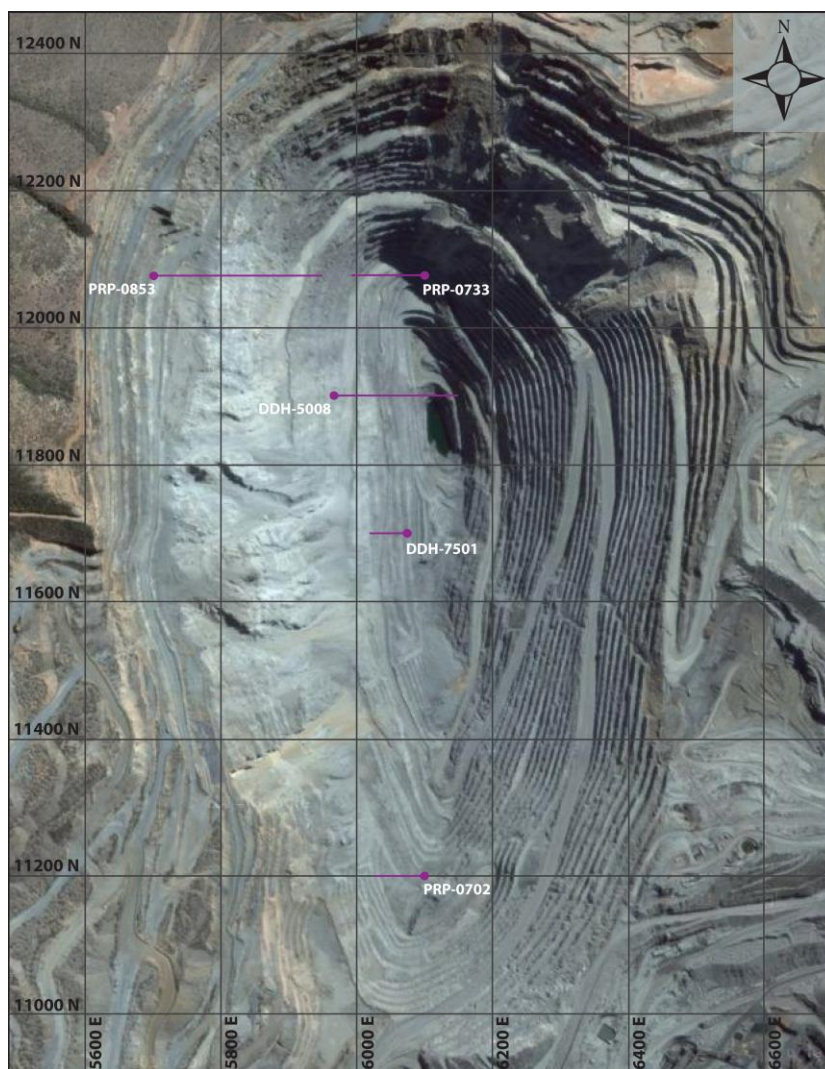
Figura 3. Imagen satelital con la ubicación de los sondajes estudiados (Fuente: SAS Planet, 2015).

Tabla 1. Coordenadas y longitud de los sondajes utilizados en este estudio.

Sondaje	Coordenadas cuello sondaje		Cota (m)	Longitud (m)
	Norte	**Este**		
PRP0733	12075.071	6103.707	59.794	432.4
PRP0853	12705	5700	360	500
DDH5008	11900.7	5966.96	169.76	436.2
DDH7501	11700	6085	34.48	337.3
PRP0702	11200	6100	100	400

CAPÍTULO 3

MARCO GEOLÓGICO

3.1. Generalidades

La zona de estudio se sitúa dentro de la zona del *flat-slab*, la cual abarca las latitudes 27ºS hasta 33ºS. Esta zona se caracteriza por la ausencia de la Depresión Central (Charrier et al., 2007) generando un relieve homogéneo entre la Cordillera de la Costa y la Cordillera Principal. El Distrito Ferrífero Minas El Romeral corresponde al conjunto de depósitos de hierro de mayor importancia en la zona. El distrito se encuentra en la Cordillera de la Costa, y está hospedado en rocas volcánicas de composición andesítica del Jurásico tardío a Neocomiano (Bookstrom, 1975) pertenecientes a la Formación La Liga, sub-miembro del Complejo Subvolcánico Agua Salada.

Estos depósitos se emplazan en una franja de 3,5 km de largo dentro de la Zona de Falla El Romeral de dirección norte-sur, zona con aparente continuidad con el sistema de falla Atacama. A esta zona se le asocian rocas miloníticas que han sido datadas obteniendo edades de 115±4 y 108±4 Ma con K-Ar en roca total y 113±3 Ma en biotita (Emparan y Pineda, Área La Serena-La Higuera, Región de Coquimbo, 1:100.000, Servicio Nacional de Geología y Minería. Servicio Nacional de Geología y Minería. Mapas Geológicos., 2000).

Los cuerpos mineralizados se conforman por cuerpos subverticales limitados al oeste por una falla NS que deja en contacto la Formación La Liga y la Diorita Romeral, y limitadas al este por un conjunto de intrusivos post-mineralización de composición principalmente granodiorítica, generando un *"roof-pendant"* y zonas de foliación con la andesita La Liga encajonada entre ambos cuerpos (Bookstrom, 1975).

3.2. Geología regional

3.2.1. Unidades litoestratigráficas

Complejo Subvolcánico Agua Salada (Jurásico Superior):

Este complejo, definido por Emparan y Pineda (2000), consiste en una sucesión de 6400 metros de lavas andesíticas, tobas, ignimbritas e intercalaciones de caliza (Charrier et al., 2007) además de *stocks* dioríticos, andesíticos y microdioríticos de piroxeno, anfíbola y localmente olivino, los cuales están intruídos por el Plutón San Juan y por dioritas del Berriasiano. Estos cuerpos afloran al oeste y entre las trazas de la Zona de falla Romeral, transponiéndose en ciertos

sectores a metabasitas de hornblenda y biotita. Junto a estas se presentan brechas de falla con lentes de hornblendita y zonas de protomilonita y esquistos miloníticos de biotita, con intensa silicificación y una alteración propilítica sobreimpuesta.

Formación Arqueros (Neocomiano):

Definida por Aguirre y Egert (1962) y modificada por Emparan y Pineda (1999), la Formación Arqueros está formada por una secuencia de andesitas porfídicas con intercalaciones de calizas fosilíferas y depósitos estratiformes de manganeso en el miembro superior, con un espesor que varía entre 260 a 600 metros y que aflora en las quebradas Santa Gracia-Salapor y al sur del río Elqui.

Esta formación se subdivide en tres miembros principales. El miembro inferior corresponde a lavas andesíticas y basaltos macizos que presentan sectores amigdaloidales con abundante calcita rellenando espacios y reemplazando parcialmente fenocristales de clinopiroxeno y anfíbola. En algunos afloramientos se describen estructuras de "almohadilla", las cuales sugieren un volcanismo en ambiente subacuático (Aguirre y Egert, 1965). Este primer miembro tiene espesores que pueden alcanzar los 600 metros y se encuentra subyaciendo en concordancia el segundo miembro. El miembro siguiente está constituido por 180 metros de calizas bioclásticas, calizas micríticas, areniscas calcáreas fosilíferas, chert y brechas sinsedimentarias con matriz calcárea. La fauna de trigonias observada permitió acotar su periodo de deposición a una edad neocomiana (Pérez y Reyes, 1998a; Pérez y Reyes, 1999a; Rubilar, 1998). Finalmente, el tercer miembro, el cual se encuentra sobreyaciendo concordantemente el miembro anterior y subyaciendo la Formación Quebrada Marquesa, se caracteriza por la presencia de areniscas laminadas en su parte inferior y por conglomerados matriz soportados en el techo del miembro, con un espesor promedio de 50 metros.

Finalmente, Morata et al. (2008) reporta edades $^{40}Ar/^{39}Ar$ en plagioclasa de 114.1±0.5 Ma, 113±0.9 Ma y 91.0±0.6 Ma para las unidades volcánicas de esta formación, constriñendo la edad del volcanismo del arco Cretácico Temprano.

Formación Quebrada Marquesa (Aptiano-Coniaciano):

Al igual que la Formación Arqueros, esta formación es definida por Aguirre y Egert (1962) y modificada, posteriormente, por Emparan y Pineda (1999). Estos autores la definen como una secuencia de rocas sedimentarias clásticas continentales y volcánicas de composición andesítica, además de lentes de arenisca calcárea fosilífera en su base, con un espesor de 1000

metros, la cual se encuentra sobreyaciendo concordantemente la Formación Arqueros y subyaciendo en discordancia la Formación Viñita.

Ésta se divide en cuatro miembros definidos por Biese (1956) cuyas relaciones de contacto son concordantes tanto en la base como en el techo. El primer miembro está constituído por brechas epiclásticas con clastos angulosos de andesitas y granitoides, en menor cantidad, además de intercalaciones de areniscas, tobas, lavas andesíticas, conglomerados y lutitas, que en su totalidad pueden alcanzar hasta 400 metros. En segundo lugar, el siguiente miembro corresponde a tobas líticas con matriz de ceniza y areniscas calcáreas, con una potencia de 75 metros, que contienen lentes de yeso, particularmente, en el distrito El Romero. Por otro lado, el tercer miembro está compuesto por 30 metros de areniscas calcáreas lacustres, las cuales subyacen el cuarto miembro constituido por tobas brechosas líticas y brechas líticas de composición andesítica con intercalaciones epiclásticas y de lavas.

Bajas razones iniciales de $^{87}Sr/^{86}Sr$ (~0.7036) y un rango de ε_{Nd} entre +4.7 y +2.9 para andesitas y andesitas basálticas del Cretácico Inferior (Formación Arqueros y Quebrada Marquesa) coinciden con una signatura isotópica de mezcla entre un MORB y plutones Jurásicos de la Cordillera de la Costa. Este proceso refleja una contaminación cortical de un magma parental máfico asociado a una extensión intra-arco (Morada y Aguirre, 2003) entre los 125 y 110 Ma debido a una baja taza de geneneración (5cm yr^{-1}) en las dorsales oceánicas en el sudeste Pacífico (Larson y Pitman, 1972).

Formación Coquimbo (Neógeno):

Definida inicialmente por Darwin (1846) y Steinmann (1895) y posteriormente modificada por Moscoso et al. (1982a), esta formación corresponde a un conjunto de sedimentos marinos y/o transicionales fosilíferos que afloran en una franja de hasta 7 km en el sector costero, entre los 28º y 30º latitud sur. En su base se tiene una facie marina caracterizada por la presencia de areniscas poco consolidadas con intercalaciones de coquina bien cementadas (Herm, 1969). En cambio, en la zona superior se tienen conglomerados de matriz arenosa calcárea que evidencian una facie regresiva, de ambiente litoral a transicional, y que contienen finas capas de materia orgánica. Esta secuencia se encuentra sobreyaciendo discordantemente las unidades intrusivas mesozoicas y engrana lateralmente con facies fluvio-aluviales de la Formación Confluencia y con los Depósitos Eólicos de Quebrada El Jardín. Basándose en el contenido fósil, esencialmente bentónicos, se asocia a un ambiente litoral a infralitoral de aguas bajas y cálidas (Martinez-Pardo, 1979; Martinez-Pardo, 1980).

3.2.2. Unidades intrusivas

Intrusivos Dioríticos (ca. 145 Ma):

Este conjunto de intrusivos está conformado por monzodioritas cuarcíferas, monzodioritas, dioritas, dioritas cuarcíferas y gabros de biotita, anfíbola y piroxeno que afloran en la zona costera, intruyendo el Complejo Subvolcánico Agua Salada. Mediante dataciones de U-Pb en circón se obtiene una edad de 145±4 Ma para estos intrusivos (Emparan y Pineda, 2000) y mediante K-Ar en biotita y en anfíbola se obtienen edades mínimas de 127 a 130 Ma y de 124±11 Ma, respectivamente (Gana, 1991).

Intrusivos Granitoides (ca. 131-125 Ma):

Estos intrusivos se subdividen en tres cuerpos principales: Plutón Las Carpas, Plutón Cerro del Cobre y Plutón Península de Coquimbo, los cuales afloran al oeste de la Zona de Falla Romeral, intruyendo al Complejo Subvolcánico Agua Salada y a las dioritas jurásico-cretácicas. Corresponden a granodioritas de biotita-piroxeno y de anfíbola, monzogranitos y sienogranitos que datados con K-Ar en biotita presentan edades que fluctúan entre 120 y 131±3 Ma (Gana, 1991; Emparan y Pineda, 2000). Al oeste del Plutón Las Carpas y en el borde oriental del Plutón Cerro del Cobre se observan esquistos miloníticos y cataclasitas porfiroclásticas (Emparan y Pineda, 2000).

Intrusivos graníticos a dioríticos (ca. 100-97 Ma):

En este sector se observan dos grupos de intrusivos de composiciones graníticas a dioríticas. El primero, de edad cretácica temprana (130-110 Ma), corresponde a un conjunto de *stocks* dioriticos y monzograníticos que intruyen a las formaciones Arqueros y Quebrada Marquesa y que se disponen en una franja norte-sur, en el sector oriental de la zona de estudio. Estos cuerpos intrusivos fueron datados mediante K-Ar en biotitas recristalizadas, otorgándole las edades mínimas mencionadas anteriormente (Emparan y Pineda, 2000). El segundo grupo de intrusivos está conformado por cuerpos elongados de dioritas porfídicas de anfíbola y piroxeno, dioritas cuarcíferas de anfíbola y piroxeno, monzodioritas cuarcíferas de piroxeno y anfíbola, granodioritas de anfíbola, monzonitas cuarcíferas de biotita, anfíbola y piroxeno, y monzogranitos de biotita-anfíbola y biotita (Emparan y Pineda, 2000). Estos cuerpos intruyen las formaciones Arqueros y Quebrada Marquesa y son intruídos por granitoides del Cretácico Superior (Emparan y Pineda, 2000). Se obtienen edades de 100±3 Ma y 96±3 Ma mediante dataciones de biotitas por K-Ar en el Plutón Gracia, cuerpo principal de este conjunto de intrusivos (Emparan y Pineda, 2000).

3.2.3. Unidades cuaternarias

Dentro de las unidades cuaternarias, definidas por Emparan y Pineda (2000), se tienen depósitos gravitacionales caracterizados por la presencia de bloques autosoportados, en las laderas de Cerros de San Juan. Lo depósitos fluviales abundan en los valles de la zona, principalmente en la cercanía del río Elqui. Se pueden diferenciar depósitos más antiguos dado el mayor grado de consolidación y debido a la conformación de terrazas laterales que pueden alcanzar hasta 15 metros de altura. Además, se tienen depósitos aluviales de brechas no consolidadas y depósitos coluviales con presencia de bloques angulosos dentro de sedimentos no consolidados. Finalmente, se observan depósitos de playa compuestos por arenas y gravas polimícticas y depósitos eólicos conformados por arenas finas que forman dunas de hasta 5 metros de altura, ambos depósitos situados a lo largo de la línea de costa.

3.2.4. Estructuras

La estructura dominante corresponde a la Zona de Falla Romeral (ZFR), sistema transcurrente de dirección norte-sur ubicada a lo largo de la Cordillera de la Costa (Taylor et al., 1998; Scheuber y Andriessen, 1990), la cual se asocia a la formación de rocas cataclásticas y miloníticas. Esta falla corresponde a una extensión de la Zona de Falla Atacama (Bookstrom, 1975), falla de carácter regional con una extensión que supera los 1000 km entre Iquique y el sur de La Serena (Charrier et al., 2007).

Esta estructura predominante separa la zona de interés en dos dominios estructurales distintos: el Dominio Costero y el Dominio Occidental (Emparan y Pineda, 2000). El primero se sitúa en el costado occidental de la ZFR y está conformado por rocas intrusivas del Jurásico-Cretácico Inferior y por el Complejo Subvolcánico Agua Salada de edad jurásica, unidades controladas por un sistema de fallas con orientación NS-NNE (Espinoza, 2000). Dentro de este dominio se observan terrazas de la Formación Coquimbo (Paskoff, 1970) que se atribuyen a periodos de deposición, alzamiento y sucesivos eventos de cese a los cuales se le asocian procesos de abrasión marina.

Por otro lado, el Dominio Occidental, el cual se sitúa al este de la ZFR, se caracteriza por la presencia de granitoides cretácicos que intruyen la Formación Arqueros y Quebrada Marquesa. En este sector se tienen sistemas de fallas normales de rumbo NNW a NS, cuyo sistema principal corresponde a la Falla El Romero de vergencia oeste y rumbo NNE. Esta estructura se interpreta como una falla de crecimiento ubicada al oeste de una cuenca extensional, la cual pondría en contacto la Formación Quebrada Marquesa y Arqueros (Pineda, 1996; Pineda y Emparan, 1997; Emparan y Pineda, 1999). Al este de esta falla se tienen sistemas de pliegues con ejes que

mantean al norte y de rumbo N5ºE y N20ºW que afectan la Formación Arqueros y Quebrada Marquesa, respectivamente (Sinclinal de Arrayán).

Dentro de la Zona de Falla Atacama se tiene evidencia de movimientos sinestrales durante el Jurásico Medio y Jurásico Tardío (St. Amand y Allen, 1960; Arabasz, 1971). Posteriormente, seguido al evento mineralizador, el sistema se invierte, generando un desplazamiento dextral de 1,5 km (St. Amand y Allen, 1960), inversión que se explica por cambios en la oblicuidad de la convergencia. Finalmente, en las etapas tardías de este sistema de fallas, se han detectado desplazamientos verticales (Arabasz, 1971; González y Carrizo, 2000; González y Carrizo, 2003). A lo largo de la traza de falla se ha detectado cizalle dúctil así como también zonas de deformación frágil posterior (Charrier et al., 2007), donde la primera se asocia al emplazamiento de complejos plutónicos del Cretácico Inferior (Grocott et al., 1994; Dallmeyer et al., 1996), seguido de un enfriamiento progresivo que genera la deformación de carácter frágil. Dentro de este periodo de transición entre deformación dúctil-frágil es cuando ascienden los fluidos primarios que generan los depósitos de tipo magnetita-apatito (Grocott y Taylor, 2002).

3.3. Geología local

3.3.1. Unidades litoestratigráficas

Andesitas La Liga (Cretácico Inferior):

Esta formación corresponde a la unidad hospedante de la mineralización y presenta una fuerte actinolitización, la cual va disminuyendo al alejarse del cuerpo macizo de hierro. Se encuentra cortada por cuerpos subverticales de magnetita maciza que se van desmembrando en sus bordes generando cuerpos brechizados con clastos angulosos y deformados de magnetita y actinolita maciza como matriz. Fuera de estos cuerpos mineralizados se observan numerosas vetillas de magnetita y actinolita que llegan a formar zonas de *stockworks* dentro de la roca caja.

Según lo observado por Moyano (1992), se presentan evidencias de dirección de flujo en esta unidad, definiéndola de esta forma como una unidad volcánica a diferencia de Bookstrom (1977) que la define como un cuerpo intrusivo andesítico.

3.3.2. Unidades intrusivas

Diorita Romeral (Neocomiano):

Este cuerpo intrusivo está constituido, esencialmente, por plagioclasa, augita y magnetita-ilmenita inmersos en una masa microcristalina de actinolita, clinozoisita y esfeno. Intruye la

Formación La Liga y aflora al oeste del cuerpo mineralizado, en contacto por falla con esta formación. Se observan zonas de *stockwork* dentro del cuerpo con presencia de vetillas y vetas de actinolita, magnetita y cloroapatito (Bookstrom, 1975), además de una fuerte alteración cuarzo-fedespática en las cercanías con el cuerpo mineralizado (Romo, 1981).

Plutón Cerro del Cobre (Barremiano-Aptiano):

Cuerpo ubicado al este de la zona de estudio, el cual está asociado a dos plutones félsicos emplazados en el dominio costero: Plutón Las Carpas y Plutón Península de Coquimbo. El Plutón Cerro del Cobre está conformado por monzogranitos de biotita-anfíbola-piroxeno, además de sienogranitos de biotita. En el borde oriental del intrusivo predominan milonitas y cataclasitas asociadas a los primeros estadíos de la falla El Romeral (Emparan y Pineda, 2000).

Batolito Punta de Piedra (Albiano-Aptiano):

Bookstrom (1975) lo define como un cuerpo intrusivo post-mineralización de composición principalmente granodiorítica, que aflora en la parte oriental del distrito. Se diferencian tres cuerpos de distinta composición. En primer lugar, se observa un cuerpo discontinuo y marginal de composición diorítica, que a diferencia de la Diorita El Romeral presenta mayor cantidad de cuarzo y de plagioclasas cálcicas. Por otro lado, se observa una zona interna granodiorítica al sudeste del distrito, cuya mineralogía se caracteriza por la presencia de plagioclasa, microclina, biotita, hornblenda, cuarzo, magnetita e ilmenita (Llaumet, 1977). Finalmente, se tiene una franja marginal granítica de 60 a 100 metros, al noreste del yacimiento, compuesta por microclina, cuarzo, plagioclasa, biotita, magnetita y esfeno, la cual corta tanto el cuerpo diorítico como el cuerpo granodiorítico (Ulloa, 1979). Debido a que intruye a la Formación Arqueros se le otorga una edad post-neocomiana, posterior al evento mineralizador (Aguirre y Egert, 1970).

Diques:

Numerosos diques aparecen dentro del yacimiento, principalmente de rumbo NW a NNW. La composición es variada, pueden ir desde rocas andesítica dentro del Cerro La Liga, diques dioríticos y estériles, con vetillas de magnetita-actinolita en la zona central del yacimiento, hasta diques aplíticos que intruyen la Diorita Romeral (Llaumet, 1977). Además, se tiene, en menor proporción, diques andesítico y estériles de rumbo NNE y con manteos entre 70° y 90° hacia el oeste. Por otro lado, se tiene un conjunto de diques dioríticos subverticales de dirección NW, cortados por vetillas de magnetita-actinolita y un último grupo de diques estériles de composición

variable que cortan el cuerpo mineralizado y que son considerados como post-mineralización (Bookstrom, 1975).

3.3.3. Estructuras

Falla Romeral (Bookstrom, 1975; Espinoza, 2000):

El sistema de mayor importancia regional corresponde al sistema de Falla Romeral, extensión del sistema de Falla Atacama. Es una falla sinestral con un desplazamiento promedio de 700 metros, rumbo NNW y manteos que varían a lo largo de la estructura con valores de 75ºE en la sección sur y 70ºW al norte. Se dispone al oeste de los cuerpos de mena generando una zona de brecha de 10 a 40 metros de espesor que contiene fragmentos deformados de magnetita, actinolita y apatito dentro de una matriz rica en apatito, con presencia de magnetita diseminada y actinolita acicular. Dentro del cuerpo principal, se observan grietas tensionales rellenas con diques intraminerales lenticulares, que presentan una orientación NW y estructuras en *échelon,* lo cual evidencia un emplazamiento directamente asociado a estas estructuras y al movimiento sinestral de la falla. Este sistema de falla controla la distribución de la mineralización tanto de alta como de baja ley dentro del yacimiento.

Falla Este (Bookstrom, 1975):

Falla post-mineralización que se sitúa al este de los cuerpos de mena con un rumbo NNW y que presenta un manteo de 65 a 70º SW. En sus primeros estadíos primaba el movimiento inverso, sin embargo, en la sección norte de la estructura se evidencia un movimiento de tipo dextral posterior que genera un desplazamiento de 150 metros dentro de los esquistos al norte de la zona de estudio. La zona de falla tiene un espesor de 50 a 60 metros y contiene cristales de cuarzo, sericita y caolinita.

Falla NNE (Bookstrom, 1975):

Corresponde a un sistema dextral de rumbo N30ºE y manteo subvertical activo posteriormente al evento mineralizador, que se sitúa al oeste del cuerpo de mena principal y al sudeste del Cerro Norte. Esta falla corta la Falla Romeral, generando una zona de falla aproximadamente 10 metros de ancho y un desplazamiento máximo de 250 metros. Dentro de esta zona la roca se encuentra fuertemente brechizada, además de presentar fragmentos de magnetita y de roca argilizada inmersos en una matriz grisácea con alto contenido de magnetita y hematita.

Sistema NE y NW (Bookstrom, 1975):

Sistema de fallas dextrales que cortan el cuerpo principal de mena generando zonas de brecha de hasta 5 metros de espesor, las cuales contienen clastos de magnetita rodeados por actinolita prismática y apatito.

3.3.4. Mineralización y alteración

Cerro Principal (Espinoza, 2000)

Se observan tres estilos de mineralización distinta en el cuerpo principal de mena. En primer lugar, se tiene un cuerpo de hierro macizo con una ley mayor al 60%, que se presenta en forma de cuerpos subverticales al noroeste del distrito.

El cuerpo de mena brechoso corresponde a una unidad de alta ley con clastos de magnetita, en ciertos casos deformados, que se encuentran rodeados por actinolita prismática. Este cuerpo se dispone en el sector oriental y sur del depósito, generalmente rodeando la mena maciza.

Finalmente, se tiene una mineralización de hierro diseminada y en vetilla dentro de la andesita actinolitizada. En este sector la ley varía entre 22 y 45%.

Cerro Norte (Espinoza, 2000)

Cerro Norte está constituido por un cuerpo oriental de alta ley con bajos contenidos en fósforo y azufre, que se dispone paralelamente a la Falla Romeral, con un rumbo N15°W y un manteo subvertical. Por otro lado, se tiene un cuerpo occidental de baja ley, el cual se encuentra limitado al oeste por la Falla Romeral y al este por esquistos de anfíbol que gradan a esquistos y filitas de biotita, rocas que separan ambos cuerpo mineralizados.

Extensión Sur (Espinoza, 2000)

Corresponde a un cuerpo de alta ley macizo que está rodeado por un cuerpo brechoso de menor ley, ubicados al sur de Cerro Principal. En la mineralización de mena se tienen altos valores de fósforo, desde 0.3% hasta 1%, y de azufre, asociado al contenido en pirita.

En la **Figura 4**, se presenta el mapa geológico regional de la zona de estudio con las principales unidades litológicas y estructuras. Por otro lado, en la **Figura 6** se aprecia la geología local, junto con las alteraciones principales de la zona.
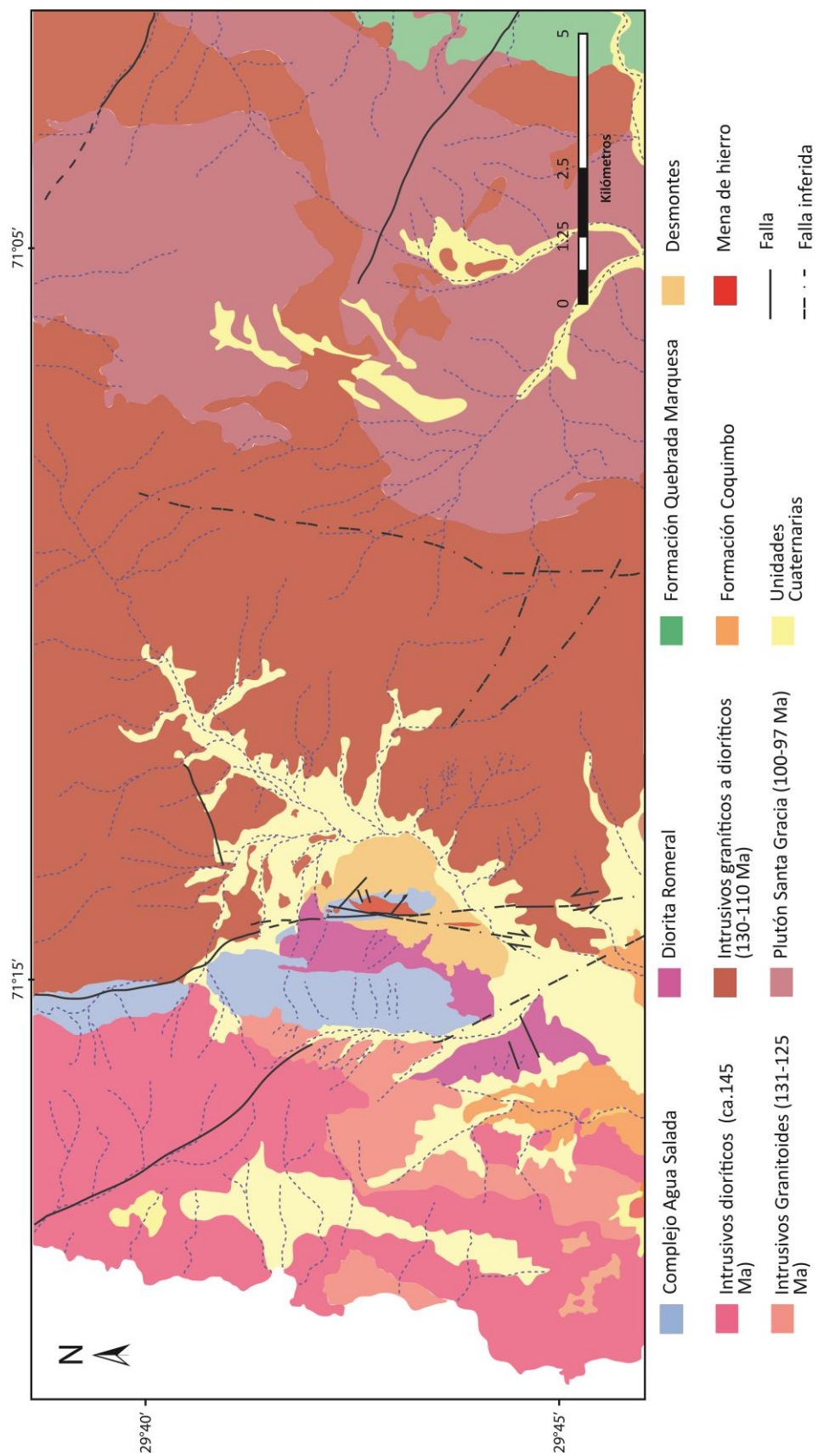
Figure 4. Mapa geológico regional (modificado de Emparan y Pineda, 2000).

Complejo Agua Salada

Intrusivos dioríticos (ca.145 Ma)

Intrusivos Granitoides (131-125 Ma)

Diorita Romeral

Intrusivos graníticos a dioríticos (130-110 Ma)

Plutón Santa Gracia (100-97 Ma)

Formación Quebrada Marquesa

Formación Coquimbo

Unidades Cuaternarias

Desmontes

Mena de hierro

Falla

Falla inferida

Kilómetros

CAPÍTULO 4

GEOLOGY AND GEOCHRONOLOGY OF THE EL ROMERAL DEPOSIT, CHILE: NEW CONSTRAINTS ON THE GENESIS OF IRON OXIDE-APATITE DEPOSITS

Paula A. Rojas[1], Fernando Barra[1], Martin Reich[1], Artur Deditius[2], Adam Simon[3], Francisco Uribe[4], Rurik Romero[1], Mario Rojo[5]

[1] Department of Geology and Andean Geothermal Center of Excellence (CEGA), Universidad de Chile, Plaza Ercilla 803, Santiago, Chile.

[2] School of Engineering and Information Technology, Murdoch University, 90 South Street, Murdoch, Western Australia 6150, Australia.

[3] Department of Earth and Environmental Sciences, University of Michigan, 1100 North University Ave, Ann Arbor, Michigan, USA.

[4] Servicio Nacional de Geología y Minería (SERNAGEOMIN), Santiago, Chile.

[5] Compañia Minera del Pacífico (CAP), Pedro Pablo Muñoz 675, La Serena, Chile.

Corresponding author:
Paula Rojas
Departamento de Geología, Universidad de Chile, Chile
paurojas@ing.uchile.cl
Phone: 56-2-29784532

ABSTRACT

Iron oxide-apatite (IOA) ore deposits are a major source of iron and potentially of rare earth elements (REE), which are essential for the development of new technologies in our growing society. However, the genesis of these deposits remains controversial and both liquid immiscibility and hydrothermal replacement models have been proposed to explain the origin of IOA deposits. El Romeral is one of the largest IOA districts in the Chilean Iron Belt in the Coastal Cordillera of northern Chile. The Cerro Principal magnetite orebody in El Romeral, comprises massive magnetite intergrown with actinolite, with minor apatite, scapolite and sulfides (pyrite ± chalcopyrite). Several types of magnetite mineralization were identified using petrographic and scanning electron microscopic (SEM) observations. The main mineralization

event is represented by zoned magnetite with an inclusion-rich core and inclusion-free rim, followed by two late hydrothermal events, a first related to magnetite veinlets and a second event associated with hydrothermal biotite. Magnetite zoning is consistent with a magmatic-hydrothermal origin for the main iron mineralization, where inclusion-rich magnetite cores are of magmatic origin and the inclusion-free rims formed by the magmatic-hydrothermal fluid exsolved from the source magma. Delta-^{34}S isotopic measurements in hydrothermal sulfides indicate a magmatic origin for sulfur (-0.8 and 2.9‰), in agreement with previous sulfur data reported for other Chilean IOA and IOCG deposits. ^{40}Ar/^{39}Ar dating of actinolite associated with the main magnetite orebody yielded ages of ca. 128 Ma, and are concordant within error with a El Romeral Diorite U-Pb zircon age of 129.0 ± 0.9 Ma (MSWD = 1.9, n =28), showing a clear temporal and genetic association between magnetite ore formation and diorite magmatism. The magnetite-biotite mineralization was constrained at ca. 118 Ma by ^{40}Ar/^{39}Ar dating of secondary biotite. This potassic alteration is ~10 Ma younger than the main mineralization episode and it is possibly related to post-mineralization dikes that crosscut the magnetite orebody. These new observations support a magmatic-hydrothermal model for the formation of IOA deposits in northern Chile, and that the El Romeral mineralization formed at ~129 Ma, followed by a more restricted hydrothermal event associated with post-ore dikes at ca. 118 Ma. Magmatism associated with the beginning of the second Andean stage characterized by a lower angle-compressive Andean-type subduction is represented in the district by the Punta de Piedra batholith (100 Ma). This change in the tectonic configuration marks the end of iron oxide-apatite deposit formation in the area.

4.1. Introduction

El Romeral iron mine is located 22 km north of La Serena, at the southern edge of the Cretaceous Chilean Iron Belt (CIB), which extends from ca. 26° to 30º lat. S in the Coastal Cordillera of northern Chile (**Figure 5**). El Romeral is currently owned by Compañía Minera del Pacífico S.A. (CMP), and it is one of the largest iron oxide-apatite (IOA) districts in Chile with current estimated resources of 451.1 Mt with 28.2% Fe (CAP Minería 2015 annual report). The deposit was discovered at the beginning of the XX century, but operation only started during the early 1960s. During the last decade ore exploitation has been intermittent due to variations of Fe international prices.

The genesis of iron oxide-apatite (IOA), also known as magnetite-apatite or Kiruna-type deposits, has been the subject of intense debate. Three main hypotheses have been proposed based on the possible origin of the mineralizing fluids. On one hand, the magmatic hypothesis proposes that the massive magnetite orebodies are formed by an iron-rich immiscible melt that later ascends and is emplaced with and/or within volcanic sequences (Frutos and Oyarzun 1975; Nyström and Henríquez 1994; Naslund et al. 2002). The hydrothermal hypothesis involves exsolution of Fe-rich magmatic fluids and metasomatic replacement of volcanic (andesite) host

rocks (Bookstrom 1977; Parak 1975; Rhodes et al. 1999; Sillitoe and Burrows 2002). A more recent hypothesis, proposes a magmatic and hydrothermal component in the formation of IOA and genetically related IOCG deposits (Knipping et al. 2015a, b). In this model, magmatic magnetite microlites crystallized from a silicate melt with fluid nucleation on magnetite crystals. The magnetite-bubble pair ascends within the magmatic chamber in a manner analogous to the mineral flotation process used in extractive metallurgy. Further growth and accumulation of primary magnetite and subsequent precipitation of iron transported as $FeCl_2$ complexes on primary magnetite results in zoned magnetite crystals with a magmatic core and a hydrothermal rim.

The El Romeral district was previously studied by Bookstrom (1975; 1977), who presented a detailed description of the geology of the district and proposed a hydrothermal origin for the magnetite orebodies. However, the genesis of iron oxide-apatite (IOA), also known as magnetite-apatite or Kiruna-type deposits, has been the subject of intense debate. Three main hypotheses have been proposed based on the possible origin of the mineralizing fluids. On one hand, the magmatic hypothesis proposes that the massive magnetite orebodies are formed by an iron-rich immiscible melt that later ascends and is emplaced with and/or within volcanic sequences (Frutos and Oyarzun 1975; Nyström and Henríquez 1994; Naslund et al. 2002). The hydrothermal hypothesis involves exsolution of Fe-rich magmatic fluids and subsequent metasomatic replacement of volcanic (andesite) host rocks (Bookstrom 1977; Parak 1975; Rhodes et al. 1999; Sillitoe and Burrows 2002). A more recent hypothesis, proposes a magmatic and hydrothermal component in the formation of IOA and genetically related IOCG deposits (Knipping et al. 2015a, b). In this model, magmatic magnetite microlites crystallized from a silicate melt with fluid nucleation on magnetite crystals. The magnetite-bubble pair ascends within the magmatic chamber in a manner analogous to the mineral flotation process used in extractive metallurgy. Further growth and accumulation of primary magnetite and subsequent precipitation of iron transported as $FeCl_2$ complexes on primary magnetite results in zoned magnetite crystals with a magmatic core and a hydrothermal rim.In this contribution we provide new geological and mineralogical information on the El Romeral as well as S isotope data in order to determine the source of sulfur in this deposit. Additionally, new $^{40}Ar/^{39}Ar$ and U-Pb zircon ages are presented to determine the timing of the deposit formation and its possible relation with mafic intrusions. The data reported here coupled with recent works on Los Colorados IOA (Knipping et al. 2015a, b; Bilenker et al. 2016; Reich et al. 2016) provide further constraints on the origin of IOA deposits in northern Chile.

4.2. Geological background

During the Early Jurassic to Early Cretaceous, the western margin of Gondwana was characterized by an extensional tectonic regime associated with the first Andean tectonic cycle (Coira et al. 1982). This tectonic setting resulted in the development of two major

morphotectonic features: a trench-parallel magmatic arc associated with shear zones, i.e., the Atacama Fault Zone (AFZ); and an eastern back-arc basin (Brown et al. 1993; Scheuber et al. 1994). These features were the result of either the ascent of the asthenospheric wedge, or by decoupling of an old and cold oceanic plate with the continental margin (Charrier et al. 2007) during the renewed subduction caused by the onset of the break-up of Gondwana (Jaillard et al. 1990).

The AFZ is a major strike-slip fault system formed during the Early Jurassic, and is characterized by an early stage with sinistral movements (Jurassic to Early Cretaceous), followed by dextral shearing (Late Cretaceous) and final vertical displacements. These displacements were caused by changes in the plate configuration and in the convergence vector of the subducting plate (Scheuber and Andriessen 1990).

Several ore deposit types are located along this >1000 km long fault zone, among them stratabound Cu-(±Ag), porphyry Cu, iron oxide-copper-gold (IOCG) and more than 50 iron oxide-apatite (IOA) deposits, which forma part of what is known as the Chilean Iron Belt (CIB) in the Coastal Cordillera of northern Chile. Ore deposits are mostly hosted in thick volcanic units such as La Negra (Middle to Late Jurassic) or Punta del Cobre Formation (Late Jurassic to Early Cretaceous). These formations comprise a sequence of basalts, basaltic-andesite, andesite and dacite lavas, tuffs and lesser sedimentary units that represent the Mesozoic magmatic arc.

Iron oxide-apatite deposits are characterized by the presence of subvertical massive low-Ti and V-rich magnetite orebodies with actinolite and minor apatite, crosscut by late hydrothermal actinolite and sulfide veinlet (mostly pyrite with subordinate chalcopyrite), and diorite to granodiorite dikes (Sillitoe 2003; Barra et al. 2017). Lateral extent of these orebodies can reach up to several tens of meters, and are usually discontinuous with massive magnetite grading to a breccia zone with magnetite clasts immersed in an actinolite matrix, followed by an outer low-grade ore zone with magnetite veinlets and disseminated magnetite grains in andesite host rocks affected by pervasive actinolite alteration. In some IOA deposits, such as El Romeral, the orebody is mylonitized in faults zones or show fluidal textures.

4.3. Deposit Geology

El Romeral is hosted by andesite lavas from La Liga Formation (Late Jurassic to Neocomian), a subunit of the Agua Salada Volcanic Complex (Emparan and Pineda 2005). This formation was intruded at the western margin of the district by diorite intrusions from Late Jurassic to Early Cretaceous (U-Pb zircon age of 145±4 Ma, Emparan and pineda 2000) and by the Cerro del Cobre batholith (**Figure 6**), which comprises Early Cretaceous (U-Pb age in zircon

of 126.5±2 Ma; Emparan and Pineda 2000) monzogranite to sienogranite intrusions. Magnetite orebodies are enclosed by the Romeral Diorite, a mafic body that intruded andesite host rocks from La Liga Formation (**Figure 7**) and which has not been dated. Near the Romeral fault both andesite and the Romeral Diorite are affected by pervasive silicification (**Figure 8A**). At more distal areas La Liga Formation shows a minor epidote alteration (**Figure 8B**). On the eastern section of the studied area, the post-ore Punta de Piedra granite to granodiorite batholith intruded the andesite sequences (**Figure 6**). These intrusions reflect the arc migration during the Early Jurassic to Late Cretaceous, which is also evidenced by extrusive units such as the Agua Salada Complex (Early Jurassic-Kimmeridgian), the Arqueros and the overlying Quebrada Marquesa Formations (Kimmeridgian-Tithonian to Albian), and the Quebrada La Totora Beds of late Early Cretaceous age (Charrier et al. 2007). Additionally, NW to NNW trending pre-, syn-, and post-ore dikes of diorite to granodiorite composition are observed cross-cutting the volcanic host rock and the Romeral Diorite (Bookstrom 1977). Pre-ore dikes have a diorite composition and may be either iron-enriched or iron-depleted, suggesting the existence of magmas with different compositions before the formation of the deposit. Syn-ore dikes display a diorite affinity with accessory Ti-rich magnetite. Post-ore dikes have a more variable composition with diorite to albite or quartz dominant intrusions. This compositional range reflects a strong differentiation after ore formation (Bookstrom 1975).

Mineralization in El Romeral is related to three main orebodies: Cerro Principal, Cerro Norte and Extensión Sur (Espinoza 2000). The largest orebody is the Cerro Principal and it is characterized by subvertical orebodies with massive magnetite and minor actinolite (**Figure 7, Figure 8C**), an outer breccia zone with deformed magnetite clasts immersed in an actinolite and scapolite matrix or with prismatic actinolite crystals (**Figure 8D, E**), and an outermost alteration halo with fine grained actinolite and disseminated magnetite in the andesite host rock. The Cerro Principal massive orebody has an iron grade exceeding 60% Fe, whereas in the breccias zone the iron grade ranges between 22% and 45%. Additionally, a secondary iron event of magnetite veinlets crosscuts the Cerro Principal magnetite orebody.

Cerro Norte and Extensión Sur are smaller uneconomic orebodies located at the outer edge of the current pit. Cerro Norte comprises the northernmost massive magnetite body with low F and S contents. The orebody is parallel to the Romeral fault and is crosscut by the East fault. On the southern section of El Romeral, the Extensión Sur mineralization comprises massive and brecciated magnetite with high contents of P (>0.3%) and S (>1%).

El Romeral magnetite orebodies were emplaced along the sinistral NNW strike-slip Romeral Fault System (RFS), which is part of the Romeral-La Silla del Gobernador segment (Charrier et al. 2007), an extension of the Atacama Fault System (**Figure 6**). Fragile and ductile domains are described in fault zones, represented by brecciated areas, along with foliation zones

in host rocks with predominant actinolite crystals oriented along faults. Previous dating of these fault zones yielded ages between 115±4 and 100±2 Ma (K-Ar on biotite and whole rock, and ^{40}Ar/^{39}Ar inverse isochron, Emparan and Pineda 2000; 2005), which reflect a basin inversion episode due to a change from a low subduction angle to a compressive or Andean-type subduction (Maksaev 1990; Scheuber and Andriessen 1990).

The Cerro Principal orebody is delimited by the NNE dextral fault on the western side and on the eastern side by the East fault (**Figure 6**). This post-ore NNW strike-slip fault with a 65-70° SW dip has a prior sinistral movement, followed by a dextral stage displacement (Bookstrom 1977). Two additional minor fault systems are described, one with a NNW direction similar to the East fault, and the other with a NE direction. Both are dextral systems with magnetite clasts immersed in an actinolite, scapolite and apatite matrix.

4.4. Samples and methods

Five drill cores within the El Romeral pit were selected for mapping and sampling; three from the northern section (drill-cores PRP-0853, 500m; PRP-0733, 432.4m; DDH-5008 436.2m), one from the central area (DDH-7501, 337.3m), and one from the southern section (PRP-0702, 400m) (**Figure 6**). Eighty-seven thin sections were studied under reflected and transmitted light microscopy in order to characterize the mineralogy of the deposit and determine the paragenetic sequence. Further mineral identification and characterization was performed using SEM-EDS. Additionally, two samples were selected for ^{40}Ar/^{39}Ar thermocronology (biotite sample URM-118t; actinolite sample URM-115t), and two samples for U-Pb dating, one from the Romeral Diorite and the other from the Punta de Piedra batholith in order to constrain magmatic history of the district.

4.4.1. Scanning Electron Microscopy-Energy Dispersive X-ray Spectroscopy (SEM-EDS) analysis

Electron microscopy analyses were performed at the CEGA Microanalysis Laboratory, Department of Geology, Universidad de Chile, Santiago, Chile using a Model FEI Quanta 250 SEM. Analyses were carried out on selected minerals to confirm petrographic identification and on scapolite crystals in order to discriminate between the different end members of the group (i.e., meionite, marialite or silvialite).

4.4.2. $^{40}Ar/^{39}Ar$ dating

Two samples were selected from drill-core DDH-5008 (283537E/6708604N) for $^{40}Ar/^{39}Ar$ dating. Sample UMR-115t (93 m a.s.l.) comprises massive magnetite intergrown with centimetric actinolite crystals. Sample URM-118t (291 m a.s.l) corresponds to the Romeral Diorite and contains disseminated magnetite associated with secondary biotite. Both samples were first studied under petrographic microscope in order to select unaltered minerals. Several actinolite grains were handpicked from the crushed sample and split in two sub-samples, and about 10 biotite crystals were selected for analysis. Samples, Fish Canyon standard and Ca and K salts were irradiated at the Nuclear Research Center of La Reina, Santiago, Chile and later stored for three months in order to decrease sample activity. Dating was performed at the SERNAGEOMIN Isotopic Geology Lab, Santiago, Chile by using a Mass Analyzer Products (MAP) Model 215-50 mass spectrometer with an electron multiplier (Johnston MM1-1SG), integrated CO_2 laser, gas extraction system (Merchantek MIR10-TP), and automated line composed of one SAES ST-101 Zr-Al getter (450°C) and two SAES ST-172 Zr-V-Fe getters (21°C and 250°C). Analyses of Ca and K salts were used for correction of isotopic interferences, and the Fish Canyon standard for determination of the J factor. Data were reduced using the ArArCALC v2.4 software (Koppers 2002).

4.4.3. U-Pb zircon dating

Two intrusion samples were selected for U-Pb zircon dating in order to constrain magmatic hidroty in the El Romeral district. Sample Rom-Gd was collected from the Punta de Piedra granodiorite batholith, from an outcrop located on the east side of the pit (284000E/6708000N; 161 m.a.s.l.), and sample ROM-109 from the Romeral Diorite, at the west margin of the main orebody (283480E/6711016N; 350 m.a.s.l.). Sample preparation and analysis were performed at the Sample Preparation Laboratory and at the CEGA Geochronology Laboratory, respectively, at the Geology Department, Universidad de Chile, Santiago, Chile. Rock grinding was performed by using first a jaw crusher followed by a disc mill. Samples were sieved and the fraction smaller than 500 µm was collected. Heavy mineral fractions were concentrated using a Gemini water table, followed by a Frantz isodynamic magnetic separator. Zircons were later separated using heavy liquids (tetrabromomethane and/or methylene iodide decantation) and final handpicking under a binocular microscope. Approximately 50 zircon grains per sample were mounted in epoxy resin with Plešovice (Sláma et al. 2008) and Temora2 (Black et al. 2004) standards. The sample-standard mount was polished before analysis and cathodoluminescence (Cl) images of zircon crystals were obtained by using a FEI Quanta 250 SEM Scanning Electron Microscope coupled with a Centaurus sensor. These images were used to identify zoning and inherited components. Uranium-Pb dating was performed by Laser Ablation Multicollector- Inductively-Coupled Plasma Mass Spectrometer (LA-MC-ICPMS). Analyses were conducted on 30 µm diameter spots using an Analyte G2 ArF excimer laser ablation system with a 193 nm wavelength. Ablated material was transported by a helium flux with a rate of 0.5

LPM into a Neptune Plus MC-ICP-MS. Measurements were performed using the sample-bracketing method, and data reduction and plots were carried out with Iolite (Patton et al. 2010) and Isoplot 4.0 (Ludwig 2010), respectively.

4.4.4. Sulfur isotopes

Eight sulfide samples were collected for sulfur isotope analysis; five from drill core PRP-0702, two from PRP-0853, and one from DDH-5008 (**Figure 6**). Samples were selected considering style of mineralization and depth. Samples ROM-017 (79.50m), ROM-018 (84.65m), and ROM-023 (133.95m) comprise pyrite and minor magnetite in quartz veinlets; samples ROM-019 (87.40m) and ROM-020 (89.95m) were collected from magnetite breccias with euhedral pyrite clasts (**Figure 8F**); samples ROM-125 (215.85m), ROM-139 (410.1m), and ROM-177 (410.13m) are located in the cataclasite zone and include magnetite, pyrite with minor quantities of actinolite, chalcopyrite and apatite; sample ROM-177 (410.75m) is an actinolite veinlet with pyrite. Mineral concentrates with >99% pure pyrite were obtained by crushing followed by hand-picking under a binocular Olympus microscope. Mineral concentrates were analyzed at the Environmental Isotope Laboratory, Department of Geosciences, University of Arizona, Tucson, Arizona, USA. A continuous-flow gas-ratio mass spectrometer (CF-IRMS) ThermoQuest Finningan Delta PlusXL model with coupled Costech elemental analyzer was used for δ^{34}S measurements. Before analyzing samples, concentrates were introduced into a combustion chamber with O_2 and V_2O_5 (Coleman and Moore 1978) obtaining a SO_2 gas at 1030°C, which is the analyzed product. System was calibrated by using two international standards; OGS-1 which is a $BaSO_4$ precipitated from seawater, and NBS123, a sphalerite sample with a δ^{34}S reported value of +17.09‰. A linear calibration between -10 and +30 ‰ was performed and a precision of ±0.15 or 1σ was estimated by diverse internal standards measurements (http://www.geo.arizona.edu/node/153).

4.5. Results

4.5.1. Ore Mineralogy

Mineralization in El Romeral comprises three orebodies: Cerro Principal, Cerro Norte and Extensión Sur. Cerro Norte and Extensión Sur are located at the outer northern and southern edges of the pit, respectively (**Figure 6**). Exploitation was developed around the Cerro Principal orebody, which comprises subvertical massive massive magnetite orebodies (**Figure 7**, **Figure 8C**) intergrown with large actinolite crystals (**Figure 8D**, **Figure 9A**). Massive magnetite grades outward to a breccia or mylonitic unit near fault zones (**Figure 8E**), and disseminated magnetite with actinolite and minor sulfides. Several granite to diorite dikes cut the main orebody, and some of them are mineralized (Bookstrom 1977).

Three types of magnetite grains have been identified in massive magnetite orebodies: an inclusion-rich sulfide-poor magnetite (magnetite I, **Figure 9B**), mainly with actinolite (I), quartz (I) and oxides (ilmenite, rutile) inclusions, an inclusion-free magnetite (magnetite II) with sulfide inclusions (pyrite I ± chalcopyrite I), and local and shallow magnetite (magnetite III) chemically zoned (Rojas et al. 2017). Magnetite I was observed surrounded by magnetite II with interstitial sulfide mineralization (pyrite II, chalcopyrite II). In magnetite II, ilmenite and magnetite "patches" as exsolution textures are recognized (**Figure 9C**). A fourth type of magnetite (magnetite IV) is observed as thin veinlets that crosscut the massive orebody (**Figure 9D**). A final restricted event of magnetite mineralization (magnetite V) is observed as fine grains associated with secondary biotite (**Figure 9E**) in the andesite host rock and in the Romeral Diorite. A primary magnetite related to the andesite from La Liga Formation is also observed, which shows ilmenite exsolution lamellaes (**Figure 9F**).

4.5.2. Gangue Mineralogy

The dominant hydrothermal alteration products in El Romeral include silicification and abundant actinolite. The former is observed as a widespread pre-ore and pervasive silicification (**Figure 8A, Figure 10A**) that affected the andesite host rocks and the Romeral Diorite, proximal to the Romeral fault zone, at the western margin of the deposit (**Figure 6**). Actinolite predominates over quartz and it is mainly associated with magnetite formation. Two forms of actinolite have been recognized, small actinolite crystals (actinolite I) with quartz (quartz II) and clinopyroxene within magnetite crystals (**Figure 10B**). The second type corresponds to a later syn-ore crystallization of acicular to tabular actinolite (actinolite II) that reaches centimetric dimensions (**Figure 9A**). Actinolite II is usually observed at shallow and/or at the margins of iron bodies, and also as an alteration halo related to the crystallization of massive magnetite. This event includes primary hornblende crystals with reaction rims altered to actinolite, followed by a chlorite alteration, and dominant fibrous to acicular actinolite disposed as oriented crystals in fault zones (**Figure 10C**), as well as larger actinolite crystals, proximal to the massive magnetite.

A late actinolite event is present as the matrix of magnetite breccias near fault zones and thin veinlets related to sulfide mineralization, i.e., pyrite (pyrite III) with drop-shaped chalcopyrite (chalcopyrite III) and pyrrhotite inclusions (**Figure 10D, E**). Chalcopyrite mineralization remains in equilibrium at low temperature conditions with disseminated chlorite and with chlorite veinlets. This event is also associated with Ca-rich fluids, where epidote aggregates, calcite and disseminated titanite was formed. Titanite is observed as euhedral diamond-shaped crystals, disseminated in the host rocks or as anhedral crystals surrounding disseminated magnetite or ilmenite crystals.

Local massive cumulates of scapolite and disseminated crystals or veinlets of apatite are also observed as part of the hydrothermal event. Scapolite was chemically analyzed using energy dispersive x-ray spectroscopy (EDS) where a solid solution between Na-Ca Cl-scapolite, with a predominance of Na over Ca was recognized.

Finally, hematite replaced magnetite through crystallographic planes, and rutile is observed in association with titanite with magnetite and ilmenite. This event is followed by a minor and local copper enrichment with chalcopyrite replaced by bornite followed by digenite and covellite (**Figure 10F**). Lastly, an acidic alteration dominated by sericite and/or clay minerals is described as a final alteration event. The paragenetic sequence is presented in **Figure 11**.

4.5.3.   Actinolite $^{40}Ar/^{39}Ar$ ages

In this study two aliquots of an actinolite II sample (sample URM-115t) were analyzed using a MAP 215-50 mass spectrometer (**Tabla 1**; **Figure 12**). Both analyses (sub-sample URM-115t-01 and sub-sample URM-115t-02) yielded consistent plateau ages with 100% of the gas released. Sub-sample URM-115t-01 has a plateau age of 127.7±1.5 Ma (2-sigma) with constant Ca/K and Cl/K ratios; excluding the first and second step for Ca and only the first step for Cl. Higher $^{36}Ar_{(Ca)}$ contributions in step four, six and seven are observed with 13%, 14% and 37% of ^{36}Ar, respectively, which resulted in a relevant Ca correction. The plateau age is the same within error as the calculated inverse isochron age of 127.8±1.8 Ma (2-sigma), and the isochron intercept is consistent with a $^{40}Ar/^{36}Ar$ atmospheric ratio (295.2±3.7). Sub-sample URM-115t-02 yielded a plateau age of 126.5±2.0 Ma, which is concordant with the previous sub-sample. Constant Ca/K and Cl/K ratio are obtained, excluding the first, second, third, and final step for Ca and only the first step for Cl. Relevant Ca correction was performed for the first step where a higher $^{36}Ar_{(Ca)}$ contribution is observed. The calculated age using the inverse isochron method (126.3±2.1 Ma; 2-sigma) is consistent with the plateau age, and the isochron intercept indicates an atmospheric contribution for the $^{40}Ar/^{36}Ar$ ratio (295.9±3.0).

4.5.4.   Hydrothermal biotite $^{40}Ar/^{39}Ar$ age

Stepwise heating technique was performed in eight steps at a potency range between 3 and 30 W. Six consecutive steps comprises 95.3% of the gas released and yielded an age of 118.3±0.2 Ma (**Figure 13**). Argon-36 contribution produced by Ca decay is negligible, evidencing a low interference signal. Age determined using the inverse isochron approach (118.5±0.2 Ma) is consistent with the plateau age. The initial 267.3±2.9 $^{40}Ar/^{36}Ar$ ratio is significantly different to the atmospheric ratio. This difference is possibly caused by the presence of a cluster of datapoints in the inverse isochron plot generating a high uncertainty (**Figure 13**). Results are reported in **Table 3**.

4.5.5. Zircon U-Pb ages

Zircons extracted from the Romeral Diorite are dominated by prismatic semitransparent, colorless crystals, with a maximum length of 200 microns. In general, besides the typical igneous oscillatory zoning, zircons display local re-crystallization zones, suggesting late-magmatic processes where impurities from unstable trace element-rich zones are expelled and then concentrated in trace element-rich convolute zones, generating a homogeneous zircon domain (Corfu et al. 2003). In order to avoid inaccurate results, these re-homogenized areas were not analyzed. Zircons extracted from the Punta de Piedra sample are clear, prismatic, and colorless and can reach up to 300 microns in length. The analyzed zircons show the typical oscillatory zoning.

Zircon U-Pb agres are presented in **Table 4** and **Table 5**, and Concordia, Tera-Wasserburg and weighted average plots are shown in **Figure 14** and **Figure 15** for the Romeral Diorite and the Punta de Piedra batholith, respectively. The Romeral Diorite sample yielded a weighted average age of 129.0±0.9 Ma (MSWD = 1.9, n = 28) (**Figure 14**). Calculated Th/U ratios range from 0.4 to 1.4 indicating a magmatic origin for zircons. The Concordia and Tera-Wasserburg plots show that the analyses are concordant. For the Punta de Piedra Batholith a weighted average age of 102.2±2.0 Ma (MSWD = 5.3, n = 12) was obtained (**Figure 15**). Th/U ratios range between 0.1 and 1.5, values that are in agreement with typical igneous zircons.

4.5.6. Sulfur isotopes analyses

In order to clarify the provenance of sulfur and, in consequence, to elucidate the source for sulfides in the deposit, sulfur isotope composition of sulfides, mainly pyrite, collected from veinlets and breccia bodies was measured. Isotopic values from sulfides, described as part of a secondary hydrothermal mineralization, are listed in **Table 6**. Delta-^{34}S values for seven pyrite samples range from -0.8 to 1.4‰ with a mean of 0.8‰ and a median of 0.5‰. A pyrite ± chalcopyrite (~30% chalcopyrite) concentrate (sample ROM-139) shows a heavier sulfur isotopic composition, with a value of 2.9‰. On the other hand, the two breccia samples (samples ROM-019 and ROM-020) show a consistent value of 0.5‰, in contrast with a more widespread δ^{34}S range for veinlets, with values between -0.3 and 1.4‰. A large range of δ^{34}S values is also observed in mylonite samples (samples ROM-125 and ROM-139), where two measurements of -0.8‰ and 2.9‰ were obtained. Finally, it is noteworthy that no correlation is observed between depth and δ^{34}S values.

4.6. Discussion

4.6.1.   Ore-forming process and paragenetic sequence

The El Romeral iron ore is found as massive, brecciated and disseminated magnetite with actinolite and minor sulfides. Five types of magnetite have been recognized (**Figure 9**): (i) a massive inclusion-rich magnetite I with euhedral quartz I inclusions and minor chalcopyrite I and pyrite I, (ii) inclusion-free magnetite II with actinolite I, quartz II, pyroxene and minor chalcopyrite II and pyrite II within interstitial spaces of subhedral magnetite crystals. This magnetite II is also related to large actinolite II crystals present at the margins of the orebody; (iii) a inclusion-free magnetite with solid solution zonations (Rojas et al. 2017); (iv) a fourth type represented by late magnetite veins, in some areas with sulfides or crosscut by apatite veinlets. Sulfide mineralization is also related to this vein event, with abundant pyrite III, subordinate chalcopyrite III and pyrrhotite associated with secondary actinolite II and chlorite; and (v) disseminated magnetite V with minor biotite. The first three magnetite types (mainly I and II) comprise the main iron ore event (Event I, **Figure 11**), whereas magnetite IV and V represent two distinct late hydrothermal events (Event II, **Figure 11**).

Event I: During the first event of ore formation, inclusion-rich magnetite cores crystallized, with minor chalcopyrite and pyrite inclusions. Quartz euhedral inclusions follow crystallographic planes in magnetite (**Figure 9B**), suggesting exsolution processes at low cooling rates (Rojas et al., submitted). Chalcopyrite is stable below 557ºC (Pankratz and King 1970) and pyrite below 770ºC at 100 MPa (Kullerud and Yoder 1959), hence these two sulfide phases are not stable at mafic igneous conditions, i.e., at temperatures ranging from 800ºC to 1000ºC (diorite crystallization temperature). Thus, the presence of an originally intermediate solid solution (Jugo et al. 1999), or a slightly S-deficient intermediate solid solution, $CuFeS_{2-x}$ (Vaughan and Craig 1978), for later chalcopyrite formation, and pyrrhotite or prior monosulfide solid solution (Edmonds and Mather 2017) for subsequent pyrite crystallization may be considered. Magnetite II is characterized by the presence of the assemblage actinolite, quartz and pyroxene observed within magnetite crystals (**Figure 10B**). This assemblage could represent accessory microlites incorporated during bubble flotation and/or the chemical composition of the bubble and, therefore, of the magmatic volatile phase or hypersaline fluid (Knipping et al. 2015a,b). In addition, at the margins of the massive magnetite orebody, large actinolite (actinolite II) crystals with minor sulfides, mainly pyrite with subordinate chalcopyrite, are present in interstitial spaces between euhedral magnetite II crystals. These sulfides are possibly precipitated from these fluid-rich bubbles. The textures of these magnetite types and the nature of the inclusions are similar to those described by Knipping et al. (2015a) for Los Colorados, and hence, a magmatic-hydrothermal origin is a plausible model to explain the origin of the ore mineralization in El Romeral.

34

In addition, high-temperature experimental work on the stability of actinolite from IOA deposits, demonstrates that actinolite with Fe-numbers (Fe#) ranging from 0 to 0.4 and Ca >1.7 a.p.f.u, is stable at igneous conditions, i.e., above the water-saturated andesite solidus (up to 900°C at 2 kbar) (Lledo and Jenkins 2008). Further, Bilenker et al. (2016) analyzed actinolite crystals from Los Colorados obtaining a Fe# between 0.23 and 0.72, yielding temperatures that range from 620 to 785ºC at 100 MPa and from 640 to 810ºC at 200 MPa, which support the idea of a magmatic origin for the actinolite. Similar conditions are obtained for El Romeral, where low Fe# in actinolite I and II indicate a crystallization temperature of 735-805°C and 770-840°C at 100 MPa and 200 MPa, respectively (Rojas et al. 2017).

Ilmenite exsolution lamellaes (**Figure 9F**) or ilmenite "patches" on grain rims (**Figure 9C**) have been observed in primary (volcanic) magnetite and in magnetite (II) grains, respectively. The former is considered as a low temperature and slow diffusion rate migration, with ilmenite or Ti remaining inside the crystal in which an increase in oxidation fugacity and diffusion will lead to the formation of Ti-rich granules or "patches" at the rims of a Ti-poor magnetite (Buddington and Lindsley 1964). In contrast, blebs-type crystals are formed by high temperature migration or "granule-oxyexsolution" associated with a loss of components from the magnetite structure (Buddington and Lindsley 1964).

On the other hand, Rojas et al. (2017) report distinct chemical zonings in magnetite III, which are related to changing conditions such as temperature or pH that affect hydrothermal fluid composition at shallow depths (<100 m).

Event II: In El Romeral, scapolite is related to magnetite type IV from the second event (**Figure 11**). In El Romeral scapolite is related to the second iron event. Sundius (1915) studied the origin of this mineral in the Kiruna district, Sweden, and proposed two main possible origins for this mineral phase: a regional-pneumatolytic origin generated by volatile contribution associated with magma crystallization, or a secondary origin caused by the remobilization of host rock components during regional metamorphism. In El Romeral, scapolite is Cl rich (marialite) with more Na than Ca. Chlorine may be sourced from fluids exsolved during the crystallization of an arc magma, which commonly contains ≤3000 ppm Cl (Johnson et al. 2010), or from the andesitic host rock (~130 ppm, Ewart 1982). The presence of scapolite in veinlets and its Na-rich nature support a hydrothermal origin for El Romeral scapolite. In addition, the epidote, calcite and titanite assemblage observed in veinlets also supports a hydrothermal event with temperatures ranging between 200º and 250°C.

Additionally, the presence of Ti-rich phases, such as titanite and ilmenite surrounded by rutile, as exsolution "patches" in magnetite II, may suggest an originally Ti-rich system in which

the Ti could be extracted from the magnetite structure and subsequently precipitated as titanite and/or ilmenite. This high-field strength (HFS) element is more incompatible than other transition element and its mobility at low temperature is usually small, especially during weathering and low grade metamorphism (Pearce and Cann 1973). Nevertheless, Ti solubility is enhanced by the formation of hydroxyfluoride (Ti(OH)$_3$F^0) or hydroxychloride (Ti(OH)$_3$)Cl^0) complexes (Purtov and KoteVnikova 1993) with increasing contents of F and Cl in acid solutions, a process that supports the hydrothermal nature for titanite and rutile.

Sulfide mineralization is characterized by the presence of pyrite with drop-shaped chalcopyrite and pyrrhotite (**Figure 10E**). These equilibrium textures suggest abrupt melt cooling. were the stability between these three mineral phases at 50 MPa (approximately 1.8 km depth) and at 360ºC, reasonable T-P conditions for this sulfide event, reflect a sulfur fugacity of ca. -9 and oxygen fugacity lower than -30 (Hezarkhani et al. 1999).

The final magnetite mineralization episode is represented by a restricted late event of disseminated magnetite type V associated with secondary biotite (**Figure 9E**). This late hydrothermal event is observed in some areas around the magnetite orebody affecting the host rocks, and is possibly related to the intrusion of post-ore dikes that resulted in a potassic alteration with temperatures between 550° and 650°C (Rojas et al. 2017).

Lastly, minor chalcopyrite grains show replacement by bornite/digenite/covellite on rims and fractures (**Figure 10F**). This Cu enrichment follows a common reaction starting with bornite and ending with the crystallization of covellite, with intermediate digenite. These reactions reflect an increase in sulfur fugacity and progressively more acidic pH values (Barton 1970). These secondary Cu sulfides evidence a minor and restricted supergene event.

4.6.2.   *Sulfur provenance using $\delta^{34}S$ signature*

Sulfur isotope signatures for pyrite from El Romeral vary within a narrow range between -0.8 and 2.9‰ and with an average of ˜0.7‰. These results indicate an exclusively magmatic contribution, i.e., without country rock assimilation or biogenic sulfur, for the last sulfide event supporting a magmatic-hydrothermal origin. Delta-34 sulfur values in El Romeral are very similar to those reported for other magnetite-apatite deposits from northern Chile (**Figure 16**). On the other hand, Chilean IOCG deposits show a much wider range of $\delta^{34}S$ values, indicating different possible sources, including a magmatic and/or evaporitic input. It is worth mention that one measurement on a pyrite±chalcopyrite sample yielded a higher value (2.9‰) than pure pyrite samples (**Table 6**). Although a more detailed study on chalcopyrite must be performed to obtain more reliable conclusions, this variation in the isotope signature may reflect a different source for sulfur for the copper phase, or a secondary fluid with different temperature, redox conditions or sulfur species (Vaughan and Craig 1978). One possible hypothesis suggests the involvement of a

fluid with a high oxygen fugacity or with heavier sulfur species, i.e., H_2S (Vaughan and Craig 1978), which may have increased the isotope signature for this sample. Regardless, this value of 2.9‰ is still considered within a magmatic field (**Figure 16**).

4.6.3.   *Geodynamic model for the deposit formation*

The timing of the El Romeral formation was constrained using U-Pb geochronology and $^{40}Ar/^{39}Ar$ thermocronology. The closure temperature for actinolite ranges between 550° and 650°C (Dahl 1996; Villa et al. 1996) whereas for biotite is slightly lower (ca. 450°C; Villa and Puxeddu 1994). As actinolite and biotite are formed during the early high temperature (>400°C) event, low temperature superimposed events did not resetted the isotopic system, as is evidenced by the Ar degassing pattern for the dated samples (**Figure 12**, **Figure 13**).Thus, the $^{40}Ar/^{39}Ar$ ages reported here can be considered reliable and provide crucial information to determine the timing of the mineralization events, whereas the U-Pb zircon ages constrain the timing of the magmatic events that occurred in the district.

During the Early Jurassic to late Early Cretaceous, a new tectonic configuration was established in the area associated with the onset of the Andean cycle, where a renew subduction with extensional conditions generated a rapidly subsiding arc at the current location of the Coastal Cordillera, a back-arc basin at the east of the arc, and the emplacement of large intrusion complexes (Coira et al. 1982, Brown et al. 1993; Morata and Aguirre 2003; Scheuber et al. 1994). In the studied area, the volcanic units are represented by the Early Jurassic to Early Cretaceous Agua Salada Subvolcanic Complex (Letelier 1977), whereas extensive magmatism is evidenced by several intrusive bodies emplaced during the initial transtensional tectonic conditions of the first Andean I substage (late Early Jurassic to Kimmeridgian). This magmatic event is represented by pre-ore diorite intrusive bodies (ca. 145 Ma, Emparan and Pineda 2000) observed near the Pacific margin. Additionally, the Romeral Diorite (~129 Ma) and the Cerro del Cobre pluton (~126 Ma; Emparan and Pineda 2000) were emplaced under these extensional conditions related to the waning stages of the first Andean I substage.

The U-Pb zircon crystallization age of 129.0 ± 0.9 Ma for the Romeral Diorite (**Figure 14**) is in good agreement with the $^{40}Ar/^{39}Ar$ ages (**Figure 12**) for actinolite associated with the main magnetite ore formation. The temporal and spatial correspondence between the orebody and the Romeral Diorite support a genetic relation of the iron ore with the diorite magmatism. Although the relation between diorite magmatism and ore has been suggested (Sillitoe 2003), this is the first geochronological data that supports a direct link between magmatism and iron ore for Kiruna type deposits in the Chilean Iron Belt.

During the second substage of the Andean I (Kimmeridgian-Tithonian to Albian) a restricted magnetite mineralization event occurred at ~118 Ma, based on the hydrothermal biotite $^{40}Ar/^{39}Ar$ age reported here. This final event could be related to post-ore dikes, which could supply Fe-rich fluids or remobilize primary magnetite resulting in a younger and lower grade iron ore.

At the end of the first Andean stage, an episode of compressive deformation during the Late Cretaceous, the so-called Peruvian Phase, inverted the former morphotectonic features, i.e., back-arc basin inversion and major fault systems (e.g., Atacama Fault System). This event can be related to plate reorganization, causing northeastward displacement of the Farellon plate and dextral oblique convergence, and to rapid ocean crust production, and therefore, to a shallower subduction angle (Charrier et al. 2007). In La Serena area (**Figura 1**), this episode is evidenced by the Punta de Piedra granite to granodiorite batholith dated here at ~100 Ma (**Figure 15**). This drastic change in composition possibly reflects a different geotectonic regime, evidencing the beginning of the second Andean stage (late Early Cretaceous to Early Paleogene) and the ending of IOA formation, characterized by a lower angle-compressive Andean-type subduction. Finally, the subduction of the Juan Fernandez Ridge resulted in a flat-slab zone with a high rate of uplift and erosion that exposed these ore deposits (**Figure 17**).

4.7. Conclusion

El Romeral is one of the largest iron oxide-apatite (IOA) deposits from the Cretaceous Chilean Iron Belt. Magnetite analysis from El Romeral show five different magnetite types: (i) an early inclusion-rich magnetite, which possibly corresponds to magmatic magnetite microlites, (ii) an inclusion-free magnetite associated with actinolite-clinopyroxene-quartz "pockets" and large actinolite crystals, and that is interpreted as related to a magmatic-hydrothermal process, (iii) an inclusion-free magnetite with compositional zonings related to hydrothermal precipitation (Rojas et al. 2017); (iv) a secondary hydrothermal event related to magnetite veinlets and the sulfide mineralization, and (v) a final and restricted hydrothermal event of disseminated magnetite-biotite aggregates. The main iron orebody comprises mainly magnetite I and II crystals and minor magnetite III, and represent a continuum from a magmatic to a magmatic-hydrothermal environment. Similar magnetite textures have also been recognized in Los Colorados IOA, where a flotation model was proposed to explain the origin of Kiruna type deposits (Knipping et al. 2015a,b).

New sulfur isotope data presented here (δ^{34}S between -0.8 and 2.9‰) coupled with previous δ^{34}S values for IOCG and IOA deposits support the notion of a hydrothermal origin for the sulfide mineralization, with sulfur derived mainly from a magmatic source.

Uranium-Pb geochronology and ^{40}Ar/^{39}Ar thermochronology analysis provide four new ages for El Romeral which constrained the timing of magnetite formation at ca. 128 Ma. These new dates support a genetic link between the Romeral Diorite and the Cerro Principal main orebody, both formed as a result of extensional conditions during the waning stages of the first substage of the Andean I. The late minor hydrothermal magnetite mineralization associated with a potassic (biotite) alteration occurred at ~118 Ma, caused by Fe remobilization related to the crystallization of post-ore dikes during the beginning of the second substage of the Andean I. The emplacement of the Punta de Piedra batholith (~100 Ma) marks the beginning of the second Andean stage and the end of the Kiruna type deposit formation in the area.

Although more investigations are needed to confirm the link between the mineralization and intrusions, temporal correlation between both, delta-sulfur isotopes analysis on sulfides and mineral textures indicate a predominant magmatic role for the formation of IOA mineralization, which is in agreement with previous works performed in Los Colorados deposit (Knipping et al. 2015a,b; Bilenker et al. 2016; Reich et al. 2016).

Acknowledgments

REFERENCES

Barra, F., Reich, M., Selby, D., Rojas, P., Simon, A., Salazar, E. and Palma, G. 2017. Unraveling the origin of the Andean IOCG clan: A Re-Os isotope approach. *Ore Geol. Rev.*, **81**, 62-78.

Barton, P.B. 1970. Sulfide petrology. *Mineral. Soc. Am.*, Special Paper, **3**, 187-198.

Bastrakov, E.N., Skirrow, R.G., and Davidson, G.J. 2007. Fluid evolution and origins of iron oxide Cu–Au prospects in the Olympic Dam District, Gawler craton South Australia. *Econ. Geol.*, **102**, 1415–1440.

Bilenker, L.D., Simon, A.C., Reich, M., Lundstrom, C.C., Gajos, N., Bindeman, I., Barra, F. and Munizaga, R. 2016. Fe-O stable isotope pairs elucidate a high-temperature origin of Chilean iron oxide-apatite deposits. *Geochim. Cosmochim. Acta*, **177**, 94-104.

Black, L.P., Kamo, S.L., Allen, C.M., Davis, D.W., Aleinikoff, J.N., Valley, J.W., Mundil, R., Campbell, I.H., Korsch, R.J., Williams, I.S. and Foudoulis, C. 2004. Improved Pb-206/U-218 microprobe geochronology by the monitoring of a trace-element-related matrix effect; SHRIMP, ID-TIMS, ELA-ICP-MS and oxygen isotope documentation for a series of zircon standards. *Chem. Geol.*, **205**, 115-140.

Bookstrom, A. 1975. *Magnetite deposits of El Romeral, Chile: physical geology, sequence of events, and processes of formation*. In partial fulfillment of the requirements for degree of Doctor of Philosophy, Stanford University, Department of Geology, Palo Alto.

Bookstrom, A. 1977. The magnetite deposits of El Romeral, Chile. *Econ. Geol.*, **72**, 1101-1130.

Brown, M., Díaz, F. and Grocott, J. 1993. Displacement History of the Atacama Fault System, 25°00'S 27°00'S, Northern Chile. *Geol. Soc. Am. Bull.*, **105**, 1165-1174.

Buddington, A.F. and Lindsley, D.H. 1964. Iron-titanium oxide minerals and synthetic equivalents *J. Petrol.*, **5**, 310-357.

Charrier, R., Pinto, L., and Rodríguez, M.P. 2007. Tectonostratigraphic evolutions of the Andean Orogen in Chile. In Moreno, T. y Gibbons W (eds) *The Geology of Chile*. Geological Society, London, 21-114.

Coira, B., Davidson, C., Mpodozis, C. and Ramos, V. 1982. Tectonic and magmatic evolution of the Andes of nothern Argentina and Chile. *Earth-Sci. Rev.*, Special Issue, **18**, 303-332.

Coleman, M.L. and Moore, M.P. 1978. Direct reduction of sulfates to sulfur dioxide for isotopic analysis. *Anal. Chem.*, **50**, 1594-1598.

Corfu, F., Hanchar, J.M., Hoskin, P.W.O. and Kinny, P. 2003 Atlas of zircon textures. *Rev. Miner. Geochem.*, **53(1)**, 469-500.

Craig, J.R. and Scott, S.D. 1974. Sulfide phase equilibria. In Ribbe, P.H. (ed) Short Course Notes-Sulfide Mineralogy. Miner Soc Am, Washington, CS1-CS110.

Crasty, R.L. and Mitchell, J.G. 1966. Single sample potassium-argon ages using the omegatron. *Earth Planet. Sci. Lett.*, **1(3)**, 121-122.

Dahl, P.S. 1996. The effects of composition on retentivity of Ar and O in hornblende and related amphiboles: a field-tested empirical model. *Geochim. Cosmochim. Acta*, **60**, 3687-3700.

Davidson, G.J. and Dixon, G.H. 1992. Two sulphur isotope provinces deduced from ores in the Mount Isa eastern succession, Australia. *Miner. Depos.*, **27**, 30-41.

Dobbs, M. 1978. *Distribución de vanadio y titanio en el Cuerpo Principal de la mina El Romeral*. Memoria para optar al Título de Geólogo. Universidad de Chile, Facultad de Ciencias Físicas y Matemáticas, Departamento de Geología, Santiago.

Edmonds, M., Brett, A., Herd, R.A., Humphreys, M.C.S. and Woods, A. 2014. Magnetite-bubble aggregates at mixing interfaces in andesite magma bodies: The Role of Volatiles in Genesis, Evolution and Eruption of Arc Magmas. *Geol. Soc. Lond. Spec. Publ.*, **410**, 95-121.

Edmonds, M., and Mather, T.A. 2017 Volcanic sulfides and outgassing,. *Elements*, **13**, 105-110.

Emparan, C. and Pineda, G. 2000. Área La Serena-La Higuera, Región de Coquimbo. Servicio Nacional de Geología y Minería, Santiago, Mapas Geológicos, no.**18**, 1:100.000.

Emparan, C. and Pineda, G. 2005. Geología del Área Andacollo-Puerto Aldea, Región de Coquimbo. Servicio Nacional de Geología y Minería, Santiago, Carta Geológica de Chile, Serie Geología Básica, no.**96**, 1:1000.000.

Espinoza, L. 2000. *Estudio petrográfico del cuerpo Cerro Principal del distrito ferrífero El Romeral IV región- La Serena, Chile*. Memoria para optar al título de geólogo, Universidad de Chile, Facultad de Ciencias Físicas y Matemáticas, Departamento de Geología, Santiago.

Ewart, A. 1982. The mineralogy and petrology of Tertiary-Recent orogenic volcanic rocks: with special reference to the andesitic-basaltic compositional range. En Thorpe, R.S. (ed) *Andesites, Orogenic Andesites, and related rocks*. Wiley, New York, 26-95.

Frutos, J. and Oyarzún, J. 1975. Tectonic and geochemical evidence concerning the genesis of El Laco magnetite lava flow deposits, Chile. *Econ. Geol.*, **70(5)**, 988-990.

Gualda, G.A.R. and Ghiorso, M.S. 2007. Magnetite scavenging and the buoyancy of bubbles in magmas. Part 2: Energetics of crystal-bubble attachment in magmas. *Contrib. Miner. Petrol.*, **154**, 479-490.

Hall, A.J. 1986. Pyrite-pyrrhotine redox reactions in nature. *Miner. Mag.*, **50**, 223-229.

Hezarkhani, A., Williams-Jones, A.E. and Gammons, C.H. 1999. Factors controlling copper solubility and chalcopyrite deposition in the Sungun porphyry copper deposit, Iran. *Miner. Depos.,* **34**, 770-783.

Jaillard, E., Soler, P., Carlier, G. and Mourier, T. 1990. Geodynamic evolution of the northern and central Andes during early to middle Mesozoic times: a Tethyan model. *J. Geol. Soc.*, **147**, 1009-1022.

Johnson, E.R., Wallace, P.J., Cashman, K.V. and Granados, H.D. 2010. Degassing of volatiles (H_2O, CO_2, S, Cl) during ascent, crystallization and eruption at mafic monogenetic volcanoes in central Mexico. *J. Volcanol. Geotherm. Res.*, **197**, 225-238.

Jugo, P.J., Candela, P.A. and Piccoli, P.M. 1999. Magmatic sulfides and Au.Cu ratios in porphyry deposits: an experimental study of copper and gold partitioning at 850°C, 100 MPa in haplogranitic melt-pyrrhotite-intermediate solid solution-gold metal assemblage, at gas saturation. *Lithos*, **46**, 573-589.

Knipping, J.L., Bilenker, L.D., Simon, A.C., Reich, M., Barra, F., Deditius, A.P., Lundstrom, C., Bindeman, I. and Munizaga, R. 2015a. Giant Kiruna-type deposits form by efficient flotation of magmatic magnetite suspensions. *Geol.*, **43**, 591-594.

Knipping, J.L., Bilenker, L.D., Simon, A.C., Reich, M., Barra, F., Deditius, A.P., Wälle, M., Heinrich, C.A., Holtz, F. and Munizaga, R. 2015b. Trace elements in magnetite from massive iron oxide-apatite deposits indicate a combined formation by igneous and magmatic-hydrothermal processes. *Geochim. Cosmochim. Acta*, **171**, 15-38.

Koppers, A.A.P. 2002. ArArCALC-software for $^{40}Ar/^{39}Ar$ age calculations. *Computers Geosci.,* **28**, 605-619.

Kristmannsdottir, D.S. 1982. Alteration in the IRDP drill hole compared with other drillholes in Iceland. *J. Geophys. Res.*, **87**, 6525-6531.

Kullerud, G. and Yoder, H.S. 1959. Pyrite stability relations in the Fe-S system. *Econ. Geol.*, **54**, 533-572.

Letelier, M. 1977. *Petrología y ambiente de depositación y estructura de las Formaciones matahuaico, Las Breas, Tres Cruces sensu lato e intrusivos permotriásicos en el área de Rivadavia-Alcohuás, valle de Elqui, IV Región, Chile*. Memoria para optar al Título de Geólogo. Universidad de Chile, Facultad de Ciencias Físicas y Matemáticas, Departamento de Geología, Santiago.

Lledo, H.L. and Jenkins, D.M. 2008. Experimental Investigation of the Upper Thermal Stability of Mg-rich Actinolite; Implications for Kiruna-Type Iron Deposits. *J. Petrol.*, **49**, 225-238.

Loyola, N. 2016. *Origen de la mineralización y alteración hidrotermal del depósito tipo IOCG Diego de Almagro, III Región de Atacama, Chile.* Memoria para optar al Título de Geólogo. Universidad de Chile, Facultad de Ciencias Físicas y Matemáticas, Departamento de Geología, Santiago.

Ludwig, K. 2010. Isoplot/Ex version 4.1, a geochronological toolkit for Microsoft Excel: Berkeley Geochronology Center, Special Publication, no.**4**.

Maksaev, V. 1990. *Metallogeny, geological evolution and thermochronology of the Chilean Andean between latitudes 21° and 26° south, and the origin of the major porphyry copper deposits*. PhD thesis, Dalhousie University, Halifax, Nova Scotia, Canada.

Marschik, R. and Fontboté, L. 2001. The Candelaria - Punta del Cobre Iron Oxide Cu-Au(-Zn-Ag) Deposits, Chile. *Econ. Geol.*, **96**, 1799-1826.

Martel, C., Pichavent, M., Holtz, F. y Scaillet, B. 1999. Effects of f_{O2} and H_2O on andesite phase relations between 2 and 4 kbar. *J. Geophys. Res.*, **104**, 453-470.

Merrihue, C.M. 1965. Trace-element determinations and potassium-argon dating by mass spectroscopy of neutron-irradiated samples. *Trans. Am. Geophys. Union.*, **46**, 125.

Merrihue, C. and Turner, G. 1966. Potassium-argon dating by activation with fast neutrons. *J. Geophy. Res.*, **71**, 2852-2857.

Mitchell, J.G. 1968. The argon-40argon-39 method for potassium-argon age determination. *Geochim. Cosmochim. Acta*, **32**, 781-790.

Morata, D., Aguirre, L. 2003. Extensional Lower Cretaceous volcanism in the Coastal Range (29°20'-30°S), Chile: geochemistry and petrogenesis. *J South Am Earth Sci*, **16**,459-476.

Naslund, H.R., Henríquez, F., Nyström, J.O., Vivallo, W. and Dobbs, F.M. 2002. Magmatic iron ores and associated mineralisation examples from the Chilean high Andes and Coastal

Cordillera. En Porter, T.M. (ed) *Hydrothermal iron oxide copper-gold & related deposits: A global perspective*. PGC Publishing, Adelaide, **2**, 207-226.

Nyström, J.O. and Henríquez, F. 1994. Magmatic features of iron ores of the Kiruna type in chile and ore textures and magnetite geochemistry. *Econ. Geol.*, **89**, 820-839.

Pankratz, L.B. and King, E.G. 1970. High-temperature enthalpies and entropies of chalcopyrite and bornite. U.S.Bureau of mines, Report of investigations, **7435**, 1:10.

Parak, T. 1975. Kiruna iron ores are not "Intrusive-magmatic ores of the Kiruna type". *Econ. Geol.*, **70**, 1242-1258.

Paton, C., Hellstrom, J., Paul, B., Woodhead, J. and Hergt, J. 2011. Iolite: Freeware for the visualization and processing of mass spectrometric data. *J. Anal. At. Spectrom.*, **26**, 2508-2518.

Pearce, J.A. and Cann, J.R. 1973. Tectonic setting of basic volcanic rocks determined using trace element analyses. *Earth Planet. Sci. Lett.*, **19**, 290-300.

Purtov, V.K. and KoteVnikova, A.L. 1993. Solubility of titanium in chloride and fluoride hydrothermal solutions. *Int. Geol. Rev.*, **35(3)**, 279-287.

Reich, M., Simon, A.C., Deditius, A., Barra, F., Chryssoulis, S., Lagas, G., Tardani, D., Knipping, J., Bilenker, L., Sánchez-Alfaro, P., Roberts, M.P. and Munizaga, R. 2016. Trace element signature of pyrite from the Los Colorados Iron oxide-apatite (IOA) deposit, Chile: A missing link between Andean IOA and iron oxide copper-gold systems? *Econ. Geol.*, **111**, 743-761.

Reich, M. and Vasconcelos, P.M. 2015. Geological and economic significance of supergene metal deposits. *Elements*, **11(5)**, 305-310.

Rhodes, A.L., Oreskes, N. and Sheets, S. 1999. Geology and rare earth element geochemistry of magnetite deposits at El Laco, Chile. En Brian, J.S. (ed) *Geology and ore deposits of the Central Andes*. Society of Economic Geologists Special Publication **7**, 299-332.

Rieger, A.A., Marschik, R., Díaz, M., Hölzl, S., Charadia, M., Akker, B. and Spangenberg, J.E. 2010. The Hypogene Iron Oxide Copper-Gold Mineralization in the Mantoverde District, Northern Chile. *Econ. Geol.*, **105**, 1271-1299.

Rojas, P.A., Barra, F., Reich, M., Deditius, A. and Simon A. 2017. Mineral chemistry of magnetite and accessory phases from El Romeral iron oxide-apatite deposit, Chile. *Goldschimdt Conference*, Paris.

Scheuber, E. 1994. Tektonische Entwicklung des nordchilenischen aktiven Kontinentalrandes: Der Einfluss von Plattenkonvergenz und Regologie. *Geotecktonische Forschungen*, **81**, 1-131.

Scheuber, E. and Andriessen, P.A.M. 1990. The kinematic and geodynamic significance of the Atacama fault zone, northern Chile. *J. Struct. Geol.*, **12**, 243-257.

Sigurgeirsson, T. 1962. Dating recent basalt by the potassium argon method (in Icelandic). Rept. Physical Laboratory of the University Iceland, p.9.

Sillitoe, R.H. and Burrows, D.R. 2002. New field evidence bearing on the origin of the El Laco magnetite deposit, northern Chile. *Econ. Geol.*, **97**, 1101-1109.

Sillitoe, R.H. 2010. Porphyry copper systems. *Econ. Geol.*, **105**, 3-41.

Simon, A.C., Pettke, T., Candela, P.A., Piccoli, P.M. and Heinrich, A.H. 2004. Magnetite solubility and iron transport in magmatic-hydrothermal environments. *Geochim. Cosmochim. Acta*, **68**, 4905-4914.

Sláma, J., Košler, J., Condon, D., Crowley, J., Gerdes, A., Hanchar, J., Horstwood, M., Morris, G., Nasdala, L., Norberg, N., Schaltegger, U., Schoene, B., Tubrett, M. and Whitehouse,

M. 2008. Plešovice zircon: A new natural reference material for U–Pb and Hf isotopic microanalysis. *Chem. Geol.*, **249(1)**, 1-35.

Sundius, N. 1915. Beitrage zur Geologie des siidlichen Teils des Kirunagebiets. *Vetensk. Prakt. Unders. Lappl.*, 1-237.

Swanson, S.E. and Fenn, P.M. 1986. Quartz crystallization in igneous rocks. *Am. Miner.*, **71**, 331-342.

Vaughan, D.J. and Craig, J.R. 1978. *Mineral chemistry of metal sulfides*. Cambridge University Press.

Villa, I.M. and Puxeddu, M. 1994. Geochronology of the Larderello geothermal field: new data and the 'closure temperature' issue. *Contrib. Miner. Petrol.*, **115**, 415-426.

Villa, I.M., Grobéty, B., Kelley, S.P., Trigila, R. and Wieler, R. 1996. Assessing Ar transport paths and mechanisms for McClure Mountains Hornblende. *Contrib. Miner. Petrol.*, **126**, 67-80.

Walther, J.V. and Helgeson, H.C. 1977. Calculation of thermodynamic properties of aqueous silica and solubility of quartz and its polymorphs at high-pressures and temperatures. *Am. J. Sci.*, **277**, 1315-1351.
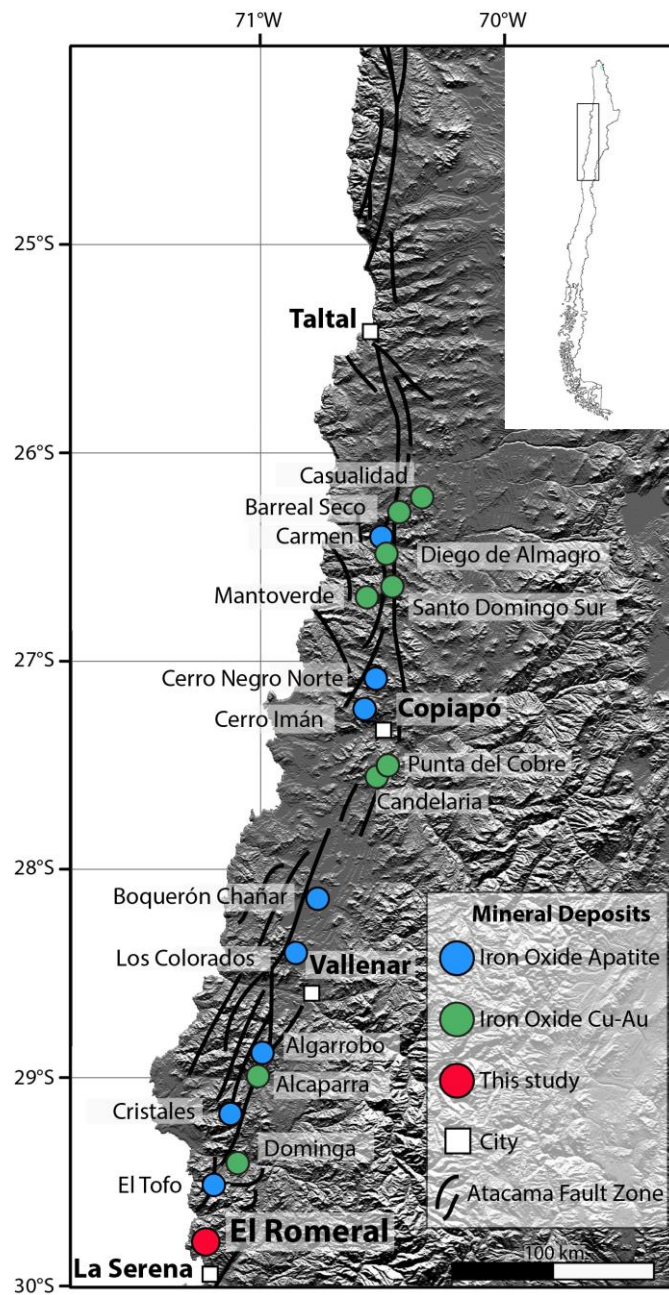
Figure 5. Map showing the location of iron oxide-apatite (IOA) and iron oxide-gold (IOCG) deposits in the Cretaceous Chilean Iron Belt, spatially and temporally associated with the Atacama Fault System (modified from Barra et al 2017).
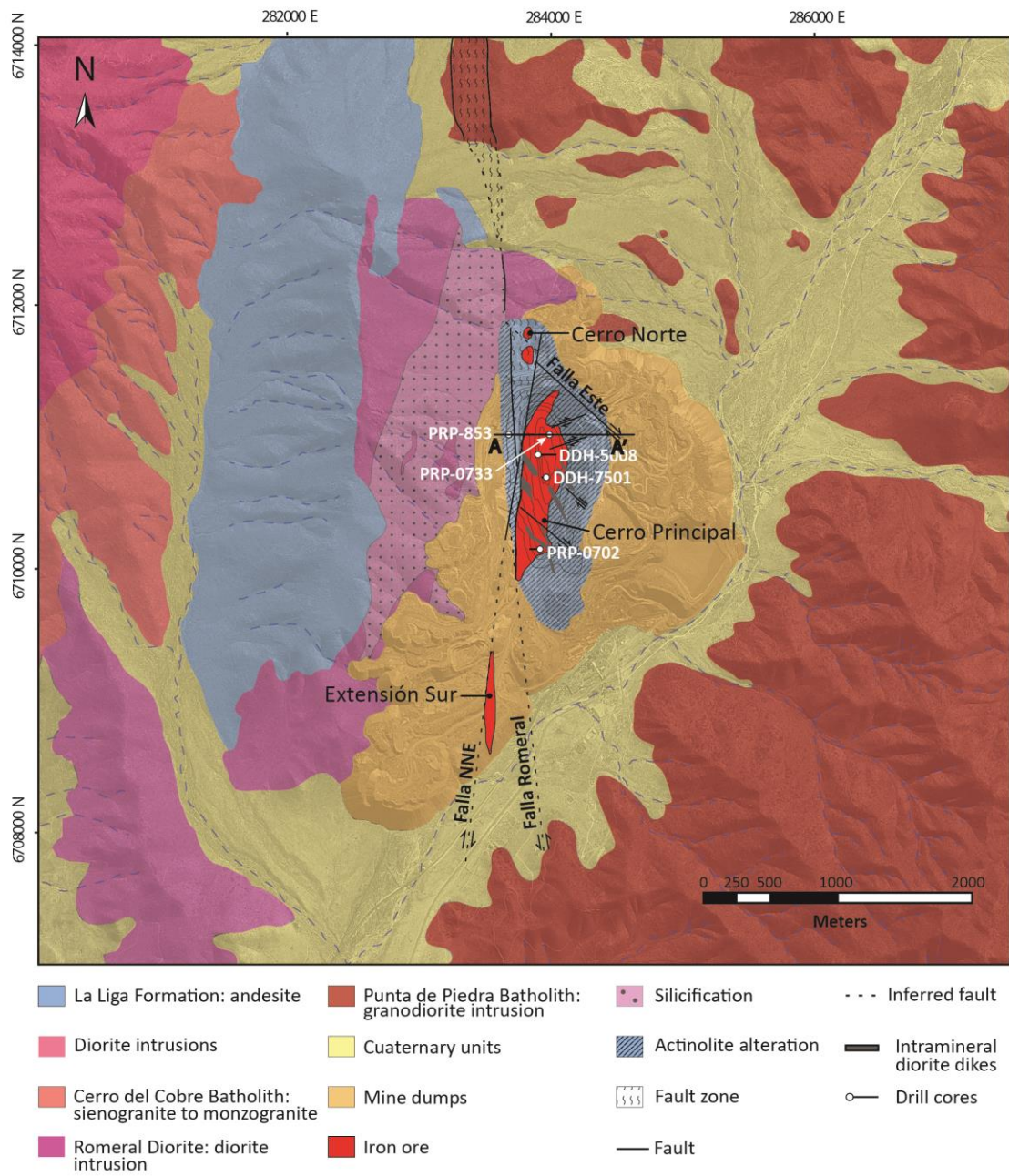
Figure 6. Geologic map of Minas El Romeral district, showing major units and main ore bodies. Location of five drill cores studied here are also shown, along with position of cross-section AA' (Modified from CAP Minería report).
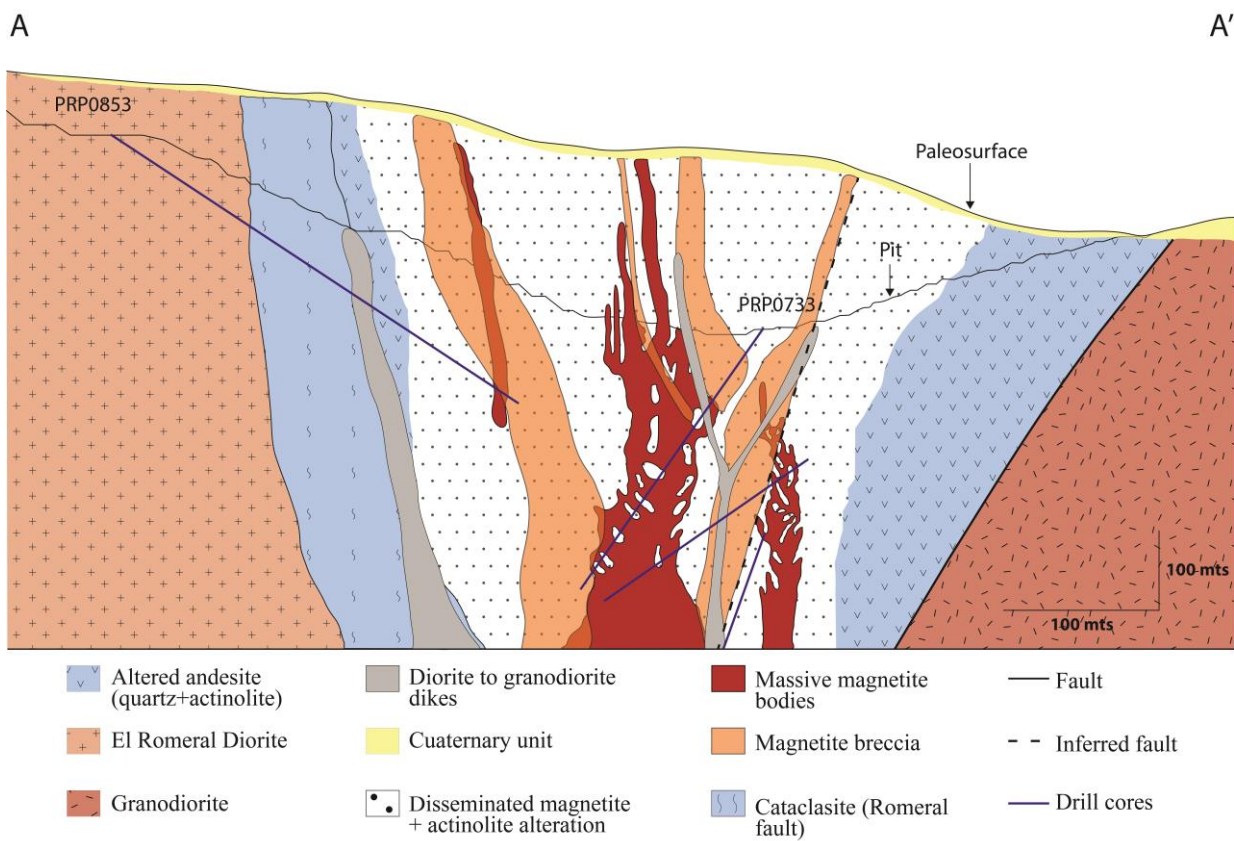
Figure 7. Cross-section (AA') of the Cuerpo Principal mineralization showing the geometry of massive magnetite subvertical bodies and the relationship with the host rock.
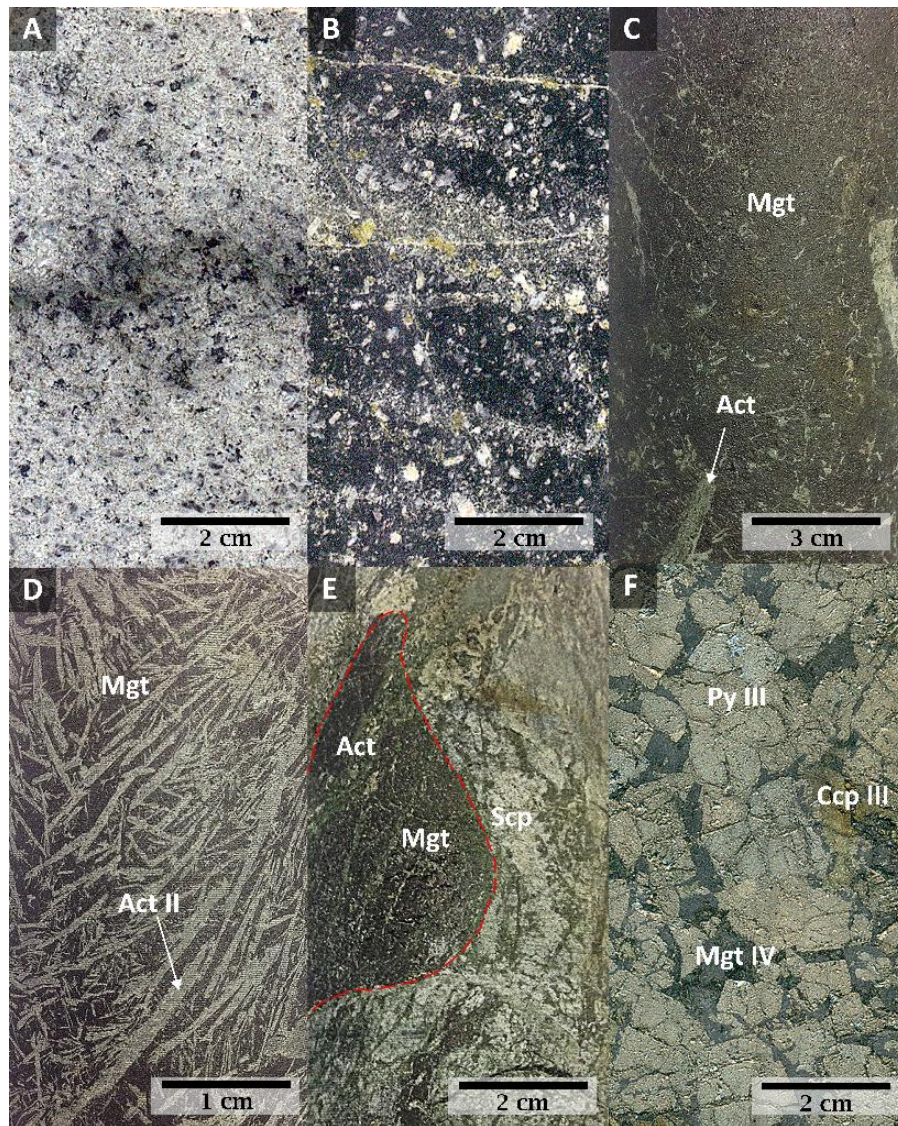
Figure 8. Hand samples from different units observed in El Romeral. A. Romeral Diorite with pervasive silicification. B. La Liga andesite with minor epidote alteration. C. Massive magnetite mineralization (magnetite I, II) with minor actinolite (actinolite I). D. Actinolite intergrown (actinolite II) with magnetite (magnetite I, II). E. Fault zones with mylonitic magnetite clasts (magnetite I, II) inmerse in a scapolite and actinolite (actinolite II) matrix. F. Sulfide (pyrite and chalcopyrite III) breccia clasts in a magnetite matrix (magnetite IV). Mgt: magnetite, Act: actinolite, Scp: scapolite, Py: pyrite, Ccp: chalcopyrite.
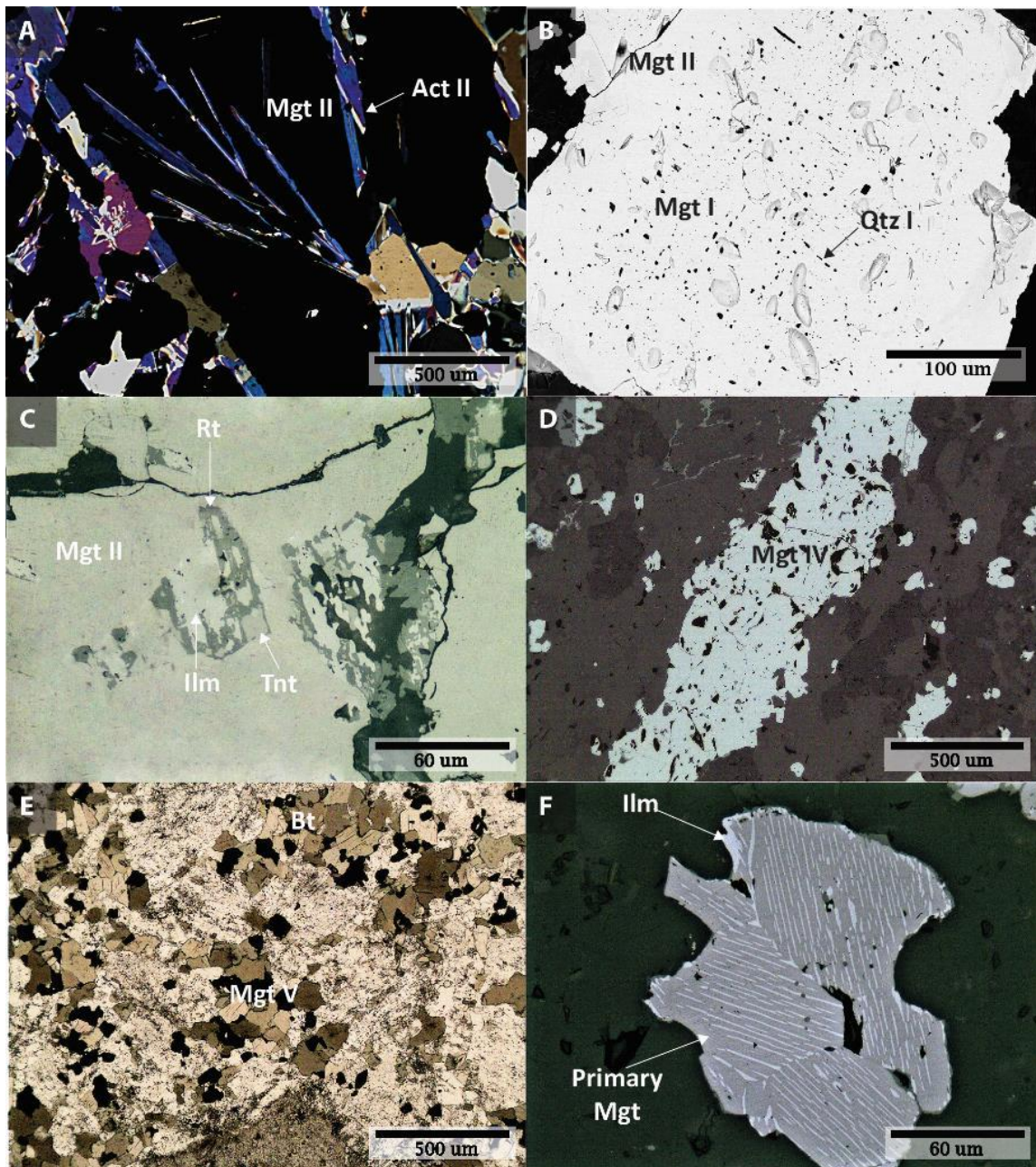
Figure 9. Photomicrographs (A, C, D, E and F) and backscattered electron images (B) of the first ore mineralization event. **A.** Actinolite II intergrown with magnetite II from the massive ore bodies (transmitted light, CPL). **B.** Two major magnetite event: inclusion-rich magnetite I with euhedral quartz I oriented inclusions and inclusion-free magnetite II. **C.** "Patches" of ilmenite and titanite, surrounded by rutile, contained in magnetite II crystals (reflected light, PPL). **D.** Magnetite (IV) veinlets crosscutting hosting rocks. **E.** Clusters of secondary biotite surrounding magnetite V (transmitted light, PPL). **F.** Primary (volcanic) magnetite with ilmenite exsolution lamellaes (reflected light, PPL). Mgt: magnetite, Act: actinolite, Qtz: quartz, Py: pyrite, Ilm: ilmenite, Tnt: titanite, Bt: biotite.
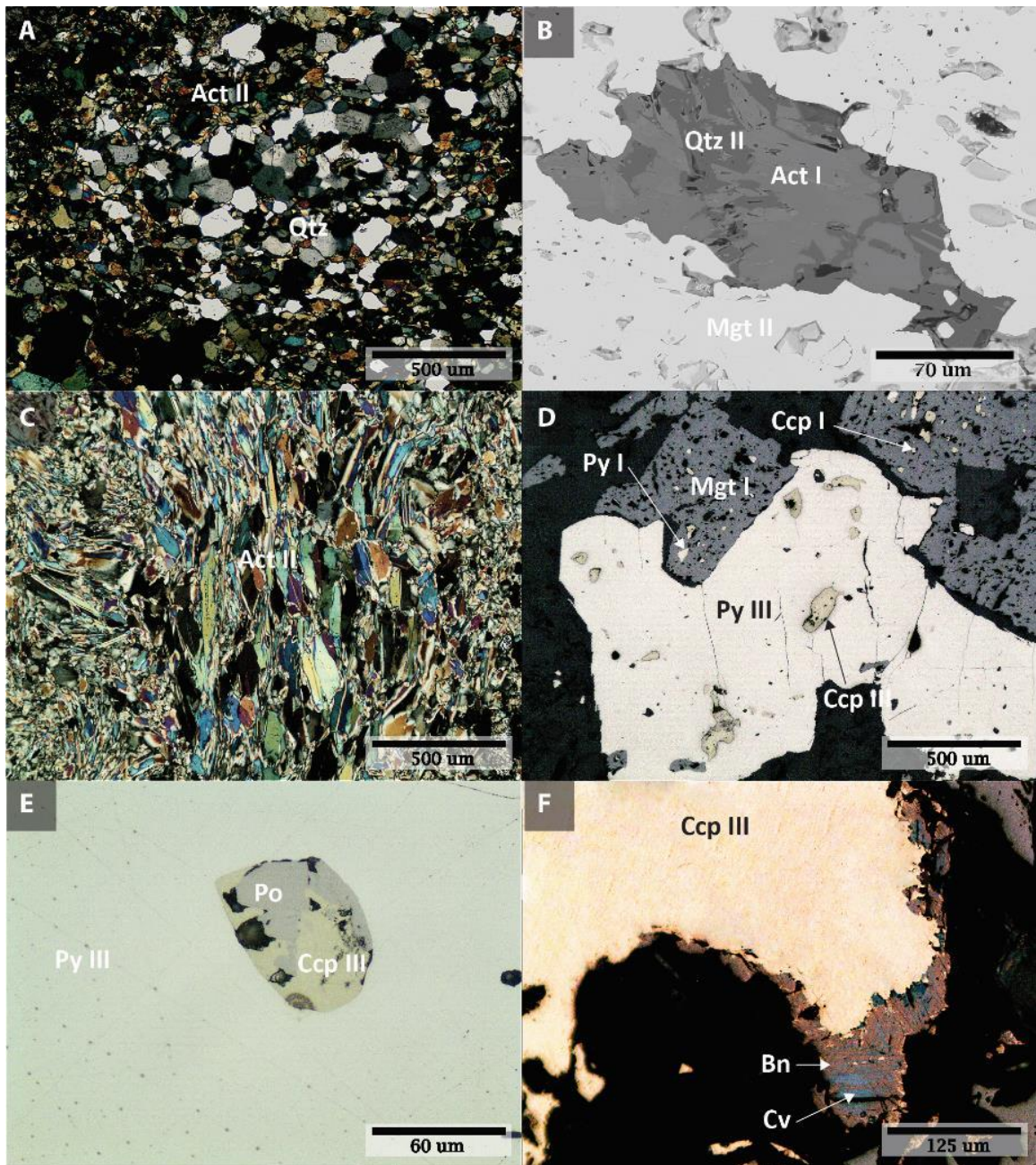
Figure 10. Photomicrographs (A, C, D, E and F) and backscattered electron image (B) of gangue and sulfide mineralization. **A.** Pervasive silicification of the andesite host rock (transmitted light, CPL). **B.** Syn-ore actinolite I with quartz II, both included in massive magnetite mineralization (magnetite II). **C.** Oriented actinolite II crystals located at fault zones (transmitted light, CPL). **D.** Two events of sulfide mineralization: i) pyrite I and chalcopyrite I contained in magnetite I, and ii) inclusions of chalcopyrite III in pyrite III, surrounding magnetite I grains (reflected light, PPL). **E.** Pyrite III with a chalcopyrite III and pyrrhotite inclusion (reflected light). **F.** Chalcopyrite III with bornite and later covellite rims (reflected light, PPL). Qtz: quartz, Act: actinolite, Mgt: magnetite, Py: pyrite, Ccp: chalcopyrite, Po: pyrrhotine, Bn: bornite, Cv: covellite.
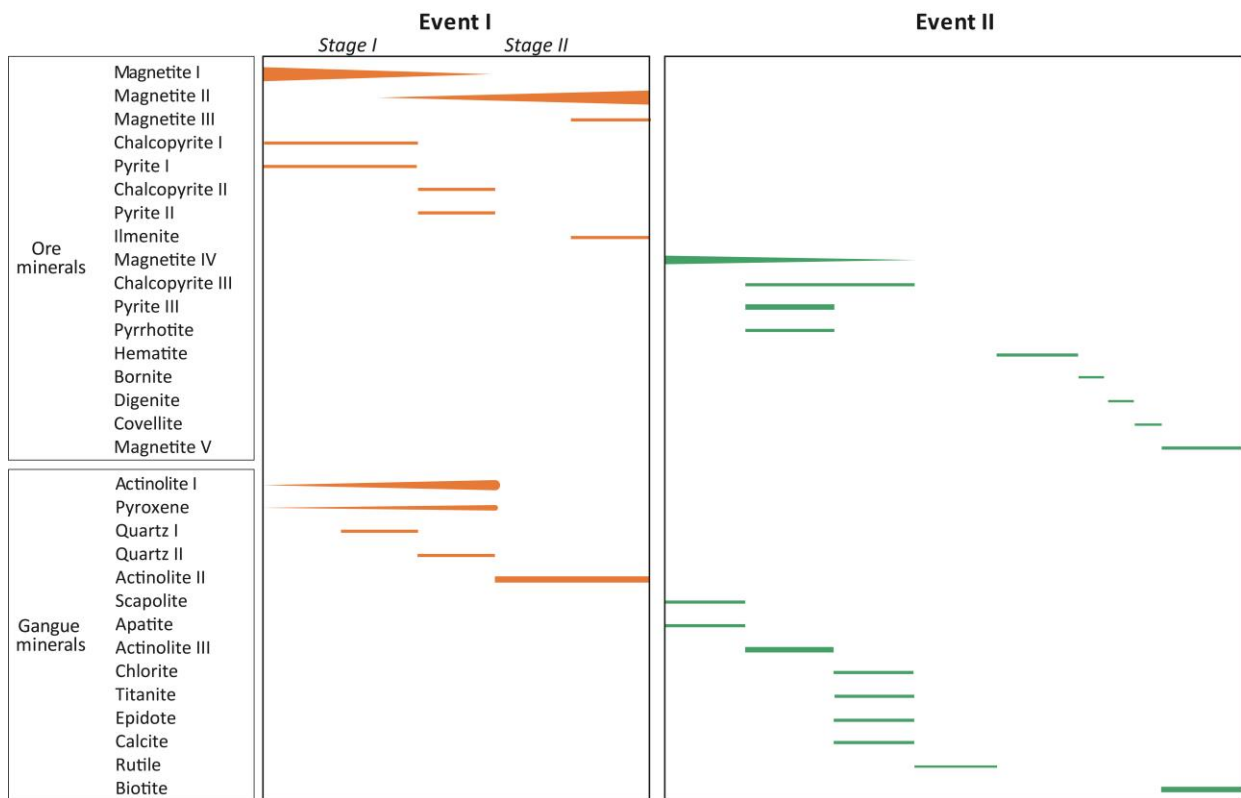
Figure 11. Paragenetic sequence showing the two defined events: i) a first event of massive magnetite ore formation with actinolite, quartz, pyroxene and minor chalcopyrite, and ii) a second event characterized by disseminated/veinlet magnetite and sulfides associated with a sodic-calcic alteration, followed by a post-ore hydrothermal event with magnetite and secondary biotite aggregates. See text for discussion.
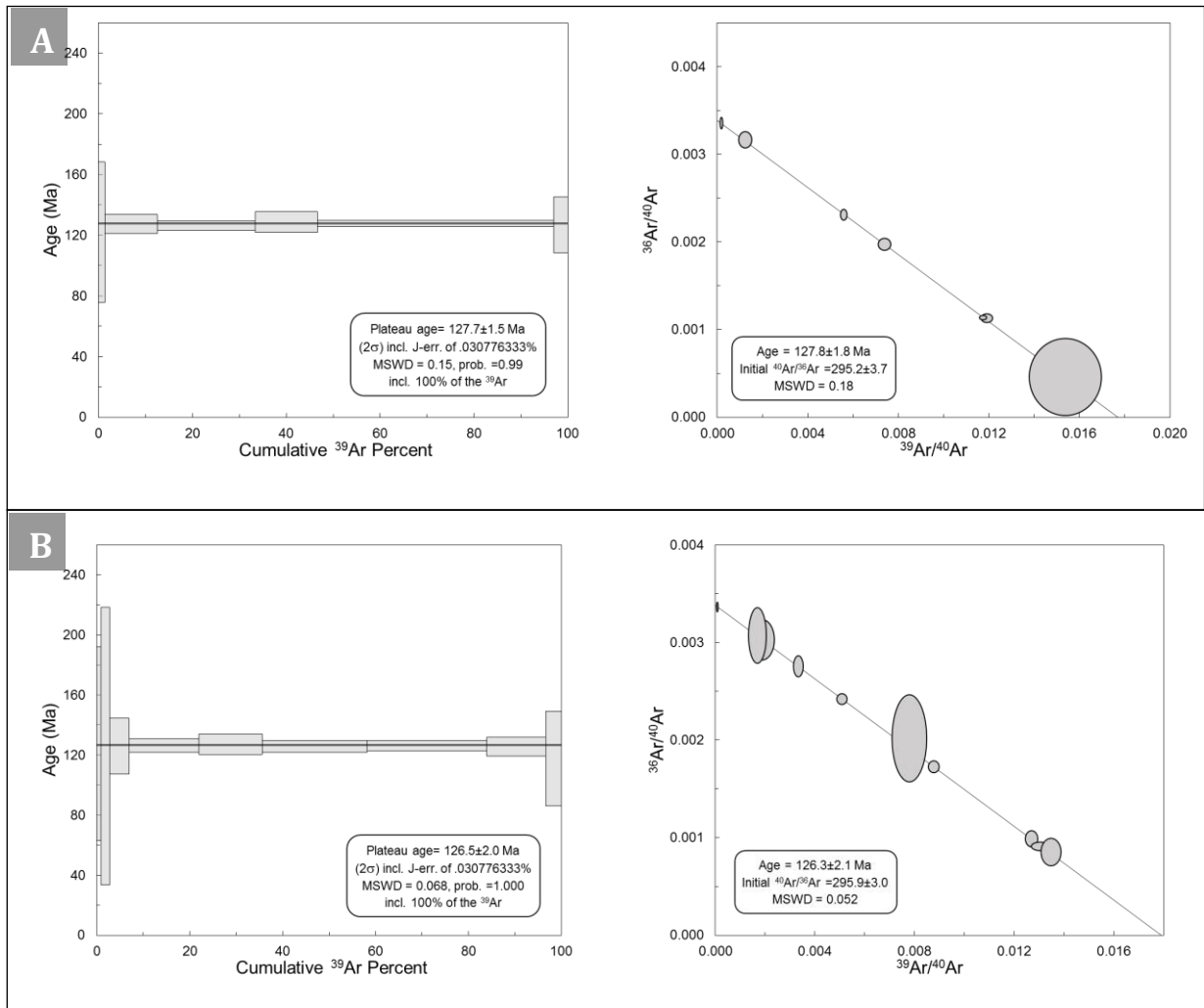
Figure 12. ^{40}Ar/^{39}Ar dating of sub-sample URM-115t with errors plot as 2-sigma. **A.** Plateau age and isochron age of run 01. **B.** Plateau age and isochron age of run 02.
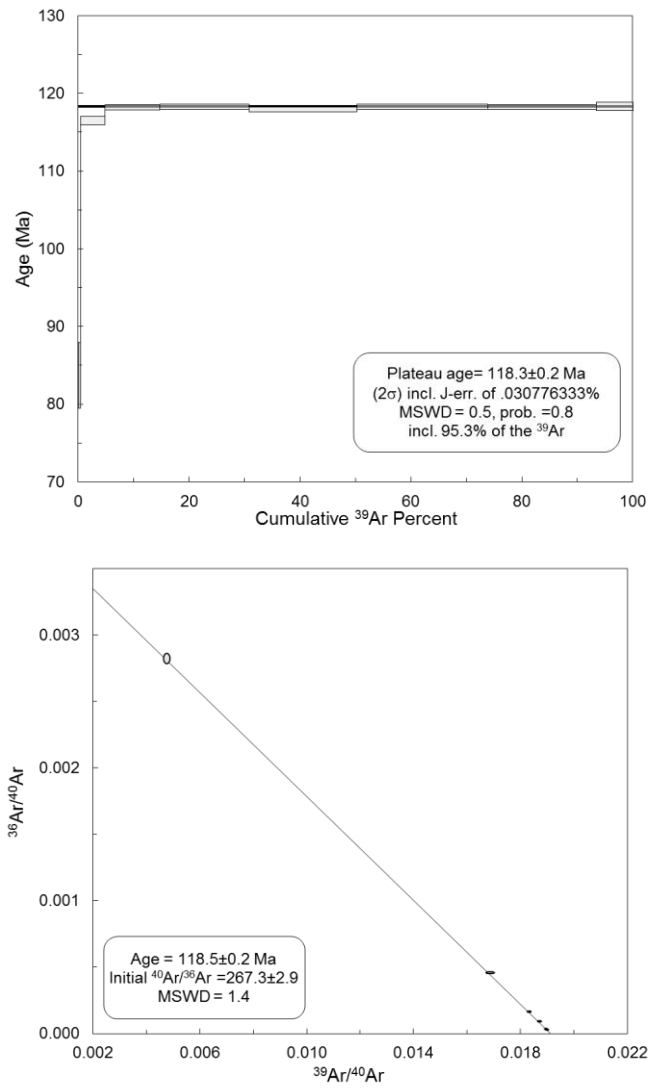
Figure 13. Results of $^{40}Ar/^{39}Ar$ dating in biotite with errors plot as 2-sigma.
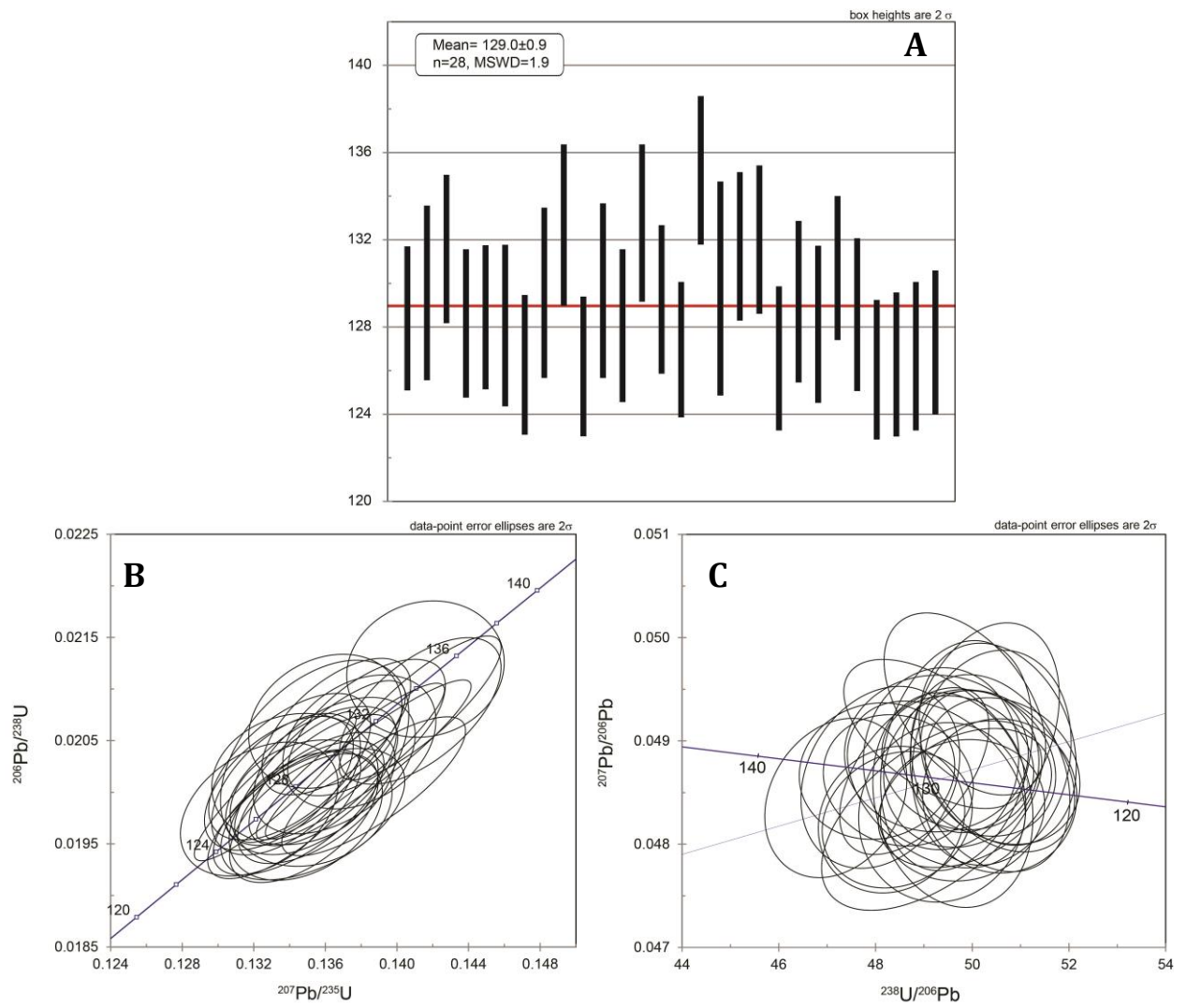
Figure 14. U-Pb ages for zircons of the Romeral Diorite. **A.** Weighted average diagrams. **B.** Concordia diagram. **C.** Tera-Wasserburg plot.
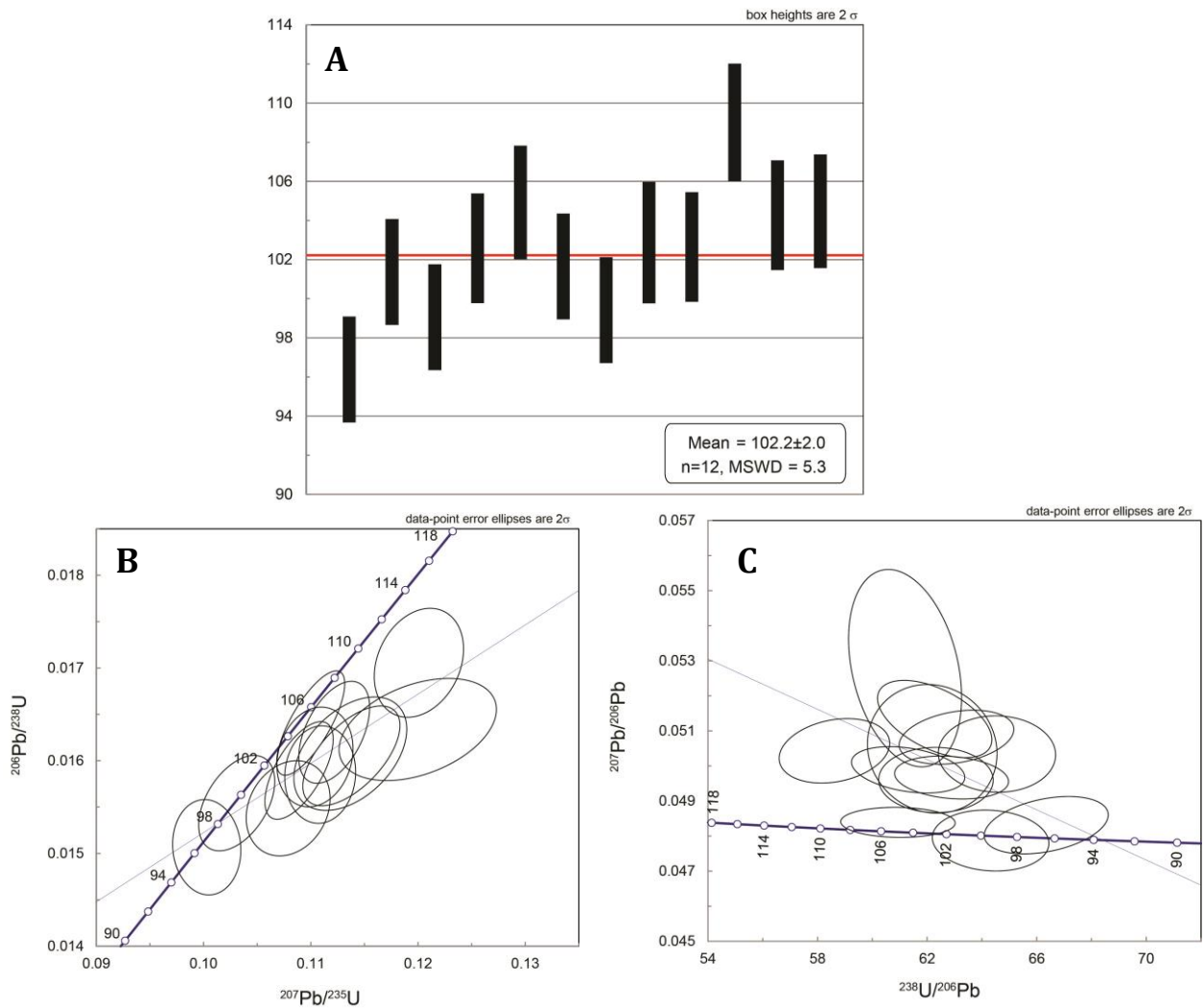
Figure 15. Punta de Piedra Batholith U-Pb zircon ages. A. Weighted average diagrams. B. Concordia diagram. C. Tera-Wasserburg diagram.
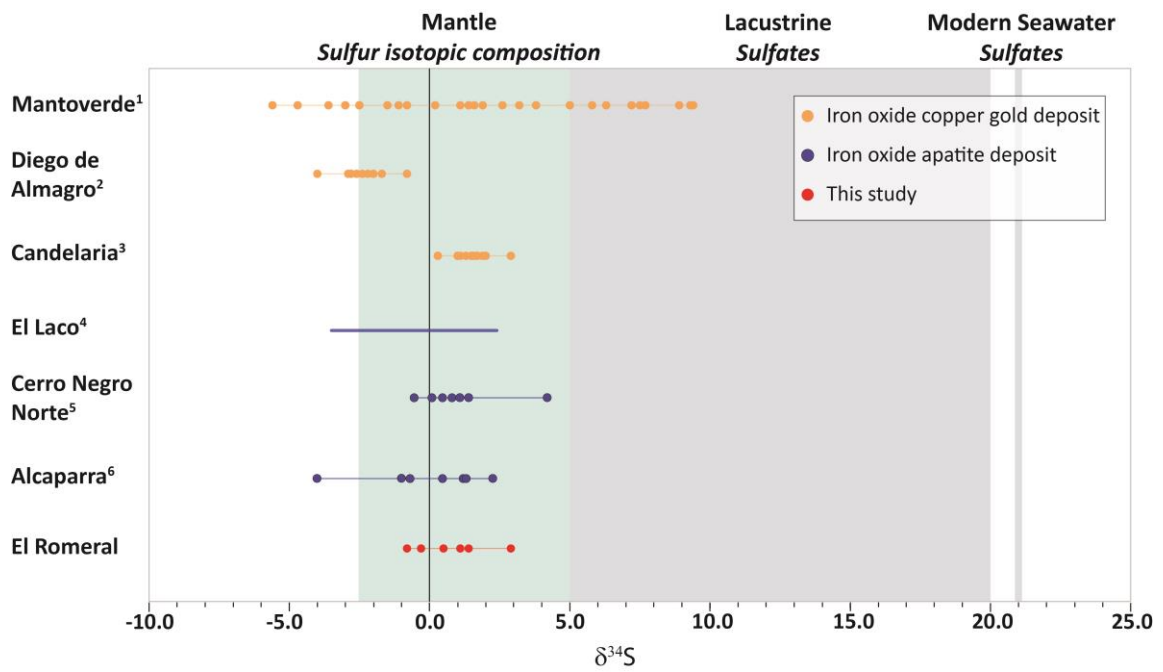
Figure 16. Diagram showing stable sulfur isotope values from IOCG and IOA deposits in the Chilean Iron Belt. References: [1]Rieger et al. (2010) [2]Loyola (2016) [3]Marschik and Fontboté (2001) [4]Henríquez (1991) [5]Salazar (2017) [6]Fredes (2017).

A. First substage Andean I (late Early Jurassic to Kimmeridgian)
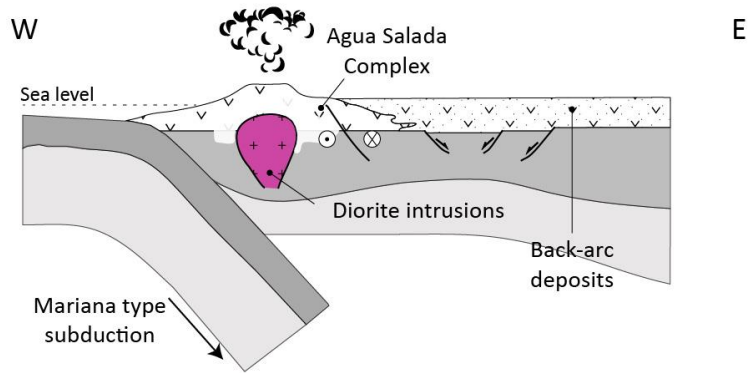
B. End of the first substage Andean I (Early Cretaceous)
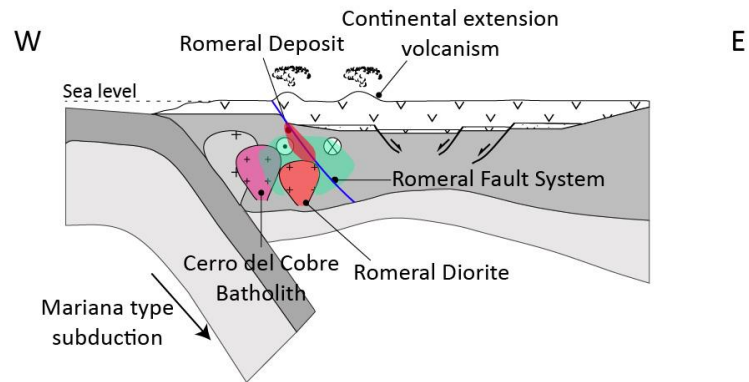
C. Second substage Andean I (Early Cretaceous to Albian)
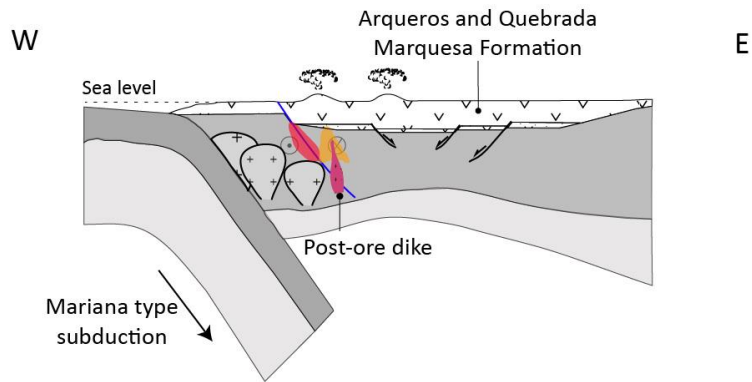
D. Beginning of the Andean II (Late Cretaceous)
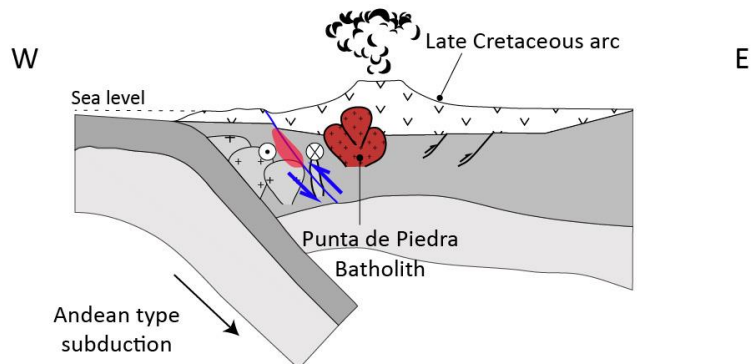
Figure 17. Schematic east-west paleogeographic sections for the Andean I and the beginning of the Andean II (Peruvian Phase). Two main characteristic morphotectonic features are illustrated: a subsiding magmatic arc and transtensional structures (e.g., El Romeral Fault System). **A.** Emplacement of diorite intrusions and development pre-ore silicification (grey halo around intrusions). **B.** Intrusion of the Cerro del Cobre and the Romeral Diorite with formation of the iron orebodies. The green halo represents abundant actinolite and calcic alteration of the volcanic units. **C.** Late hydrothermal magnetite with secondary biotite (orange) is interpreted as formed by fluids exsolved from post-ore dikes. **D.** Emplacement of the Punta de Piedra batholith during the beginning of the Andean II phase under a compressive regime. Note displacement change of the Romeral Fault System during Late Cretaceous.

Table 2. Results of actinolite $^{40}\text{Ar}/^{39}\text{Ar}$ dating.

Power [W]	Ca/K	Cl/K	$^{36}\text{Ar}/^{39}\text{Ar}$	$\%^{36}\text{Ar(Ca)}$	$^{40}\text{Ar*}/^{39}\text{Ar}$	$^{39}\text{Ar}/^{40}\text{Ar}$	$\%\pm$	$^{36}\text{Ar}/^{40}\text{Ar}$	$\%\pm$	%Step	Cum.%	$\%^{40}\text{Ar*}$	Age (Ma)	$\pm$Age
Actinolite sample URM-115t-01 (run 01); integrated age of 127±3.2 Ma; plateau age (100%) of 127.73±0.77 Ma; J of 0.0013±0.0308%; 1-sigma														
10	38.03	5.48	20.95341	0.0	55.46239	0.00016	17.2	0.00336	0.8	0.8	0.8	0.9	125.6	105.8
12	56.75	1.74	2.57773	0.3	53.92807	0.00121	9.8	0.00317	1.2	1.1	1.9	6.5	122.2	23.1
14	101.48	1.30	0.27343	5.3	56.42921	0.00737	1.6	0.00198	1.4	10.5	12.4	41.6	127.7	3.2
16	95.22	1.29	0.10600	12.9	55.90692	0.11890	0.9	0.00113	1.8	21	33.3	66.5	126.5	1.6
18	104.51	1.35	0.41506	3.6	56.99921	0.00570	1.1	0.00231	1.1	13.3	46.6	31.7	128.9	3.4
25	101.24	1.32	0.10849	13.6	56.62107	0.01172	0.6	0.00114	1.0	50.2	96.9	66.4	128.1	1.0
30	119.02	1.31	0.04597	37.0	56.18172	0.01537	4.2	0.00046	38.7	3.1	100.0	86.3	127.1	9.2
Actinolite sample URM-115t-02 (run 02); integrated age of 126.6±4.5 Ma; plateau age (99.5%) of 126.48±0.99 Ma; J of 0.030776%; 1-sigma														
0	36.02	7.79	52.90556	0.0	92.01712	0.00006	0.6	0.00337	0.6	0.5	0.5	0.6	208.8	209.8
12	9.04	0.18	1.62597	0.1	56.54776	0.00186	2.8	0.00303	2.8	0.9	1.4	10.5	127.9	32.3
14	26.72	0.79	1.82755	0.2	55.72254	0.00167	3.8	0.00307	3.8	1.5	2.9	9.3	126.1	46.2
16	86.40	1.60	0.81718	1.5	55.81583	0.00332	1.6	0.00276	1.6	4.0	6.9	18.6	126.3	9.3
18	93.15	1.30	0.20465	6.6	55.92876	0.00875	1.4	0.00173	1.4	15.1	21.9	48.9	126.4	2.2
20	86.66	1.31	0.47719	2.6	56.32333	0.00506	0.9	0.00242	0.9	13.5	35.5	28.5	127.5	3.4
22	93.63	1.21	0.08897	15.2	55.75415	0.01269	3.4	0.00099	3.4	22.6	58.1	70.8	126.2	2.0
24	101.06	1.33	0.08206	17.7	55.96461	0.01305	1.9	0.00091	1.9	25.8	83.9	73.0	126.7	1.7
26	96.62	1.26	0.07509	18.5	55.53837	0.01347	6.8	0.00085	6.8	12.7	96.6	74.8	125.7	3.2
30	50.83	0.62	0.26262	2.8	51.94318	0.00777	9.0	0.00208	9.0	3.4	100.0	40.4	117.9	15.8

Table 3. Results of biotite ^{40}Ar/^{39}Ar dating.

Power [W]	Ca/K	Cl/K	^{36}Ar/^{39}Ar	%^{36}Ar(Ca)	^{40}Ar*/^{39}Ar	^{39}Ar/^{40}Ar	%±	^{36}Ar/^{40}Ar	%±	%Step	Cum.%	%^{40}Ar*	Age (Ma)	±Age
Biotite sample URM-118t Run 13442-01; integrated age of 127±3.2 Ma; plateau age (100%) of 127.73±0.77 Ma; J of 0.0013±0.0308%; 1-sigma														
3	0.14	0.06	0.56521	0.0	36.56646	0.00492	0.9	0.00278	0.5	0.3	0.3	18.0	83.8	2.1
6	0.03	0.05	0.02801	0.0	51.37207	0.01677	0.2	0.00047	0.6	4.4	4.7	86.1	116.6	0.3
9	0.01	0.05	0.00779	0.0	52.13695	0.01837	0.1	0.00014	0.8	9.9	14.6	95.8	118.3	0.2
12	0.01	0.04	0.00514	0.0	52.18515	0.01862	0.1	0.00010	0.8	16.1	30.7	97.2	118.4	0.2
16	0.01	0.04	0.00208	0.0	52.04096	0.01899	0.1	0.00004	1.2	19.5	50.2	98.8	118.1	0.2
20	0.01	0.05	0.00200	0.0	52.17699	0.01895	0.1	0.00004	1.2	23.6	73.8	98.9	118.2	0.2
25	0.01	0.04	0.00159	0.0	52.16149	0.01900	0.1	0.00003	1.6	19.6	93.4	99.1	118.3	0.2
30	0.01	0.04	0.00176	0.0	52.19024	0.01897	0.2	0.00003	3.2	6.6	100.0	99.0	118.4	0.3

Table 4. LA-ICP-MS-MC U-Pb data on zircons from the Romeral Diorite (sample ROM-109).

Spot	Contents [ppm]		Th/U	Isotope ratios and propagated errors						Ages and propagated errors [Ma]				Best age [Ma]	
	U	Th		$^{207}Pb/^{206}Pb$	2σ	$^{207}Pb/^{235}U$	2σ	$^{206}Pb/^{238}U$	2σ	$^{207}Pb/^{235}U$	2σ	$^{206}Pb/^{238}U$	2σ	$^{206}Pb/^{238}U$	2σ
3	544.0	330.5	0.61	0.04879	0.00053	0.13589	0.00340	0.02012	0.00052	129.4	3.0	128.4	3.3	128.4	3.3
4	157.4	63.8	0.41	0.04888	0.00062	0.13570	0.00390	0.0203	0.00064	129.2	3.5	129.6	4.0	129.6	4.0
5	396.0	389.7	0.98	0.04862	0.00052	0.13830	0.00360	0.02063	0.00054	131.5	3.2	131.6	3.4	131.6	3.4
6	276.0	199.0	0.72	0.04873	0.00062	0.13340	0.00340	0.02009	0.00053	127.2	3.1	128.2	3.4	128.2	3.4
9	121.8	64.1	0.53	0.04886	0.00091	0.13430	0.00380	0.02013	0.00052	128.0	3.4	128.5	3.3	128.5	3.3
10	479.9	435.0	0.91	0.04845	0.00055	0.13320	0.00370	0.02006	0.00059	127.0	3.3	128.1	3.7	128.1	3.7
11	183.0	113.0	0.62	0.04871	0.00064	0.13370	0.00350	0.01979	0.00051	127.4	3.2	126.3	3.2	126.3	3.2
12	372.0	271.0	0.73	0.04858	0.00066	0.13740	0.00430	0.0203	0.00062	130.7	3.9	129.6	3.9	129.6	3.9
13	159.0	72.0	0.45	0.04865	0.00072	0.14130	0.00370	0.02079	0.00058	134.2	3.3	132.7	3.7	132.7	3.7
16	273.6	129.9	0.47	0.04847	0.00061	0.13490	0.00350	0.019774	0.00051	128.5	3.2	126.2	3.2	126.2	3.2
17	370.0	195.0	0.53	0.04907	0.00059	0.13840	0.00470	0.02032	0.00063	131.6	4.2	129.7	4.0	129.7	4.0
18	221.0	119.3	0.54	0.04936	0.00072	0.13870	0.00420	0.02006	0.00055	132.4	4.0	128.1	3.5	128.1	3.5
19	570.0	499.0	0.88	0.04871	0.00054	0.14130	0.00370	0.02082	0.00057	134.2	3.3	132.8	3.6	132.8	3.6
21	248.0	223.0	0.90	0.04883	0.00072	0.13650	0.00370	0.02026	0.00054	129.9	3.3	129.3	3.4	129.3	3.4
22	222.0	134.8	0.61	0.04913	0.00083	0.13520	0.00370	0.019897	0.0005	128.8	3.3	127.0	3.1	127.0	3.1
23	386.7	421.3	1.09	0.04845	0.00063	0.14160	0.00360	0.021196	0.00054	134.5	3.2	135.2	3.4	135.2	3.4
24	344.0	312.0	0.91	0.04828	0.00075	0.13540	0.00430	0.02034	0.00077	129.0	3.8	129.8	4.9	129.8	4.9
25	434.5	285.6	0.66	0.04824	0.00054	0.13661	0.00340	0.02064	0.00054	130.0	3.1	131.7	3.4	131.7	3.4
26	427.0	292.0	0.68	0.04824	0.00058	0.1360	0.00350	0.02069	0.00053	129.5	3.1	132.1	3.4	132.0	3.4
27	237.0	130.6	0.55	0.04884	0.00085	0.1323	0.00360	0.01984	0.00053	126.2	3.2	126.6	3.3	126.6	3.3
28	363.0	241.0	0.66	0.04831	0.00071	0.1340	0.00370	0.02025	0.00058	127.7	3.4	129.2	3.7	129.2	3.7
29	1211.0	1034.0	0.85	0.04833	0.00056	0.13380	0.00340	0.02008	0.00056	127.5	3.1	128.2	3.6	128.2	3.6
30	305.0	206.1	0.68	0.04871	0.00066	0.13790	0.00350	0.02049	0.00053	131.2	3.1	130.7	3.3	130.7	3.3
31	452.0	424.2	0.94	0.04843	0.00085	0.13520	0.00390	0.02016	0.00055	128.7	3.4	128.6	3.5	128.6	3.5
32	874.0	1180.0	1.35	0.04871	0.00058	0.13480	0.00340	0.019751	0.00051	128.4	3.1	126.1	3.2	126.1	3.2
33	177.2	126.7	0.72	0.04897	0.00080	0.13530	0.00420	0.01979	0.00052	128.8	3.7	126.3	3.3	126.3	3.3
34	286.0	287.0	1.00	0.04869	0.00078	0.13450	0.00390	0.01985	0.00053	128.1	3.5	126.7	3.4	126.7	3.4
35	455.0	476.0	1.05	0.04879	0.00058	0.13550	0.00360	0.019948	0.00052	129.1	3.2	127.3	3.3	127.3	3.3

Table 5. LA-ICP-MS-MC U-Pb data on zircons from the Punta de Piedra Batholith (sample ROM-Gd)

Spot	Contents [ppm]		Th/U	Isotope ratios and propagated errors						Ages and propagated errors [Ma]				Best age [Ma]	
	U	Th		$^{207}Pb/^{206}Pb$	2σ	$^{207}Pb/^{235}U$	2σ	$^{206}Pb/^{238}U$	2σ	$^{207}Pb/^{235}U$	2σ	$^{206}Pb/^{238}U$	2σ	$^{206}Pb/^{238}U$	2σ
3	191.0	148.0	0.77	0.04832	0.00067	0.10030	0.00260	0.01507	0.00042	97.1	2.4	96.4	2.7	96.4	2.7
7	186.0	121.0	0.65	0.05083	0.00063	0.11089	0.00270	0.01585	0.00043	106.8	2.5	101.4	2.7	101.4	2.7
12	188.5	129.0	0.68	0.05035	0.00089	0.10790	0.00320	0.01549	0.00042	104.1	3.0	99.1	2.7	99.1	2.7
22	151.0	104.6	0.69	0.04961	0.00076	0.11040	0.00290	0.01604	0.00044	106.3	2.7	102.6	2.8	102.6	2.8
26	1495.0	2270.0	1.52	0.04840	0.00035	0.11000	0.00260	0.01641	0.00046	106.0	2.4	105.0	2.9	105.0	2.9
27	210.9	234.0	1.11	0.04968	0.00050	0.10891	0.00260	0.01590	0.00043	105.0	2.4	101.7	2.7	101.7	2.7
28	100.8	64.7	0.64	0.04788	0.00071	0.10310	0.00290	0.01555	0.00042	99.7	2.7	99.5	2.7	99.5	2.7
29	166.0	84.3	0.51	0.05050	0.00150	0.11370	0.00430	0.01608	0.00050	109.3	3.9	102.9	3.1	102.9	3.1
31	79.1	56.1	0.71	0.05135	0.00090	0.11380	0.00370	0.01606	0.00044	109.4	3.4	102.7	2.8	102.7	2.8
32	159.0	102.4	0.64	0.05044	0.00075	0.12010	0.00340	0.01706	0.00048	115.2	3.1	109.0	3.0	109.0	3.0
33	193.0	157.2	0.82	0.04990	0.00054	0.11220	0.00270	0.01631	0.00045	108.0	2.5	104.3	2.8	104.3	2.8
34	56.1	74.0	1.32	0.05280	0.00230	0.12000	0.00600	0.01634	0.00045	115.0	5.5	104.5	2.9	104.5	2.9

Table 6. δ^{34}S values of selected samples.

Sample	Drill core	δ^{34}S‰	Description
ROM-017	PRP0702	-0.3	Pyrite veinlet
ROM-018	PRP0702	0.5	Pyrite veinlet (<10% chalcopyrite)
ROM-019	PRP0702	0.5	Pyrite breccia (<10% chalcopyrite)
ROM-020	PRP0702	0.5	Pyrite breccia (<10% chalcopyrite)
ROM-023	PRP0702	1.1	Pyrite veinlet
ROM-117	PRP0853	1.4	Pyrite veinlet
ROM-125	PRP0853	-0.8	Fault zone with disseminated pyrite
ROM-139	DDH5008	2.9	Fault zone with disseminated pyrite and chalcopyrite (2:1)

CAPÍTULO 5

NEW CONTRIBUTIONS TO THE UNDERSTANDING OF KIRUNA-TYPE IRON OXIDE-APATITE DEPOSITS REVEALED BY MAGNETITE ORE AND GANGUE MINERALS GEOCHEMISTRY AT THE EL ROMERAL DEPOSIT, CHILE

Paula A. Rojas[1], Fernando Barra[1], Artur Deditius[2], Martin Reich[1], Adam Simon[3], Maolcolm Roberts[4], Mario Rojo[5]

[1] Department of Geology and Andean Geothermal Center of Excellence (CEGA), Universidad de Chile, Plaza Ercilla 803, Santiago, Chile.

[2] School of Engineering and Information Technology, Murdoch University, 90 South Street, Murdoch, Western Australia 6150, Australia.

[3] Department of Earth and Environmental Sciences, University of Michigan, 1100 North University Ave, Ann Arbor, Michigan, USA.

[4] Center for Microscopy, Characterisation and Analysis (CMCA), University of Western Australia, Crawley, Western Australia 6009, Australia

[5] Compañia Minera del Pacífico (CAP), Pedro Pablo Muñoz 675, La Serena, Chile.

Corresponding author:
Paula Rojas
Departamento de Geología, Universidad de Chile, Chile
paurojas@ing.uchile.cl
Phone: 56-2-29784532

ABSTRACT

Iron oxide-apatite (IOA) or Kiruna-type deposits are an important source of iron and other elements including REE, U, Ag and Co. The genesis of these deposits remains controversial, with models that range from a purely magmatic origin to others that involve variable degrees of hydrothermal fluid involvement. To elucidate the formation processes of this deposit type, we focused on the Chilean Iron Belt of Cretaceous age and performed geochemical analyses on samples from El Romeral, one of the largest IOA deposits in northern Chile. We present a comprehensive field emission electron microprobe analysis (FE-EMPA) database of magnetite, apatite, actinolite, pyroxene, biotite, pyrite and chalcopyrite, obtained in representative samples retrieved from drill cores that cross-cut the Fe-P mineralization and alteration. Two different

magnetite types are recognized representing the main iron mineralization which conformed massive magnetite dikes. An early inclusion-rich magnetite (Type I); and a pristine inclusion-free magnetite (Type II) that usually appears as an overgrowths around Type I magnetite. High V (~2500-2800 ppm) and Ti concentrations ~80-3000), and the presence of high-temperature silicate mineral inclusions (e.g. pargasite, ~800-1020) determined by micro-Raman analysis indicate a magmatic origin for Type I magnetite. On the other hand, high V (2300-2700 ppm) contents and lower Ti (50-400 ppm) concentrations of the pristine, inclusion-free Type-II magnetite indicate a shift from magmatic to hydrothermal conditions for this mineralization event. The chemical features of primary actinolite (Ca- and Mg-rich cores) within Type-II magnetite, the presence of F-rich apatite and high Co:Ni ratios (>1-10) of late stage pyrite mineralization are consistent with a high temperature (up to 840°C) genesis for the deposit. At shallow depths of the deposit, the presence of pyrite with low Co:Ni ratios (<0.5) and OH-rich apatite which contains higher Cl concentrations relative to F record a dominance of lower temperature hydrothermal conditions (<600ºC) and lesser magmatic contribution. This vertical zonation, which correlates with subvertical shape of the massive iron orebodies, is concordant with a transition from magmatic to hydrothermal domains described in several IOA deposits along the Chilean Iron Belt, and support a magmatic-hydrothermal model for the formation of the El Romeral. The close spatial and temporal association of the deposit with the Atacama Fault Zone suggests that pressure drops related to changes in tectonic stress had a significant impact on Fe solubility, triggering ore precipitation.

5.1. Introduction

Iron oxide-apatite (IOA) deposits, also known as Kiruna type and magnetite-apatite deposits, are considered as the Cu-deficient end member of the iron oxide-copper-gold (IOCG) clan (Williams et al., 2005). Both of these deposit types are economically important as a source of several commodities such as Fe, Cu, Au, U, and REE (Barton, 2014), making them a topic of scientific interest. These deposits are found in several metallogenic provinces around the world and are distributed evenly throughout geologic time, from the Archean (e.g.Carajás Province, Brazil; Réquia et al., 2003) to early Proterozoic (e.g., Kiruna district, Sweden; Jonsson et al., 2013; Westhues et al., 2017), middle Proterozoic (e.g. Pea Ridge and Pilot Knob, U.S.A.; Day et al., 2016; Childress et al., 2016) to the Pliocene (e.g., El Laco, Chile; Maksaev et al., 1988). The genesis of and potential genetic relationship between IOA and IOCG deposits has been subject of a long-standing controversy, where three main hypotheses have been proposed. On one hand, the magmatic hypothesis invokes liquid immiscibility between a silicate melt and a conjugate Fe-rich melt with an important, large volatile component (Nyström and Henríquez, 1994; Naslund et al., 2002; Velasco et al., 2016; Tornos et al., 2016). The second hypothesis involves replacement of intermediate composition plutonic or volcanic units by hydrothermal fluids of non-magmatic (basinal brines, connate fluids) or magmatic origin exsolved from mafic intrusions (Menard, 1995; Rhodes and Oreskes, 1999; Rhodes et al., 1999; Sillitoe and Burrows, 2002; Dare and Barnes, 2015).

Among other magmatic-hydrothermal models proposed recently to explain the formation of some IOAs (e.g., Kiruna, Westhues et al., 2016, 2017), Knipping et al. (2015a, b) proposed a new model that reconciles the purely magmatic vs. hydrothermal viewpoints. This model states that the flotation and coalescence of primary magmatic magnetite-bubble pairs within a magma chamber is an efficient mechanism for magnetite ore concentration. During magmatic flotation of the magnetite froth, the exsolved bubbles (i.e. magmatic-hydrothermal fluid) efficiently scavenge metals such as Fe, Cu and Au, as well as S, owing to the large positive fluid/melt partition coefficients for these elements (Chou and Eugster, 1977; Boctor et al., 1980; Simon et al., 2004; Williams-Jones and Heinrich, 2005; Simon and Ripley, 2011; Zajacz et al., 2012), as well as REE (Reed et al., 2000) and other metals (e.g. Ag; Simon et al., 2008) from the melt. Rapid ascent of the bubble-magnetite suspension through regional scale structures results in the formation of massive subvertical iron oxide orebodies or "dikes". The change from magmatic to hydrothermal conditions in magnetite is evidenced by characteristic trace element zoning patterns and isotopic signatures that shift from heavy to lighter $\delta^{56}Fe$ and $\delta^{18}O$ values (Knipping et al., 2015a, b; Bilenker et al., 2016). Additionally, this model suggests a possible genetic link between IOCGs and IOA deposits, where an IOCG deposit could form at a shallower crustal level or at a distal lateral position from the IOA deposit (Reich et al., 2016).

In this contribution we present and discuss new mineral chemistry data for magnetite and associated sulfide and gangue minerals (i.e., pyrite, amphibole, pyroxene, biotite, and apatite) from El Romeral deposit in Chile that supports Knipping et al. (2015a, b) model, pointing to a combination of efficient magmatic and hydrothermal processes of Fe concentration. The El Romeral is one of the largest IOA deposits in the Cretaceous Chilean Iron Belt, which extends ~1000 km along the Coastal Cordillera of northern Chile and contains >50 deposits with >40 MTon Fe (**Figure 18**). Mineral phases including magnetite, apatite, actinolite, pyroxene, biotite, pyrite and chalcopyrite were analyzed by using high-resolution, field emission electron microprobe analyzer (FE-EMPA) techniques. Additionally, micro-Raman spectroscopy was used to identify the nature of mineral inclusions within magnetite crystals in order to determine the crystallization history of the magnetite ore. Because the El Romeral and many other Chilean IOA deposits are intimately associated with transtensional structures within the Atacama Fault System, we further explore the effects of decompression on Fe solubility, and its effects on magnetite ore precipitation.

5.2. Geological background

The development of the mid-Cretaceous Chilean Iron Belt occurred under an extensional tectonic regime caused by renewed subduction on the western margin of Gondwana (Coira et al., 1982; Jaillard et al., 1990). These extensional conditions resulted in the formation of a subsiding

trench-parallel magmatic arc and a back-arc basin (Brown et al., 1993; Scheuber et al., 1994; Charrier et al., 2007).

The El Romeral IOA deposit is located at the southern end of the Chilean Iron Belt, between latitudes 29º44'S and 29º42'S. Resources have been estimated at about 450 Mt with a 28.3% iron grade (2014 Annual Report, CAP Minería) and up to 1.1% vanadium (Dobbs, 1978). Ore mineralization is hosted by the late Jurassic to Neocomian La Liga Formation, which is an andesite lava flow from the Agua Salada Volcanic Complex (Emparan and Pineda, 2005). Emplacement of the magnetite orebodies was controlled by the sinistral NNW strike-slip Romeral fault, which is an extension of the Atacama Fault System (AFS). The El Romeral deposit is limited to the west and north by the Romeral Diorite (129.0 ± 0.9 Ma U-Pb zircon age, Rojas et al., 2017) and to the SE by the post-ore granitic to granodioritic Punta de Piedra intrusion (102.2 ± 2.0 Ma U-Pb zircon age, Rojas et al., 2017). The Cerro del Cobre monzogranite and syenogranite batholith (U-Pb zircon age of 126.5 ± 2 Ma; Emparan and Pineda, 2000) intrudes the volcanic sequences of La Liga Formation on the western side of the deposit (**Figure 19**). Additionally, several NW to NNW post- and syn-ore diorite to granodiorite dikes have been described in the deposit (Bookstrom, 1977).

Three orebodies have been identified at the El Romeral, from north to south: Cerro Norte, Cerro Principal, and Extensión Sur (**Figure 19**; Espinoza, 2000). Cerro Norte comprises subvertical massive magnetite bodies with low P and sulfur, whereas Extensión Sur is composed by a massive and brecciated iron ore with higher contents of P and sulfur, possibly caused of the presence of abundant apatite and pyrite associated with the magnetite ore. Cerro Principal is the main orebody and comprises a massive, vertical magnetite ore body that contains minor actinolite. The massive magnetite ore body grades outward to disseminated magnetite, forming a transition zone with iron grades ranging between 22 to 45% Fe. Actinolite from the massive magnetite ore body yields radiometric $^{40}Ar/^{39}Ar$ ages of ca. 128 Ma (Rojas et al., 2017).

Brecciated rocks with magnetite clasts, which in some cases display plastic deformation, embedded in an actinolite matrix are observed near fault zones, particularly at the eastern and southern margins of the deposit (Espinoza, 2000). Late magnetite veinlets are also described cross-cutting the main orebodies and the andesite host rocks.

5.3. Analytical Methods

Samples were collected from five drill cores along a NS transect in the Cerro Principal orebody (**Figure 19**). Ten polished sections were inspected using a scanning electron microscope (SEM), and nine of these samples were further analyzed by using a field emission electron

microprobe analyzer (FE-EMPA). Two samples were further analyzed by using micro-Raman spectroscopy.

5.3.1. Scanning electron microscope (SEM)

Carbon coated polished sections were studied by using two different SEMs at the Centre of Microscopy, Characterisation and Analyses (CMCA), University of Western Australia, Perth, Australia: a TESCAN VEGA3 SEM with an acceleration voltage of 20 kV and a beam intensity of 10 nA equipped with an Oxford Instruments X-Max 50 silicon drift EDS system, and a FEI Verios XHR SEM with an acceleration voltage of 15 kV and a beam intensity of 1.6 nA. Backscattered-electron (BSE) images were obtained by using both instruments and qualitative energy dispersive X-ray (EDX) elemental maps of mineral inclusions in magnetite were obtained using the FEI instrument. For compositional maps, Na$K\alpha$, Mg$K\alpha$, Al$K\alpha$, Si$K\alpha$, Cl$K\alpha$, K$K\alpha$, Ca$K\alpha$, Ti$K\alpha$, Mn$L\alpha$ and Fe$L\alpha$ lines were monitored with a 80 mm^2 Oxford Instrument X-Max SDD EDX detector. AZtec and INCA softwares were used for measurements and data processing.

5.3.2. Electron microprobe analyses (EMPA)

Electron microprobe analyses were carried out at the CMCA, University of Western Australia by using a JEOL 8530F FE-EMPA equipped with five wavelength-dispersive crystal spectrometers and an optical microscope for focusing. Single-spot microanalyses were performed on carbon coated polished sections, with an accelerating voltage of 20 kV, a beam current of 50 nA and fully focused beam for magnetite; 25 kV, 40 nA and focused beam for sulfides; 15 kV, 15 nA and focused beam for silicates; and 15kV, 15nA and beam size of 10 μm for apatite. The MAN correction method was used for the data acquisition and correction. Analytical conditions including counting time and standards are listed in the **Supplementary Materials** (**Table SM1**). For magnetite and ilmenite Si, Al, Na, Mg, Ti, Ca, K, Fe, Cr, Ni, V, Mn, Zn, and Cu were analyzed, and interference corrections were performed for Na$K\alpha$, Fe$K\alpha$, Cr$K\alpha$, V$K\alpha$ and Mn$K\alpha$. Sulfur, As, Sb, Fe, Se, Au, Te, Cu, Pb, Ni, Co, Ag, Bi, Si, Pd, Hg, Re, Os, Pt, Cd and Zn were measured in pyrite and line overlap corrections were carried out for S$K\alpha$, As$L\alpha$, Fe$K\alpha$, Se$L\alpha$, Te$L\alpha$, Pb$M\alpha$, Bi$M\alpha$, Hg$L\alpha$, Re$L\alpha$, Os$L\alpha$, Pt$L\alpha$ and Zn$K\alpha$. For silicate phases (actinolite, biotite and pyroxene) F, Cl, Ca, Si, Mg, Al, Mn, Na, Ti, K, Cr, Fe, and V were analyzed and interference corrections were performed for Mn$K\alpha$, Cr$K\alpha$, Fe$K\alpha$ and V$K\alpha$. Oxygen and H contents in hydrated silicates were calculated based on ideal formulas. Only total weight percent results between 97 and 103% were used, except for some silicates, where the stoichiometric method for O and H is not an accurate approximation, however for these minerals only total concentrations between 90 and 103 are considered. Finally, F, Cl, Ca, P, Sr, La, Ce, Nd, Si, Mg, Al, S, Mn, Na, and As were measured in apatite grains and overlap corrections were made on F$K\alpha$, Cl$K\alpha$, P$K\alpha$, Sr$L\alpha$, Nd$L\alpha$, Si$K\alpha$, Al$K\alpha$, Mn$K\alpha$ and As$K\alpha$. Quantitative wavelength dispersive X-ray (WDX)

maps of Si, Al, Na, Mg, Ti, Ca, Fe, V, Mn, and S were obtained by using an acceleration voltage of 20 kV, a beam current of 50 nA and a counting time of 80 s/element for unknown samples. ZAF corrections were applied for all elements and interference corrections were performed for $FeK\alpha$ and $VK\alpha$ because of $MnK\beta$ and $TiK\beta$ overlap, respectively.

5.3.3. Micro-Raman Spectroscopy

Raman measurements were performed at the Department of Chemistry, Universidad de Chile, Santiago, by using a Renishaw micro-Raman (RM 1000) system, equipped with laser lines 514, 633 and 785 nm, a Leica microscope DMLM and an electrically cooled CCD camera. The Raman signal was calibrated to the 520 cm^{-1} line of Si wafer and a 50X objective. Laser power was less than 2 mW. Resolution was set to 4 cm^{-1} and 1-10 scans between 10 and 20s per accumulation. Spectral data were obtained using the 785 nm laser line and were recorded between 100 and 3500 cm^{-1}. Analytical data processing was performed with CrystalSleuth software (Laesch and Downs, 2006) and Origin software (OriginLab, Northampton, MA).

5.3.4. Magnetite precipitation modeling

Iron solubility modeling was performed by using the GEMS software (Kulik et al., 2012). A reported Fe concentration of 7.2 wt.%, along with a minimum bulk salinity of 35 wt.%, obtained in synthetic fluid inclusions from magnetite solubility experiments (Simon et al., 2004), were used as input data, considering speciation of Fe as $FeCl_2$ complexes. PSI/Nagra (Hummel et al., 2002) and SUPCRT92 (Johnson et al., 1992) thermodynamic data were used in the model. For $FeCl_2$ solubility and magnetite precipitation calculations, a temperature and pressure variation of 10°C and 20 MPa were used over a temperature and pressure range of 620-380°C and 200-60 MPa, respectively.

5.4. Results

5.4.1. Magnetite textures, chemistry and mineral inclusions

The magnetite ore body at the El Romeral comprises an aggregate of massive magnetite (>95% modal) with actinolite found mainly at the margins of the ore body. Massive magnetite is composed by three types of magnetite (**Table 7**), which exhibit significant textural variations with depth: Inclusion-rich magnetite (Type I) surrounded by inclusion-free magnetite (Type II) rims occur at the deeper parts of the system (**Figure 20A**), as well as disseminated crystals in the volcanic host rocks and in the Romeral Diorite (Type I and II).

Different mineral inclusions are hosted by Type I magnetite, including oriented (**Figure 20C**) or randomly distributed polycrystalline and one-phase inclusions, some of them nano-sized (**Figure 20D**). Some larger inclusions contain actinolite and Ti-rich mineral phases (co-crystallizing phases), mainly ilmenite and rutile, whereas smaller inclusions are characterized by aggregates of rutile, ilmenite, titanite, chlorite and/or biotite (**Figure 21**, **Figure 22A**), as well as NaCl and pargasite with Ca, Al, Mg and minor Ti, K, Cl, Na, and Mn. The latter phase is also associated with K-feldspar aggregates and titanite at lower depths (<150 m), or with ilmenite and rutile in deeper zones (>300 m). Euhedral Si-rich inclusions are observed in shallow samples (<100 m), which are aligned along magnetite crystallographic planes (**Figure 22B**).

Several mineral inclusions were identified in Type I magnetite by using micro-Raman spectroscopy. These include ilmenite, titanite, rutile, clinochlore (**Figure 23A**), calcite, phlogopite, tremolite, and pargasite (**Figure 23B**). Ti-pargasite inclusion shows two distinct peaks 436 and 670 cm^{-1} that match with pargasite peaks 423 and 668 cm^{-1}. Nervertheless, the first peak (232-288 cm^{-1}) measured on the inclusion is not as pronounced as 236 cm^{-1} pargasite peak, result that may be influenced by magnetite signal (background) and/or the incorporation of Ti in pargasite structure. Euhedral prismatic Si-rich inclusions spectra coincide with the characteristic α-quartz peaks at 462, 355 and 206 cm^{-1} and do not agree with Si-rich glass or other polymorph quartz spectra (**Figure 23C**).

At shallow depths, inclusion-free, chemically-zoned magnetite grains (Type III) is predominant and this magnetite has fractures that are filled with pyrite and actinolite (Figure 20**B**). Chemical zoning, as detected in BSE images, is only observed in inclusion-free magnetite grains (Type III, **Figure 20B**) at the margins and shallow portions of the massive orebodies.

Elemental WDS maps of Fe, V, Ti, Si, Al, and Mg for Type I and Type II magnetite are shown in **Figure 24**, and for Type III magnetite in **Figure 25**. Type I magnetite is slightly depleted in Fe and enriched in Si, Al, Mg, Ca and slightly in Ti in comparison with Type II (**Figure 24**). The Si, Al, Mg and Ca enrichment is most likely caused by the abundant presence of silicate inclusions. On the other hand, V and Na are homogeneously distributed throughout the grain, with the exception of some inclusions that are slightly depleted in V. Type III magnetite shows a distinct zoning with a Si-Al-Ca-Mg-Ti (slightly)Na-rich cores and Fe-rich rims (**Figure 25**). A pronounced oscillatory zoning for Si is observed in rims on Type III magnetite grains. A less distinct oscillatory zoning is also observed for Al, whereas the V is homogeneously distributed throughout Type III magnetite. Electron microprobe spot analyses were performed on Type I and II magnetite.

Electron microprobe spot analyses were performed only on Type I and II magnetite, because they are the more abundant types in the deposit and conform the massive iron ore (main mineralization event). Type I magnetite has between 100-1000 ppm Si, 80-3000 ppm Ti, 2500-2800 ppm V, 120-1000 ppm Ca and 100-800 ppm Mn. For Type II magnetite values yielding between 100-5100 ppm for Si, 50-400 ppm for Ti, 2300-2700 ppm for V, 130 600 ppm for Ca and 120-200 ppm for Mn. Measurements without important inclusion chemistry contribution. Higher Cr (200 ppm) values are observed in inclusion-free disseminated magnetite (Type II) associated with ilmenite and rutile aggregates at depth, along with high V (2800 to 3300 ppm) and Ti (200 ppm to 1.14 wt%) contents. Representative analyses for Type I and II magnetite are shown in **Table 8**, and all results are reported in **Table SM2**.

A fourth magnetite textural type (Type IV) is represented by veinlets with inclusion-free magnetite that crosscut the massive magnetite orebody. Primary magnetite from the Romeral Diorite containing ilmenite exsolution lamellae or ilmenite-actinolite inclusions following magnetite crystallographic planes (**Figure 20E**, **F**) are also described.

5.4.2.   *Sulfide trace and minor elements composition*

Cobalt, Ni and Cu concentrations of pyrite from the magnetite ore body and disseminated grains in the host rocks are shown in **Table 9,** and complete measurements for pyrite and chalcopyrite are reported in **Table SM3**. Analyzed pyrite grains are anhedral and correspond to a post-magnetite mineralization event (**Figure 26A**), with the exception of one sample where the pyrite crystal is completely surrounded by inclusion-free magnetite grains, suggesting a syn-formation with Type II magnetite (**Figure 26B**). Pyrite is characterized by a high Co and Ni contents that range between 0.01-2.24 wt.%, and from 0.01-0.76 wt.%, respectively. In some grains, high concentrations of Cu are detected reaching up to 1.56 wt.%. Arsenic, Ag, Au and other elements were not detected by EMPA.

Chalcopyrite analyses indicate generally constant concentrations of S (34.75-37.48 w.t.%) and Fe (29.32-36.55 wt%), and slightly variable concentrations of Cu (28.27-34.68 wt%). Zinc in chalcopyrite is relatively homogeneous with concentrations between 0.02 wt.% and 0.08 wt.%. Some spot analyses revealed minor concentrations of Se (500-700 ppm), Ag (400-500 ppm), Si (100-1200 ppm), Pd (300-600 ppm), Hg (500 ppm), and Cd (500 ppm).

5.4.3.   *Gangue mineral geochemistry*

The main gangue phases in the deposit are actinolite, minor clinopyroxene, quartz, apatite, biotite, chlorite, titanite, and calcite. Actinolite is the most abundant gangue mineral and is

characterized by different textures and mineral associations. Actinolite I is paragenetically related to Type II magnetite with quartz and clinopyroxene within the inclusion-free magnetite grains in the massive orebody (**Figure 27A**). Large (up to cm-size) acicular crystals of actinolite (actinolite II) are intergrown with Type II magnetite (**Figure 27B**), usually at the margins of the massive magnetite dike. A third type of actinolite (actinolite III) is present in veinlets with chlorite and sulfides, mainly pyrite and minor chalcopyrite. Representative analyses of actinolite I, II and III are reported in **Table 10** and **Table SM4**. Actinolite I is Ca-rich (up to 9.30 wt.% Ca) with slightly more Fe (up to 11.44 wt.%) than Mg (up to 9.30 wt.%), and shows zoning with Ca and Mg-rich cores and Fe and Al-rich rims. Minor elements are Na (up to 0.19 wt.%), Mn and V with a maximum concentration of 0.1 wt.% and 0.08 wt.%, respectively. Actinolite II is characterized by a high Mg content (up to 11.5 wt.%) in comparison with Ca (up to 9.83 wt%) and Fe (up to 8.97 wt.%), along with a pronounced zoning with increasing Ca contents from core to rim. Detectable concentrations of F and Cl are observed in most samples, mainly in the grain cores. Sodium is also present and shows a sharp pattern with decreasing values from the core to the rim. The calculated Fe numbers (Fe# = Fe/(Fe+Mg), molar) for all generations of actinolite vary from 0.18 to 0.36, with an average of 0.34 for actinolite I, 0.23 for actinolite II, and 0.23 for actinolite veinlets (actinolite III).

Clinopyroxene found in association with actinolite I was also analyzed, as well as biotite related to a final event (10 Ma younger, Rojas et al., 2017) of magnetite mineralization. Two types of pyroxene are observed: (i) a V and K-rich augite with similar concentrations of Ca (~9.0 wt.%), Mg (~8.4 wt.%) and Fe (~11.6 wt.%), and (ii) a V and Ti-rich augite with similar concentrations of Ca (~22.9 wt.%) and Fe (~19.7 wt.%), and minor Mg (~0.02 wt.%). Biotite crystals have an eastonite composition with F and Cl replacing the hydroxyl site, and a considerable amount of Ti (up to 1.27 wt.%) and minor V contents (<0.07 wt.%). EMPA data for clinopyroxene and biotite are listed in **Tables SM5 and SM6**, respectively.

Apatite is a minor mineral phase in this deposit compared to magnetite and actinolite. It is usually present as disseminated grains (**Figure 28A)** or in sinuous veinlets that crosscut the main orebody at different depths. In veinlets, apatite crystals are usually subhedral to anhedral and in contact with pyrite grains. These apatite grains can contain several sulfide and silicate inclusions (**Figure 28B**). Hydroxyl content was estimated by using stoichiometric approximation and assuming a fully occupied Z site (general formula $A_5(XO_4)_3Z$). Two different apatite compositions are identified (**Table 11** and **SM7**): (i) a subhedral to hexagonal, F-rich apatite found at depth (~300 m) (**Figure 28A**), and (ii) a OH-rich apatite found in shallower levels (~50 m) (**Figure 28B**). Fluorine-rich apatite has a F content of 1.72-2.01 wt%, and Cl contents between 0.1 and 0.13 wt.%, whereas OH-rich apatite has higher Cl concentrations (up to 0.24 wt.%) and F yielding between 200 and 140 ppm. Silica content in F-rich apatite is <0.09 wt.%. In contrast, OH-rich apatite crystals have concentrations between 0.01 wt.% and 0.56 wt.%. Sulfur and Mn are also detected in both apatite types, but contents are higher in F-rich apatite, i.e., 0.67

wt.% S and 0.11 wt.% Mn. In contrast, the maximum S content in OH-rich apatite is 0.02 wt.%, while Mn reaches 0.08 wt.%. Additionally, La, Ce and Nd were detected in some spots analyses, mainly in F-rich apatite, with La yielding between ~570 and 270 ppm, Ce between ~1300 and 270 ppm and Nd from 230 to 500 ppm. No zoning was observed in apatite grains.

5.5. Discussion

5.5.1. A magmatic hydrothermal origin of magnetite at the El Romeral

Recently, several compositional diagrams that use minor and trace elements abundances in magnetite have recently been proposed to discriminate magnetite among different ore deposit types and help to elucidate the origin of iron oxides for a variety of ore systems (Dare et al., 2014; Dupuis and Beaudoin, 2011; Knipping et al., 2015b; Nadoll et al., 2012; Nadoll et al., 2014a). Regardless of the type of diagram used, the usefulness of these discriminant plots will strongly depend on the accuracy of the analytical measurements and on the rigorousness of the previous petrographic observations to distinguish textures, zonings, and the presence and nature of mineral inclusions that may affect magnetite chemical measurements by microbeam techniques. As described in the previous section, magnetite from El Romeral ore deposit contain abundant micron- to nano-scale mineral inclusions, particularly in the core of magnetite grains from the massive magnetite ore body (Type I magnetite). The presence of textural type was also described by Nold et al. (2014) at the Pilot Knob deposit, a Proterozoic IOA Fe deposit in Missouri, USA, and by Knipping et al. (2015a, b) for the Cretaceous Los Colorados IOA deposit, in Chilean Iron Belt. The cited authors have interpreted the inclusion-rich magnetite cores as a common feature of primary (magmatic?) magnetite.

One of the most widely used discriminant diagrams was presented by Dupuis and Beaudoin (2011) and later modified by Nadoll et al. (2014a), who proposed the use of Al, Mn, Ti and V abundances as a tool to distinguish magnetite from different mineral deposit types (**Figure 29**). Most of the analyses for magnetite grain from El Romeral magnetite grains plot within and below the Kiruna field, which suggests that this field could be extended further to lower Al + Mn compositions (dashed line in **Figure 29**).

Chemical data were divided into magnetite (disseminated and massive) with abundant inclusions (Type I), and inclusion-free or pristine magnetite (Type II). Type II magnetite samples with high Cr contents and spatially related to ilmenite and rutile were excluded due to anomalous Ti concentrations, inferred as measurements affected by Ti-rich inclusions. The data shows that Type II magnetite are confined to a restricted Ti+V range (0.24-0.7 wt.%) and to low Al+Mn (mostly <0.1 wt.%) concentrations, whereas Type I magnetite show a more widespread distribution **(Figure 29).**

76

As mentioned previously, the V content is generally constant for all samples (~2500-3300 ppm), except for magnetite in veinlets that has low V contents (1700 ppm). In contrast, the concentration of Ti in magnetite is more variable (~100-8000 ppm) because of the presence of (exsolved?) Ti-rich inclusions. The widespread distribution of Type I magnetite analyses plausibly reflects that several probe measurements (spot size ~1 micron) are affected by the presence of micron- to nano-scale inclusions of different types (silicate-rich and Ti-rich inclusions). Type I magnetite measurements affected by the presence of inclusions correspond to spots where different "enrichments" are observed. Titanium enrichment is related to titanite inclusions whereas Ti-Mn enrichment is related to ilmenite and rutile inclusions. The few samples that plot within the Porphyry field in **Figure 29** are enriched in Al, which plausibly reflects a contribution from silicate inclusions, such as biotite, chlorite or amphibole.

Knipping et al. (2015a, b) reported geochemical data for several textural types of magnetite from the Los Colorados IOA deposit, Chile (**Figure 18**). These authors recognized magnetite grains with high concentrations of [Ti+V] and [Al+Mn] that plotted at the boundary between the fields for Porphyry and Fe-Ti, V deposits. Knipping et al. (2015a, b) interpreted those compositions as magmatic magnetite. Texturally, the magmatic magnetite grains from Los Colorados contain abundant micron- to nano-scale inclusions, similar to those observed in Type I magnetite in the present study. In addition, Knipping et al. (2015a, b) recognized a decreasing trend in the concentrations of Ti and Al from magmatic magnetite cores to rims, which those authors was interpreted to represent a post-magmatic hydrothermal event. When plotted on the magnetite [Ti+V] and [Al+Mn] discriminant diagram, the composition of these "transitional" magnetite grains define an almost linear trend from the border of the Porphyry/Fe-Ti, V fields, through the Porphyry field, and in to the Kiruna field. However, Knipping et al. (2015a, b) report that the compositions of magnetite from late stage hydrothermal veinlets plot in all six fields on the [Ti+V] vs. [Al+Mn] diagram. A similar trend is observed for the different types of magnetite from the El Romeral, where high [Al+Mn] and [Ti+V] values are obtained for Type I massive magnetite that contains abundant silicate and Ti-rich inclusions, and "transitional" [Al+Mn] and [Ti+V] values are observed in Type I disseminated and Type II inclusion-free magnetite grains.

Nadoll et al. (2014a, b) reported compositions for magnetite from different ore deposits of hydrothermal and igneous origin that revealed specific ranges for certain elements. Those authors found that high Mg (>1 wt.%) and Mn (<100-50400 ppm) contents are distinctive of hydrothermal magnetite, whereas low Mg concentrations (<3940 ppm) and Mn contents between 102 and 12500 ppm are characteristic of igneous magnetite. Type I magnetite grains from (the?) The El Romeral have concentrations between ~100 and 3600 ppm Mg and between ~100 and 1500 ppm Mn, values that are consistent with an igneous magnetite composition. Additionally, V concentrations in the El Romeral magnetite (Types I and II) range between 2300 and 3300 ppm, which plot within the overlap of the igneous and high temperature hydrothermal range (**Figure 30**). Similarly, magnetites Types I and II contain 100-1000 ppm Ti, with some samples reaching

up to 8000 ppm Ti owing plausibly to the presence of micron- and nano-Ti-bearing mineral inclusions. This range is consistent with a high temperature hydrothermal origin (<3500 ppm) and with the lowermost concentrations measured in igneous magnetite (50-97800 ppm). These ranges confirm a high temperature affinity for Type I and II magnetite at the El Romeral.

Figure 30 shows the Ti vs. V diagram from Knipping et al. (2015b), where they reported that magnetite compositions plot in the overlap between the high temperature hydrothermal field and the igneous field. Type I inclusion-free magnetite from El Romeral, unaffected by mineral inclusions, plot dominantly within this overlapping high-temperature hydrothermal – igneous area, with Ti and V values ranging between ~80-3000 ppm and ~2500-2800 ppm, respectively. The V concentrations (~2300-2700) of pristine, inclusion-free, Type II magnetite grains from El Romeral are consistent with high-temperature hydrothermal magnetite and igneous magnetite; however, Type II magnetite grains have lower Ti concentrations (~50-400 ppm) that plot outside the hydrothermal field defined by data reported in Nadoll et al. (2014b) and Knipping et al. (2015b). These lower Ti concentrations for Type II magnetite from El Romeral suggest a high-hydrothermal origin for the pristine, inclusion-free magnetite, in contrast with a magmatic affinity for Type I magnetite.

Chromium was used by Knipping et al. (2015b) to discriminate magnetite from IOA, porphyry, IOCG and Fe-Ti/V deposits. Those authors showed that magnetite from IOA deposits has lower Cr concentration than porphyry and Fe-Ti/V deposits, and are enriched in V relative to IOCG deposits. The low Cr concentrations in magnetite from IOA deposits may reflect the high mobility of Cr^{6+} in high temperature hydrothermal fluid (James, 2003), or augite fractionation in the source magma for a magmatic-hydrothermal fluid, which depletes the melt in Cr. The elevated V contents (>500 ppm) of magnetite from IOA deposits is consistent with crystallization of magnetite at high temperatures. In **Figure 31**, the Cr and V concentrations for magnetite from El Romeral are plotted along with fields based on the study of Knipping et al. (2015b). The data for Types I and II magnetite crystals from El Romeral plot in the IOA field except for a few analyses (4, not plotted) from Type II magnetite grains that are affected by ilmenite inclusions, reaching a Cr concentration of ~240 ppm. Hence, our results for magnetite from El Romeral support the use of this plot as a discriminant diagram for magnetite deposit types.

Mineral inclusions are common features of igneous and hydrothermal minerals and their composition can provide important constraint on the genesis of the sample. Diverse types of mineral inclusions in magnetite have been reported including phosphates, silicates and sulfides (e.g., Bau and Alexander, 2009; Knipping et al., 2015a, 2015b; Nadoll and Koeing, 2011; Nadoll, 2013; Nold et al., 2014). Mineral inclusion phases in the El Romeral magnetite crystals were identified using SEM and micro-Raman spectroscopy. In the deeper portions of the deposit, Type I magnetite from the massive dike contains mineral inclusions such as titanite, rutile, ilmenite,

clinochlore, the most stable member of Mg-chlorite, at external zones of cores and Ti-pargasite at cores (**Figure 23**). At 200 MPa, pargasite stability is estimated between ~800°C and ~1020°C (Jenkins, 1983), although stability can increase with the incorporation of Ti as it has been reported for kaersutite (Stewart, 1980). At similar pressure conditions, clinochlore breaks down at ~780°C (Staudigel and Schreyer, 1977). Thus, and based on the mineral inclusion assemblages, the formation of Type I magnetite cores may have fluctuated between 800°C and 1020°C, with decreasing temperatures towards external areas of cores (below 780ºC). At shallow parts of the deposit, Type I magnetite hosts rutile, phlogopite, K-feldespar, minor pargasite and α-quartz inclusions, as determined using micro-Raman (**Figure 23**). The α-quartz inclusions are arranged as oriented prismatic euhedral crystals (**Figure 20C**), following magnetite crystallographic planes. The presence of α-quartz may be relevant since most Si-rich domains in magnetite have been attributed to the presence of Si in solid solution and/or small silicate inclusions (Newberry et al., 1982; Huberty et al., 2012). It is likely that crystal habit and orientation of α-quartz inclusions may indicate exsolution processes related to slow cooling rates, although hydrothermal crystallization of quartz along microfractures and/or inclusion phase changes during cooling or alteration cannot be ruled out.

5.5.2. Silicate phases and formation conditions

Three different generations of actinolite were analyzed: (i) actinolite (I) grains included in Type II magnetite and in contact with clinopyroxene and quartz (**Figure 27A**), (ii) late pegmatitic actinolite (II) intergrown with Type II magnetite and located at the margins of the magnetite orebodies (**Figure 27B**), and (iii) secondary actinolite (III) from veinlets and in disseminated aggregates, linked to the final hydrothermal sulfide event. The first two types of actinolite associated with Type II magnetite show two distinct patterns in a Ca-Mg-Fe diagram (**Figure 32**). Primary or early actinolite (I) shows a trend from slightly Ca- and Mg-rich cores to lower Ca concentration and higher Fe contents towards the rims. In contrast, late pegmatitic actinolite crystals display a more disperse pattern with increasing Ca concentrations from core to rims. The strong difference between these two patterns is consistent with the presence of two distinct actinolite generations. Further, the (early) actinolite I trend at the El Romeral is consistent with experiments that indicate a compositional, lower temperature re-equilibration with Fe-rich and Ca-poor cummingtonite overgrowths on the original high-temperature tremolite (Lledo and Jenkins, 2008). However, the more pronounced Ca depletion reported in experimental charges by Lledo and Jenkins (2008), compared to El Romeral actinolites, may be associated with the miscibility gap between actinolite and cummingtonite. The latter has an upper stability temperature of 840°C at 5 kbar, temperature that was reached during the first steps of the experimental re-equilibration of tremolite, generating early and strong cummingtonite nucleation (Lledo and Jenkins, 2008).

Published experimental data and thermodynamic modeling indicate that actinolite with Fe-numbers in the range of 0 to 0.4 are stable at 750-900°C (Lledo and Jenkins, 2008). Those authors determined experimentally that actinolite (Fe-number=0.22) breaks down to clinopyroxene, orthopyroxene, quartz and water at 780-850°C and 1-4 kbar. This mineral assemblage (i.e., actinolite, clinopyroxene, orthopyroxene, quartz) is similar to that observed for the early actinolite (I) event in samples from El Romeral, and the compositional variations in high-temperature amphibole are concordant with the pattern obtained for early actinolite (I) samples from El Romeral. These observations are consistent with a magmatic origin for this mineralization. Furthermore, the low Fe-numbers for the three type of actinolite (Type I=0.34; Type II=0.23; Type 3=0.23) in samples from El Romeral are consistent with actinolite crystallization at high-temperatures (i.e., circa magmatic temperatures). The relationship between temperature and actinolite Fe-number relation, which was experimentally determined by Lledo and Jenkins (2008) for amphibole with 1.7-2.0 a.p.f.u Ca, yield temperatures ranging from 735-805°C and 770-840°C at 1 and 2kbar respectively, for the actinolite I and II events associated with Type II magnetite, as well as for actinolite III associated to a later veinlet event. We note that a magmatic origin for actinolite associated with magnetite in the Los Colorados IOA deposit established based on the O and H isotope composition of actinolite (Bilenker et al., 2016), and together with the data from El Romeral supports a magmatic-hydrothermal origin for IOA deposits.

Actinolite (I) is enclosed by magnetite crystals along with quartz and augite (**Figure 27A**). Microprobe data indicate that the augite has a considerable amount of V (up to ~0.4 wt.%, **Table SM5**), and some augite grains are enriched in Ti (0.01-0.4 wt.%). Vanadium and Ti contents are, in some cases, higher than those reported for magnetite, consistent with crystallization from a V-Ti-rich fluid. Augite grains show a dominant Mg-rich composition with Fe-rich patches, indicating changes in composition and/or external conditions during crystallization, such variations are also observed in actinolite and are attributed to temperature fluctuations.

5.5.3. *Late magmatic stage of apatite formation*

Apatite is a common accessory mineral in many rock types and is a ubiquitous phase in IOA deposits. Its chemistry can be complex (general formula $A_5(XO_4)_3Z$, Sommerauer and Katz-Lehnert, 1985). The A-site, occupied by Ca^{2+}, can host REE^{3+}, Eu^{2+} and other trace elements such as Cd, U, Th, Sr, Ba, among others. The X site or P^{5+} allow the incorporation of S, Si, V and As, while halogens (F and Cl), OH and S can be hosted at the anionic Z site. Elemental accommodation is strongly dependent on external conditions, allowing the use of apatite as a powerful petrogenetic indicator and as a fluid tracer (Webster and Piccoli, 2015). Particularly, halogen concentrations in apatite are considered a good monitor of volatile fugacity during magmatic-hydrothermal crystallization (Nash, 1984). Based on halogen content, two types of

apatite are recognized: a F-rich (1.72-2.01 wt%) apatite confined to deeper samples in the deposit, and a OH-rich apatite with a high Cl content (up to 0.24 wt.%), associated with apatite veinlets at shallower depths in the deposit. **Figure 33** shows compositional fields for apatite from different sources (igneous, hydrothermal and sedimentary), and the results for apatite grains from El Romeral, with F-apatite grains plotting in the ore-forming intrusive field. Igneous apatite usually contains higher F concentrations over Cl (Webster and Piccoli, 2015); apatites containing more than 3.5 wt.% Cl are very rare in igneous rocks (Webster and Piccoli, 2015) due to the smaller radius (1.33Å) and higher compatibility of F$^-$ in apatite. In contrast, the larger Cl anion (1.81Å) partitions preferentially into the fluid phase, resulting in a trend where igneous apatite progressively becomes depleted in F and enriched in Cl as hydrothermal conditions become more predominant (**Figure 33**). This trend is observed at the El Romeral, with F-rich apatite found at depth and hence formed at higher temperature than OH-rich Cl-apatite is found at shallow depths. It follows then that F-apatite formed at a late magmatic stage (Piccoli and Candela, 1994), whereas OH-apatite found in veinlets associated with the late sulfide event are of hydrothermal origin. Incorporation of OH over Cl in apatite at the El Romeral may have been controlled by the pH of a deep and high temperature acidic hydrothermal fluid (Zhu and Sverjensky, 1991; Kusebauch et al., 2015).

Apatite composition is used to estimate halogen contents in a silicate melt and exsolved volatile phase (Piccoli and Candela, 1994). Considering an igneous origin for F-rich apatite at the El Romeral, some compositional calculations can be performed to get information about the ore-forming igneous body and exsolved phases. Assuming a temperature of 800°C for the actinolite event associated with F-apatite crystallization (Lledo and Jenkins, 2008), and a corresponding pressure of 200 MPa, the molality of HCl can be obtained using the following equation from Piccoli and Candela (1994):

$$m_{HCl}^{aq} \sim \frac{X_{ClAp}^{Ap}}{X_{HAp}^{Ap}} \cdot \frac{1000}{8} \cdot \frac{1}{10^{[0.04661 + \frac{2535.8}{T} + \frac{0.0303.(P-1)}{T}]}}$$

where X_{ClAp}^{Ap} and X_{HAp}^{Ap} are the mole fractions of Cl and OH in apatite, respectively, T is the apatite crystallization temperature in Kelvin and P is pressure in bars. A hydrochloric acid molality ranging between 0.0137 and 0.0185 was obtained for the magmatic volatile phase when F-apatite crystallized. If we assume that the melt has a metaluminous composition, the approximation of HCl:Cl ratio after Shinohara (1987) can be employed (log (HCl/Σ Cl)^{aq} = -0.63-0.00035*P(bars)) to determine the concentration of Cl in the volatile phase. Following this approach in(?) the volatile phase contained a maximum of 6.2 wt.% Cl. By using an aqueous phase/melt partition coefficient of 43.35 for Cl (Shinohara, 1987) at 1.2 kbar and 810ºC, a Cl content of about 1000-1400 ppm was obtained for a melt in equilibrium with F-apatite. Following Piccoli and Candela (1994), and considering a volatile/melt partition coefficient of 0.184 for F (Webster, 1990),

concentrations of F in the volatile phase and in the melt were calculated, with values of 8.1-11.0 ppm and ~44- 60 ppm, respectively. The low F/Cl ratio in melt may indicate that F-apatite scavenged F from the melt resulting in higher residual Cl content. Moreover, low Cl content in volatile phase (6.2 wt%) in contrast with high salinity generally associated with these systems (35 wt% $NaCl_{eq}$) may also suggest that F-apatite crystallized at a different magmatic stage. This event may be related to a late-stage exsolution of a low salinity (~6 wt.% $NaCl_{eq}$) fluid, unlike a prior event of single-phase fluid exsolution that at the solvus intersection will form an hypersaline (35 wt% $NaCl_{eq}$) Fe-rich fluid and a low-density aqueous vapor. Chlorine concentrations in melt and volatile phase are concordant with the incompatible behavior that characterizes this element.

5.5.4. Hydrothermal sulfide stage

Pyrite is a common phase in ore deposits, and in IOA deposits pyrite is the most abundant sulfide mineral, frequently with subordinate amounts of chalcopyrite. Pyrite has the capacity to incorporate important and variable concentrations of metals and metalloids of economic relevance such as Au, Ag, Cu, Pb, Co, Ni, Zn, As, Sb, Te, Tl, Bi, among others (e.g., Cook and Chryssoulis, 1990; Huston et al., 1995; Reich et al., 2005; Large et al., 2009; Deditius et al., 2014; Reich et al., 2016), in both solid solution and/or nanoparticulate phases. El Romeral pyrite contains <1.0 wt.% Co and Ni (**Table 9**). Cobalt shows a negative correlation with Fe (**Figure 34A)**, which suggests substitution of Co by Fe in octahedral sites, as well as for Zn where a substitution of Fe^{2+} for Zn^{2+} may be suggested. In contrast, Ni does not follow a correlation with Fe or Co (**Figure 34B**), a pattern previously reported by Reich et al. (2016) for Los Colorados pyrite, and that is suggestive of a complex and heterogeneous incorporation of Ni. Copper content in pyrite is scarce, and its presence could be related to chalcopyrite nanoparticles (Reich et al., 2013; Reich et al., 2016), or solid solution incorporation by replacement of Fe through a coupled substitution with As (Radcliffe and McSween, 1969; Pacevsky et al., 2008). However, no significant As was detected by microprobe analyses. Selenium, Pd and Hg contents are associated with the presence of nanoparticles or with solid solution incorporation, where Se replaces S isovalently, incorporation enhanced at low temperature conditions (Huston et al., 1995), and Pd or Hg substitute Fe.

The Co:Ni ratio is a useful tool employed as a petrogenetic indicator in different deposit types (Loftus-Hills and Solomon, 1967; Bajwah et al., 1979; Bralia et al., 1979; Mookherjee and Philip, 1979). A high Co:Ni ratio (>1) in pyrite indicates a magmatic-hydrothermal affinity, associated with high-temperature mafic sources (Bajwah et al., 1979). A low Co:Ni ratio (i.e., <1.0) indicates a sedimentary or diagenetic origin for pyrite (Loftus-Hills and Solomon, 1967; Campbell and Ethier, 1984; Koglin et al., 2010). Additionally, several authors have defined compositional fields for pyrite from different deposit, based on its Co and Ni content (**Figure 35**).

Pyrite from El Romeral yielded a wide range of Co and Ni concentrations within different grains, possibly due to the existence of different events of sulfide mineralization. Previous petrographic studies on El Romeral samples defined three main sulfide events, a syn-ore event associated with Type I magnetite, a later event related to Type II magnetite, and a post-magnetite mineralization event related to hydrothermal veinlets (Rojas et al., 2017). Concordant to these observations, most of the samples plot above a Co:Ni ratio of 0.5, reflecting a hydrothermal origin for low Co:Ni values (~0.5) and magmatic-hydrothermal sources for high Co:Ni ratios (>1.0), particularly for one sample with a high Co content, corresponding to a pyrite related to Type II magnetite (**Figure 26B,** red point in **Figure 35**). Lower Co:Ni ratios (<0.5) are measured for pyrite disseminated in host rocks and for a possible late event of pyrite veinlet mineralization, which crosscut the magnetite dike at shallow levels, suggesting a greater contribution of meteoric or diagenetic fluids at upper levels.

Furthermore, there is a partial overlap for pyrite from El Romeral and pyrite from the Los Colorados deposit (Reich et al., 2016); however most analyses of pyrite from El Romeral plot in the IOCG field, which is consistent with a hydrothermal origin for the main sulfide event and a probable magmatic-hydrothermal source for pyrite associated with Type II magnetite mineralization (red point in **Figure 35**). The sulfur isotope composition of pyrite from El Romeral fingerprint a magmatic-hydrothermal source for sulfur in the El Romeral deposit (δ^{34}S for pyrite ranges from -0.8 to 2.9 ‰ Rojas et al., 2017).

5.5.5. *Late magnetite mineralization event*

A late magnetite mineralization event has been suggested to be coeval with post-ore dikes at the El Romeral. This event has been dated at ~118 Ma (^{40}Ar/^{39}Ar in hydrothermal biotite, Rojas et al., 2017), which is 10 Ma younger than the main magnetite event (~127 Ma, ^{40}Ar/^{39}Ar in actinolite II, Rojas et al., 2017). Biotite grains associated with this younger mineralization event have an eastonite composition, with predominant Fe content over Mg, and high Al concentrations. By using the Ti-in biotite geothermometer proposed by Henry et al., (2005) in biotite:

$$T = ([\ln(\text{Ti}) - a - c(X_{Mg})^3]/b)^{0.333}$$

where T is temperature in ºC, Ti (apfu) is calculated by a normalization to 22 O, and a, b and c are -2.3594, 4.6482e-9 and -1.7283, respectively, a temperature range between 560ºC and 637ºC was obtained for late stage biotite from El Romeral.

The halogen content in biotite can be used to estimate the fugacity ratio $(fH_2O/fHCl)^{fluid}$ following Munoz (1992):

$$\log(fHF/fHCl)^{fluid} = \log\left(\frac{X_F}{X_{Cl}}\right) - \frac{1000}{T}(1.22 + 1.65X_{Mg}) + 0.25$$

$$\log(fH_2O/fHCl)^{fluid} = \log\left(\frac{X_{OH}}{X_{Cl}}\right) + \frac{1000}{T}(1.15 + 0.55X_{Mg}) + 0.68$$

$$\log(fH_2O/fHF)^{fluid} = \log\left(\frac{X_{OH}}{X_F}\right) + \frac{1000}{T}(2.37 + 1.1X_{Mg}) + 0.43$$

where X_{OH}, X_{Cl}, X_F stand for mole fractions of OH, Cl and F in biotite, respectively, X_{Mg} is calculated as (sum of Mg)/(sum of octahedral cations number) and T is the equilibration temperature in Kelvin between hydrothermal fluid and biotite. A temperature range between 550°C and 650°C was used for the fugacity ratio estimation based on the results of the Ti-in biotite geothermometry results. Calculated fugacity ratios (**Figure 36**) indicate two distinct trends: an increasing $\log(fHF/fHCl)^{fluid}$ from -2.6 to -1.6 with increasing temperature (**Figure 36B**); and a decreasing fugacity ratio with increasing temperature, including $\log(fH_2O/fHCl)^{fluid}$ between 4.5 and 4.9 (**Figure 36C**), and a $\log(fH_2O/fHF)^{fluid}$ that ranges from 5.6 to 6.6 (**Fig. 19C**). These trends reflect the behavior of halogens with changing temperature, suggesting that fHF increases with increasing temperature, yielding higher $\log(fHF/fHCl)^{fluid}$.

These model results based on mineral compositions in samples from El Romeral indicate that: (i) the hydrothermal fluid at this late magnetite stage was relatively Cl-rich and (ii) that late-stage biotite and associated secondary magnetite crystallized in the presence of a hydrothermal fluid characterized by a high $fH_2O/fHCl$ and fH_2O/fHF. The model fugacity ratios obtained for biotite crystals from El Romeral are similar to fugacity ratios reported for porphyry Cu systems (Bao et al., 2016), and are consistent with the post-mineralization dikes at the El Romeral forming from a hydrothermal fluid exsolved from a magmatic source.

5.5.6. *Effect of pressure in Fe solubility*

The sum of the data for samples from El Romeral indicate that a hydrothermal fluid was responsible for mineralization transporting Fe, which may be supply by the Romeral Diorite. Knipping et al. (2015a) modeled the size of a magma chamber required to the formation of the 343 Mt Los Colorados deposit. These authors proposed that considering an exsolution of 8 wt.% of magnetite microlites, a 20% of degassing and a 0.4 wt.% FeO transport in a magmatic-hydrothermal system, only a 55 km^3 magma chamber is necessary for the formation of the Los Colorados deposit. If a 50% of depositional efficiency is assumed, a 20 wt.% of magnetite

microlite is required, which is very similar to the 35 modal% observed for El Romeral, according to petrographic observations. Thus, it is not needed a large magma chamber for the deposition of 350 Mt Fe, and therefore, for the formation of the ~128 Mt Fe (450 Mt with a 28% iron grade) El Romeral deposit following the bubble-flotation model.

On the other hand, data from natural systems and experimental studies demonstrate that hydrothermal fluids are enriched in Fe over a wide range of temperature and pressure, and that the concentration of Fe is positively correlated with the Cl content of the fluid (Chou and Eugster, 1977; Heinrich et al., 1992; Audétat et al., 2000; Simon et al., 2004; Williams-Jones and Heinrich, 2005). Considering that El Romeral and all IOA deposits are fundamentally magnetite ore bodies, it is important to assess the ability for a hydrothermal fluid to transport a sufficient quantity of Fe to form an IOA deposit. Published studies indicate that $FeCl_2$ is the main dissolved complex of Fe in supercritical chloride bearing aqueous solutions (Chou and Eugster, 1977; Boctor et al., 1980), and that the precipitation of magnetite from an Fe-bearing hydrothermal fluid occurs by the following reaction:

$$3FeCl_{2(aq)} + 4H_2O = Fe_2O_{4(s)} + 6HCl_{(aq)} + H_{2(aq)}$$
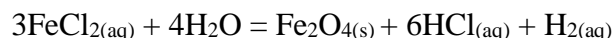
We do not have an independent constraint on the total salinity of the hydrothermal fluid responsible for mineralization at the El Romeral. Knipping et al. (2015a) report the presence of halite-bearing fluid inclusions in magnetite rims for samples from the Los Colorados IOA deposit that are identical to Type II magnetite described in the present study. Those authors report that the presence of halite indicates a minimum salinity of 35 wt.% $NaCl_{eq}$ based on experimental data summarized in Bodnar and Vityk (1994). We used a fluid salinity of 35 wt.% $NaCl_{eq}$ to model the solubility of magnetite as a function of pressure and temperature (**Figure 37**). Experimental data at 800°C demonstrate that pressure plays an important role controlling magnetite solubility (Simon et al., 2004). Considering that the El Romeral and most magnetite-apatite deposits in the Chilean Iron Belt are genetically related to major transtensional fault systems, particularly to sinistral driven Riedel shear zones, the effect of pressure on magnetite solubility is likely a crucial control on mineralization. In **Figure 37**, the model results for magnetite solubility shows a strong dependence on pressure, especially at temperatures between ~450° and 620°C. The model results show that the solubility of $FeCl_2$ in aqueous fluid decreases significantly with decreasing pressure (**Figure 37A**), which results in the precipitation of magnetite (**Figure 37B**). The results also indicate that the rate of decompression affects the efficiency of magnetite precipitation. For example, a $FeCl_2$-bearing hydrothermal fluid at 600°C will precipitate ~50% more magnetite at 100 MPa compare with the volume of magnetite precipitated at 120 MPa. Thus, for hydrothermal fluid with a given quantity of Fe dissolved as $FeCl_2$, rapid decompression favors formations of a larger magnetite ore body.

5.5.7.   A magmatic-hydrothermal process

The data presented in this study show that evolution of the El Romeral Fe deposit was characterized by different conditions and formation processes, leading to significant textural and chemical variations at both macro- and micro-scale. Two distinct magnetite mineralization events are recognized in the massive magnetite orebodies: (i) inclusion-rich magnetite cores (Type I), followed and (ii) inclusion-free magnetite (Type II magnetite), generally observed as rims and overgrowths over primary magnetite (Type I) crystals. The inclusion-rich magnetite cores have higher Ti contents than pristine rims, whereas V is relatively constant in both. Furthermore, Type I magnetite cores display a variation in the nature of inclusions with depth, where magnetite from the deeper portions of the massive ore contain high-temperature (~700-1020ºC) inclusions such as Ti-pargasite and clinochlore. In contrast, magnetite cores from shallower samples are characterized by crystallographycally-oriented α-quartz inclusions that are suggestive of lower cooling rates. These features support a magmatic origin for the first magnetite event, i.e., the inclusion-rich magnetite cores (Type I magnetite).

The presence of a distinct textural and chemical variation between core and rims may be explained by a transition from magmatic to magmatic-hydrothermal conditions. Similar observations were reported by Knipping et al. (2015a, b), who proposed a magmatic-hydrothermal flotation model for the formation of IOA deposits (**Figure 38**). Type I magnetite cores identified in the present study are consistent with crystallization of magnetite microlites from magma silicate melt. Crystals surfaces of magnetite serve as nucleation sites to promote the exsolution of a magmatic-hydrothermal fluid from the silicate melt (**Figure 38A**) (Hurwits and Navon, 1994; Gualda and Ghiorso, 2007). The exsolved fluid phase efficiently scavenges Cl, Fe and other metals from the silicate melt owing to the large fluid/melt partition coefficients for these elements (Zajacz et al., 2008). The small diameter of the magnetite microlites allows them to be entrained by the exsolved fluid phase, and a positive buoyancy force promotes ascent of the magnetite-bubble pairs through the magma body (**Figure 38B**). Ascent of the magnetite-bearing magmatic-hydrothermal phase is focused along the pre-existing transtentional fault system. A sharp decrease in pressure triggers precipitation of hydrothermal magnetite, evidenced by the presence of Type II inclusion-free magnetite rim (**Figure 38C**). The pronounced compositional zoning observed in pristine Type III magnetite crystals (**Figure 20B** and **Figure 25B**), including increasing Si, Al and Mg contents from rims to cores reflects fluctuating conditions affecting hydrothermal fluid composition.

Pristine, hydrothermal Type II magnetite precipitates with minor pyrite and pyroxene, actinolite and quartz. Some of these mineral phases may have been transported as microlites, mineral phases crystallized from the magmatic-hydrothermal fluid during ascent (**Figure 38C**). At the margins of the dike-shaped orebody, pegmatitic actinolite (II) crystals formed, texturally related to this secondary hydrothermal event. Actinolite data reflect two different compositional

trends: (i) early actinolite (I), related to pyroxene and quartz, with decreasing Ca and Mg contents and increasing Fe detected values from core to rims, and (ii) secondary pegmatitic actinolite (II) with increasing Ca contents from core to rim. These different trends are concordant with actinolite crystallization from two different events. Furthermore, the first trend is very similar to the compositional variation reported by Lledo and Jenkins (2008) for magmatic tremolite with decreasing temperature, supporting a high temperature origin (735-805°C and 770-840°C at 1 and 2 kbar, respectively) for the two actinolite events. Based on this mineralogy and its association to inclusion-free magnetite, a temperature <840°C is defined for Type II magnetite mineralization.

Late pulses of hydrothermal fluid are evidenced by the presence of magnetite and sulfides+chlorite veinlets that crosscut the main magnetite orebodies (**Figure 38D**). Lower V contents (1700 ppm) in the late stage magnetite (Type IV magnetite) support the notion of a minor magmatic contribution for this stage compared to primary magnetite from the massive orebody (V content ranging between 2300-2800 ppm). The concentrations of Co and Ni in pyrite from the main mineralization event, where the Co/Ni ratio in pyrite is >0.5 and, as high as >10, are consistent with a mafic magmatic source for the magmatic-hydrothermal ore fluids, indicate a contribution of non-magmatic fluid(s) for late stage mineralization at shallow level of the deposit. A final stage of magnetite mineralization spatially related to hydrothermal biotite crystals is also reported, possibly associated with post-mineralization dikes (Rojas et al., 2017).

5.6. Conclusions

This study presents and interprets new geochemical data from the El Romeral IOA deposit, located in the Cretaceous Chilean Iron Belt (CIB), in order to better understand the genesis of one of the largest magnetite-apatite ore bodies in the CIB. Microprobe analyses, in combination with petrological studies, SEM and micro-Raman data, reveal two main mineralization events: (i) a first magnetite mineralization (Type I) represented by high-temperature, inclusion-rich magnetite cores at deep levels of the deposit, and, at shallow levels of the deposit, by magnetite cores or disseminated crystals with α-quartz inclusions oriented along crystallographic planes evidencing a slow cooling system; and, (ii) a second magnetite event recognized as inclusion-free pristine magnetite (Type II), usually surrounding primary magnetite cores. Both events are characterized by magnetite that is enriched in V (~2300-2800 ppm), and has variable Ti concentrations (~50-3000 ppm). High Ti contents (~80-3000 ppm) in primary magnetite cores, coupled with an assemblage of micron- to nano-scale high-temperature (800-1020°C) mineral inclusion assemblage identified in magnetite cores, are consistent with a magmatic origin for the first magnetite mineralization event. On the other hand, high V (~2300-2700 ppm) and lower Ti (~50-400 ppm) contents, along with marked zonations in magnetite crystals found at shallow depths of the deposit, are consistent with hydrothermal precipitation of magnetite from a magmatic-hydrothermal fluid with strongly fluctuating composition as a result

of decompression and decreasing temperature. Actinolite crystals at deeper levels of the deposit yield low #Fe numbers, reflecting temperatures of crystallization between 735°C and 840°C, which is consistent with crystallization from a high-temperature hydrothermal fluid. The compositions of pyrite and apatite also record a distinct change from magmatic-hydrothermal fluid to lower-temperature hydrothermal fluids. This trend is reflected in Co:Ni ratios in pyrite, where deeper early pyrite mineralization yields ratios mostly ≥0.5, and shallow, late stage pyrite yields lower ratios. Additionally, the abundances of F, Cl and OH in apatite vary strongly with depth, where F-rich apatite occurs in deeper zones of the deposit and OH-apatite with higher Cl contents occurs in veinlets at shallow levels.

Regarding the mechanisms for Fe accumulation, an Fe solubility model is presented that shows that magnetite precipitation occurs by decompression at temperatures ≥380°C. Iron oxide-apatite deposits in the Chilean Iron Belt are spatially associated with major transtensional fault zones (i.e., the Atacama Fault Zone), and the model results are consistent with strong structural control for ascent of hydrothermal fluid and ore accumulation/precipitation. The style of mineralization at the El Romeral is nearly identical to all IOA deposits and thus it seems plausible to suggest that the formation of IOA deposits is enhanced by extensional forces related to tectonic movements, and that they reflect a transition from magmatic to hydrothermal dominated processes.

Acknowledgments

REFERENCES

Audétat, A., Günther, D. and Heinrich, C.A. 2000. Causes for large-scale metal zonation around mineralized plutons: fluid inclusion LA-ICP-MS evidence from the Mole Granite, Australia. *Economic Geology*, **95**, 1563-1581.

Bajwah, Z.U., Secombe, P.K. and Offler, R. 1987. Trace element distribution, Co:Ni ratios and genesis of the Big Cadia iron-ore deposit, New South Wales, Australia. *Mineralium Deposita*, **22**, 292–300.

Bao, B., Webster, J.D., Zhang, D., Goldoff, B.A. and Zhang, R. 2016. Compositions of biotite, amphibole, apatite and silicate melt inclusions from the Tongchang mine, Dexing porphyry deposit, SE China: Implications for the behavior of halogens in this mineralized porphyry system. *Ore Geology Reviews*, **79**, 443-462.

Barth, A.P. and Dorais, M.J. 2000. Magmatic anhydrite in granitic rocks: First occurrence and potential petrologic consequences. *American Mineralogist*, **85**, 430-435.

Barton, M.D. 2014. Iron oxide (-Cu-Au-REE-P-Ag-U-Co) systems. *Treatise on Geochemistry*, **13**, 515-541.

Bau, M. and Alexander, B.W. 2009. Distribution of high field strength elements (Y, Zr, REE, Hf, Ta, Th, U) in adjacent magnetite and chert band and in reference standards FeR-3 and FeR-4 from the Temagami iron-formation, Canada, and the redox level of the Neoarchean ocean. *Precambrian Res*., **174**, 337-346.

Belousova, E.A., Walters, S., Griffin, W.L. and O'Reilly, S.Y. 2001. Trace-element signatures of apatites in granitoids from the Mt Isa Inlier, northwestern Queensland. *Australian Journal of Earth Sciences*, **48**, 603-619.

Bilenker, L.D., Simon, A.C., Reich, M., Lundstrom, C.C., Gajos, N., Bindeman, I., Barra, F. and Munizaga, R. 2016. Fe-O stable isotope pairs elucidate a high-temperature origin of Chilean iron oxide-apatite deposits. *Geochimica et Cosmochimica Acta*, **177**, 94-104.

Boctor, N.Z., Popp, R.K. and Frantz, J.D. 1980. Mineral-solution equilibria-IV. Solubilities and the thermodynamic propoerties of $Fe_2O_3^0$ in the system Fe_2O_3-H_2-H_2O-HCl. *Geochimica et Cosmochima Acta*, **44**, 1509-1518.

Bodnar, R.J., and Vityk, M.O. 1994. Interpretation of microthermometric data for H₂O-NaCl flud inclusions. *In:* De Vivo, B., and Frezzotti, M.L. (eds) *Fluid Inclusions in Minerals, Methods and Applications*, Virginia tech, Blacksburg, VA, 117-130.

Bookstrom, A. 1975. *Magnetite deposits of El Romeral, Chile: physical geology, sequence of events, and processes of formation.* In partial fulfillment of the requirements for degree of Doctor of Philosophy, Stanford University, Department of Geology, Palo Alto.

Bralia, A., Sabatini, G. and Troja, P. 1979. A reevaluation of the Co/Ni ratio in pyrite as geochemical tool in ore genesis problems. *Mineralium Deposita*, **14**, 353–374.

Campbell, F.A. and Ethier, V.G. 1984. Nickel and cobalt in pyrrhotite and pyrite from the Faro and Sullivan orebodies. *Canadian Mineralogist*, **22**, 503–506.

CAP Minería. 2014. *Memoria Anual*. Obtenido de http://www.capmineria.cl/wp-content/uploads/2015/03/cap_mineria_memoria_2014.pdf

Charrier, R., Pinto, L. and Rodríguez, M.P. 2007. Tectonostratigraphic evolutions of the Andean Orogen in Chile. *In:* Moreno, T. and Gibbons, W. (eds.) *The Geology of Chile*, The Geological Society of London, London, 21-114.

Childress, T.M., Simon, A.C., Day, W.C., Lundstrom, C.C., and Bindeman, I.N. 2016. Iron and oxygen isotope signatures of the pea ridge and pilot knob magnetite-apatite deposits, Southeast Missouri, USA. *Economic Geology*, **111(8)**, 2033-2044.

Chou, I.C. and Eugster, H.P. 1977. Solubility of magnetite in supercritical chloride solutions. *American Journal of Science*, **277**, 1296-1314.

Cook, N.J. and Chryssoulis, S.L. 1990. Concentrations of invisible gold in the common sulfides. *Canadian Mineralogist*, **28**, 1–16.

Dare, S.A.S., Barnes, S. and Beaudoin, G. 2015. Did the massive magnetite "lava flows" of El Laco (Chile) form by magmatic or hydrothermal processes? New contraints from magnetite composition by LA-ICP-MS. *Mineralium Deposita*, **50**, 607-617.

Day, W.C., Slack, J.F., Ayuso, R.A., and Seeger, C.M. 2016. Regional geologic and petrologic framework for iron oxide ±apatite ±rare earth element and iron oxide copper-gold deposits of the Mesoproterozoic St. Francois Mountains Terrane, Southeast Missouri, USA. *Economic Geology*, **111**, 1825-1858.

Deditius, A., Reich, M., Kesler, S.E., Utsunomiya, S., Chryssoulis, S., Walshe,J.L., Hough, R. and Ewing, R.C. 2014. The coupled geochemistry of Au and As in pyrite from hydrothermal ore deposits. *Geochimica et Cosmochimica Acta*, **140**, 644–670.

Dobbs, M. 1978. *Distribución de vanadio y titanio en el Cuerpo Principal de la mina El Romeral.* Memoria para optar al Título de Geólogo. Universidad de Chile, Facultad de Ciencias Físicas y Matemáticas, Departamento de Geología, Santiago, p.86.

Donovan, J.J., Snyder, D.A. and Rivers, M.L. 1993. An improved interference correction for trace element analysis. *Microbeam Analysis*, **2**, 23-28.

Douce, A.E.P., Roden, M.F., Chaumba, F., Fleisher, C. and Yogodzinsky, G. 2011. Compositional variability of terrestrial mantle apatites, thermodynamic modeling of apatite volatile contents, and the halogen and water budgets of planetary mantles. *Chemical Geology*, **288**, 14-31.

Emparan, C. and Pineda, G. 2000. Área La Serena-La Higuera, Región de Coquimbo. Servicio Nacional de Geología y Minería, Santiago, no.**18**, 1:100.000.

Emparan, C. and Pineda, G. 2005. Geología del Área Andacollo-Puerto Aldea, Región de Coquimbo. Servicio Nacional de Geología y Minería, Santiago, no.**96**, 1:1000.000.

Espinoza, L. 2000. *Estudio petrográfico del cuerpo Cerro Principal del distrito ferrífero El Romeral IV región- La Serena, Chile*. Memoria para optar al título de geólogo.

Universidad de Chile, Facultad de Ciencias Físicas y Matemáticas, Departamento de Geología, Santiago, Chile.

Gana, P. 1991. Mapa geológico de la Cordillera de la Costa entre La Serena y Quebrada El Teniente. Servicio Nacional de Geología y Minería, Santiago, no.**3**, 1:100.000.

Gualda, G.A.R., and Ghiorso, M.S. 2007. Magnetite scavenging and the buoyancy of bubbles in magmas. Part 2: Energetics of crystal-bubble attachment in magmas. *Contribution to Mineralogy and Petrology*, **154**, 479-490.

Heinrich, C.A., Ryan, C.G., Mernagh, T.P. and Eadington, P.J. 1992. Segregation of ore metals between magmatic brine and vapor. *Economic Geology*, **87**, 1566-1583.

Henry, D.J., Guidotti, C.V. and Thomson, J.A. 2005. Ti-saturation surface for low-to-medium pressure metapelitic biotites: Implications for geothermometry and Ti-substitution mechanisms. *American Mineralogist*, **90**, 316-328.

Huberty, J.M., Konishi, H., Heck, P.R., Fournelle, J.H., Valley, J.W. and Xu, H. 2012. Silician magnetite from the Dales Gorge Member of the Brockman Iron Formations, Hamersley Group, Western Australia. *American Mineralogist*, **97**, 26-37.

Hummel, W., Berner, U., Curti, E., Pearson, F.J. and Thoenen, T. 2002. Nagra/PSI chemical Thermodynamic Data Base 01/01. Nagra NTB 02-16, Nagra, Wettingen, Switzerland.

Hurwitz, S., and Navon, O. 1994. Bubble nucleation in rhyolitic melts: Experiments at high pressure, temperature, and water content. *Earth and Planetary Science Letters*, **122**, 267-280.

Huston, D.L., Sie, S.H., Suter, G.F., Cooke, D.R. and Both, R.A. 1995. Trace elements in sulfide minerals from eastern Australian volcanic-hosted massive sulfide deposits: Part I. Proton microprobe analyses of pyrite, chalcopyrite, and sphalerite, and Part II. Selenium levels in pyrite: Comparison with $\delta^{34}S$ values and implications for the source of sulfur in volcanogenic hydrothermal systems. *Economic Geology*, **90**, 1167–1196.

Jaillard, E., Soler, P., Carlier, G. and Mourier, T. 1990. Geodynamic evolution of the northern and central Andes during early to middle Mesozoic times: a Tethyan model. *Journal of the Geological Society*, **147**, 1009-1022.

James, B.R. 2003. Chromium. *In:* Stewart, B.A., and Howell, T.A., (eds) *Encyclopedia of Water Science*, Marcel Dekker Inc., 77-82

Jenkins, D.M. 1983. Stability and composition relations of calcic amphiboles in ultramafic rocks. *Contributions to Mineralogy and Petrology*, **83**, 375-384.

Johnson, J.W., Oelkers, E.H., Helgeson, H.C. 1992. SUPCRT92: A software package for calculating the standard molal thermodynamic properties of minerals, gases, aqueous species, and reactions from 1 to 5000 bar and 0 to 1000°C. *Computers and Geosciences*, **18**, 899-947.

Jonsson, E., Troll, V.R., Högdahl, K., Harris, C., Weis, F., Nilsson, K.P., and Skelton, A. 2013. Magmatic origin of giant 'Kiruna-type' apatite-iron-oxide ores in Central Sweden. *Scientific Reports*, **3.**

Knipping J.L., Bilenker, L.D., Simon, A.C., Reich, M., Barra, F., Deditius, A.P., Lundstrom, C., Bindeman, I. and Munizaga, R. 2015a. Giant Kiruna-type deposits form by efficient flotation of magmatic magnetite suspensions. *Geology*, **43**, 591-594.

Knipping J.L., Bilenker, L.D., Simon, A.C., Reich, M., Barra, F., Deditius, A.P., Wälle, M., Heinrich, C.A., Holtz, F. and Munizaga, R. 2015b. Trace elements in magnetite from massive iron oxide-apatite deposits indicate a combined formation by igneous and magmatic-hydrothermal processes. *Geochimica et Cosmochimica Acta*, **171**, 15-38.

Koglin, N., Frimmel, H.E., Minter, W.E.L. and Brätz, H. 2010. Trace-element characteristics of different pyrite types in Mesoarchaean to Palaeoproterozoic placer deposits. *Mineralium Deposita*, **45**, 259–280.

Krneta, S., Ciobanu, C.L., Cook, N.J., Ehrig, K. and Kontonikas-Charos, A. 2016. Apatite at Olympic Dam, South Australia: A petrogenetic tool. *Lithos*, **262**, 470-485.

Kusebauch, C., John, T., Whitehouse, M.J., Klemme, S. and Putnis, A. 2015. Distribution of halogens between fluid and apatite during fluid-mediated replacement processes. *Geochimica et Cosmochimica Acta*, **170**, 225-246.

Laetsch, T. and Downs, T. 2006. Software for identification and refinement of cell parameters from powder diffraction data of minerals using the RRUFF project and American Mineralogist Crystal Structure databases. *19th General Meeting of the International Mineralogical Association*, Kobe, Japan, **23**, p.28.

Lagas, G.A. 2016. *Estudio de la química mineral de la pirita del yacimiento magnetita-apatito de Los Colorador, III región de Atacama, Chile.* Memoria para optar al título de geólogo. Universidad de Chile, Facultad de Ciencias Físicas y Matemáticas, Departamento de Geología, Santiago, Chile.

Large, R.R., Danyushevsky, L., Hollit, C., Maslennikov, V., Meffre, S., Gilbert,S., Bull, S., Scott, R., Emsbo, P., Thomas, H., Singh, B. and Foster,J. 2009. Gold and trace element zonation in pyrite using a laser imaging technique: Implications for the timing of gold in orogenic and Carlin-style sediment-hosted deposits. *Economic Geology*, **104**, 635–668.

Lledo, H.L. and Jenkins, D.M. 2008. Experimental Investigation of the Upper Thermal Stability of Mg-rich Actinolite; Implications for Kiruna-Type Iron Deposits. *Journal of Petrology*, **49**, 225-238.

Loftus-Hills, G. and Solomon, M. 1967. Cobalt, nickel and selenium in sulphides as indicators of ore genesis. *Mineralium Deposita*, **2**, 228–242.

Lorca, G. 1990. *Caracterización geoquímica y cristalográfica de las piritas de los yacimiento de Fe El Algarrobo y El Romeral.* Memoria para optar al título de geólogo. Universidad de Chile, Facultad de Ciencias Físicas y Matemáticas, Departamento de Geología, Santiago, Chile.

Maksaev, V., Gardeweg, M., Ramírez, C.F., and Zentilli, M. 1998. Aplicación de método de trazas de fisión a la datación de cuerpo de magnetita de El Laco e Incahuasi en el Altiplano de la Región de Antofagasta. *V Congreso Geológico Chileno*, Actas **1**, B1-B23

Marks, M.A.W., Wenzel, T., Whitehouse, M.J., Loose, M., Zack, T., Barth, M., Worgard, L., Krasz, V., Eby, N., Stosnach, H. and Marki, G. 2012. The volatile inventory (F, Cl, Br, S, C) of magmatic apatite: An integrated analytical approach. *Chemical Geology*, **291**, 241-255.

Ménard, J.J. 1995. Relationship between altered pyroxene diorite and the magnetite mineralization in the Chilean Iron Belt, with emphasis on the El Algarrobo iron deposits (Atacama region, Chile). *Mineralium Deposita*, **30**, 268-274.

Mookherjee, A. and Philip, R. 1979. Distribution of copper, cobalt and nickel in ores and host-rocks, Ingladhal, Karnataka, India. *Mineralium Deposita*, **14**, 33–55.

Munoz, J.L. 1992. Calculation of HF and HCl fugacities from biotite compositions: revised equations. *Geological Society of America*, **24**, A221.

Nadoll, P. 2013. Mineral Inclusions in magnetite as a guide to exploration-Preliminary results. *12ᵗʰ SGA Biennial Meeting 2013 Proceedings*, **1**, 280-282.

Nadoll, P. and Koenig, A.E. 2011. LA-ICP-MS of magnetite: methods and reference materials. *Journal of Analytical Atomic Spectrometry*, **26**, 1872-1877.

Nadoll, P., Angerer, T., Mauk, J.L., French, D. and Walshe, J. 2014a. The chemistry of hydrothermal magnetite: a review. *Ore Geology Reviews*, **61**, 1-32.

Nadoll, P., Mauk, J.L., Richard, A.L. and Koenig, A.E. 2014b. Geochemistry of magnetite from porphyry Cu and skarn deposits in the southwestern United States. *Mineralium Deposita*. http://dx.doi.org/10.1007/s00126-014-0539-y

Naranjo, J.A., Henríquez, F. and Nyström, J.O. 2010. Subvolcanic contact metasomatism at El Laco Volcanic Complex, Central Andes. *Andean Geology*, **37**, 110-120.

Nash, W.P. 1984. Phosphate minerals in terrestrial igneous and metamorphic rocks. *In:* Nriagu, J.O. and Moore, P.B. (eds.) *Phosphate Minerals*, Springer-Verlag, New York, 215-241.

Naslund, H.R., Henríquez, F., Nyström, J.O., Vivallo, W. and Dobbs, F.M. 2002. Magmatic iron ores and associated mineralization: Examples from the Chilean high Andes and Coastal Cordillera. *In:* Porter, T.M. (ed.) *Hydrothermal Iron Oxide Copper-Gold & Related Deposits: A Global Perspective*, PGC Publishing, Adelaide, **2**, 207-226.

Newberry, N.G., Peacor, D.R., Essene, E.J., and Geissman, J.W. 1982. Silicon in magnetite: high resolution microanalysis of magnetite-ilmenite intergrowths. *Contributions to Mineralogy and Petrology*, **80(4)**, 334–340.

Nold, J.L., Dudley, M.A. and Davidson, P. 2014. The southeast Missouri (USA) Proterozoic iron metallogenic province-Types of deposits and genetic relationships to magnetite-apatite and iron oxide-copper-gold deposits. *Ore Geology Reviews*, **57**, 154-171.

Nyström, J.O. and Henríquez, F. 1994. Magmatic features of iron ores of the Kiruna type in Chile and Sweden: Ore textures and magnetite geochemistry. *Economic Geology*, **89**, 820-839.

Pacevski, A., Libowitzky, E., Zivkovic, P., Dimitrijevic, R. and Cvetkovic, L. 2008. Copper-bearing pyrite from the Coka Marin polymetallic deposit, Serbia: mineral inclusions or true solid solution? *The Canadian Mineralogist*, **46**, 249-261.

Piccoli, P. and Candela, P. 1994. Apatite in felsic rocks: A model for the estimation of initial halogen concentrations in the Bishop tuff (Long Valley) and Tuolumne intrusive suite (Sierra Nevada Batholith) magmas. *American Journal of Science*, **294**, 92-135.

Piña, R., Gervilla, F., Barnes, S.J., Ortega, L. and Lunar, R. 2013. Platinum-group elements-bearing pyrite from the Aguablanca Ni-Cu sulphide deposit (SW Spain): a LA-ICP-MS study. *European Journal of Mineralogy*, **25**, 241-252.

Radcliff, D. and McSween, H.Y. 1969. Copper zoning in pyrite from Cerro de Pasco, Perú: a discussion. *American Mineralogist*, **55**, 527-528.

Reed, M.J., Candela, P.A., and Piccoli, P.M. 2000. The distribution of rare earth elements between monzogranitic melt and the aqueous volatile phase in experimental investigations at 800°C and 200 MPa. *Contirbutions to Mineralogy and Petrology*, **140**, 251-262.

Reich, M., Kesler, S.E., Utsunomiya, S., Palenik, C.S., Chryssoulis, S. and Ewing, R.C. 2005. Solubility of gold in arsenian pyrite. *Geochimica et Cosmochimica Acta*, **69**, 2781–2796.

Reich, M., Deditius, A., Chryssoulis, S., Li, J., Ma, C.Q., Parada, M.A., Barra, F. and Mittermayr, F. 2013. Pyrite as a record of hydrothermal fluid evolution in porphyry copper system: A SIMS/EMPA trace element study. *Geochimica et Cosmochimica Acta*, **104**, 42-62.

Reich, M., Simon, A.C., Deditius, A., Barra, F., Chryssoulis, S., Lagas, G., Tardani, D., Knipping, J., Bilenker, L., Sánchez-Alfaro, P., Roberts, M.P. and Munizaga, R. 2016. Trace element signature of pyrite from the Los Colorador Iron oxide-apatite (IOA) deposit, Chile: a missing link between Andean IOA and Iron oxide copper-gold systems. *Economic Geology*, **111**, 743-761.

Réquia, K., Stein, H., Fontboté, L., Chiaradia, M. 2003. Re-Os and Pb-Pb geochronology of the Archean Salobo iron oxide copper-gold deposit, Carajá Mineral Province, northern Brazil. *Mineralium Deposita*, **38**, 727-738.

Rhodes, A.L. and Oreskes, N. 1999. Oxygen Isotope composition of magnetite deposits at El Laco, Chile: Evidence of formation from isotopically heavy fluids: Geology and ore deposits of the Central Andes. *In:* Skinner, B.J. (ed.)., *Society of Economic Geologists Special Publications*, **7**, 333-351.

Rhodes, A.L., Oreskes, N. and Sheets, S. 1999. Geology and rare earth element geochemistry of magnetite deposits at El Laco, Chile: Geology and ores deposits of the Central Andes. *In:* Skinner, B.J. (ed.) *Society of Economic Geologists Special Publication*, **7**, 299-332.

Rojas, P.A., Barra, F., Reich, M., Deditius, A. and Simon A. 2017. Mineral chemistry of magnetite and accessory phases from El Romeral iron oxide-apatite deposit, Chile. *Goldschimdt Conference*, Paris.

Romer, R.L., Martinsson, O., and Perdahl, J.A. 1994. Geochronology of the Kiruna Iron Ores and Hydrothermal Alterations. *Economic Geology*, **89**, 1249-1264.

Rusk, B., Oliver, N., Cleverley, J., Blenkinsop, T., Zhang, D., Williams, P. and Habermann, P. 2010. Physical and chemical characteristics of the Ernest Henry iron oxide copper gold deposit, Australia; implications for IOCG genesis. *In:* Porter, T.M. (ed.) *Hydrothermal Iron Oxide Copper-Gold & Related Depotis: a global perspective-advances in the understanding of IOCG deposits*, **3**, 201-218.

Scher, S., Williams-Jones, A.E. and Williams-Jones, G. 2013. Fumarolic activity, acid-sulfate alteration, and high sulfidation epithermal precious metal mineralization in the crater of Kawah Ijen Volcano, Java, Indonesia. *Economic Geology*, **108**, 1099-1118.

Scott, J.A.J., Humphreys, M.C.S., Mather, T.A., Pyle, D.M. and Stock, M.J. 2015. Insights into the behaviour of S, F, and Cl at Santiaguito Volcano Guatemala, from apatite and glass. *Lithos*, **232**, 375-394.

Shinohara, H., *ms*, 1987, Partition of chlorine compounds in the system silicate melt and hydrothermal solutions. *Unpublished D.Sc.Dissertation, Tokyo Institute of Technology*, p.192.

Sillitoe, R.H. and Burrows, D.R. 2002. New field evidence bearing on the origin of the El Laco magnetite deposit, northern Chile. *Economic Geology*, **97**, 1101-1109.

Sillitoe, R. H. 2010. Porphyry copper systems. *Economic geology*, **105**, 3-41.

Simon, A.C., Pettke, T., Candela, P.A., Piccoli, P.M. and Heinrich, A.H. 2004. Magnetite solubility and iron transport in magmatic-hydrothermal environments. *Geochimica et Cosmochimica Acta*, **68**, 4905-4914.

Simon, A.C., Pettke, T., Candela, P.A., and Piccoli, P.M. 2008. The partitioning behavior of silver in a vapor-brine-rhyolite melt assemblage. *Geochimica et Cosmochimica Acta*, **72(6)**, 1638-1659.

Simon, A.C., and Ripley, E.M. 2011. The role of magmatic sulfur in the formation of ore deposits. *In:* Behrens, H., Webster, J.D. (eds) *Sulfur in Magmas and Melts: Its importante for natural and technical processes*, Mineralogical Society of America, **73**, 513-578

Soltani Dehnavi, A., Lentz, D.R. and McFarlane, C.R.M. 2015. LA-ICPMS analyses of volatile trace elements in massive sulphides and host rocks of selected VMS deposits of the Bathurst mining camp, New Brunswick: Methodology and application to exploration. *Geological Survey of Canada Open File,* **7853**, p.214.

Sommerauer, J. and Katz-Lehnert, K. 1985. A new partial substitution mechanism of $CO_3^{(2-)}$/$CO_3OH^{(3-)}$ and $SiO_4^{(4-)}$ for the $PO_4^{(3-)}$ group in hydroxyapatite from the Kaiserstuhl alkaline complex (SW-Germany). *Contributions to Mineralogy and Petrology*, **91**, 360-368.

Staudigel, H. and Schreyer, W. 1977. The Upper Thermal Stability of Clinochlore, $Mg_5Al[AlSi_3O_{10}](OH)_8$, at 10-35kb PH_2O. *Contributions to Mineralogy and Petrology*, **61**, 187-198.

Stewart, D.C. 1980. *A petrographic, chemical, and experimental study of kaersutite occurences at Dish Hill, California, with implications for volatiles in the upper mantle*. PhD.Thesis, The Pennsylvania State University, p.88.

Swanson, S.E. and Fenn, P.M. 1986. Quartz crystallization in igneous rocks. *American Mineralogist*, **71**, 331-342.

Treloar, P.J. and Colley, H. 1996. Variations in F and Cl contents in apatites from magnetite-apatite ores in northern Chile, and their ore-genetic implications. *Mineralogical Magazine*, **60(2)**, 285-301.

Velasco, F., Tornos, F. and Hanchar, J.M. 2016. Immiscible iron-and silica-rich melts and magnetite geochemistry at the El Laco volcano (northern Chile): Evidence for a magmatic origin for the magnetite deposits. *Ore Geology Reviews*, **79**, 346-366.

Webster, J.D. 1990. Partitioning of F between H_2O and CO_2 fluids and topaz rhyolite melt: Implications for mineralizing magmatic-hydrothermal fluids in F-rich granitic systems. *Contributions to Mineralogy and Petrology*, **104**, 424-438.

Webster, J.D. and Piccoli, P.M. 2015. Magmatic apatite: a powerful, yet deceptive mineral. *Elements*, **11**, 177–182.

Westhues, A., Hanchar, J.M., LeMessurier, M., and Whitehouse, M.J. 2017. Evidence for hydrothermal alteration and source regions for the Kiruna iron oxide-apatite ore (northern Sweden) from zircon Hf and O isotopes. *Geology*, **45(6)**, 571-574.

Williams, P.J., Barton, M.D., Johnson, D.A., Fontboté, L., De Haller, A., Mark, G., Oliver, N.H.S. and Marschik, R. 2005. Iron oxide copper-gold deposits: Geology, space-time distribution, and possible modes of origin. *Economic Geology*, 371-405.

Williams-Jones, A.E., and Heinrich, C.A. 2005. Vapor transport of metals and the formation of magmatic-hydrothermal ore deposits. *Economic Geology*, **100(7)**, 1287-1312.

Zajacz, Z., Halter, W.E., Pettke, T., and Guillong, M. 2008. Determination of fluid/melt partition coefficients by LA-ICPMS analysis of co-existing fluid and silicate melt inclusions: Controls on element partitioning. *Geochimica et Cosmochimica Acta*, **71**, 2169-2197.

Zajacz, Z., Candela, P.A., Piccoli, P.M., and Sanchez-Valle, C. 2012. The partitioning of sulfur and chlorine between andesite melts and magmatic volatiles and the exchange coefficients of major cations. *Geochimica et Cosmochimica Acta*, **89**, 81-101.

Zhu C. and Sverjensky D. A. 1991. Partitioning of F–Cl–Oh between minerals and hydrothermal fluid. *Geochimica et Cosmochimica Acta*, **55**, 1837–1858.
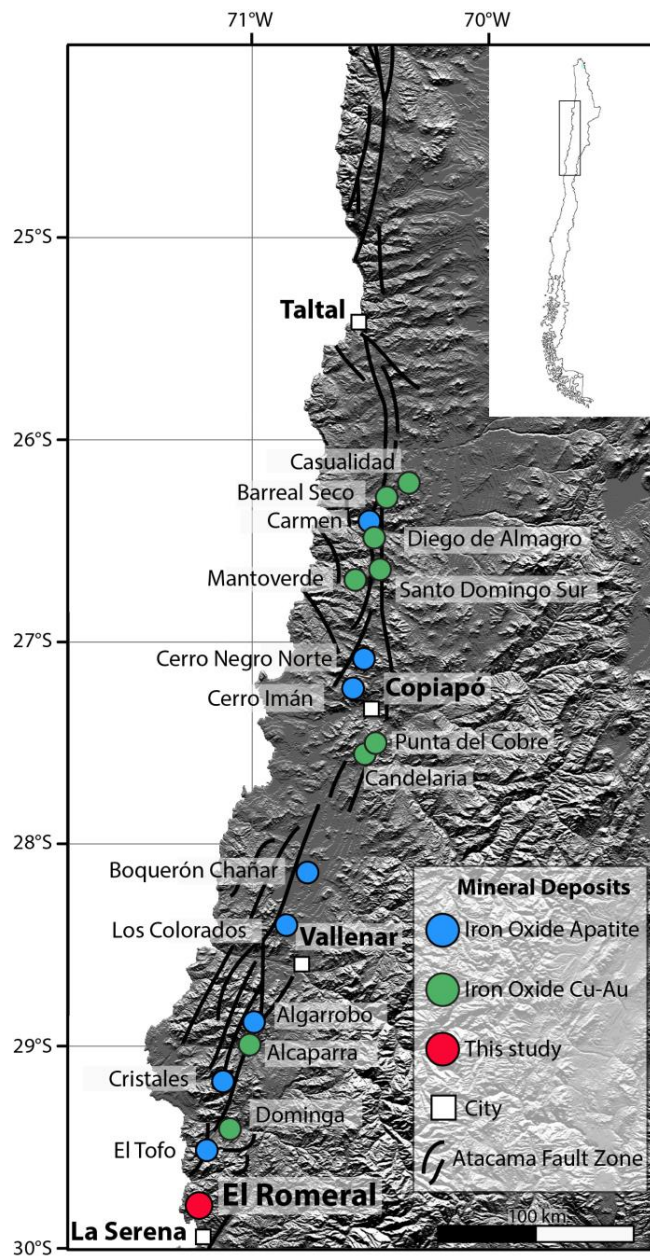
Figure 18. Map showing the location of major iron oxide-apatite (IOA) and iron oxide-copper-gold (IOCG) deposits from the Cretaceous Chilean Iron Belt along the Atacama Fault System. Modified from Barra et al. (2017).
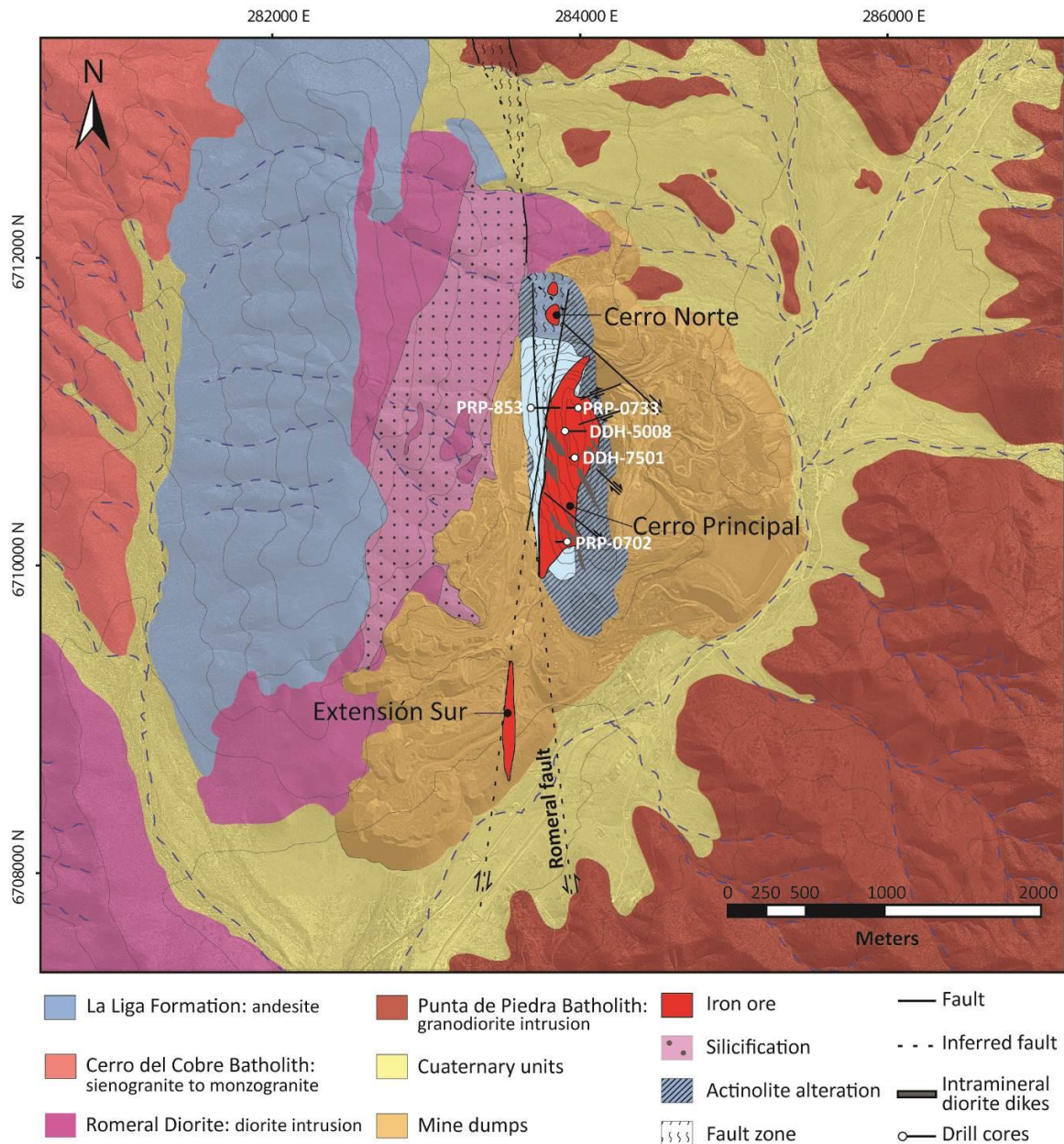
Figure 19. Geological map of the El Romeral district showing major geologic units and the main iron orebodies. Location of the five drill cores studied is also shown (Modified from CAP Minería report).
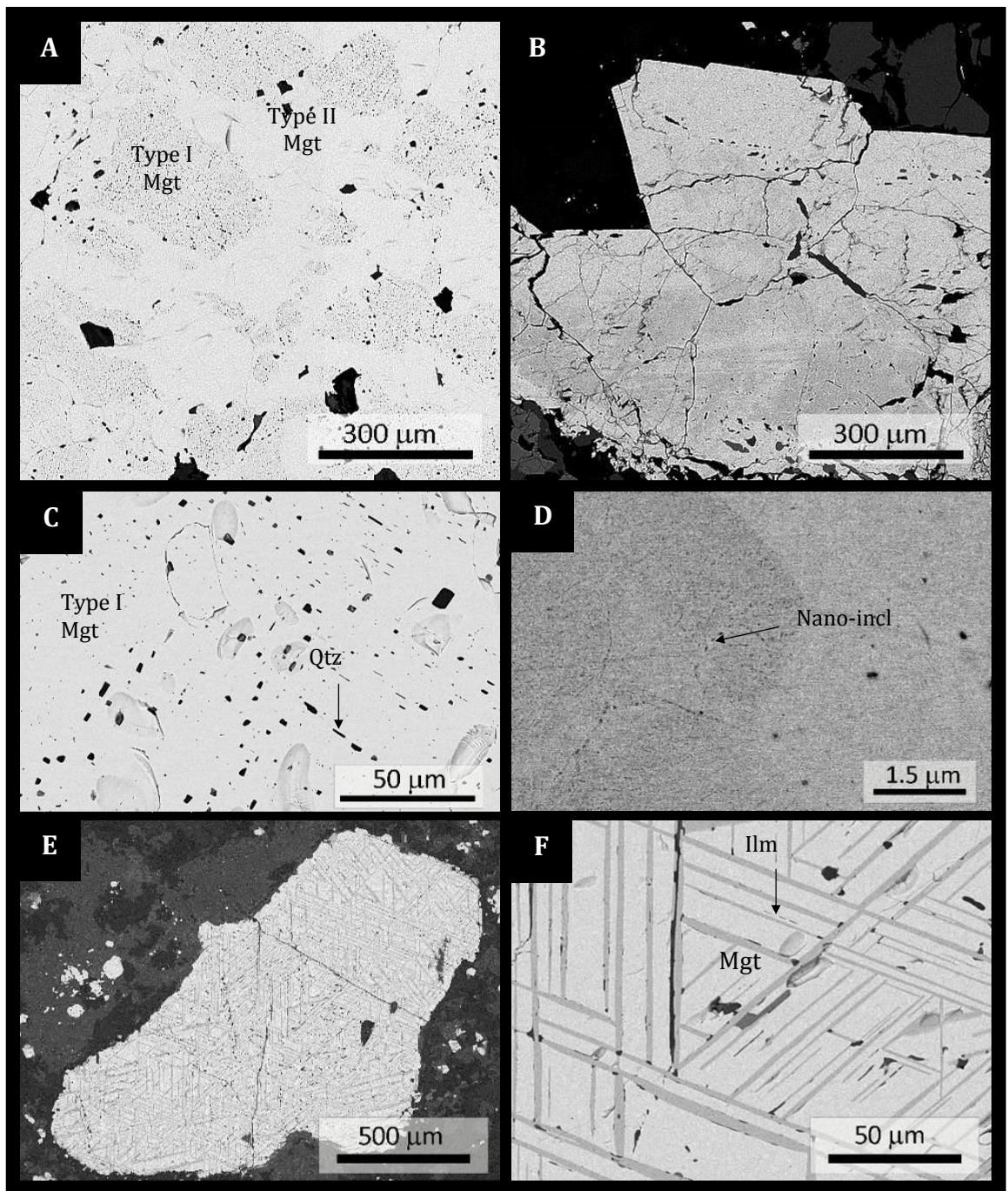
Figure 20. Back-scattered electron images of magnetite textures. A. Inclusion-rich magnetite (Type I) surrounded by inclusion-free magnetite (Type II). Sample collected from the massive orebody at 347 m depth. B. Type III Magnetite with distinct zonation; sample collected from the massive orebody at a 139 m depth. C. Type I Magnetite with mineral inclusions aligned along crystallographic planes in magnetite. D. Zoned magnetite with abundant nano-inclusions. E-F. Disseminated (primary) magnetite with ilmenite oriented following crystallographic planes. Mgt: magnetite, Ilm: ilmenite, Qtz: quartz, Nano-incl: nano-inclusions.
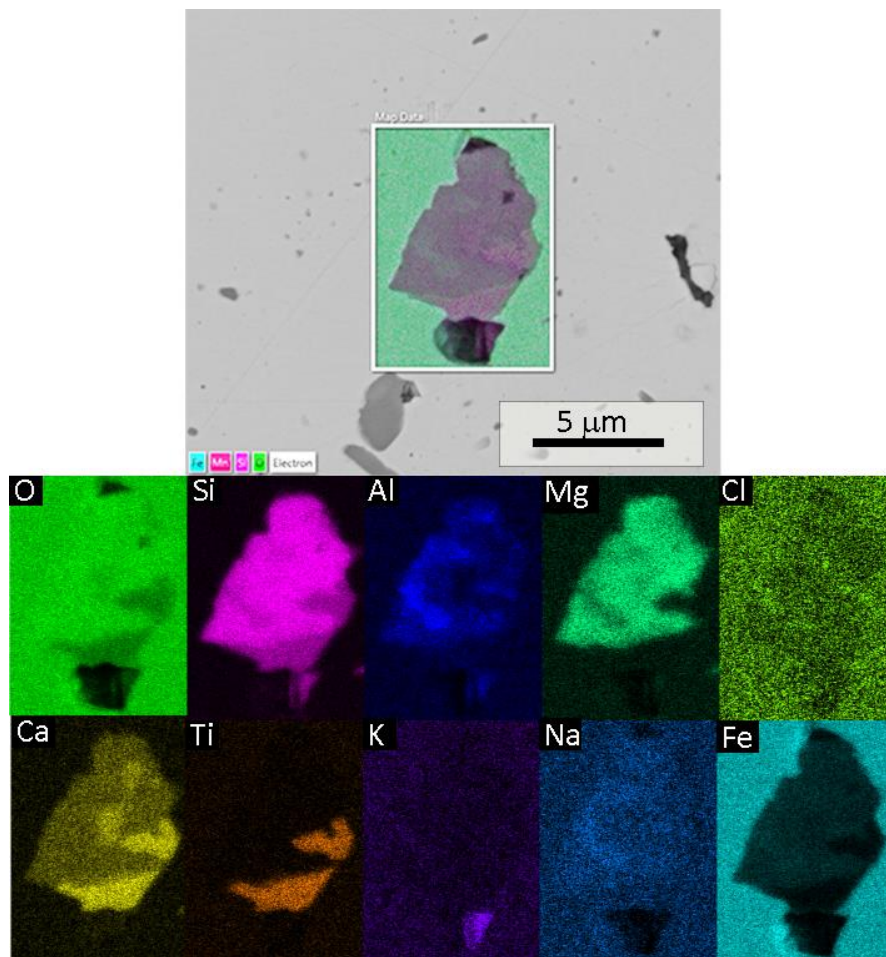
Figure 21. EDX elemental map of a representative mineral inclusion hosted in magnetite (Type I) from the massive dike orebody. The inclusion contains chlorite with minor Na content, associated with titanite.
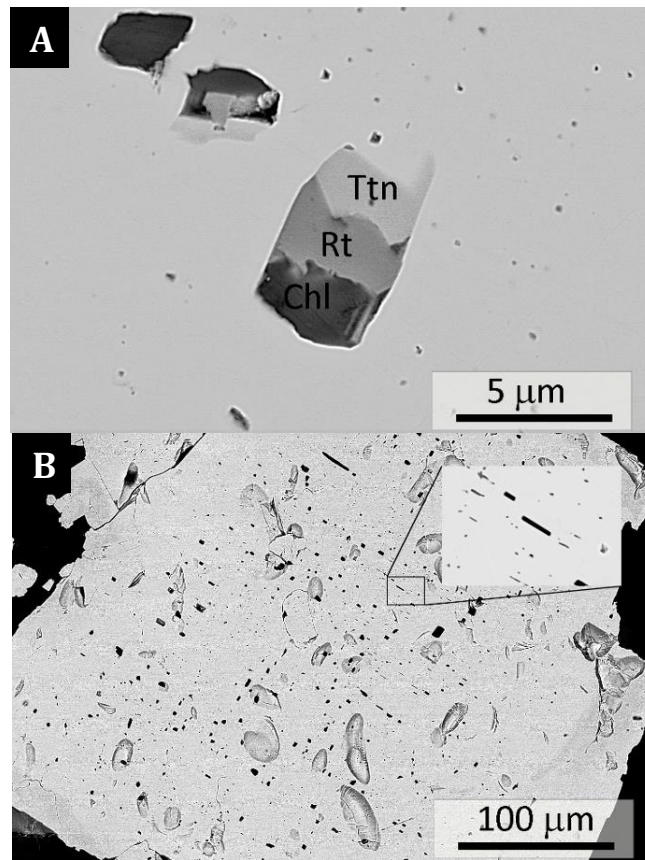
Figure 22. Back-scattered electron images of mineral inclusions in Type I magnetite: **A.** polycristalline inclusion with titanite, rutile and chlorite. **B.** Euhedral oriented quartz inclusions, following crystallographic planes. Chl: chlorite, Rt: rutile, Ttn: titanite.
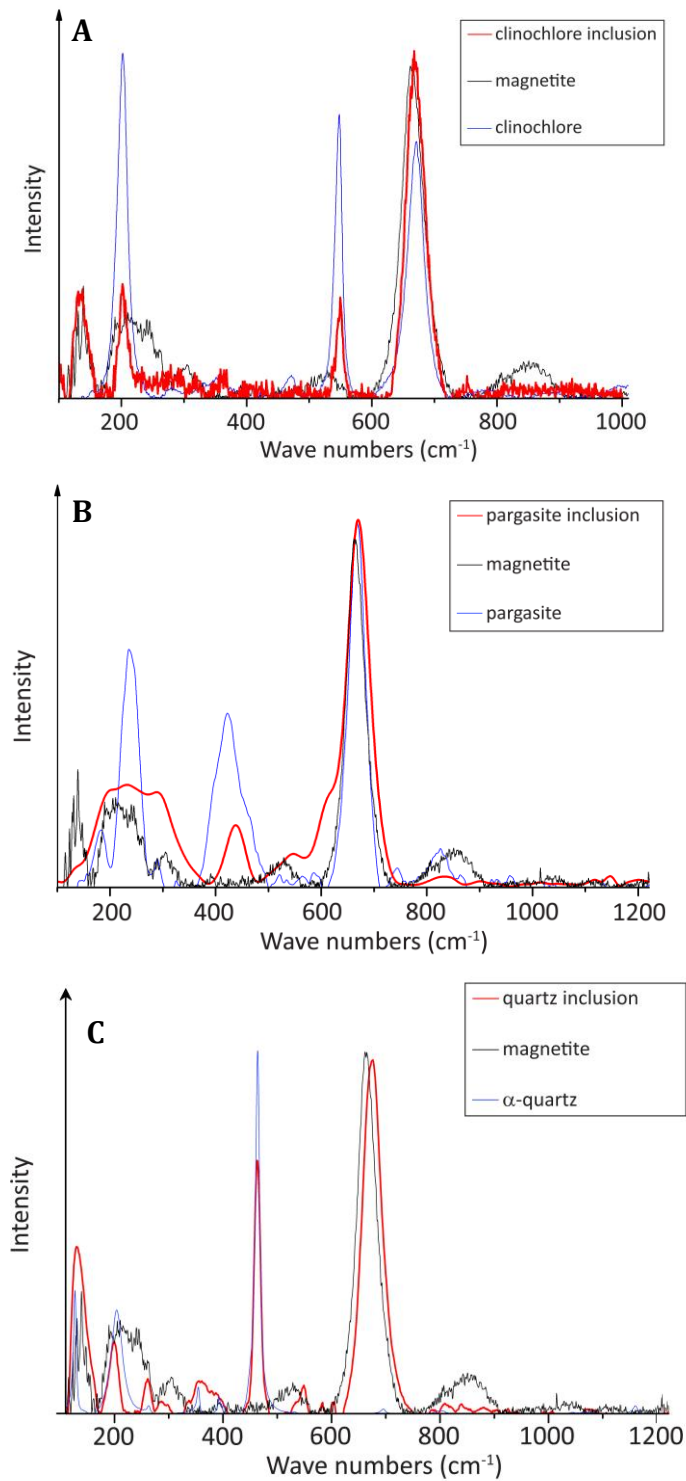
Figure 23. Representative micro-Raman spectra for **A.** clinochlore, **B.** Ti-pargasite and **C.** quartz inclusions (red) from Type I magnetite, showing characteristic peaks for magnetite (black) corresponding to background signal and respective minerals (blue), which match with inclusions spectra.
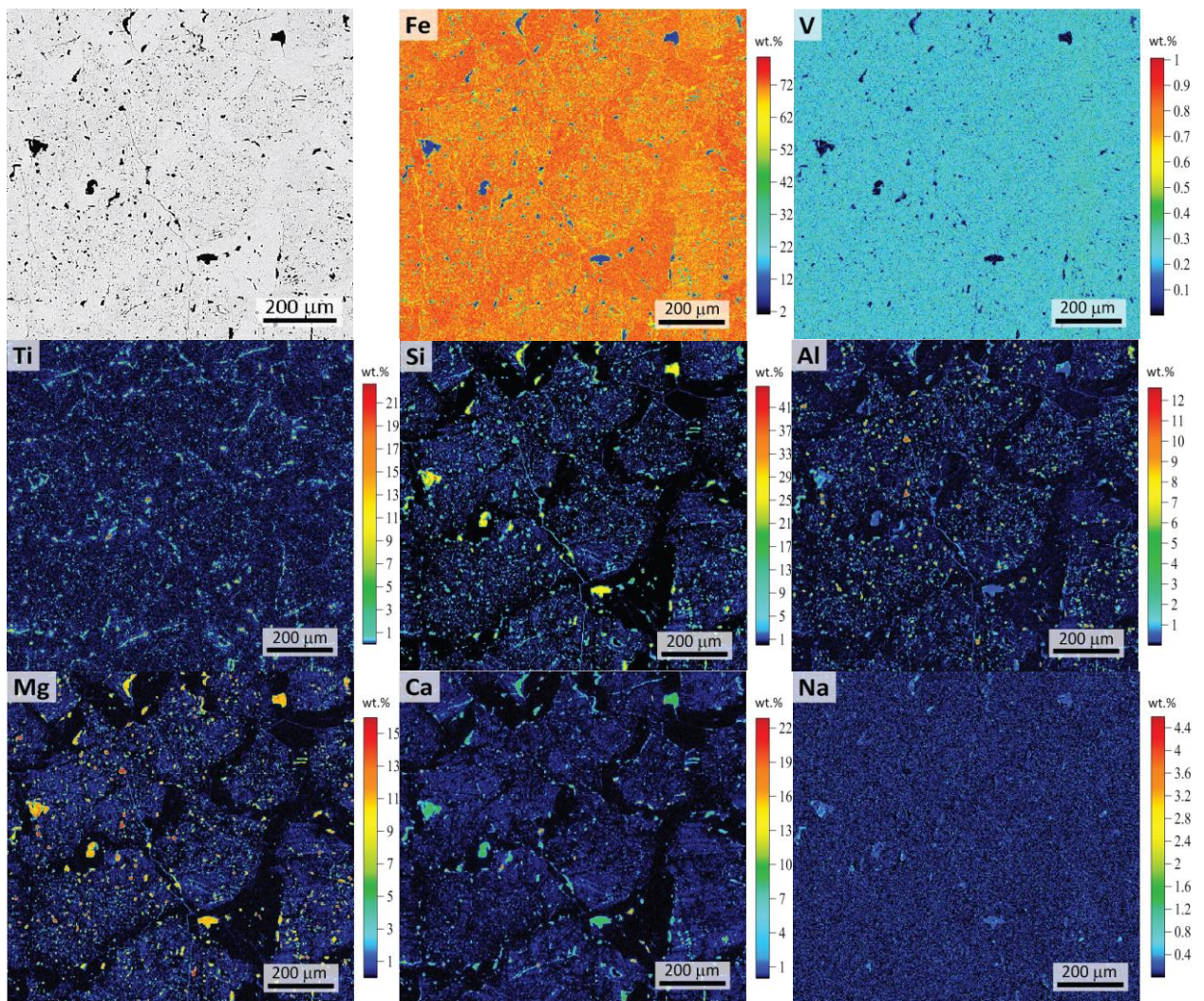
Figure 24. Elemental WDS maps for representative sample from massive magnetite orebody. Note high Si, Al, and Mg content, and minor Ti concentration in inclusion-rich magnetite (Type I), contrasting with inclusion-free rims (Type II magnetite). Vanadium content is high and generally homogeneous for both magnetite types.
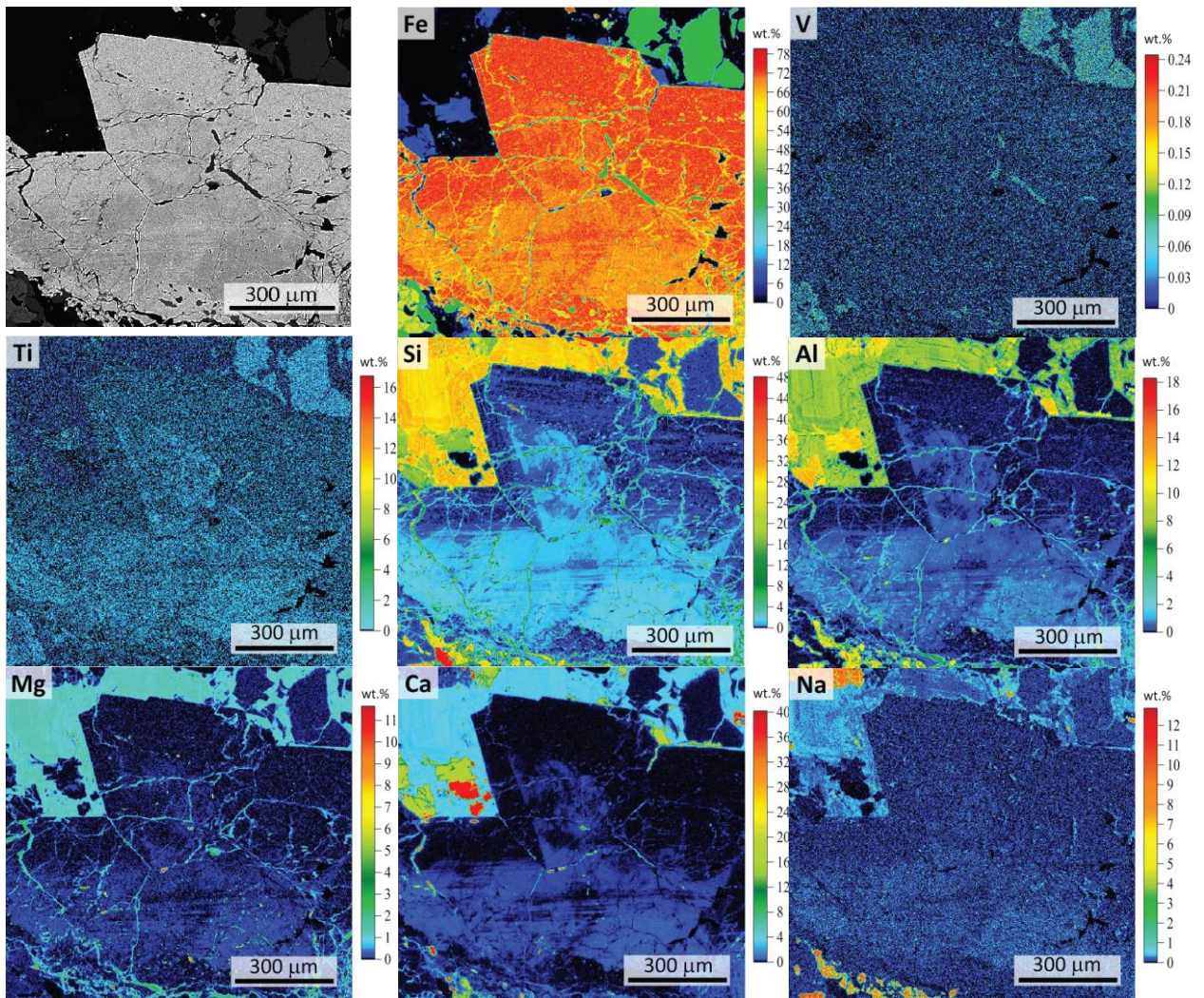
Figure 25. Elemental WDS maps for sample shown in Fig. 3B (Type III magnetite) showing a distinct Si, Al, Mg, Ti and Fe zonation. Vanadium content is high and generally homogeneous.
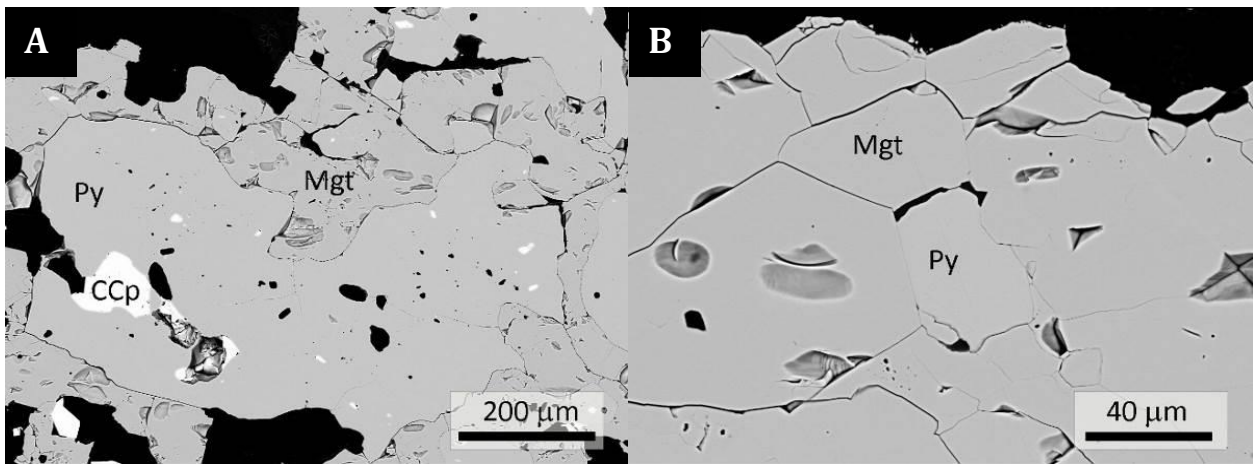
Figure 26. Back-scattered electron images of pyrite from two different events of mineralization: **A.** Post-magnetite anhedral pyrite with chalcopyrite inclusions. **B.** Syn-mineralization pyrite surrounded by Type II inclusion-free magnetite. Ccp: chalcopyrite, Mgt: magnetite, Py: pyrite.
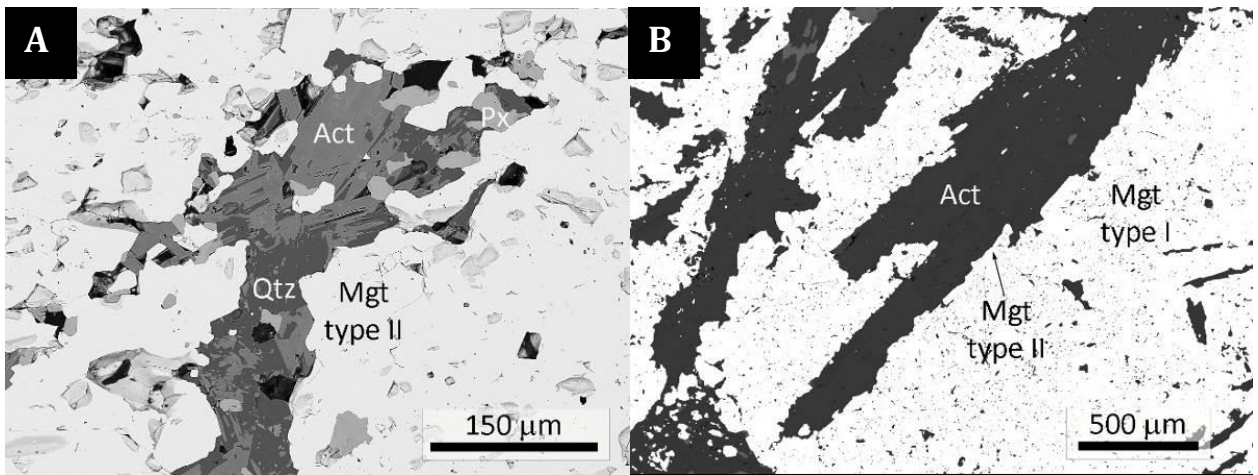
Figure 27. Back-scattered electron images of gangue minerals from two different mineralization events: **A.** First syn-ore event, with actinolite, pyroxene and quartz within pristine magnetite (Type II magnetite), and **B.** Second syn-ore event characterized by the presence of large actinolite crystals intergrown with massive iron ore. Act: actinolite, Mgt: magnetite, Px: pyroxene, Qtz: quartz.
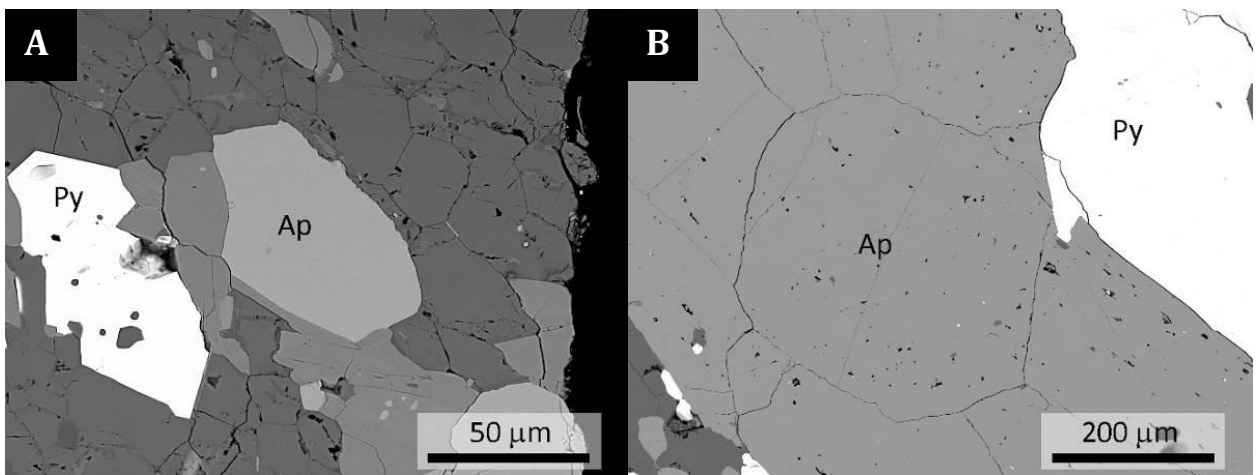
Figure 28. Back-scattered electron images of apatite grains. **A.** F-rich apatite (sample 042; depth 300 m) **B.** Cl-rich apatite with silicate and pyrite inclusions and in contact with a large pyrite grain (sample 147; depth 50 m). Ap: apatite, Py: pyrite.
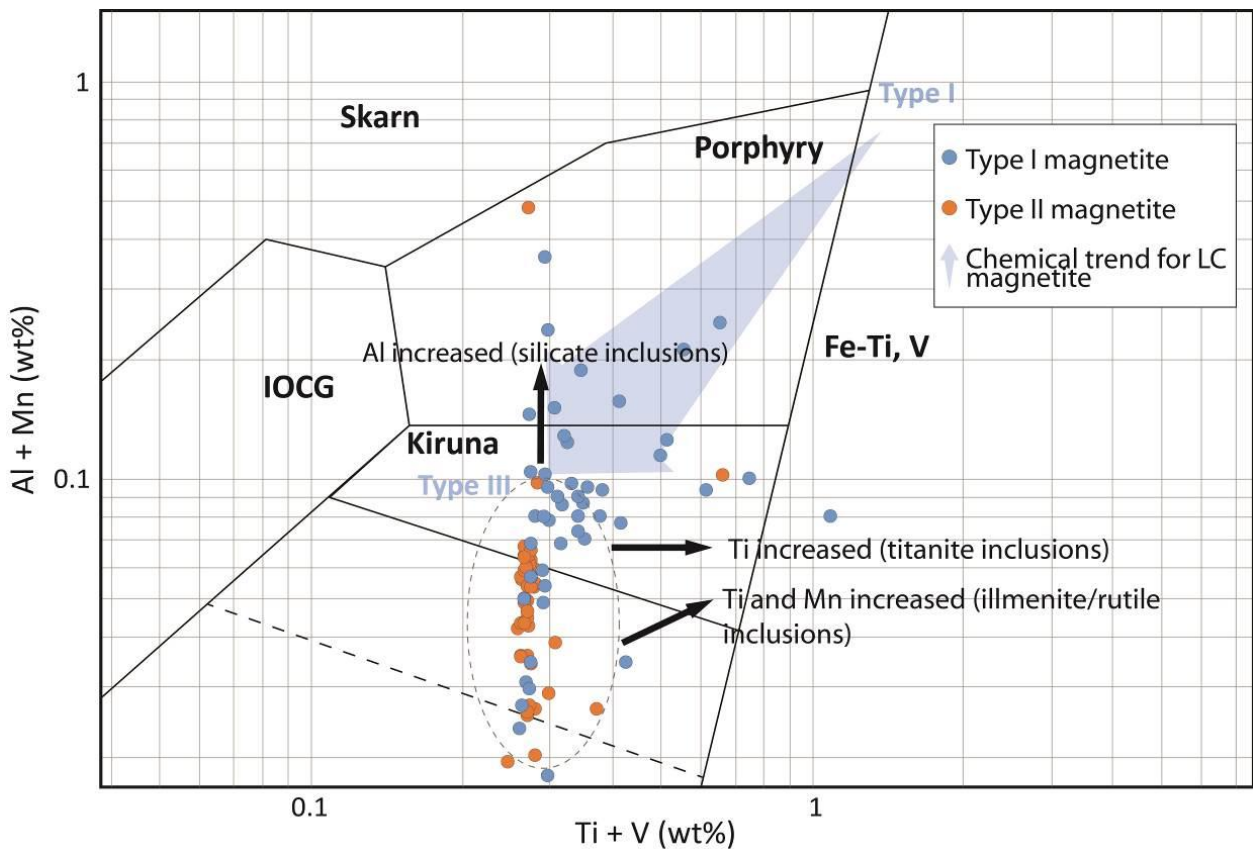
Figure 29. Al+Mn vs. Ti+V discrimination diagram proposed by Dupuis and Beaudoin (2011) and modified by Nadoll et al. (2014a). Chemical compositions of magnetite cores from the massive orebody and from disseminated grains (Type I magnetite), and pristine magnetite observed at Type I magnetite rims (Type II magnetite) are plotted. Mostly all samples plot in the Kiruna-type field, with some exception for Type I magnetite with Ti or Al-rich mineral inclusions. Compositional trend reported by Knipping et al. (2015a, b) for Los Colorados (LC) magnetite grains, which shows decreasing Ti+V (wt.%) and Al+Mn (wt.%) contents from cores (Type I magnetite) to rims (Type III magnetite, which is similar to Type II magnetite from the El Romeral).

112
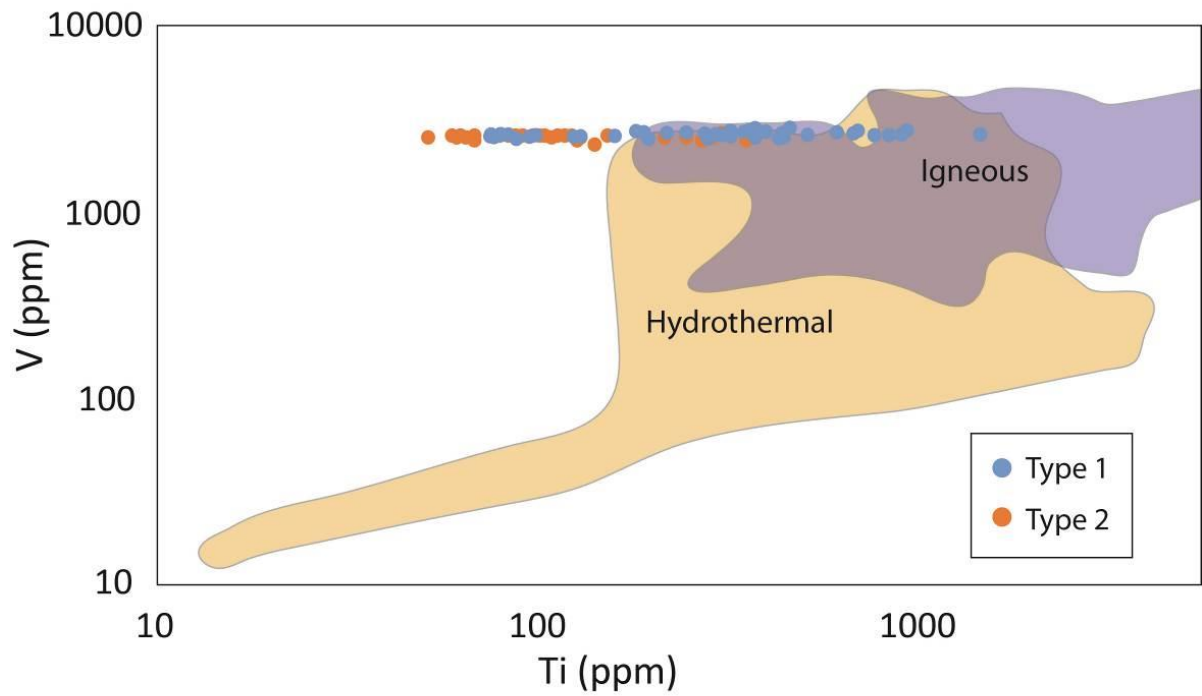
Figure 30. Ti vs V concentration plot after Nadoll et al. (2014b) with igneous and hydrothermal fields proposed by Knipping et al. (2015b). Vanadium is relatively constant in El Romeral magnetite, but high Ti concentrations are found in inclusion-rich (Type I) magnetite cores and lower Ti values for inclusion-free (Type II) magnetite rims.
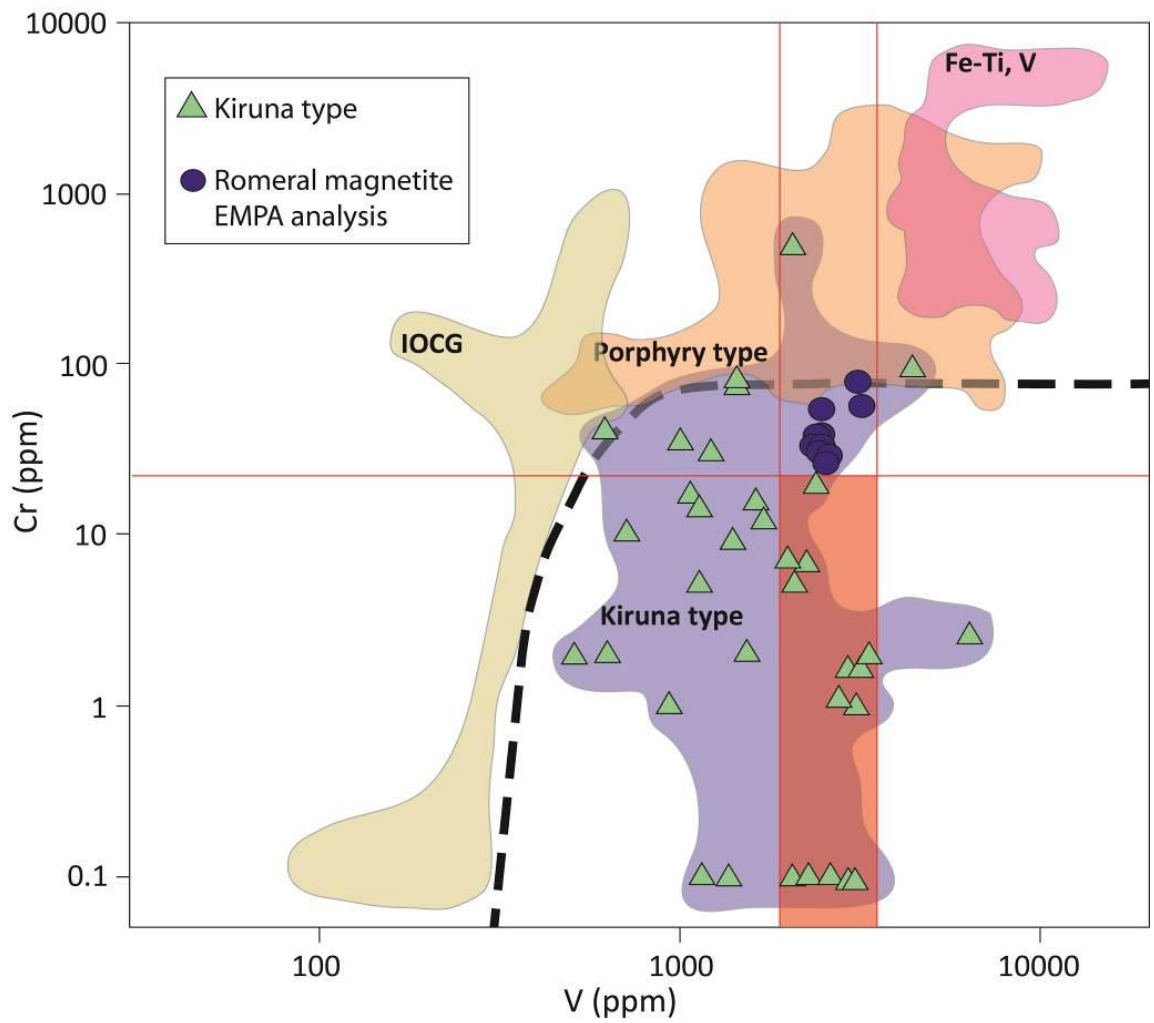
Figure 31. Discriminant diagram with concentrations of Cr vs V (Knipping et al., 2015b). El Romeral magnetite analyses plot in the Kiruna-type field (Cr<1000 ppm and V>500 ppm). Horizontal red line indicates the analytical detection limit for Cr, vertical red lines indicate the V range for all magnetite samples and orange box shows compositional field of El Romeral magnetite for analyses below detection limit.
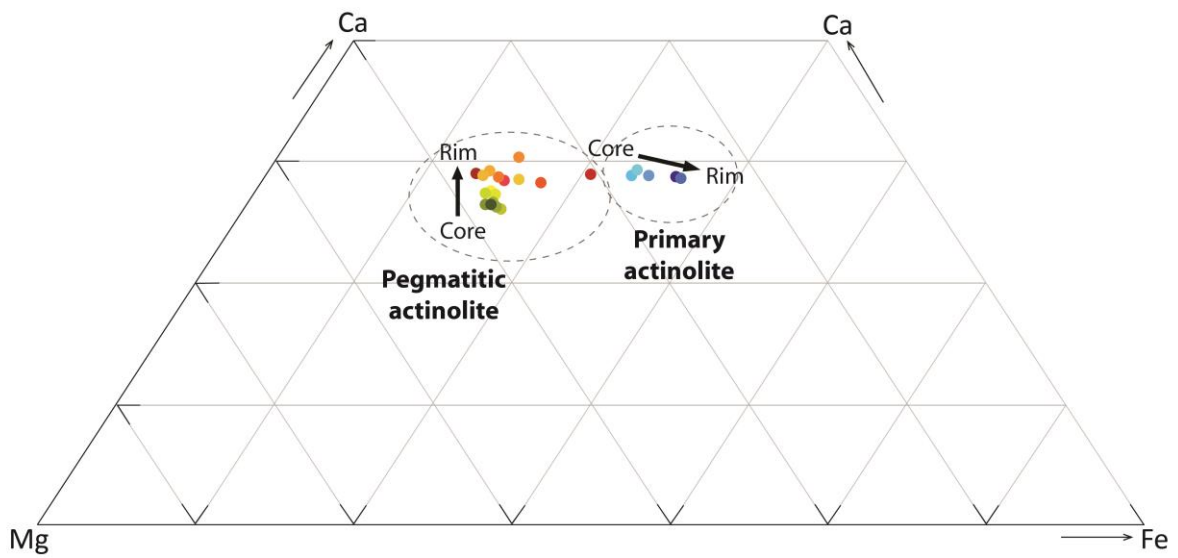
Figure 32. Compositional trends obtained by electron microprobe analysis of primary actinolite crystals within magnetite (type II) and later pegmatitic actinolite intergrown with massive iron ore. Two different trends are defined: (i) a first trend with Ca- and Fe-rich cores and Fe-rich and Ca-poor rims, similar to the trend reported by Lledo and Jenkins (2008), and (ii) a second trend with Ca-poor cores and Ca-rich rims for Mg-rich pegmatitic actinolite crystals.
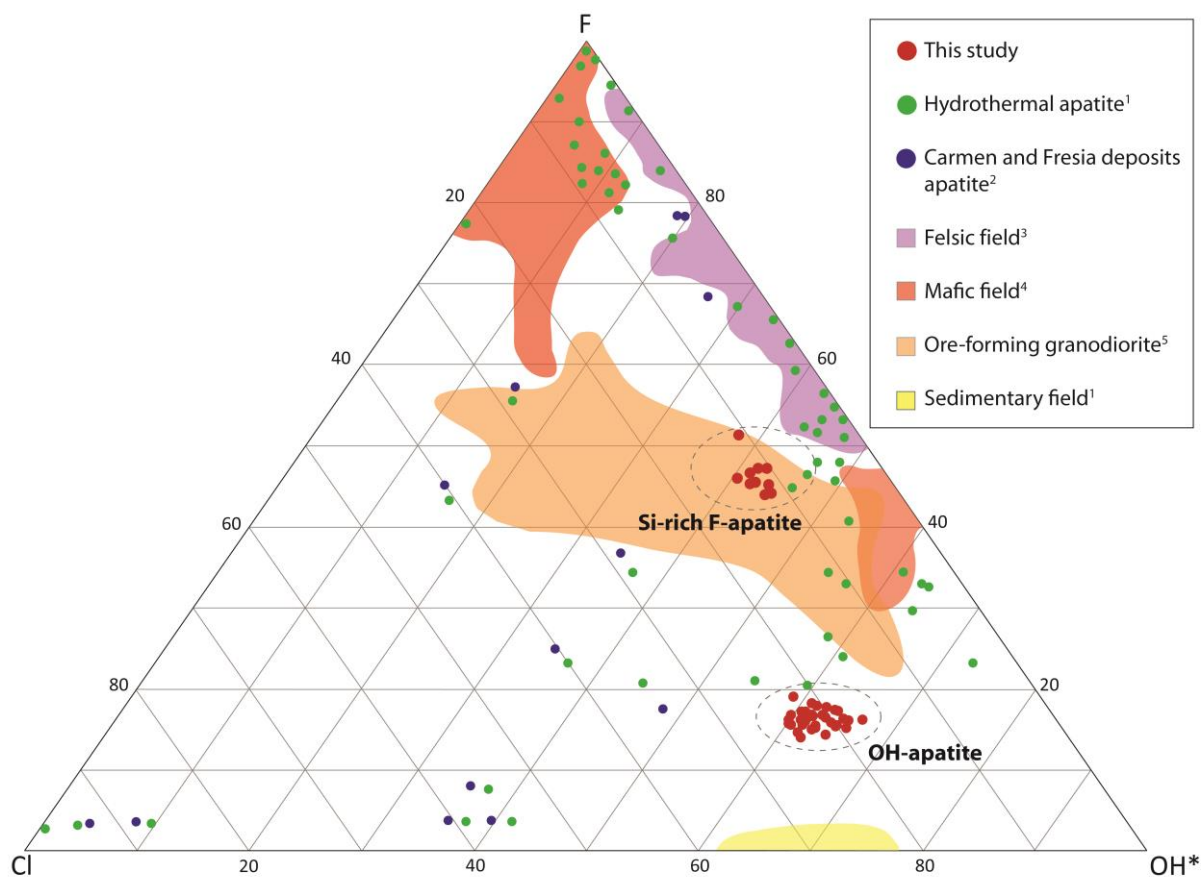
Figure 33. Ternary compositional diagram of Z-site species in apatite, which shows the different apatite types recognized in El Romeral, i.e., a deep F-rich apatite and a shallow OH-apatite. Apatite compositions for igneous, hydrothermal and sedimentary deposits are also plotted, as well as halogens analysis on apatite from two Chilean IOA deposits (Carmen and Fresia). See text for discussion. Source of data: [1]Webster and Piccoli (2015); [2]Treloar and Colley (1996); [3]Barth and Dorais (2000), Belousova et al. (2001), Krneta et al. (2016); [4]Marks et al. (2012), Douce et al. (2011); [5]Bao et al. (2016).
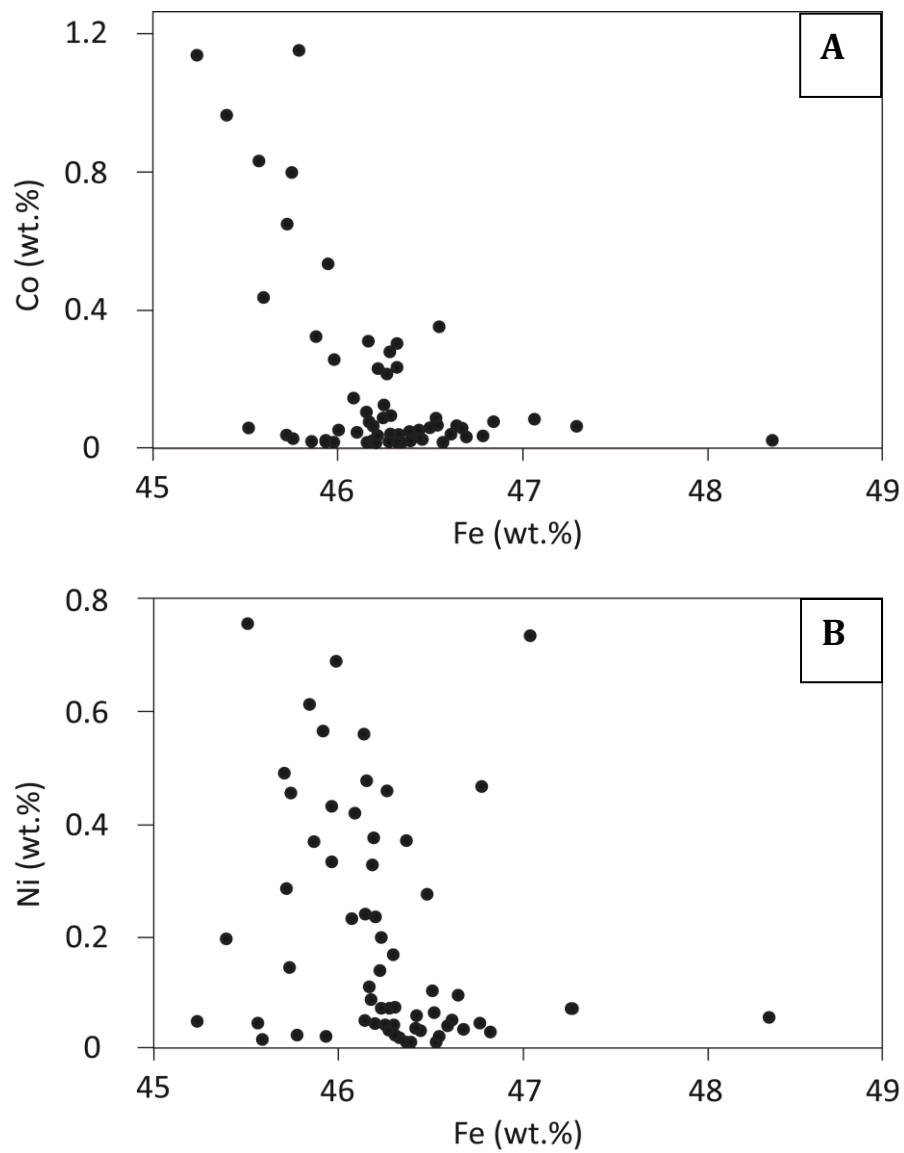
Figure 34. The concentration of Co and Ni vs Fe in total weight percent (wt.%). **A.** Cobalt and Fe show a well defined negative correlation. **B.** Nickel and Fe contents have a random distribution, probably associated with a more complex incorporation of Ni in pyrite.
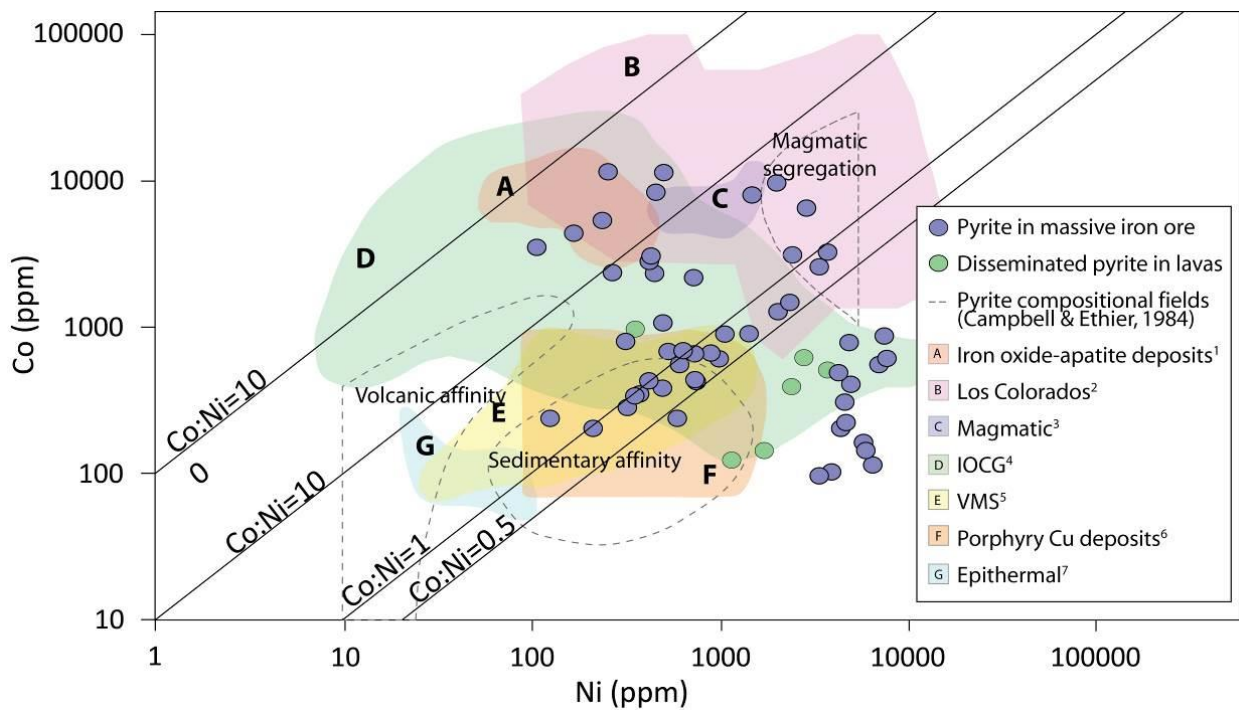
Figure 35. Co vs Ni correlation diagram showing chemical analysis of pyrite from the El Romeral deposit. Most samples have Co:Ni>0.5, with the highest Co content found in a pyrite crystal associated with the Type II magnetite. Lower Co values (Co:Ni<0.5) are generally associated with disseminated pyrite in host rocks or to a final event of sulfide mineralization at shallow levels. Plot modified from Reich (2016). Source of data: [1]Lorca (1990), [2]Reich (2016), [3]Piña et al. (2013), [4]Rusk et al. (2010), [5]Soltani et al. (2014), [6]Reich et al. (2013), [7]Scher et al. (2013).
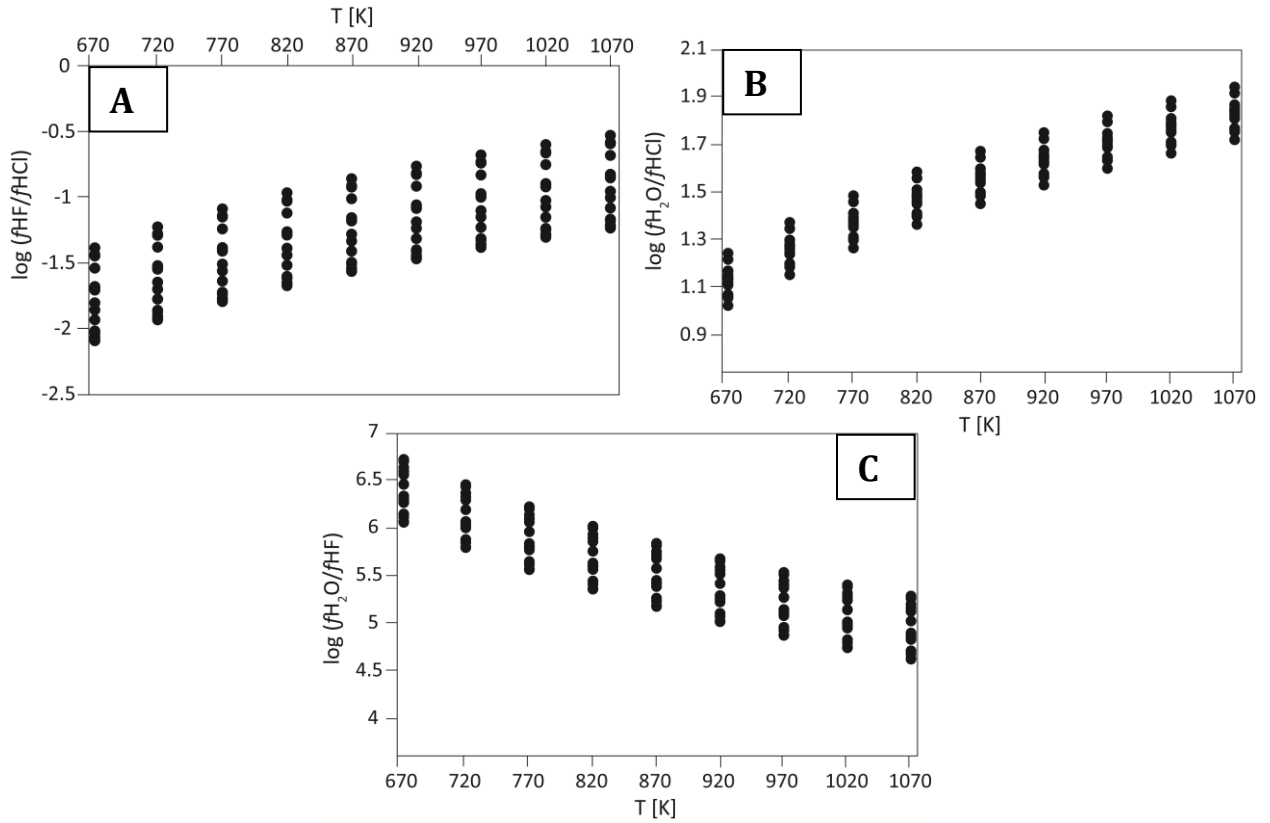
Figure 36. Log of fugacity ratios vs T [K] plots from a hydrothermal fluid in equilibrium with biotite from the late event (10 Ma younger than the main mineralization event), associated with degassing of a post-ore intrusive body. **A.** log (*f*HF/*f*HCl) vs T data shows a positive trend and negative fugacity ratios, which reflects the low *f*HF compared to *f*HCl **B.** log (*f*H₂O/*f*HCl) vs T graphic presents an inverse pattern, as. **C.** log (*f*H₂O/*f*HF) vs T diagram which shows lower fugacity values with increasing temperature.
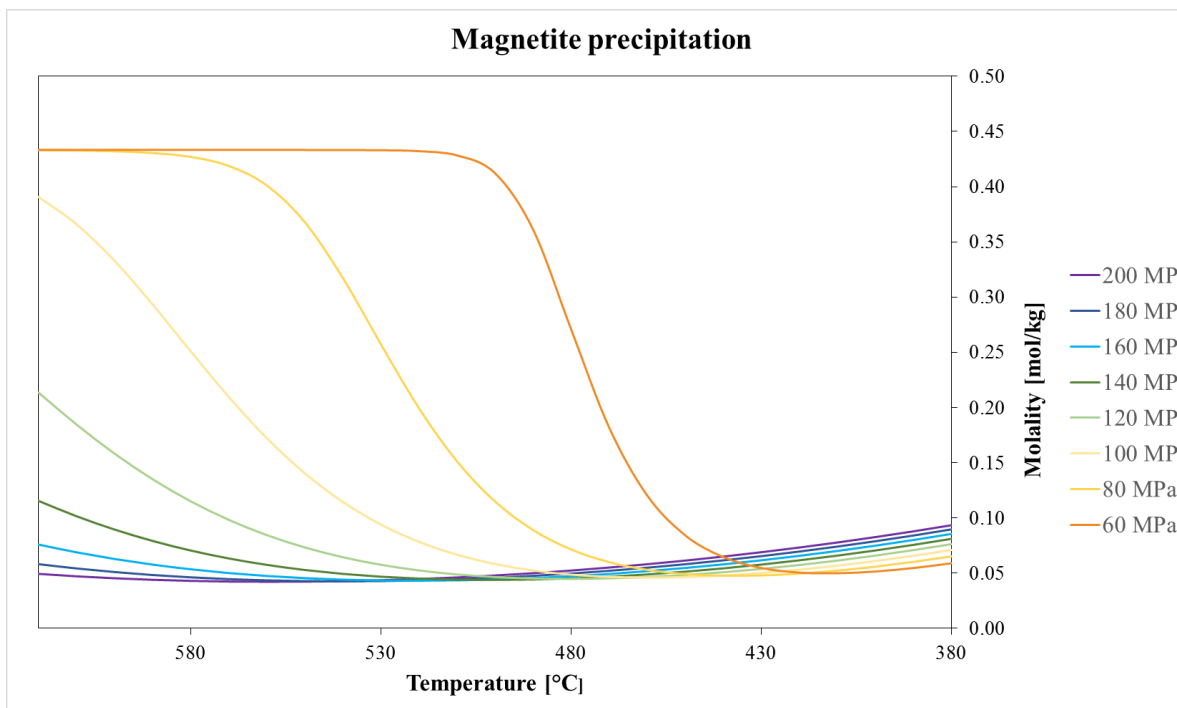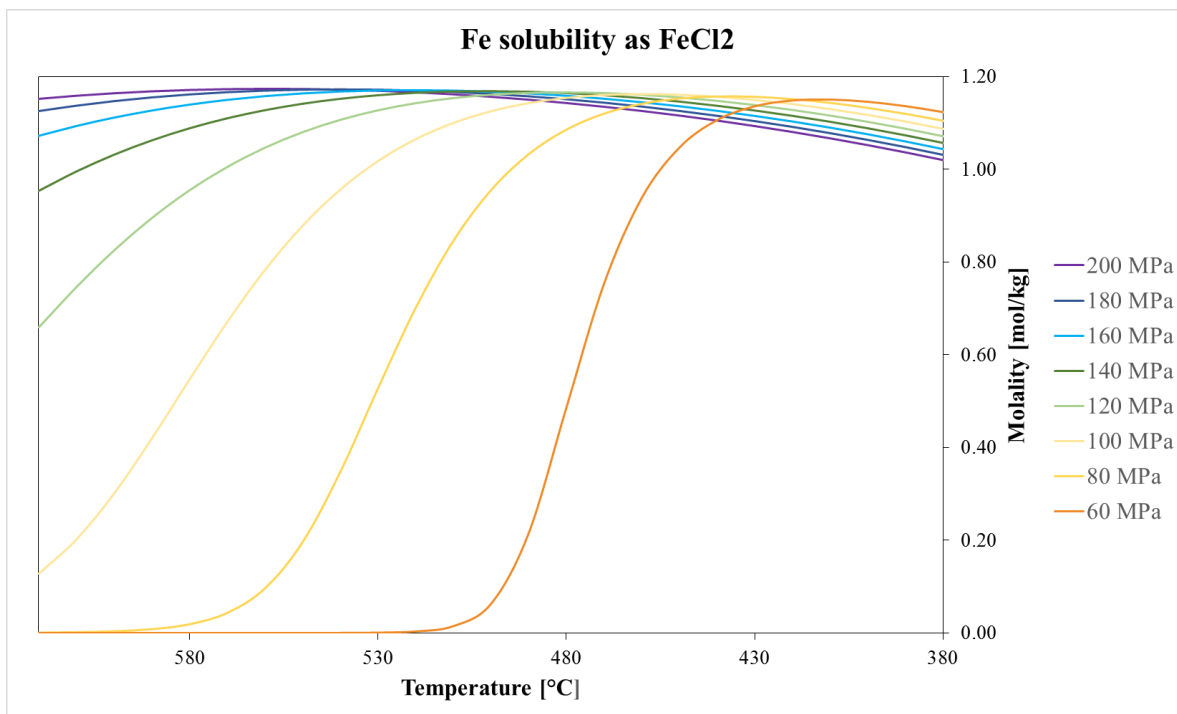
Figure 37. Molality of $FeCl_2$ vs T[°C] plots obtained by geochemical modeling. **A.** Iron solubility as $FeCl_2$. The model results indicate that at high pressure (180-200 MPa) $FeCl_2$ is more soluble at temperatures >500°C, but as pressure drops, $FeCl_2$ becomes unstable, resulting in the precipitation of magnetite. **B.** Model results indicate that magnetite precipitation is enhanced (higher efficiency) by rapid decompression. Efficiency: $100*(moles_{Mgt\ (final\ pressure)} - moles_{Mgt\ (initial\ pressure)}) / moles_{Mgt\ (final\ pressure)}$.

Temperature <600°C

D

Romeral fault system

Temperature <840°C

C

Andesite hosting rock

Pressure, depth and temperature

B

↑ Buoyancy force

FeCl$_2$

Hypersaline fluid

A

Temperature ~ [1020°-800°C]

Mineral inclusions

Inclusion-rich magnetite crystals

Melt

Silicate crystals

Actinolite alteration

Hypersaline magmatic fluid

Hydrothermal magnetite

Pyroxene-anfíbol-quartz "pockets"

Primary sulfides

Actinolite crystals

Magnetite veinlets

Figure 38. Schematic magmatic-hydrothermal model modified from Knipping et al. (2015a, b). **A.** Inclusion-rich magnetite crystallization from an intermediate composition silicate melt, where mineral inclusions are trapped in magnetite structure. **B.** Bubble nucleation on magnetite surface allows crystals to ascend by positive buoyancy force. The hypersaline magmatic fluid transports iron as a chloride complex and scavenges other metals such as Cu and Au as well as S. **C.** Sudden pressure drop due to extensional faults reduces the solubility of Fe causing the precipitation of hydrothermal magnetite over primary magnetite cores (Type I). From this hydrothermal fluid other minerals form, such as pyroxene, actinolite, quartz and sulfides, which can be trapped within magnetite crystals. Additionally, large actinolite crystals (actinollite II) can form simultaneously with Type II magnetite, mainly at the margins of the magnetite dike. **D.** Final hydrothermal stage (<600°C) represents by magnetite veinlets crosscutting the main orebody.

Table 7. Different magnetite types described at the El Romeral deposit.

Magnetite type	Main features
Type I	Inclusion-rich magnetite with high-temperature inclusions (up to 1020°C). Massive orebodies (~35 modal%) and as disseminated grains.
Type II	Inclusion-free magnetite. Usually as an overgrowth around type I magnetite. Lower temperature event (up to 840°C). Massive orebodies (~60 modal %) and as disseminated grains.
Type III	Inclusion-free, chemically-zoned magnetite. At local shallow zones from the massive ore bodies (~5 modal%).
Type IV	Magnetite veinlets that crosscut the massive magnetite ore bodies (later event).

Table 8. Representative EMPA analyses for different magnetite grains (Type I and II) from drill cores PRP-0702 and PRP-0733.

Element	Type I Magnetite								Type II Magnetite							
	Massive				Disseminated				Massive				Disseminated			
Si	0.19	0.36	0.07	0.19	0.01	0.01	0.06	0.04	0.01	0.01	0.01	0.02	0.04	0.04	0.20	0.03
Al	0.03	0.21	0.01	0.09	0.01	0.01	B.D.L.	B.D.L.	0.03	0.04	0.04	0.02	0.02	0.01	0.09	0.01
Na	B.D.L.	0.03	0.20	0.19	0.03	0.14	0.15	0.19	0.02	B.D.L.	B.D.L.	B.D.L.	0.05	0.06	B.D.L.	B.D.L.
Mg	0.04	0.22	B.D.L.	0.08	B.D.L.	0.01	B.D.L.	B.D.L.	0.01	B.D.L.	B.D.L.	B.D.L.	B.D.L.	B.D.L.	0.07	B.D.L.
Ti	0.03	0.04	0.35	0.14	0.03	0.15	0.10	0.04	0.01	0.01	0.01	0.01	0.03	0.01	0.04	0.03
Ca	0.12	0.08	0.08	0.08	0.01	0.01	0.03	0.03	0.01	0.01	B.D.L.	0.11	0.02	0.02	0.04	0.01
K	0.09	0.05	0.02	0.03	0.05	0.03	0.03	0.02	B.D.L.	B.D.L.	B.D.L.	B.D.L.	0.04	0.04	0.08	0.05
Fe	71.54	71.52	70.17	70.87	72.08	71.53	71.36	71.26	72.30	72.66	72.67	72.11	71.30	71.14	71.65	72.12
Cr	B.D.L.	B.D.L.	B.D.L.	B.D.L.	B.D.L.	B.D.L.	B.D.L.	B.D.L.	B.D.L.	B.D.L.	B.D.L.	B.D.L.	B.D.L.	B.D.L.	B.D.L.	B.D.L.
V	0.26	0.25	0.26	0.27	0.27	0.28	0.28	0.28	0.26	0.26	0.25	0.24	0.25	0.23	0.24	0.25
Mn	0.02	0.02	0.08	0.07	0.01	0.03	0.07	0.06	0.02	0.02	0.02	0.02	0.01	0.01	0.01	0.01
O	27.81	28.26	27.38	27.76	27.72	27.65	27.61	27.53	27.80	27.94	27.94	27.75	28.02	27.54	27.74	27.48
Total	100.13	101.04	98.64	99.75	100.20	99.85	99.67	99.45	100.44	100.93	100.95	100.29	99.78	99.10	100.16	99.98

Note: Detection limits for all elements is 0.01 wt.%, except for Na which is 0.02 wt.%. All concentrations reported in wt.%.

B.D.L: Below detection limit.

Table 9. EMPA measurements of Co, Ni and Cu from pyrite crystals from drill cores PRP-0853 and DDH-5008.

Elements	149-01	149-01	149-01	149-01	149-02	149-02	149-02	149-02	149-02	149-02	149-02	149-02	149-02	149-02	149-02	149-02
Cu	0.87	0.09	0.05	0.03	B.D.L	B.D.L	B.D.L	1.56	0.01	B.D.L	B.D.L	B.D.L	B.D.L	B.D.L	B.D.L	B.D.L
Ni	0.02	0.02	B.D.L	0.05	0.01	B.D.L	B.D.L	0.06	B.D.L	0.03	0.04	0.03	0.02	B.D.L	B.D.L	0.05
Co	0.44	0.54	0.83	1.14	0.35	0.02	0.53	0.02	0.62	0.08	0.04	0.03	0.02	0.02	0.01	0.04

Elements	149-02	149-02	149-02	149-02	149-02	149-02	149-02	149-04	149-04	149-04	149-04	149-06	149-06	149-06	149-06	149-06
Cu	B.D.L	B.D.L	0.01	0.04	0.04	0.06	0.07	0.02	B.D.L	B.D.L	0.08	B.D.L	B.D.L	B.D.L	B.D.L	B.D.L
Ni	B.D.L	0.07	B.D.L	B.D.L	0.04	0.04	0.04	B.D.L	B.D.L	0.20	0.56	0.02	0.11	0.17	0.06	0.74
Co	0.02	0.04	0.04	0.32	0.23	0.28	0.31	0.78	0.09	0.13	0.02	0.01	0.01	B.D.L	B.D.L	0.09

Elements	149-06	149-06	149-06	149-06	149-07	149-07	149-07	149-09	149-09	149-09	149-09	149-09	149-09	149-09	149-09	149-09
Cu	B.D.L	B.D.L	B.D.L	B.D.L	B.D.L	0.03	0.39	B.D.L	B.D.L	B.D.L	B.D.L	0.01	B.D.L	0.01	0.02	B.D.L
Ni	0.48	0.69	0.17	0.76	0.05	0.03	0.14	B.D.L	0.05	0.28	0.33	0.20	0.15	0.24	0.23	0.01
Co	0.08	0.06	0.01	0.06	0.07	0.24	0.09	1.65	0.11	0.65	0.26	0.97	0.80	0.31	0.15	0.02

Elements	149-09	149-09	149-09	149-09	149-09	149-09	149-09	149-10	149-10	149-10	149-10	149-10	149-10	149-10	149-10	149-10
Cu	B.D.L	0.01	B.D.L	B.D.L	B.D.L	B.D.L	B.D.L	0.03	0.03	0.02	0.01	0.01	0.03	0.03	0.03	0.08
Ni	0.07	B.D.L	B.D.L	B.D.L	B.D.L	B.D.L	B.D.L	B.D.L	B.D.L	0.04	0.04	0.10	0.06	0.07	0.09	0.07
Co	0.22	1.70	2.24	1.79	1.98	1.94	1.91	0.03	0.03	0.03	0.04	0.06	0.06	0.04	0.07	0.07

Elements	149-10	149-10	157-01	157-01	157-02	157-03	157-03	157-04	157-04	157-04	157-04	157-04	157-04	157-04	157-04	157-04
Cu	0.14	0.10	0.01	B.D.L	0.01	B.D.L	B.D.L	B.D.L	0.01	B.D.L	B.D.L	B.D.L	0.02	B.D.L	B.D.L	B.D.L
Ni	0.11	0.06	0.03	B.D.L	0.33	0.51	0.04	0.06	0.38	0.57	0.49	0.37	0.67	0.42	0.50	0.51
Co	0.09	0.07	1.15	0.73	0.01	B.D.L	B.D.L	B.D.L	0.01	0.01	0.04	B.D.L	B.D.L	B.D.L	B.D.L	B.D.L

Elements	157-04	157-04	157-04	157-04	157-04	157-04	157-04	157-04	157-04	157-04	157-04	157-07	133-01	133-02	133-05	133-05
Cu	B.D.L	B.D.L	B.D.L	B.D.L	B.D.L	B.D.L	B.D.L	B.D.L	B.D.L	B.D.L	B.D.L	B.D.L	B.D.L	0.15	B.D.L	B.D.L
Ni	0.52	0.49	0.47	0.45	0.55	0.48	0.37	0.45	0.43	0.42	0.46	0.61	0.04	0.24	0.28	0.37
Co	B.D.L	B.D.L	B.D.L	B.D.L	B.D.L	B.D.L	0.33	0.03	0.02	0.05	0.02	0.01	0.10	0.04	0.06	0.05

Note: Detection limit for Cu, Co, and Ni is 0.01 wt.%. All concentrations reported in wt.%

B.D.L: Below detection limit.

Table 10. Representative EMPA analyses for actinolite crystals (Types I, II and III) from drill cores PRP-0702, PRP-0733 and DDH-5008.

Element	Actinolite I					Actinolite II					Actinolite III				
F	B.D.L	0.12	B.D.L	0.02	B.D.L	0.14	0.17	0.11	0.11	0.29	0.12	0.14	B.D.L	0.11	0.04
Cl	B.D.L	B.D.L	B.D.L	B.D.L	B.D.L	B.D.L	B.D.L	0.03	0.02	0.02	0.03	0.02	0.03	0.03	0.04
Ca	9.05	9.05	9.30	9.22	9.16	9.47	9.27	8.61	8.52	8.63	8.34	8.35	8.26	8.33	8.53
Si	23.72	23.78	24.50	24.83	24.78	26.10	25.77	25.94	26.10	26.17	24.44	24.11	23.86	24.79	24.61
Mg	8.60	8.62	9.10	9.30	9.07	11.40	10.74	11.39	11.31	11.38	10.36	10.49	10.40	10.96	10.71
Al	1.49	1.35	0.71	0.70	0.76	0.65	0.34	0.37	0.36	0.35	2.12	2.16	2.43	1.95	2.48
Mn	0.10	0.10	0.08	0.09	0.09	B.D.L	0.05	0.05	B.D.L	B.D.L	0.28	0.36	0.37	0.34	0.39
Na	0.19	0.17	0.07	0.07	0.09	0.12	0.04	0.29	0.31	0.28	0.49	0.48	0.54	0.43	0.54
Ti	B.D.L	B.D.L	B.D.L	B.D.L	B.D.L	B.D.L	B.D.L	B.D.L	B.D.L	B.D.L	0.16	0.14	0.13	0.14	0.15
K	0.09	0.07	B.D.L	0.02	B.D.L	B.D.L	0.01	0.05	0.03	0.02	0.03	0.05	0.10	B.D.L	0.10
Cr	B.D.L	B.D.L	B.D.L	B.D.L	B.D.L	B.D.L	B.D.L	B.D.L	B.D.L	B.D.L	B.D.L	B.D.L	B.D.L	B.D.L	B.D.L
Fe	11.29	11.44	10.71	10.28	10.20	6.05	8.10	7.21	7.13	7.04	6.97	7.17	7.79	6.88	7.71
V	0.07	0.08	0.04	0.04	0.05	B.D.L	B.D.L	B.D.L	B.D.L	B.D.L	0.03	B.D.L	0.04	B.D.L	B.D.L
O	42.84	42.83	43.21	43.58	43.38	45.29	44.65	44.90	44.95	45.07	44.13	43.94	44.00	43.67	44.08
H	0.23	0.23	0.23	0.23	0.23	0.24	0.23	0.24	0.24	0.24	0.24	0.24	0.23	0.24	0.35
Total	97.68	97.82	97.95	98.37	97.81	99.46	99.37	99.20	99.08	99.49	97.74	97.67	98.16	97.87	99.72
Fe#	0.36	0.37	0.34	0.32	0.33	0.19	0.25	0.22	0.22	0.21	0.23	0.23	0.25	0.21	0.24

Note: Detection limits for all elements is 0.01 wt.%, except for F, Mn, and Fe which is 0.03 wt.%. All concentrations reported in wt.%

B.D.L: Below detection limit.

Table 11. Halogen contents (formula values) in apatite from drill cores PRP-0702 (~300 m depth for sample 042) and PRP-0853 (~50 m depth for sample 147).

Element	OH-apatite											
	147-01	147-01	147-01	147-01	147-01	147-01	147-01	147-01	147-01	147-01	147-01	147-01
F Formula	0.17	0.16	0.15	0.16	0.16	0.14	0.17	0.18	0.18	0.17	0.16	0.18
Cl Formula	0.20	0.19	0.24	0.20	0.22	0.24	0.21	0.20	0.19	0.22	0.22	0.21
OH Formula	0.63	0.65	0.61	0.64	0.62	0.62	0.63	0.63	0.63	0.61	0.61	0.61

Element	OH-apatite											
	147-01	147-01	147-01	147-01	147-01	147-01	147-01	147-01	147-01	147-01	147-01	147-01
F Formula	0.17	0.17	0.16	0.15	0.15	0.17	0.16	0.14	0.15	0.17	0.17	0.17
Cl Formula	0.21	0.23	0.23	0.22	0.22	0.22	0.22	0.22	0.22	0.19	0.22	0.21
OH Formula	0.62	0.61	0.61	0.62	0.63	0.61	0.61	0.64	0.62	0.64	0.61	0.62

Element	OH-apatite											
	147-02	147-02	147-03	147-03	147-04	147-04	147-04	147-04	147-05	147-05	147-05	147-05
F Formula	0.16	0.16	0.16	0.16	0.16	0.17	0.17	0.16	0.16	0.18	0.16	0.19
Cl Formula	0.17	0.19	0.19	0.20	0.24	0.24	0.23	0.20	0.22	0.21	0.24	0.22
OH Formula	0.66	0.65	0.65	0.64	0.61	0.60	0.60	0.64	0.62	0.61	0.60	0.59

Element	F-apatite											
	042-01	042-01	042-01	042-02	042-02	042-03	042-03	042-03	042-03	042-03		
F Formula	0.47	0.44	0.46	0.51	0.46	0.47	0.44	0.45	0.47	0.46		
Cl Formula	0.12	0.12	0.13	0.11	0.13	0.11	0.11	0.11	0.10	0.12		
OH Formula	0.41	0.44	0.42	0.38	0.40	0.42	0.44	0.44	0.42	0.42		

CAPÍTULO 6

CONCLUSIÓN

En el presente trabajo de tesis se ha estudiado la controversial formación de depósitos tipo magnetita apatito o *iron oxide-apatite* (IOA), enfocándose en el depósito El Romeral ubicado en la Franja Ferrífera Chilena, en la región de Coquimbo. Este depósito se caracteriza por la presencia de distintos cuerpos subverticales de magnetita maciza fuertemente asociados a sistemas de fallas (presencia de milonitas con clastos de magnetita), principalmente a la Falla Romeral. Estos cuerpos están hospedados en rocas andesíticas del Neocomiano (Formación La Liga), rocas que a su vez están intruídas por distintos cuerpos intrusivos, en donde cabe destacar, la presencia de la Diorita Romeral en la zona occidental del depósito y el Batolito Punta de Piedra, intrusivo granodiorítico emplazado al este de la zona de estudio.

Mediante estudios petrográficos se han logrado definir tres eventos principales de mineralización de la magnetita: (i) un evento primario caracterizado por la presencia de magnetita (magnetita I) rica en inclusiones tanto silicatadas como oxidados, (ii) un segundo evento en donde precipita magnetita prística o con ausencia de inclusiones (magnetita II), la cual se puede presentar rodeando cristales de magnetita I o como cristales individuales. Esta última está asociada a cristales de actinolita (actinolita I), cuarzo y piroxeno, los cuales están entrampados entre cúmulos de magnetita, además de una segunda actinolita (actinolita II) acicular, la cual alcanza tamaños pegmatíticos y que se presenta principalmente en los bordes de los cuerpos. Tanto el evento (i) como el evento (ii) corresponden a la formación de los cuerpos de magnetita maciza subverticales. Finalmente, el evento (iii) se caracteriza por la presencia de vetillas de magnetita y posterior mineralización de sulfuros, principalmente pirita con calcopirita subordinada, en vetillas y diseminada, asociada con clorita y/o actinolita. Se define además un evento aislado de cúmulos de biotita asociados a magnetita, el cual se presenta localmente en las rocas hospedantes.

Dataciones radiométricas de $^{40}Ar/^{39}Ar$ en cristales de actinolita II y de biotita, del evento aislado, entregaron edades de 127.7±1.5 Ma y 118.3±0.2 Ma, respectivamente. Este gap de 10 Ma se explicaría por un segundo pulso mineralizador de menor envergadura asociado a diques post-minerales los cuales cortan los cuerpos macizos de magnetita. Por otro lado, mediante dataciones radiométricas de U-Pb en circones se obtuvieron edades de 128.97±0.93 Ma para la Diorita Romeral y de 102.2 ± 2.0 Ma para el Batolito Punta de Piedra. La edad del intrusivo diorítico sugiere una posible relación entre la mineralización principal y la cristalización de este cuerpo intrusivo espacialmente asociado a la mineralización. El emplazamiento de este intrusivo se enmarca dentro del fin de la primera subetapa del Andino I, durante el periodo de máxima extensión, etapa en la cual se forman otros depósitos tipo IOA y tipo hierro-cobre-oro o *iron*

oxide-copper-gold (IOCG). En cambio, el Batolito Punta de Piedra, estaría indicando el fin del Andino I y el comienzo del Andino II, asociado a una subducción tipo chilena en donde el régimen extensional da paso a un régimen compresivo y en donde el principal evento de formación de este tipo de depósitos cesa.

Con el fin de determinar el origen de la mineralización, se realizaron análisis mediante microsonda electrónica tanto en magnetita como en actinolita, sulfuros, apatito, entre otros. Análisis químicos en magnetita de los cuerpos principales junto con micro-Raman en inclusiones minerales hospedadas en cristales de magnetita I, reflejan dos eventos principales los cuales concuerdan con los eventos definidos mediante estudios petrográficos. Se observa (i) un primer evento de mineralización de magnetita (magnetita I) caracterizada por inclusiones de alta temperatura (>800ºC) en profundidad que van gradando a inclusiones de menor temperatura en superficie (<600ºC). En zonas más someras se observan inclusiones de α-cuarzo euhedrales orientadas según los planos cristalográficos de la magnetita, textura que podría evidenciar un proceso de exsolución por enfriamiento lento. (ii) El segundo evento está conformado por magnetita prístina (magnetita II), generalmente rodeando cristales de magnetita I o como cristales individuales en el borde de los cuerpos y en zonas más superficiales. Esta última presenta fuertes zonaciones de Al, Si, Mg y, en menor medida, Ti en zonas someras. Ambos eventos presentan alto contenido de V (~2300-2700 ppm) y contenidos variables de Ti (~ 50-3000 ppm). Los mayores contenidos de V reportados en cristales de magnetita I, junto con la presencia de inclusiones minerales de alta temperatura (800-1020ºC) son consistentes con un primer evento de origen magmático. Por otro lado, los altos contenidos de V (~2300-2700 ppm), con los menores contenidos de Ti (~50-400 ppm), además de la presencia de fuertes zonaciones a niveles someros observados en la magnetita II podrían indicar una precipitación a partir de fluidos hidrotermales de proveniencia magmática, que a bajas temperaturas evidenciarían una marcada variación composicional. Las altas temperaturas reportadas para la mineralización de magnetita son concordantes con la composición química obtenida para los dos eventos de actinolita asociados a la mineralización de magnetita II, en donde los bajos números de #Fe reportados sugerirían altas temperaturas que fluctúan entre 735ºC y 840ºC.

Asimismo, esta transición de un sistema de alta temperatura a uno de baja temperatura se puede reafirmar con la química de minerales accesorios, principalmente pirita y apatito. Para la pirita se obtuvieron razones de Co:Ni menores a 0.5 para la mineralización de sulfuros tardíos. En cambio, razones mayores de Co:Ni, alcanzando incluso razones mayores a 10, se midieron en cristales asociados a eventos tempranos, particularmente para una muestra relacionada con la mineralización de magnetita II en donde se reportó la mayor concentración de Co (1.2 wt.%). Estas altas razones de Co:Ni son concordantes con los resultados de isótopos estables de S en pirita, en donde los valores de $\delta^{34}S$ caen dentro del campo magmático, sugiriendo una proveniencia magmática para el S del evento principal de mineralización de sulfuros. En el caso de la química de apatitos, la predominancia de F-apatito en profundidad (>300 m), en contraste

con la presencia de OH-apatito con mayor contenidos de Cl a niveles someros (50 m), evidenciaría el mismo patrón de temperatura creciente con la profundidad.

Finalmente, dado que estos sistemas están fuertemente asociados a grandes sistemas de fallas (e.g. Sistema de Falla El Romeral), se realizó una primera aproximación para modelar la solubilidad de Fe mediante cambios de presión, con la cual se corrobora que a temperaturas superiores a 380ºC la precipitación de magnetita está fuertemente influenciada por cambios de presión, principalmente a presiones inferiores a 100 MPa. Por lo tanto, se sugiere que cambios abruptos de presión permitirían una mayor precipitación de magnetita en sistemas hidrotermales, cuantificando el efecto que ejercerían estos sistemas de fallas transtensionales en la formación de depósitos tipo IOA de la Franja Ferrífera de la Cordillera de la Costa.

De esta manera, se concluye que la formación de estos sistemas involucra un proceso de transición entre un sistema magmático, evidenciado por la presencia de magnetitas primarias tipo I (microlitos), y un sistema hidrotermal, asociado a granos de magnetita II y minerales accesorios tales como actinolita y pirita, el cual va gradando desde un fluido de mayor temperatura a uno de menor temperatura a medida que va disminuyendo la profundidad. Por último, la ocurrencia de estos depósitos depende de dos factores principales: (i) la presencia de cuerpos intrusivos que proveerían al sistema de cristales de magnetita primaria (Tipo I), además de fluidos ricos en $FeCl_2$, y (ii) la presencia de grandes sistemas de fallas (e.g. Zona de Falla Atama), las cuales permitirían generar zonas de descompresión, que finalmente conllevarían a la pérdida de solubilidad del Fe generando una precipitación abrupta de magnetita a lo largo de estas estructuras.

BIBLIOGRAFÍA

Aguirre, L. y Egert, E. 1962. Las formaciones manganesíferas de la región de Quebrada Marquesa, Provincia de Coquimbo. *Minerales*, **76**, 25-37.

Aguirre, L. y Egert, E. 1970. Cuadrángulo Lambert (La Serena), Provincia de Coquimbo: Insituto de Investigaciones Geológicas, Carta Geológica de Chile no. **23**, p.14, 1:50.000.

Alva-Valdivia, L.M., Rivas-Sánchez, M.L., Goguitchaichvili, A., Urrutia-Fucugauchi, J., Gonzalez, A. y Vivallo, W. 2003. Integrated magnetic studies of the El Romeral iron-ore deposit, Chile: implications for ore genesis and modeling of magnetic anomalies. *Journal of Applied Geophysics*, **53**, 137-151.

Arabasz, W. 1971. *Geological and geophysical studies of Atacama fault zone in northern Chile*. Ph.D.Thesis, California Institute of Technology, Pasadena.

Betzhold, J. 1981. *Estudio geológico del Cuerpo Oeste de Baja Ley, Yacimiento El Romeral, IV región.* Memoria de Título, Universidad de Chile, Facultad de Ciencias Físicas y Matemáticas, Departamento de Geología, Santiago.

Biese, W. 1956. Los yacimientos de manganeso de Chile. *XX Congreso Geológico Internacional, Simposio sobre yacimientos de manganeso III*, México, 377-416.

Bookstrom, A. 1975. *Magnetite deposits of El Romeral, Chile: physical geology, sequence of events, and processes of formation.* In partial fulfillment of the requirements for degree of Doctor of Philosophy, Stanford University, Department of Geology, Palo Alto.

Bookstrom, A. 1977. Magnetite deposits of El Romeral, Chile. *Economic Geology*, **72**, 1101-1130.

Bookstrom, A. 1995. Magmatic features of iron ores of the Kiruna type in Chile and Sweden: ore textures and magnetite geochemistry-a discussion. *Economic Geology*, **90**, 469-473.

Broman, C., Nyström, J.O., Henríquez, F. y Elfman, M. 1999. Fluid inclusions in magnetite-apatite ore from a cooling magmatic system at El Laco, Chile. *GFF*, **121**, 253–267.

CAP Minería. 2014. Obtenido de www.capmineria.cl/empresa/historia

CAP Minería. 2014. *Memoria Anual*. Obtenido de http://www.capmineria.cl/wp-content/uploads/2015/03/cap_mineria_memoria_2014.pdf

Charrier, R., Pinto, L. y Rodríguez, M. 2007. Tectonostratigraphic evolution of the Andean Orogen in Chile. En T. Moreno, W. *In:* Gibbons, W. y Moreno, T. G. (eds) *The Geology of Chile.* The Geological Society of London, London, 21-114.

Cox, D. y Singer, A. 2007. Descriptive and grade-tonnage models and database for Iron Oxide Cu-Au deposits. U.S Geological Survey, Open-File Report **1155**.

Dallmeyer, D., Brown, M., Grocott, J., Taylor, G. y Treloar, P. 1996. Mesozoic Magmatic and Tectonic Events Within the Andean Plate Boundary Zone, 26"-27"50', North Chile: Constraints from 40Ar/39Ar Mineral Ages. *Journal of Geology*, **104**, 19-40.

Darwin, C. 1846. *Geological observations of South America. In:* Smith, Elder y Co. (eds) *Part III of The geology of the voyage of the Beagle*, London.

Dobbs, M. 1978. *Distribución de vanadio y titanio en el Cuerpo Principal de la mina El Romeral.* Memoria para optar al Título de Geólogo. Universidad de Chile, Facultad de Ciencias Físicas y Matemáticas, Departamento de Geología, Santiago, p.86.

Emparan, C. y Pineda, G. 1999. Área Condoriaco-Rivadavia, Región de Coquimbo. Servicio Nacional de Geología y Minería, Santiago, Mapas Geológicos no. **12**, 1:100.000.

Emparan, C. y Pineda, G. 2000. Área La Serena-La Higuera, Región de Coquimbo. Servicio Nacional de Geología y Minería, Santiago, Mapas Geológicos no. **18**, 1:100.000.

Espinoza, L. 1996. *Geología del cuerpo Cerro Principal Distrito Ferrífero El Romeral.* Taller de título, Universidad de Chile, Facultad de Ciencias Físicas y Matemáticas, Departamento de Geología, Santiago.

Espinoza, L. 2000. *Estudio petrográfico del cuerpo Cerro Principal del distrito ferrífero El Romeral IV región- La Serena, Chile*. Memoria para optar al título de geólogo. Santiago, Universidad de Chile, Facultad de Ciencias Físicas y Matemáticas, Departamento de Geología, Santiago.

Gana, P. 1991. Mapa geológico de la Cordillera de la Costa entre La Serena y Quebrada El Teniente. Servicio Nacional de Geología y Minería, Santiago, Documentos de Trabajo no. **3**, 1:100.000.

González, G. y Carrizo, D. 2000. Caracterización cinemática de la deformación pliocena del Sistema de falla de Atacama, inmediaciones del Salar del Carmen, norte de Chile. *Proceedings 9th Congreso Geológico Chileno*, Puerto Varas, 578-582.

González, G. y Carrizo, D. 2003. Segmentación, cinemática y cronología relativa de la deformación tardía en la Falla Salar del Carmen, Sistema de Fallas Atacama (23°40'S), norte de Chile. *Revista Geológica de Chile,* **30**, 223-244.

Grocott, J. y Taylor, G. 2002. Magmatic arc fault systems, deformation partitioning and emplacement of granitic complexes in the Coastal Cordiller, north Chilean Andes (25°30'S to 27°00'S). *Journal of the Geological Society,* **159**, 425-442.

Grocott, J., Brown, M., Dallmeyes, G., Taylor, G. y Treloar, P. 1994. Mechanism of continental grow in extensionals arcs: an example from the Andean Plate Boundary Zone. *Geology,* **22**, 391-394.

Henríquez, F. y Martin, R.F. 1978. Crystal-growth textures in magnetite flows and feeder dykes, El Laco, Chile. *Canadian Mineralogist*, **16**, 581-589.

Henríquez, F., Naslund, H.R., Nyström, J.O., Vivallo, W., Aguirre, R., Dobbs, F.M. y Lledó, H. 2003. New field evidence bearing on the origin of the El Laco magnetite deposit, northern Chile—a discussion. *Economic Geology,* **98**, 1497–1500.

Herm, D. 1969. Marines Pliozän und Pleistozän in Nord- und Mittel-Chile unter besonderer Berücksichtigung der Entwicklung der Mollusken-Faunen. *Zitteliana*, **2**, 1-159.

Hitzman, M., Oreskes, N. y Einaudi, M. 1992. Geological characteristics and tectonic setting of the Proterozoic iron oxide (Cu-U-Au-REE) deposits. *Precambrian Research,* **58**, 241-287.

Knipping, J., Bilenker, L., Simon, A., Reich, M., Barra, F., Deditius, A. y Munizaga, R. 2015. Giant Kiruna-type deposits form by efficient flotation of magmatic magnetite suspensions. *Geology,* **43(7)**, 591-594.

Larson, R.L. y Pitman, W.C. 1972. Worldwide correlation of Mesozoic magnetic anomalies, and its implications. *Geological Society of American Bulletin*, **83**, 3645-3662.

Llaumet, C. 1977. *Evaluación geológica del depósito ferrífero "El Romeral", IV región, Chile.* Inédito de Compañía Minera del Pacífico, p.80.

Lorca, G. 1990. *Caracterización geoquímica y cristalográfica de las piritas de los yacimientos de hierro El Algarrobo y El Romeral*. Memoria para optar al título de geólogo. Universidad de Chile, Facultad de Ciencias Físicas y Matemáticas, Departamento de Geología, Santiago, p.138.

Martínez-Pardo, R. 1980. Hallazgo de foraminíferos miocénicos cerca de Puerto Aldea, Bahía de Tongoy, Provincia de Coquimbo, Chile. *Revista Geologógica de Chile*, **8**, 65-78.

Martínez-Pardo, R. y Caro, R. 1980. Microfósiles silíceos de las diatomitas de Tongoy, Provincia de Coquimbo, Chile: Su significado biocronoestratigráfico, biocrono-geológico, paleoecológico y paleogeográfico. *Revista Geológica de Chile*, **10**, 33-53.

Melo, O. 1975. *Geología económica del yacimiento de hierro El Romeral, La Serena, Chile.* Universidad de Chile, Ingeniería Civil de Minas, Santiago.

Ménard, J. 1995. Relationship between altered pyroxene diorite and the magnetite mineralization in the Chilean Iron Belt, with emphasis on the El Algarrobo iron deposits (Atacama region, Chile). *Miner Deposita*, **30**, 268–274.

Morata, D. y Aguirre, L. 2003.Extensional Lower Cretaceous volcanism in the Coastal Range (29°20'-30°S), Chile: geochemistry and petrogenesis. *Journal of South American Earth Sciences*, **16**, 459-476.

Morata, D., Féraud, G., Aguirre, L., Arancibia, G., Belmar, M., Morales, S. y Carrillo, J. 2008. Geochronology of the Lower Cretaceous volcanism from the Coastal Range (29°20'-30°S), Chile. *Revista Geológica de Chile*, **35(1)**, 123-145.

Moscoso, R., Nasi, C. y Salinas, P. 1982a. Hoja Vallenar y parte norte de La Serena. Servicio Nacional de Geología y Minería, Santiago, Carta Geológica de Chile no. **55**, 1-100, 1:250.00.

Moyano, V. 1992. *Geología y geoquímica de las rocas andesíticas y brechas asociadas del Cordón de La Liga, Distrito Minero El Romeral, IV Región.* Informe de avance del Taller de Título I, Universidad de Chile, Departamento de Geología, Santiago.

Nyström, J.O. y Henriquez, F. 1994. Magmatic features of iron ores of the Kiruna type in Chile and Sweden: ore textures and magnetite geochemistry. *Economic Geology*, **89**, 820–839.

Nyström, J.O. y Henríquez, F. 1995. Magmatic features of iron ores of the Kiruna type in Chile and Sweden: ore textures and magnetite geochemistry-a reply. *Economic Geology,* **90**, 473-475.

Park, C.F. 1961. A magnetite "flow" in northern Chile. *Economic Geology*, **56**, 431–436.

Paskoff, R. 1970. *Le Chili semi-aride: recherches géomorphologiques. Biscaye Frères, Imprimeurs.* Bordeaux, France.

Pérez, E. y Reyes, R. 1998a. *Fauna de Trigonias del Hauteriviano (Cretácico Inferior), proveniente de diversas localidades ubicadas al norte y al sur del valle río Elqui, hoja La Serena, IV Región, norte de Chile.* Informe Inédito, Servicio Nacional de Geología y Minería, Santiago, p.14.

Pérez, E. y Reyes. R. 1999a. *Invertebrados del Cretácico Inferior, provenientes de diversas localidades ubicadas al norte y sur del valle río Elqui, Hoja La Serena, IV Región, norte de Chile. Se excluyen Ostreacea y la mayor parte de los Trigonioda y Cephalopoda.* Informe Inédito, Servicio Nacional de Geología y Minería, Santiago, p.14.

Pineda, G. 1996. *Geología del área central-norte de la provincia de Elqui, entre las coordenadas 29°45'-30°00' Lat. Sur y 70°39'-71°05' Long. Oeste.* Memoria de título (Inédito), Universidad de Chile, Facultad de Ciencias Físicas y Matemáticas, Departamento de Geología, Santiago.

Pineda, G. y Emparan, C. 1997. Nuevos antecedentes de la estratigrafía y geocronología del norte del río Elqui: Evidencias de tectónica extensional. *Congreso Geológico Chileno* Antofagasta, no. 8, Actas, **1**, 215-219.

Rhodes, A.L. y Oreskes, N. 1999. Oxygen isotope composition of magnetite deposits at El Laco, Chile: Evidence of formation from isotopically heavy fluids. *Society of Economic Geologists*, Special Publication, **7**, 333–351.

Rhodes, A.L.; Oreskes, N. y Sheets, S. 1999. Geology and Rare Earth Element geochemistry of magnetite deposits at El Laco, Chile. *Society of Economic Geology*, Special Publication, **7**, 299-332.

Rivano, S. y Sepúlveda, P. 1991. Hoja Illapel. Servicio Nacional de Geología y Minería, Carta Geológica de Chileno no. **69**, Santiago, p.132, 1:250.000.

Romo, C. 1981. *Geología y evaluación geológica de reservas del cuerpo de hierro Cerro Norte. Minas El Romeral. IV Región.* Memoria para optar al título de geólogo. Universidad de Chile, Departamento de Geología, Santiago, p.122.

Rubilar, A. 1998. *Fauna de ostras del Cretácico Inferior (Neocomiano), proveniente de localidades ubicadas al norte y sur del valle del río Elqui, Hoja La Serena, IV Región, norte de Chile*. Informe Inédito, Servicio Nacional de Geología y Minería, Santiago, p.17.

Ruiz, C., Aguirre, L., Corvalán, J., Klohn, C., Klohn, E. y Levi, B. 1965. Geología y yacimientos metalíferos de Chile. Instituto de Investigaciones Geológicas, Santiago. p.302.

Ruiz, C., Ortiz, F., Moraga, A. y Aguilar, A. 1968. Genesis of the Chilean iron ore deposits of Mesozoic Age. *International Geological Congress*, 23rd, Prague, **7**, 323–338.

Saint Amand, P. y Allen, C. 1960. Strike-slip faulting in northern Chile. *Geological Society of America Bulletin Abstract,* **71**, 391-426.

Scheuber, E. y Andriessen, P. 1990. The kinematic and geodinamic significance of the Atacama fault zona, northern Chile. *Journal of Structural Geology,* **12(2)**, 243-257.

Sheets, S.A. 1997. Fluid inclusion study of the El Laco magnetite deposits, Chile: Unpublished M.Sc. thesis, Hanover, New Hampshire, Dartmouth College, p.94.

Sillitoe, R.H. y Burrows, D.R. 2002. New field evidence bearing on the origin of the El Laco magnetite deposit, northern Chile. *Economic Geology,* **97**, 1101–1109.

Sillitoe, R.H. 2003. Iron oxide-copper-gold deposits: an Andean view. *Mineralium Deposita,* **38**, no.7, 787-812.

Sillitoe, R.H. y Burrows, D. 2003. New field evidence bearing on the origin of the El Laco magnetite deposit, northern Chile-a reply. *Economic Geology*, **97**, no.5, 1101-1109.

Steinmann, G. 1895. Die Cephalopoden der Quiriquina-Schichten. *Neues Jahrbuch für Mineralogie, Geologie und Paläontologie, Beilage-Band,* **10**, 64-94.

Taylor, G., Grocott, J., Pope, A. y Randall, D. 1998. Mesozoic fault systems, deformation and fault block rotation in the andean forearc: a crustal scale strike-slip duplex in the Coastal Cordillera of northern Chile. *Tectonophysics*, **299**, 93-109.

Travisany, V.; Henríquez, F. y Nyström, J.O. 1995. Magnetite lava flow in the Pleito-Melon district of the Chilean Iron Belt. *Economic Geology*, **90**, 438-444.

Ulloa, G. 1979. *Geología del Yacimiento ferrífero El Romeral y distribución de azufre y fósforo dentro del cuerpo denominado Cerro Principal.* Memoria para optar al título de geólogo, Universidad de Chile, Departamento de Geología, Santiago.

Zeballos, J. 1986. *Estudio geológico mineral de baja ley de Mina El Romeral.* Compañia Minera del Pacífico.

ANEXOS

ANEXO A. Condiciones analíticas

Table SM1. EMPA conditions for iron oxide, sulfides, silicates and apatite analysis at University of Western Australia - JEOL 8530F.

Magnetite-ilmenite analysis: 20 kV, 50 nA, focused beam

Element (X-ray line)	Standard	Analyzing crystal	Counting time (s)
Si ($K\alpha$)	Wollastonite	TAP	120
Al ($K\alpha$)	Corundum	TAP	120
Na ($K\alpha$)	Jadeite	TAP	60
Mg ($K\alpha$)	Periclase	TAP	120
Ti ($K\alpha$)	Rutile	PETJ	120
Ca ($K\alpha$)	Wollastonite	PETJ	120
K ($K\alpha$)	Orthoclase	PETJ	60
Fe ($K\alpha$)	Magnetite	LiF	40
Cr ($K\alpha$)	Cr_2O_3	LiFH	120
Ni ($K\alpha$)	Ni metal	LiF	120
V ($K\alpha$)	V metal	LiFH	120
Mn ($K\alpha$)	Mn metal	LiFH	120
Zn ($K\alpha$)	Zn metal	LiF	120
Cu ($K\alpha$)	Cu metal	LiF	120

Sulfides analysis: 25 kV, 40 nA, focused beam

Element (X-ray line)	Standard	Analyzing crystal	Counting time (s)
S ($K\alpha$)	Pyrite or Chalcopyrite	PETJ	50
As ($L\alpha$)	Asp200	TAP	50
Sb ($L\alpha$)	Sb metal	PETH	50
Fe ($K\alpha$)	Pyrite or Chalcopyrite	LiF	50
Se ($L\alpha$)	Bi_2Se_3	TAP	50
Au ($L\alpha$)	Au metal	LiF	50
Te ($L\alpha$)	Te metal	LiF	50
Cu ($K\alpha$)	Chalcopyrite	LiF	50
Pb ($M\alpha$)	Galena	PETH	50
Ni ($K\alpha$)	Ni metal	LiF	50
Co ($K\alpha$)	Co metal	LiF	50
Ag ($L\alpha$)	Ag metal	PETJ	50
Bi ($K\alpha$)	Bi metal	PETH	50
Si ($K\alpha$)	Wollastonite	TAP	50
Pd ($L\alpha$)	Pd metal	PETJ	50
Hg ($L\alpha$)	Syn HgTe (Coloradoite)	LiF	50
Pt ($L\alpha$)	Pt metal	LiF	50
Cd ($L\alpha$)	Cd metal	PETJ	40
Zn ($K\alpha$)	Zn metal	LiF	40

Silicates analysis: 15 kV, 15 nA and focused beam.

Element (X-ray line)	Standard	Analyzing crystal	Counting time (s)
F ($K\alpha$)	Fluorite	LDE1	70
Cl ($K\alpha$)	Tugtupite	PETJ	60
Ca ($K\alpha$)	Wilberforce Apatite	PETJ	60
P ($K\alpha$)	Wilberforce Apatite	PETJ	60
Sr ($L\alpha$)	Celestite	PETJ	60
La ($L\alpha$)	LaPO$_4$	LiFH	80
Ce ($L\alpha$)	CePO$_4$	LiFH	80
Nd ($L\alpha$)	NdPO$_4$	LiFH	80
Si ($K\alpha$)	Wollastonite	TAP	60
Mg ($K\alpha$)	Periclase	TAP	60
Al ($K\alpha$)	Spessartine	TAP	60
S ($K\alpha$)	Anhydrite	PETJ	100
Mn ($K\alpha$)	Mn metal	LiF	80
Na ($K\alpha$)	Jadeite	TAP	60
As ($L\alpha$)	GaAs	TAP	60

Apatite analysis: 15kV, 15nA and beam size of 10 μm.

Element (X-ray line)	Standard	Analyzing crystal	Counting time (s)
F ($K\alpha$)	Wilberforce Apatite	LDE1	50
Cl ($K\alpha$)	Tugtupite	PETJ	50
Ca ($K\alpha$)	Wollastonite	PETJ	50
Si ($K\alpha$)	Wollastonite or Biotite	TAP	50
Mg ($K\alpha$)	Periclase or Biotite	TAP	50
Al ($K\alpha$)	Corundum or Biotite	TAP	50
Mn ($K\alpha$)	Mn	LiF	50
Na ($K\alpha$)	Jadeite	TAP	50
Ti ($K\alpha$)	Rutile	LiFH	50
K ($K\alpha$)	Orthoclase	PETJ	50
Cr ($K\alpha$)	Cr_2O_3	LiFH	50
Fe ($K\alpha$)	Magnetite or Biotite	LiF	50
V ($K\alpha$)	V metal	LiFH	50

ANEXO B. Análisis EMPA

Table SM2. EMPA results for different magnetite grains (Type I, II and IV magnetite) from drill cores PRP-0702 and PRP-0733.

Element (wt.%)	D.L.	Massive														
Si	0.01	0.03	0.19	0.01	0.14	0.29	0.02	0.36	0.03	0.91	0.68	0.50	0.33	0.04	1.40	1.15
Al	0.01	0.01	0.03	B.D.L.	0.06	0.15	B.D.L.	0.21	0.01	0.05	0.03	0.04	0.01	0.01	0.07	0.05
Na	0.02	B.D.L.	B.D.L.	0.02	B.D.L.	0.06	0.05	0.03	0.04	0.03	0.02	0.03	0.04	0.03	0.03	0.03
Mg	0.01	0.01	0.04	B.D.L.	0.04	0.36	B.D.L.	0.22	B.D.L.	0.42	0.19	0.35	0.16	0.01	0.88	0.35
Ti	0.01	0.01	0.03	B.D.L.	0.05	B.D.L.	0.01	0.04	0.01	0.82	0.02	0.01	0.01	0.01	0.01	0.03
Ca	0.01	0.12	0.12	0.04	0.06	0.06	0.01	0.08	0.02	0.95	0.27	0.11	0.10	0.02	0.36	0.52
K	0.01	B.D.L.	0.09	0.13	0.04	0.13	0.07	0.05	0.05	0.13	0.08	0.09	0.04	0.04	0.10	0.11
Fe	0.01	72.16	71.54	71.72	71.09	71.49	72.80	71.52	72.67	68.51	70.19	72.02	72.61	73.00	69.80	68.72
Cr	0.01	B.D.L.	B.D.L.	B.D.L.	B.D.L.	B.D.L.	B.D.L.	B.D.L.	B.D.L.	B.D.L.	B.D.L.	B.D.L.	B.D.L.	B.D.L.	0.01	B.D.L.
V	0.01	0.25	0.26	0.25	0.25	0.26	0.26	0.25	0.25	0.26	0.26	0.26	0.25	0.26	0.26	0.25
Mn	0.01	0.02	0.02	0.03	0.02	0.04	0.03	0.02	0.02	0.03	0.02	0.03	0.02	0.02	0.03	0.03
O	-	27.79	27.81	27.61	27.58	28.21	28.00	28.26	27.96	28.63	28.01	28.54	28.42	28.10	29.03	28.23
Total	-	100.38	100.13	99.83	99.32	101.03	101.24	101.04	101.06	100.73	99.78	101.99	101.99	101.54	101.98	99.47

Element (wt.%)	D.L.	Massive														
Si	0.01	0.63	3.47	0.04	0.12	0.11	0.03	0.55	0.04	0.39	0.05	0.07	0.10	0.07	0.20	0.09
Al	0.01	0.03	0.11	B.D.L.	0.01	B.D.L.	0.01	0.02	0.03	0.20	0.01	0.01	0.04	0.01	0.22	0.02
Na	0.02	0.03	0.07	B.D.L.	0.02	B.D.L.	B.D.L.	0.02	0.12	0.05	0.15	0.20	0.20	0.20	0.28	0.21
Mg	0.01	0.20	1.91	0.01	0.02	0.03	0.1	0.23	B.D.L.	0.16	B.D.L.	B.D.L.	0.03	B.D.L.	0.18	0.01
Ti	0.01	0.03	0.02	0.01	0.01	0.01	0.01	0.01	0.09	0.29	0.15	0.08	0.11	0.35	0.39	0.49
Ca	0.01	0.25	0.81	0.02	0.06	0.05	0.03	0.21	0.04	0.13	0.06	0.03	0.03	0.08	0.09	0.09
K	0.01	0.08	0.03	0.02	0.04	0.02	0.06	0.06	0.02	0.08	0.02	0.03	0.04	0.02	0.12	0.04
Fe	0.01	71.10	66.48	72.71	72.21	72.34	72.08	70.54	71.33	70.40	71.63	70.58	70.37	70.17	70.14	70.38
Cr	0.01	B.D.L.	0.01	B.D.L.	B.D.L.	B.D.L.	B.D.L.	B.D.L.	B.D.L.	B.D.L.	B.D.L.	B.D.L.	B.D.L.	B.D.L.	0.01	B.D.L.
V	0.01	0.25	0.25	0.26	0.26	0.26	0.26	0.26	0.26	0.26	0.26	0.26	0.27	0.26	0.25	0.26
Mn	0.01	0.03	0.03	0.02	0.02	0.02	0.03	0.03	0.04	0.01	0.06	0.07	0.06	0.08	0.02	0.08
O	-	28.31	28.01	27.99	27.91	27.93	27.74	27.99	27.58	28.02	27.75	27.34	27.35	27.38	27.90	27.59
Total	-	100.95	101.21	101.08	100.66	100.76	100.35	99.93	99.54	99.99	100.14	98.67	98.60	98.64	99.82	99.24

Element (wt.%)	D.L.	Massive														
Si	0.01	0.13	0.06	0.06	0.04	1.25	0.07	0.05	0.03	0.07	0.02	0.02	0.07	0.10	0.07	0.08
Al	0.01	0.05	0.02	0.01	0.01	0.30	0.04	0.01	B.D.L.	0.03	B.D.L.	B.D.L.	B.D.L.	B.D.L.	0.02	0.04
Na	0.02	0.22	0.23	0.20	0.16	0.18	0.27	0.15	0.23	0.16	0.07	0.12	0.17	0.16	0.21	0.19
Mg	0.01	0.03	B.D.L.	B.D.L.	B.D.L.	0.62	0.04	B.D.L.	B.D.L.	B.D.L.	B.D.L.	B.D.L.	B.D.L.	0.01	0.01	0.04
Ti	0.01	0.25	0.09	0.05	0.03	0.03	0.02	0.04	0.10	0.22	0.04	0.30	0.39	0.32	0.07	0.06
Ca	0.01	0.08	0.03	0.03	0.02	0.27	0.03	0.02	0.05	0.03	0.01	0.01	0.03	0.03	0.03	0.06
K	0.01	0.03	0.02	0.02	0.01	0.02	0.01	0.02	0.05	0.02	0.02	0.01	0.02	0.02	0.01	0.02
Fe	0.01	70.36	70.90	70.75	70.70	67.12	70.92	70.78	69.78	70.98	71.74	71.07	71.23	70.65	71.13	70.45
Cr	0.01	B.D.L.	0.01	0.01	B.D.L.	B.D.L.	0.01	B.D.L.	B.D.L.	0.01	0.01	B.D.L.	0.01	0.01	0.01	B.D.L.
V	0.01	0.26	0.26	0.27	0.27	0.26	0.27	0.27	0.27	0.27	0.25	0.26	0.25	0.25	0.27	0.27
Mn	0.01	0.07	0.07	0.07	0.04	0.06	0.06	0.06	0.15	0.08	0.02	0.03	0.07	0.05	0.07	0.06
O	-	27.52	27.47	27.37	27.28	28.08	27.50	27.34	27.81	27.60	27.61	27.55	27.77	27.54	27.55	27.34
Total	-	99.00	99.17	98.84	98.55	98.20	99.25	98.75	98.48	99.48	99.78	99.38	100.01	99.16	99.44	98.60

Element (wt.%)	D.L.	Massive							Disseminated							
Si	0.01	0.09	0.06	0.15	0.05	0.11	0.19	0.19	0.01	0.05	0.05	0.01	0.06	0.04	0.26	0.10
Al	0.01	0.03	0.01	0.07	0.01	0.03	0.09	0.13	0.01	0.01	B.D.L.	0.01	B.D.L.	B.D.L.	0.09	0.02
Na	0.02	0.19	0.27	0.25	0.20	0.27	0.19	0.27	0.03	0.17	0.04	0.14	0.15	0.19	0.12	0.15
Mg	0.01	0.03	B.D.L.	0.05	B.D.L.	0.01	0.08	0.11	B.D.L.	B.D.L.	B.D.L.	0.01	B.D.L.	B.D.L.	0.07	0.01
Ti	0.01	0.04	0.02	0.03	0.02	0.05	0.14	0.09	0.03	0.07	0.05	0.15	0.10	0.04	0.04	0.07
Ca	0.01	0.04	0.03	0.06	0.02	0.03	0.08	0.05	0.01	0.02	0.01	0.01	0.03	0.03	0.04	0.03
K	0.01	0.02	0.02	0.03	0.02	0.08	0.03	0.04	0.05	0.02	0.02	0.03	0.03	0.02	0.01	0.09
Fe	0.01	70.58	70.57	69.83	70.73	70.62	70.87	69.56	72.08	71.26	71.85	71.53	71.36	71.26	71.48	71.24
Cr	0.01	B.D.L.	B.D.L.	B.D.L.	B.D.L.	B.D.L.	B.D.L.	B.D.L.	B.D.L.	B.D.L.	B.D.L.	B.D.L.	B.D.L.	B.D.L.	B.D.L.	B.D.L.
V	0.01	0.27	0.27	0.27	0.27	0.26	0.27	0.26	0.27	0.27	0.28	0.28	0.28	0.28	0.28	0.27
Mn	0.01	0.06	0.08	0.08	0.07	0.09	0.07	0.06	0.01	0.08	0.03	0.03	0.07	0.06	0.03	0.06
O	-	27.36	27.31	27.23	27.33	27.07	27.76	27.29	27.72	27.55	27.70	27.65	27.61	27.53	27.96	27.62
Total	-	98.70	98.65	98.06	98.72	98.65	99.75	98.05	100.20	99.50	100.04	99.85	99.67	99.45	100.39	99.66

		Type II Magnetite												
Element (wt.%)	D.L.	Massive												
Si	0.01	0.02	0.01	0.01	0.01	B.D.L.	B.D.L.	1.19	0.01	0.01	0.01	0.01	B.D.L.	B.D.L.
Al	0.01	0.02	0.03	0.03	0.03	0.03	0.04	0.17	0.04	0.04	0.04	0.04	0.03	0.02
Na	0.02	B.D.L.	0.02	B.D.L.	B.D.L.	B.D.L.	B.D.L.	0.07	B.D.L.	B.D.L.	B.D.L.	B.D.L.	B.D.L.	B.D.L.
Mg	0.01	B.D.L.	0.01	B.D.L.	B.D.L.	B.D.L.	B.D.L.	0.07	B.D.L.	B.D.L.	B.D.L.	0.01	B.D.L.	B.D.L.
Ti	0.01	0.01	0.01	0.01	0.01	0.02	0.01	B.D.L.	0.01	0.01	0.01	0.01	0.01	0.01
Ca	0.01	0.06	0.01	0.01	B.D.L.	B.D.L.	B.D.L.	0.05	B.D.L.	B.D.L.	B.D.L.	B.D.L.	0.01	0.01
K	0.02	B.D.L.	B.D.L.	B.D.L.	B.D.L.	0.01	B.D.L.	0.03	B.D.L.	B.D.L.	B.D.L.	B.D.L.	B.D.L.	B.D.L.
Fe	0.01	72.37	72.30	72.56	72.53	72.62	72.79	69.28	72.58	72.45	72.50	72.43	72.94	72.65
Cr	0.01	B.D.L.	B.D.L.	B.D.L.	0.01	B.D.L.	B.D.L.	0.01	B.D.L.	B.D.L.	B.D.L.	B.D.L.	B.D.L.	B.D.L.
V	0.01	0.25	0.26	0.26	0.26	0.25	0.25	0.26	0.26	0.26	0.26	0.26	0.26	0.25
Mn	0.01	0.02	0.02	0.02	0.02	0.02	0.02	0.03	0.02	0.02	0.02	0.02	0.02	0.02
O	-	27.84	27.80	27.89	27.87	27.92	27.98	28.22	27.90	27.85	27.87	27.85	28.02	27.91
Total	-	100.60	100.44	100.78	100.73	100.88	101.08	99.37	100.82	100.64	100.70	100.63	101.28	100.87
Element (wt.%)	D.L.	Massive												
Si	0.01	0.01	0.51	0.01	0.02	B.D.L.	B.D.L.	0.01	0.01	0.04	0.01	0.01	B.D.L.	0.01
Al	0.01	0.01	0.46	0.01	0.02	0.03	0.03	0.04	0.04	0.04	0.04	0.04	0.04	0.04
Na	0.02	B.D.L.	B.D.L.	B.D.L.	B.D.L.	B.D.L.	B.D.L.	B.D.L.	B.D.L.	B.D.L.	B.D.L.	B.D.L.	B.D.L.	B.D.L.
Mg	0.01	B.D.L.	0.59	B.D.L.	B.D.L.	B.D.L.	B.D.L.	B.D.L.	B.D.L.	B.D.L.	0.01	B.D.L.	B.D.L.	B.D.L.
Ti	0.01	0.01	0.03	0.01	0.01	0.01	0.01	0.01	0.01	0.01	0.01	0.01	0.01	0.01
Ca	0.01	0.03	0.03	0.02	0.11	0.01	B.D.L.	B.D.L.	B.D.L.	B.D.L.	B.D.L.	B.D.L.	B.D.L.	B.D.L.
K	0.02	B.D.L.	0.06	B.D.L.	B.D.L.	B.D.L.	B.D.L.	B.D.L.	B.D.L.	B.D.L.	B.D.L.	B.D.L.	B.D.L.	B.D.L.
Fe	0.01	72.59	70.09	72.62	72.11	73.03	72.65	72.67	72.72	72.67	72.82	72.67	72.64	72.67
Cr	0.01	B.D.L.	B.D.L.	B.D.L.	B.D.L.	B.D.L.	B.D.L.	B.D.L.	B.D.L.	B.D.L.	0.01	B.D.L.	B.D.L.	B.D.L.
V	0.01	0.25	0.24	0.26	0.24	0.26	0.26	0.26	0.26	0.26	0.26	0.25	0.26	0.26
Mn	0.01	0.02	0.02	0.02	0.02	0.02	0.02	0.02	0.02	0.02	0.02	0.02	0.02	0.02
O	-	27.89	28.32	27.90	27.75	28.06	27.92	27.94	27.95	27.98	28.01	27.94	27.93	27.94
Total	-	100.80	100.34	100.85	100.29	101.42	100.88	100.95	101.01	101.02	101.18	100.95	100.89	100.95

Element (wt.%)	D.L.	Massive												
Si	0.01	0.06	0.01	0.01	B.D.L.	0.01	B.D.L.	0.01	0.01	0.01	B.D.L.	B.D.L.	0.01	0.01
Al	0.01	0.08	0.04	0.04	0.04	0.04	0.04	0.04	0.03	0.02	0.02	0.02	0.04	0.05
Na	0.02	B.D.L.	B.D.L.	0.02	B.D.L.	B.D.L.	B.D.L.	B.D.L.	B.D.L.	B.D.L.	B.D.L.	B.D.L.	B.D.L.	B.D.L.
Mg	0.01	0.04	B.D.L.	B.D.L.	B.D.L.	B.D.L.	B.D.L.	B.D.L.	B.D.L.	0.01	B.D.L.	B.D.L.	B.D.L.	B.D.L.
Ti	0.01	0.40	0.01	0.01	0.01	0.01	0.01	0.01	0.01	0.01	0.02	0.01	0.01	0.01
Ca	0.01	0.03	B.D.L.	B.D.L.	B.D.L.	B.D.L.	0.01	0.01	B.D.L.	0.01	0.02	0.01	B.D.L.	B.D.L.
K	0.02	B.D.L.	B.D.L.	B.D.L.	B.D.L.	B.D.L.	B.D.L.	B.D.L.	B.D.L.	B.D.L.	B.D.L.	B.D.L.	B.D.L.	B.D.L.
Fe	0.01	71.56	72.34	72.50	72.55	72.49	72.51	72.66	72.70	72.30	72.49	72.42	72.61	72.70
Cr	0.01	B.D.L.	B.D.L.	B.D.L.	B.D.L.	B.D.L.	B.D.L.	B.D.L.	B.D.L.	B.D.L.	B.D.L.	B.D.L.	B.D.L.	B.D.L.
V	0.01	0.26	0.26	0.26	0.25	0.26	0.26	0.26	0.26	0.26	0.26	0.26	0.26	0.26
Mn	0.01	0.02	0.02	0.02	0.02	0.02	0.02	0.02	0.02	0.02	0.02	0.02	0.02	0.02
O	-	27.91	27.82	27.88	27.89	27.87	27.88	27.94	27.94	27.79	27.86	27.82	27.92	27.96
Total	-	100.36	100.50	100.74	100.78	100.71	100.72	100.93	100.96	100.42	100.67	100.55	100.87	101.00

Element (wt.%)	D.L.	Disseminated												**Magnetite IV**
Si	0.01	0.02	0.02	0.02	0.01	0.01	0.04	0.01	0.04	0.03	0.02	0.03	0.20	0.04
Al	0.01	0.01	0.01	0.01	0.01	B.D.L.	0.02	0.01	0.01	0.02	0.01	0.01	0.09	B.D.L.
Na	0.02	B.D.L.	B.D.L.	B.D.L.	B.D.L.	B.D.L.	0.05	0.07	0.06	0.07	0.05	B.D.L.	B.D.L.	0.02
Mg	0.01	0.01	B.D.L.	B.D.L.	B.D.L.	B.D.L.	B.D.L.	B.D.L.	B.D.L.	0.02	B.D.L.	B.D.L.	0.07	B.D.L.
Ti	0.01	0.01	1.14	0.79	0.02	0.03	0.03	0.10	0.01	0.04	0.03	0.03	0.04	0.01
Ca	0.01	0.06	0.06	0.05	0.02	0.02	0.02	0.01	0.02	0.01	0.01	0.01	0.04	0.04
K	0.02	0.03	B.D.L.	0.01	B.D.L.	B.D.L.	0.04	0.01	0.04	0.01	0.01	0.05	0.08	0.04
Fe	0.01	72.51	72.08	72.09	72.78	72.80	71.30	71.43	71.14	71.50	71.41	72.12	71.65	71.74
Cr	0.01	B.D.L.	0.02	0.02	0.01	0.01	B.D.L.	B.D.L.	B.D.L.	B.D.L.	0.01	B.D.L.	B.D.L.	B.D.L.
V	0.01	0.26	0.28	0.29	0.33	0.33	0.25	0.27	0.23	0.27	0.26	0.25	0.24	0.17
Mn	0.01	0.02	0.04	0.03	0.01	0.01	0.01	0.02	0.01	0.02	0.02	0.01	0.01	0.01
O	-	27.89	27.99	28.51	28.27	28.01	28.02	27.48	27.54	27.39	27.56	27.48	27.74	27.62
Total	-	100.81	101.64	101.80	101.46	101.21	99.78	99.41	99.10	99.36	99.38	99.98	100.16	99.68

D.L.: Detection limit; B.D.L: Below detection limit.

146

Table SM3. EMPA results for sulfides from drill cores PRP-0853 and DDH-5008.

A. Pyrite analyses

Element (wt.%)	D.L.	149-10	149-10	157-01	157-01	157-02	157-03	157-03	157-04	157-04	157-04	157-04	157-04	157-04	157-04	157-04	157-04
S	0.01	53.21	53.26	53.33	53.15	53.08	53.39	53.40	53.33	53.24	53.25	53.31	53.01	53.37	53.33	53.34	53.18
As	0.03	B.D.L	B.D.L	B.D.L	B.D.L	B.D.L	B.D.L	B.D.L	B.D.L	B.D.L	B.D.L	B.D.L	B.D.L	B.D.L	B.D.L	B.D.L	B.D.L
Sb	0.01	B.D.L	B.D.L	B.D.L	B.D.L	B.D.L	B.D.L	B.D.L	B.D.L	B.D.L	B.D.L	B.D.L	B.D.L	B.D.L	B.D.L	B.D.L	B.D.L
Fe	0.01	46.53	46.54	45.79	46.61	46.20	46.66	47.21	46.65	46.21	45.94	45.72	46.02	46.04	46.02	46.01	45.56
Se	0.02	B.D.L	B.D.L	B.D.L	B.D.L	B.D.L	B.D.L	B.D.L	B.D.L	B.D.L	0.03	0.03	B.D.L	B.D.L	B.D.L	B.D.L	B.D.L
Au	0.03	B.D.L	B.D.L	B.D.L	B.D.L	B.D.L	B.D.L	B.D.L	B.D.L	B.D.L	B.D.L	B.D.L	B.D.L	B.D.L	B.D.L	B.D.L	B.D.L
Te	0.04	B.D.L	B.D.L	B.D.L	B.D.L	B.D.L	B.D.L	B.D.L	B.D.L	B.D.L	B.D.L	B.D.L	B.D.L	B.D.L	B.D.L	B.D.L	B.D.L
Cu	0.01	0.14	0.10	0.01	0.01	0.01	B.D.L	B.D.L	B.D.L	0.01	B.D.L	B.D.L	B.D.L	0.02	B.D.L	B.D.L	B.D.L
Pb	0.02	B.D.L	B.D.L	B.D.L	B.D.L	B.D.L	B.D.L	B.D.L	B.D.L	B.D.L	B.D.L	B.D.L	B.D.L	B.D.L	B.D.L	B.D.L	B.D.L
Ni	0.01	0.11	0.06	0.03	B.D.L	0.33	0.51	0.04	0.06	0.38	0.57	0.49	0.37	0.67	0.42	0.50	0.51
Co	0.01	0.09	0.07	1.15	0.73	0.01	B.D.L	B.D.L	B.D.L	0.01	0.01	0.04	B.D.L	B.D.L	B.D.L	B.D.L	B.D.L
Ag	0.03	B.D.L	B.D.L	B.D.L	B.D.L	B.D.L	0.03	B.D.L	B.D.L	B.D.L	B.D.L	B.D.L	B.D.L	B.D.L	B.D.L	B.D.L	B.D.L
Bi	0.02	B.D.L	B.D.L	B.D.L	B.D.L	B.D.L	B.D.L	B.D.L	B.D.L	B.D.L	B.D.L	B.D.L	B.D.L	B.D.L	B.D.L	B.D.L	B.D.L
Si	0.01	B.D.L	B.D.L	B.D.L	B.D.L	B.D.L	B.D.L	B.D.L	B.D.L	B.D.L	B.D.L	B.D.L	B.D.L	B.D.L	B.D.L	B.D.L	B.D.L
Pd	0.03	B.D.L	B.D.L	B.D.L	B.D.L	B.D.L	B.D.L	B.D.L	B.D.L	B.D.L	B.D.L	B.D.L	B.D.L	0.03	B.D.L	B.D.L	B.D.L
Hg	0.04	B.D.L	B.D.L	B.D.L	B.D.L	B.D.L	B.D.L	B.D.L	B.D.L	B.D.L	B.D.L	B.D.L	B.D.L	B.D.L	B.D.L	B.D.L	B.D.L
Pt	0.03	B.D.L	B.D.L	B.D.L	B.D.L	B.D.L	B.D.L	B.D.L	B.D.L	B.D.L	B.D.L	B.D.L	B.D.L	B.D.L	B.D.L	B.D.L	B.D.L
Cd	0.04	B.D.L	B.D.L	0.05	B.D.L	B.D.L	B.D.L	B.D.L	B.D.L	B.D.L	B.D.L	B.D.L	B.D.L	B.D.L	B.D.L	B.D.L	B.D.L
Zn	0.02	B.D.L	B.D.L	B.D.L	B.D.L	B.D.L	B.D.L	B.D.L	B.D.L	B.D.L	B.D.L	B.D.L	B.D.L	B.D.L	B.D.L	B.D.L	B.D.L
Total	-	100.14	100.07	100.40	100.51	99.69	100.65	100.73	100.09	99.87	99.85	99.64	99.46	100.18	99.79	99.90	99.30

Element (wt.%)	D.L.	157-04	157-04	157-04	157-04	157-04	157-04	157-04	157-04	157-04	157-04	157-04	157-07	133-01	133-02	133-05	133-05
S	0.01	53.24	53.12	53.10	53.22	53.36	53.35	53.24	53.31	53.16	53.04	53.12	53.54	53.37	53.38	53.88	54.22
As	0.03	B.D.L	B.D.L	B.D.L	B.D.L	B.D.L	B.D.L	B.D.L	B.D.L	B.D.L	B.D.L	B.D.L	B.D.L	B.D.L	B.D.L	B.D.L	B.D.L
Sb	0.01	B.D.L	B.D.L	B.D.L	B.D.L	B.D.L	B.D.L	B.D.L	B.D.L	B.D.L	B.D.L	B.D.L	B.D.L	B.D.L	B.D.L	B.D.L	B.D.L
Fe	0.01	46.09	45.75	45.85	45.75	45.74	45.82	45.88	45.76	45.98	46.10	46.28	45.86	46.29	46.22	46.50	46.39
Se	0.02	B.D.L	B.D.L	B.D.L	B.D.L	B.D.L	B.D.L	B.D.L	B.D.L	B.D.L	B.D.L	B.D.L	B.D.L	B.D.L	B.D.L	B.D.L	B.D.L
Au	0.03	B.D.L	B.D.L	B.D.L	B.D.L	B.D.L	B.D.L	B.D.L	B.D.L	B.D.L	B.D.L	B.D.L	B.D.L	B.D.L	B.D.L	B.D.L	B.D.L
Te	0.04	B.D.L	B.D.L	B.D.L	B.D.L	B.D.L	B.D.L	B.D.L	B.D.L	B.D.L	B.D.L	B.D.L	B.D.L	B.D.L	B.D.L	B.D.L	B.D.L
Cu	0.01	B.D.L	B.D.L	B.D.L	B.D.L	B.D.L	B.D.L	B.D.L	B.D.L	B.D.L	B.D.L	B.D.L	B.D.L	B.D.L	B.D.L	0.15	0.10
Pb	0.02	B.D.L	B.D.L	B.D.L	B.D.L	B.D.L	B.D.L	B.D.L	B.D.L	B.D.L	B.D.L	B.D.L	B.D.L	B.D.L	B.D.L	B.D.L	B.D.L
Ni	0.01	0.52	0.49	0.47	0.45	0.55	0.48	0.37	0.45	0.43	0.42	0.46	0.61	0.04	0.24	0.28	0.37
Co	0.01	B.D.L	B.D.L	B.D.L	B.D.L	B.D.L	B.D.L	0.33	0.03	0.02	0.05	0.02	0.01	0.10	0.04	0.06	0.05
Ag	0.03	B.D.L	B.D.L	B.D.L	B.D.L	B.D.L	B.D.L	B.D.L	B.D.L	B.D.L	B.D.L	B.D.L	B.D.L	B.D.L	B.D.L	B.D.L	B.D.L
Bi	0.02	B.D.L	B.D.L	B.D.L	B.D.L	B.D.L	B.D.L	B.D.L	B.D.L	B.D.L	B.D.L	B.D.L	B.D.L	B.D.L	B.D.L	B.D.L	B.D.L
Si	0.01	B.D.L	B.D.L	B.D.L	B.D.L	B.D.L	B.D.L	B.D.L	B.D.L	B.D.L	B.D.L	B.D.L	B.D.L	B.D.L	0.01	0.01	0.02
Pd	0.03	B.D.L	B.D.L	B.D.L	0.03	B.D.L	B.D.L	B.D.L	B.D.L	B.D.L	B.D.L	B.D.L	B.D.L	B.D.L	B.D.L	B.D.L	0.04
Hg	0.04	B.D.L	B.D.L	B.D.L	B.D.L	B.D.L	B.D.L	B.D.L	B.D.L	B.D.L	B.D.L	B.D.L	B.D.L	0.04	B.D.L	B.D.L	B.D.L
Pt	0.03	B.D.L	B.D.L	B.D.L	B.D.L	B.D.L	B.D.L	B.D.L	B.D.L	B.D.L	B.D.L	B.D.L	B.D.L	B.D.L	B.D.L	B.D.L	B.D.L
Cd	0.04	0.05	B.D.L	B.D.L	B.D.L	B.D.L	B.D.L	B.D.L	B.D.L	B.D.L	B.D.L	B.D.L	B.D.L	B.D.L	B.D.L	0.04	B.D.L
Zn	0.02	B.D.L	B.D.L	B.D.L	B.D.L	B.D.L	B.D.L	B.D.L	B.D.L	B.D.L	B.D.L	B.D.L	B.D.L	B.D.L	B.D.L	B.D.L	B.D.L
Total	-	99.90	99.45	99.48	99.49	99.71	99.68	99.84	99.57	99.70	99.66	99.94	100.10	99.86	99.94	100.94	101.23

D.L: Detection limit; B.D.L: Below detection limit.

B. Chalcopyrite analyses

Elements (wt.%)	D.L.	149-01	149-01	149-01	149-01	149-01	149-01	149-01	149-02	149-02	149-02	149-02	149-03	149-03	149-04
S	0.01	35.13	34.97	35.16	35.17	35.27	35.51	35.53	35.21	35.00	36.19	35.31	34.75	34.84	35.44
As	0.04	B.D.L	B.D.L	B.D.L	B.D.L	B.D.L	B.D.L	B.D.L	B.D.L	B.D.L	B.D.L	B.D.L	B.D.L	B.D.L	B.D.L
Sb	0.01	B.D.L	B.D.L	B.D.L	B.D.L	B.D.L	B.D.L	B.D.L	B.D.L	B.D.L	B.D.L	B.D.L	B.D.L	B.D.L	B.D.L
Fe	0.01	30.59	30.57	30.73	30.62	30.71	30.89	30.52	30.69	30.65	34.30	32.31	30.40	30.08	31.63
Se	0.03	B.D.L	B.D.L	B.D.L	B.D.L	B.D.L	B.D.L	B.D.L	B.D.L	B.D.L	B.D.L	B.D.L	B.D.L	B.D.L	B.D.L
Au	0.03	B.D.L	B.D.L	B.D.L	B.D.L	B.D.L	B.D.L	B.D.L	B.D.L	B.D.L	B.D.L	B.D.L	B.D.L	B.D.L	B.D.L
Te	0.04	B.D.L	B.D.L	B.D.L	B.D.L	B.D.L	B.D.L	B.D.L	B.D.L	B.D.L	B.D.L	B.D.L	B.D.L	B.D.L	B.D.L
Cu	0.01	34.51	34.53	34.52	34.68	34.55	34.55	34.35	34.26	34.50	30.44	32.67	33.81	33.39	33.44
Pb	0.02	B.D.L	B.D.L	B.D.L	B.D.L	B.D.L	B.D.L	B.D.L	B.D.L	B.D.L	B.D.L	B.D.L	B.D.L	B.D.L	B.D.L
Ni	0.01	B.D.L	B.D.L	B.D.L	B.D.L	B.D.L	B.D.L	B.D.L	B.D.L	B.D.L	B.D.L	B.D.L	B.D.L	B.D.L	B.D.L
Co	0.01	B.D.L	B.D.L	B.D.L	B.D.L	B.D.L	B.D.L	B.D.L	B.D.L	B.D.L	B.D.L	0.09	B.D.L	B.D.L	0.01
Ag	0.03	B.D.L	B.D.L	B.D.L	B.D.L	B.D.L	B.D.L	0.04	B.D.L	B.D.L	B.D.L	B.D.L	B.D.L	B.D.L	B.D.L
Bi	0.02	B.D.L	B.D.L	B.D.L	B.D.L	B.D.L	B.D.L	B.D.L	B.D.L	B.D.L	B.D.L	B.D.L	B.D.L	B.D.L	B.D.L
Si	0.01	B.D.L	B.D.L	B.D.L	B.D.L	B.D.L	B.D.L	B.D.L	B.D.L	B.D.L	B.D.L	B.D.L	B.D.L	B.D.L	B.D.L
Pd	0.03	B.D.L	B.D.L	B.D.L	B.D.L	B.D.L	B.D.L	B.D.L	B.D.L	B.D.L	B.D.L	B.D.L	B.D.L	B.D.L	B.D.L
Hg	0.04	B.D.L	B.D.L	B.D.L	B.D.L	B.D.L	B.D.L	B.D.L	B.D.L	B.D.L	B.D.L	B.D.L	B.D.L	B.D.L	B.D.L
Pt	0.03	B.D.L	B.D.L	B.D.L	B.D.L	B.D.L	B.D.L	B.D.L	B.D.L	B.D.L	B.D.L	B.D.L	B.D.L	B.D.L	B.D.L
Cd	0.04	B.D.L	B.D.L	B.D.L	B.D.L	B.D.L	B.D.L	B.D.L	B.D.L	B.D.L	B.D.L	B.D.L	B.D.L	B.D.L	B.D.L
Zn	0.02	0.03	0.02	0.04	0.03	B.D.L	B.D.L	0.04	0.03	0.03	0.08	0.04	0.02	B.D.L	0.03
Total	-	100.25	100.09	100.45	100.50	100.53	100.96	100.48	100.19	100.18	101.01	100.41	99.03	98.42	100.56

Elements (wt.%)	D.L.	149-05	149-05	149-07	149-09	149-11	157-02	157-02	157-04	157-05	157-05	157-05	157-05	157-06	157-06
S	0.01	35.18	35.05	35.06	34.99	35.10	35.15	35.44	37.29	34.78	34.90	34.88	35.83	35.38	35.49
As	0.04	B.D.L	B.D.L	B.D.L	B.D.L	B.D.L	B.D.L	B.D.L	B.D.L	B.D.L	B.D.L	B.D.L	B.D.L	B.D.L	B.D.L
Sb	0.01	B.D.L	B.D.L	B.D.L	B.D.L	B.D.L	B.D.L	B.D.L	B.D.L	B.D.L	B.D.L	B.D.L	B.D.L	B.D.L	B.D.L
Fe	0.01	31.74	31.34	36.55	30.69	32.72	31.42	31.45	32.54	31.56	31.94	32.55	32.52	30.83	31.15
Se	0.03	B.D.L	B.D.L	B.D.L	B.D.L	B.D.L	B.D.L	B.D.L	B.D.L	B.D.L	B.D.L	B.D.L	B.D.L	B.D.L	B.D.L
Au	0.03	B.D.L	B.D.L	B.D.L	B.D.L	B.D.L	B.D.L	B.D.L	B.D.L	B.D.L	B.D.L	B.D.L	B.D.L	B.D.L	B.D.L
Te	0.04	B.D.L	B.D.L	B.D.L	B.D.L	B.D.L	B.D.L	B.D.L	B.D.L	B.D.L	B.D.L	B.D.L	B.D.L	B.D.L	B.D.L
Cu	0.01	34.29	34.46	28.27	34.37	33.77	33.73	33.45	31.32	34.19	34.11	33.86	33.88	34.12	34.11
Pb	0.02	B.D.L	B.D.L	B.D.L	B.D.L	B.D.L	B.D.L	B.D.L	B.D.L	B.D.L	B.D.L	B.D.L	B.D.L	B.D.L	B.D.L
Ni	0.01	B.D.L	B.D.L	0.01	B.D.L	B.D.L	B.D.L	0.01	B.D.L	B.D.L	B.D.L	B.D.L	B.D.L	B.D.L	B.D.L
Co	0.01	B.D.L	B.D.L	0.03	0.05	B.D.L	B.D.L	B.D.L	0.08	B.D.L	B.D.L	B.D.L	B.D.L	B.D.L	B.D.L
Ag	0.03	B.D.L	B.D.L	B.D.L	B.D.L	B.D.L	B.D.L	B.D.L	B.D.L	B.D.L	B.D.L	B.D.L	B.D.L	B.D.L	B.D.L
Bi	0.02	B.D.L	B.D.L	B.D.L	B.D.L	B.D.L	B.D.L	B.D.L	B.D.L	B.D.L	B.D.L	B.D.L	B.D.L	B.D.L	B.D.L
Si	0.01	B.D.L	B.D.L	B.D.L	B.D.L	B.D.L	B.D.L	B.D.L	B.D.L	B.D.L	B.D.L	0.01	B.D.L	B.D.L	B.D.L
Pd	0.03	B.D.L	B.D.L	B.D.L	B.D.L	B.D.L	B.D.L	B.D.L	B.D.L	B.D.L	B.D.L	B.D.L	B.D.L	B.D.L	B.D.L
Hg	0.04	B.D.L	B.D.L	B.D.L	B.D.L	B.D.L	B.D.L	B.D.L	B.D.L	0.05	B.D.L	B.D.L	B.D.L	B.D.L	B.D.L
Pt	0.03	B.D.L	B.D.L	B.D.L	B.D.L	B.D.L	B.D.L	B.D.L	B.D.L	B.D.L	B.D.L	B.D.L	B.D.L	B.D.L	B.D.L
Cd	0.04	B.D.L	B.D.L	B.D.L	B.D.L	B.D.L	B.D.L	B.D.L	B.D.L	B.D.L	B.D.L	B.D.L	B.D.L	B.D.L	B.D.L
Zn	0.02	0.02	0.02	0.04	0.04	0.02	0.03	B.D.L	B.D.L	0.03	B.D.L	B.D.L	B.D.L	0.02	B.D.L
Total	-	101.22	100.87	99.96	100.14	101.61	100.33	100.35	101.23	100.60	100.95	101.30	102.23	100.35	100.75

Elements (wt.%)	D.L.	157-06	157-06	157-06	157-06	157-06	157-07	133-04	133-05	133-05	133-05	133-05	133-05	133-05	133-05
S	0.01	35.35	35.14	35.53	35.46	36.07	35.48	35.38	35.39	35.48	35.44	37.48	35.32	35.49	35.64
As	0.04	B.D.L	B.D.L	B.D.L	B.D.L	B.D.L	B.D.L	B.D.L	B.D.L	B.D.L	B.D.L	B.D.L	B.D.L	B.D.L	B.D.L
Sb	0.01	B.D.L	B.D.L	B.D.L	B.D.L	B.D.L	B.D.L	B.D.L	B.D.L	B.D.L	B.D.L	B.D.L	B.D.L	B.D.L	B.D.L
Fe	0.01	31.42	31.03	30.93	30.96	31.04	31.42	29.32	31.88	31.93	32.12	32.85	30.39	30.39	30.86
Se	0.03	B.D.L	B.D.L	B.D.L	B.D.L	0.07	B.D.L	B.D.L	0.05	B.D.L	B.D.L	B.D.L	B.D.L	B.D.L	B.D.L
Au	0.03	B.D.L	B.D.L	B.D.L	B.D.L	B.D.L	B.D.L	B.D.L	B.D.L	B.D.L	B.D.L	B.D.L	B.D.L	B.D.L	B.D.L
Te	0.04	B.D.L	B.D.L	B.D.L	B.D.L	B.D.L	B.D.L	B.D.L	B.D.L	B.D.L	B.D.L	B.D.L	B.D.L	B.D.L	B.D.L
Cu	0.01	34.18	34.22	34.05	34.10	34.09	33.26	33.79	34.13	34.28	33.93	31.05	34.36	34.43	34.14
Pb	0.02	B.D.L	B.D.L	B.D.L	B.D.L	B.D.L	B.D.L	B.D.L	B.D.L	B.D.L	B.D.L	B.D.L	B.D.L	B.D.L	B.D.L
Ni	0.01	B.D.L	B.D.L	B.D.L	B.D.L	B.D.L	0.02	B.D.L	B.D.L	B.D.L	B.D.L	B.D.L	B.D.L	B.D.L	B.D.L
Co	0.01	B.D.L	B.D.L	B.D.L	B.D.L	B.D.L	0.03	B.D.L	B.D.L	B.D.L	B.D.L	0.01	B.D.L	B.D.L	B.D.L
Ag	0.03	B.D.L	B.D.L	0.05	B.D.L	0.04	B.D.L	B.D.L	B.D.L	B.D.L	B.D.L	B.D.L	B.D.L	B.D.L	B.D.L
Bi	0.02	B.D.L	B.D.L	B.D.L	B.D.L	B.D.L	B.D.L	B.D.L	B.D.L	B.D.L	B.D.L	B.D.L	B.D.L	B.D.L	B.D.L
Si	0.01	B.D.L	B.D.L	B.D.L	B.D.L	B.D.L	B.D.L	0.12	B.D.L	B.D.L	B.D.L	B.D.L	B.D.L	B.D.L	B.D.L
Pd	0.03	B.D.L	B.D.L	0.03	B.D.L	0.06	B.D.L	B.D.L	B.D.L	B.D.L	B.D.L	B.D.L	B.D.L	0.03	B.D.L
Hg	0.04	B.D.L	B.D.L	B.D.L	B.D.L	B.D.L	B.D.L	B.D.L	B.D.L	B.D.L	B.D.L	B.D.L	B.D.L	B.D.L	B.D.L
Pt	0.03	B.D.L	B.D.L	B.D.L	B.D.L	B.D.L	B.D.L	B.D.L	B.D.L	B.D.L	B.D.L	B.D.L	B.D.L	B.D.L	B.D.L
Cd	0.04	B.D.L	B.D.L	B.D.L	B.D.L	B.D.L	0.05	B.D.L	B.D.L	B.D.L	B.D.L	B.D.L	B.D.L	B.D.L	B.D.L
Zn	0.02	B.D.L	B.D.L	0.02	B.D.L	B.D.L	B.D.L	B.D.L	B.D.L	0.02	B.D.L	B.D.L	B.D.L	0.03	0.02
Total	-	100.94	100.39	100.61	100.52	101.37	100.24	98.62	101.46	101.71	101.49	101.39	100.06	100.37	100.66

D.L.: Detection limit; B.D.L: Below detection limit

Table SM4. EMPA results for actinolite crystals from drill cores PRP-0702, PRP-0733 and DDH-5008.

Element (wt.%)	D.L	Actinolite I					Actinolite II								
F	0.03	B.D.L	0.12	B.D.L	0.02	B.D.L	0.14	0.04	0.08	0.17	0.09	B.D.L	0.17	0.18	0.22
Cl	0.01	B.D.L	B.D.L	B.D.L	B.D.L	B.D.L	B.D.L	0.02	B.D.L	B.D.L	B.D.L	0.02	B.D.L	B.D.L	B.D.L
Ca	0.01	9.05	9.05	9.30	9.22	9.16	9.47	9.09	9.29	9.27	9.33	9.83	9.38	9.32	9.38
Si	0.01	23.72	23.78	24.50	24.83	24.78	26.10	22.42	24.98	25.77	25.86	24.75	24.92	25.20	25.44
Mg	0.01	8.60	8.62	9.10	9.30	9.07	11.40	9.57	11.01	10.74	11.09	10.65	11.01	11.22	10.96
Al	0.01	1.49	1.35	0.71	0.70	0.76	0.65	3.20	1.27	0.34	0.41	1.29	0.87	0.54	0.51
Mn	0.03	0.10	0.10	0.08	0.09	0.09	B.D.L	0.06	B.D.L	0.05	0.08	0.04	0.08	0.07	0.07
Na	0.01	0.19	0.17	0.07	0.07	0.09	0.12	0.69	0.23	0.04	0.06	0.24	0.17	0.08	0.06
Ti	0.01	B.D.L	B.D.L	B.D.L	B.D.L	B.D.L	B.D.L	0.07	B.D.L	B.D.L	B.D.L	0.04	0.03	0.02	B.D.L
K	0.01	0.09	0.07	B.D.L	0.02	B.D.L	B.D.L	0.12	0.02	0.01	B.D.L	0.07	0.04	0.03	B.D.L
Cr	0.01	B.D.L	B.D.L	B.D.L	B.D.L	B.D.L	B.D.L	B.D.L	B.D.L	B.D.L	B.D.L	B.D.L	B.D.L	B.D.L	B.D.L
Fe	0.03	11.29	11.44	10.71	10.28	10.20	6.05	8.97	6.87	8.10	6.78	6.95	6.24	6.22	7.37
V	0.01	0.07	0.08	0.04	0.04	0.05	B.D.L	0.06	B.D.L	B.D.L	B.D.L	0.04	0.03	B.D.L	B.D.L
O	-	42.84	42.83	43.21	43.58	43.38	45.29	43.08	44.49	44.65	44.73	44.30	43.95	44.04	44.42
H	-	0.23	0.23	0.23	0.23	0.23	0.24	0.23	0.24	0.23	0.24	0.24	0.24	0.24	0.24
Total	-	97.68	97.82	97.95	98.37	97.81	99.46	97.61	98.46	99.37	98.67	98.45	97.14	97.17	98.64
Fe#	-	0.36	0.37	0.34	0.32	0.33	0.19	0.29	0.21	0.25	0.21	0.22	0.20	0.19	0.23

Element (wt.%)	D.L	Actinolite II													
F	0.03	0.23	0.16	B.D.L	0.08	0.32	0.11	0.15	0.18	0.19	0.07	0.17	0.19	0.11	0.15
Cl	0.01	0.03	0.03	0.02	0.03	0.02	0.03	0.03	0.02	0.03	0.03	0.02	0.03	0.02	0.02
Ca	0.01	8.89	9.00	8.98	8.48	8.59	8.61	8.52	8.44	8.56	8.65	8.62	8.58	8.52	8.64
Si	0.01	25.90	26.15	26.07	25.27	25.39	25.94	26.00	26.10	25.83	25.48	25.59	25.87	26.10	25.93
Mg	0.01	11.21	11.44	11.44	11.26	11.26	11.39	11.24	11.24	11.29	11.23	11.29	11.34	11.31	11.30
Al	0.01	0.38	0.41	0.40	0.38	0.37	0.37	0.37	0.36	0.39	0.40	0.35	0.36	0.36	0.35
Mn	0.03	B.D.L	B.D.L	0.04	0.03	0.05	0.05	B.D.L	B.D.L	0.05	0.05	B.D.L	B.D.L	B.D.L	0.06
Na	0.01	0.17	0.17	0.17	0.26	0.27	0.29	0.30	0.30	0.29	0.26	0.30	0.28	0.31	0.29
Ti	0.01	B.D.L	B.D.L	B.D.L	B.D.L	B.D.L	B.D.L	B.D.L	B.D.L	B.D.L	B.D.L	B.D.L	B.D.L	B.D.L	B.D.L
K	0.01	0.07	0.05	0.10	0.09	0.07	0.05	0.07	0.06	0.07	0.06	0.09	0.10	0.03	0.09
Cr	0.01	B.D.L	B.D.L	B.D.L	B.D.L	B.D.L	B.D.L	B.D.L	B.D.L	B.D.L	B.D.L	B.D.L	B.D.L	B.D.L	0.04
Fe	0.03	6.73	6.99	6.75	7.29	6.99	7.21	6.83	6.73	7.25	6.90	7.02	7.13	7.13	7.00
V	0.01	B.D.L	B.D.L	B.D.L	B.D.L	B.D.L	B.D.L	B.D.L	B.D.L	B.D.L	B.D.L	B.D.L	B.D.L	B.D.L	B.D.L
O	-	44.68	45.25	45.10	44.02	44.10	44.90	44.72	44.77	44.72	44.22	44.36	44.74	44.95	44.78
H	-	0.24	0.24	0.24	0.24	0.24	0.24	0.24	0.24	0.24	0.24	0.24	0.24	0.24	0.24
Total	-	98.52	99.89	99.32	97.43	97.66	99.20	98.48	98.43	98.90	97.59	98.04	98.87	99.08	98.89
Fe#	-	0.21	0.21	0.20	0.22	0.21	0.22	0.21	0.21	0.22	0.21	0.21	0.21	0.22	0.21

Element (wt.%)	D.L	Actinolite II							Actinolite III					
F	0.03	0.29	0.16	0.24	0.17	0.12	B.D.L	0.09	0.12	0.14	B.D.L	0.12	0.11	0.04
Cl	0.01	0.02	0.02	0.03	0.04	0.02	0.03	0.03	0.03	0.02	0.03	0.03	0.03	0.04
Ca	0.01	8.63	8.65	8.75	8.87	9.04	9.00	8.90	8.34	8.35	8.26	8.51	8.33	8.53
Si	0.01	26.17	25.96	26.06	25.19	25.30	25.51	25.40	24.44	24.11	23.86	23.20	24.79	24.61
Mg	0.01	11.38	11.34	11.41	11.44	11.49	11.36	11.47	10.36	10.49	10.40	10.12	10.96	10.71
Al	0.01	0.35	0.38	0.35	0.44	0.47	0.39	0.43	2.12	2.16	2.43	2.91	1.95	2.48
Mn	0.03	B.D.L	B.D.L	B.D.L	0.05	B.D.L	0.05	0.04	0.28	0.36	0.37	0.26	0.34	0.39
Na	0.01	0.28	0.26	0.25	0.20	0.17	0.18	0.18	0.49	0.48	0.54	0.63	0.43	0.54
Ti	0.01	B.D.L	B.D.L	B.D.L	B.D.L	B.D.L	B.D.L	B.D.L	0.16	0.14	0.13	0.05	0.14	0.15
K	0.01	0.02	0.06	0.04	0.05	0.04	0.05	0.05	0.03	0.05	0.10	0.03	B.D.L	0.10
Cr	0.01	B.D.L	B.D.L	B.D.L	B.D.L	B.D.L	B.D.L	B.D.L	B.D.L	B.D.L	B.D.L	B.D.L	B.D.L	B.D.L
Fe	0.03	7.04	6.95	6.59	6.63	6.02	6.44	7.01	6.97	7.17	7.79	7.48	6.88	7.71
V	0.01	B.D.L	B.D.L	B.D.L	B.D.L	B.D.L	B.D.L	B.D.L	0.03	B.D.L	0.04	0.03	B.D.L	B.D.L
O	-	45.07	44.81	44.89	44.04	44.10	44.31	44.41	44.13	43.94	44.00	43.43	43.67	44.08
H	-	0.24	0.24	0.24	0.24	0.24	0.24	0.24	0.24	0.24	0.23	0.23	0.24	0.35
Total	-	99.49	98.84	98.85	97.38	97.00	97.55	98.26	97.74	97.67	98.16	97.04	97.87	99.72
Fe#	-	0.21	0.21	0.20	0.20	0.19	0.20	0.21	0.23	0.23	0.25	0.24	0.21	0.24

D.L.: detection limit; B.D.L: Below detection limit.

Table SM5. EMPA results for pyroxene crystals from drill cores DDH-5008.

Element (wt.%)	D.L.	157-01	157-01	157-03	157-03
F	0.04	B.D.L	0.08	B.D.L	0.07
Cl	0.01	B.D.L	B.D.L	B.D.L	B.D.L
Ca	0.01	8.90	9.02	22.58	23.26
Si	0.01	22.44	23.33	15.89	16.18
Mg	0.01	8.03	8.79	0.01	0.03
Al	0.01	2.10	1.19	0.48	2.12
Mn	0.03	0.08	0.11	B.D.L	B.D.L
Na	0.01	0.25	0.11	B.D.L	B.D.L
Ti	0.01	B.D.L	B.D.L	0.04	0.36
K	0.01	0.08	0.05	B.D.L	B.D.L
Cr	0.01	B.D.L	B.D.L	B.D.L	B.D.L
Fe	0.03	12.03	11.22	21.31	18.01
V	0.01	0.09	0.07	0.30	0.38
O	-	39.90	40.37	33.84	35.21
Total	-	93.90	94.36	94.48	95.66

D.L.: Detection limit; B.D.L: Below detection limit.

Table SM6. EMPA results for biotite crystals from drill cores PRP-0702.

Element (wt.%)	D.L.	003-02	003-02	003-02	003-02	003-02	003-03	003-03	003-03	003-04	003-04	003-04	003-04
F	0.03	B.D.L	0.039	0.06	0.08	0.04	0.13	0.08	0.12	0.03	0.05	B.D.L	0.08
Cl	0.01	0.08	0.07	0.07	0.07	0.09	0.08	0.07	0.06	0.07	0.08	0.08	0.07
Ca	0.01	0.04	0.06	0.07	0.14	0.07	0.08	0.16	0.04	0.03	0.02	0.05	0.04
Si	0.01	17.41	16.23	16.75	17.15	17.36	17.62	16.91	17.73	17.50	17.58	16.48	17.52
Mg	0.01	9.61	10.99	10.42	9.94	9.75	10.46	10.47	10.25	10.00	9.92	11.39	10.69
Al	0.01	8.26	8.37	7.95	7.78	7.87	7.81	7.84	7.84	7.82	7.81	7.80	7.91
Mn	0.03	0.10	0.15	0.13	0.14	0.13	0.08	0.08	0.09	0.14	0.11	0.11	0.10
Na	0.01	0.08	0.05	0.06	0.04	0.09	0.09	0.10	0.10	0.10	0.10	0.03	0.05
Ti	0.01	1.09	0.74	0.79	1.00	0.88	0.88	1.00	1.00	1.17	1.16	0.98	1.00
K	0.01	7.84	5.56	6.42	6.89	7.10	6.86	5.93	8.16	7.53	7.91	2.83	6.63
Cr	0.01	B.D.L	B.D.L	B.D.L	B.D.L	B.D.L	B.D.L	B.D.L	B.D.L	B.D.L	B.D.L	B.D.L	B.D.L
Fe	0.03	10.58	10.22	10.02	10.32	10.10	9.49	9.83	9.88	10.14	9.78	11.58	10.55
V	0.01	0.03	0.04	0.03	0.05	0.04	0.04	0.04	0.06	0.05	0.05	0.04	0.05
O	-	42.59	41.51	41.48	41.82	41.90	42.39	41.64	42.83	42.44	42.43	41.57	42.82
H	-	0.46	0.46	0.46	0.46	0.46	0.46	0.46	0.46	0.46	0.46	0.47	0.46
Total	-	98.18	94.51	94.71	95.89	95.88	96.47	94.60	98.63	97.46	97.45	93.45	97.98

Element (wt.%)	D.L.	003-04	003-04	003-04	003-04	003-04	003-04	003-04	003-04	003-05	003-05	003-05
F	0.03	B.D.L	0.08	B.D.L	0.09	0.14	0.15	B.D.L	0.03	0.08	0.06	0.09
Cl	0.01	0.07	0.09	0.07	0.07	0.06	0.07	0.08	0.07	0.07	0.09	0.07
Ca	0.01	0.04	0.02	0.08	0.06	0.10	0.09	0.08	0.12	0.11	0.02	0.02
Si	0.01	16.43	17.37	17.43	17.68	17.29	17.56	17.16	17.18	18.07	17.17	17.49
Mg	0.01	11.39	9.85	9.97	10.39	10.12	10.23	10.84	10.70	10.00	9.59	10.14
Al	0.01	8.19	8.05	7.69	7.71	7.69	7.75	7.87	7.84	7.60	7.69	7.73
Mn	0.03	0.13	0.09	0.08	0.08	0.07	0.09	0.10	0.08	0.11	0.08	0.11
Na	0.01	0.06	0.09	0.08	0.07	0.07	0.06	0.07	0.09	0.09	0.12	0.07
Ti	0.01	0.95	1.02	1.03	1.05	0.93	0.96	0.91	0.98	1.12	1.27	1.06
K	0.01	4.84	7.63	7.35	6.84	6.56	6.90	5.76	5.51	7.20	7.15	7.57
Cr	0.01	B.D.L	B.D.L	B.D.L	B.D.L	B.D.L	B.D.L	B.D.L	B.D.L	B.D.L	B.D.L	B.D.L
Fe	0.03	10.50	9.48	9.78	9.61	9.52	10.29	9.68	10.40	9.87	10.11	10.31
V	0.01	0.04	0.05	0.06	0.05	0.06	0.07	0.05	0.04	0.04	0.03	0.05
O	-	41.91	42.13	42.02	42.47	41.67	42.40	42.04	42.16	42.77	41.65	42.40
H	-	0.46	0.46	0.46	0.46	0.46	0.46	0.47	0.46	0.46	0.46	0.46
Total	-	95.02	96.43	96.10	96.64	94.73	97.07	95.10	95.67	97.59	95.47	97.57

D.L.: Detection limit; B.D.L: Below detection limit.

Tabla SM7. EMPA results for apatite crystals from drill cores PRP-0702 and PRP-0853.

Element (wt.%)	D.L.	147-01	147-01	147-01	147-01	147-01	147-01	147-01	147-01	147-01	147-01	147-01	147-01	147-01	147-01	147-01
F	0.02	0.65	0.63	0.58	0.62	0.63	0.56	0.65	0.70	0.68	0.68	0.64	0.69	0.67	0.65	0.62
Cl	0.01	1.47	1.35	1.72	1.48	1.60	1.71	1.49	1.44	1.40	1.60	1.64	1.48	1.55	1.65	1.69
Ca	0.01	39.22	38.82	39.27	39.21	39.20	39.00	39.19	39.30	39.03	39.32	38.90	38.73	39.22	39.01	39.00
P	0.01	18.32	18.23	18.17	18.78	18.71	18.15	18.25	18.55	18.51	18.66	18.66	18.10	18.41	18.36	18.82
Sr	0.03	B.D.L	B.D.L	B.D.L	B.D.L	B.D.L	B.D.L	B.D.L	B.D.L	B.D.L	B.D.L	B.D.L	B.D.L	B.D.L	B.D.L	B.D.L
La	0.03	B.D.L	B.D.L	B.D.L	B.D.L	B.D.L	B.D.L	B.D.L	B.D.L	B.D.L	0.05	B.D.L	B.D.L	B.D.L	0.03	B.D.L
Ce	0.02	B.D.L	B.D.L	B.D.L	B.D.L	0.03	B.D.L	B.D.L	B.D.L	B.D.L	B.D.L	B.D.L	B.D.L	B.D.L	B.D.L	B.D.L
Nd	0.02	B.D.L	B.D.L	B.D.L	B.D.L	B.D.L	B.D.L	B.D.L	B.D.L	B.D.L	B.D.L	0.03	B.D.L	B.D.L	0.03	B.D.L
Si	0.01	0.01	0.01	B.D.L	B.D.L	0.01	B.D.L	B.D.L	B.D.L	B.D.L	B.D.L	B.D.L	0.01	B.D.L	B.D.L	0.01
Mg	0.01	B.D.L	B.D.L	B.D.L	B.D.L	B.D.L	B.D.L	B.D.L	B.D.L	B.D.L	B.D.L	B.D.L	0.01	B.D.L	B.D.L	0.01
Al	0.01	B.D.L	B.D.L	B.D.L	B.D.L	B.D.L	B.D.L	B.D.L	B.D.L	B.D.L	B.D.L	B.D.L	B.D.L	B.D.L	B.D.L	B.D.L
S	0.01	0.01	B.D.L	0.01	B.D.L	0.01	0.01	0.02	0.01	B.D.L	0.01	0.01	0.01	0.01	0.01	0.01
Mn	0.02	B.D.L	0.04	0.05	B.D.L	0.03	0.04	B.D.L	0.03	B.D.L	0.08	0.04	0.07	0.03	B.D.L	B.D.L
Na	0.01	B.D.L	B.D.L	0.03	0.01	B.D.L	B.D.L	B.D.L	0.02	0.02	B.D.L	0.02	B.D.L	0.02	0.02	0.04
As	0.02	B.D.L	B.D.L	B.D.L	B.D.L	B.D.L	B.D.L	B.D.L	B.D.L	B.D.L	0.02	B.D.L	B.D.L	B.D.L	B.D.L	B.D.L
O	-	39.34	39.06	39.20	39.93	39.85	39.05	39.25	39.68	39.51	39.86	39.67	38.90	39.47	39.33	39.92
Total	-	99.07	98.17	99.08	100.11	100.09	98.57	98.88	99.80	99.21	100.32	99.64	98.03	99.42	99.13	100.16

Element (wt.%)	D.L.	147-01	147-01	147-01	147-01	147-01	147-01	147-01	147-01	147-01	147-02	147-02	147-03	147-03	147-04	147-04
F	0.02	0.60	0.60	0.69	0.65	0.56	0.60	0.69	0.66	0.66	0.64	0.64	0.60	0.62	0.62	0.66
Cl	0.01	1.62	1.61	1.62	1.62	1.58	1.64	1.41	1.60	1.56	1.24	1.38	1.39	1.45	1.73	1.73
Ca	0.01	39.06	38.59	39.04	39.06	39.12	39.20	39.25	39.20	38.93	38.77	38.87	37.91	39.03	39.01	38.94
P	0.01	18.37	18.09	18.68	18.75	18.56	18.59	18.78	18.36	18.42	18.40	18.45	17.79	18.36	18.55	18.73
Sr	0.03	B.D.L	B.D.L	0.04	B.D.L	B.D.L	B.D.L	B.D.L	B.D.L	B.D.L	B.D.L	0.06	B.D.L	B.D.L	B.D.L	B.D.L
La	0.03	B.D.L	B.D.L	B.D.L	B.D.L	B.D.L	B.D.L	B.D.L	0.03	0.03	B.D.L	0.06	B.D.L	B.D.L	B.D.L	B.D.L
Ce	0.02	B.D.L	B.D.L	B.D.L	0.03	B.D.L	B.D.L	B.D.L	B.D.L	B.D.L	B.D.L	B.D.L	0.13	B.D.L	B.D.L	B.D.L
Nd	0.02	0.02	0.03	B.D.L	0.02	0.03	B.D.L	B.D.L	B.D.L	B.D.L	B.D.L	B.D.L	B.D.L	B.D.L	B.D.L	B.D.L
Si	0.01	0.01	0.48	B.D.L	B.D.L	B.D.L	0.01	B.D.L	B.D.L	B.D.L	B.D.L	B.D.L	0.56	B.D.L	B.D.L	B.D.L
Mg	0.01	B.D.L	0.29	B.D.L	B.D.L	0.01	B.D.L	B.D.L	0.01	B.D.L	B.D.L	B.D.L	0.01	B.D.L	B.D.L	B.D.L
Al	0.01	B.D.L	B.D.L	B.D.L	B.D.L	B.D.L	B.D.L	B.D.L	B.D.L	B.D.L	B.D.L	B.D.L	0.43	B.D.L	B.D.L	B.D.L
S	0.01	0.01	0.01	0.01	B.D.L	B.D.L	0.01	0.01	0.01	0.02	0.01	B.D.L	B.D.L	B.D.L	0.01	0.01
Mn	0.02	0.08	0.04	0.08	B.D.L	B.D.L	0.04	0.04	B.D.L	0.05	0.03	B.D.L	B.D.L	0.04	0.04	B.D.L
Na	0.01	B.D.L	0.02	0.03	0.02	B.D.L	B.D.L	B.D.L	B.D.L	0.02	B.D.L	B.D.L	B.D.L	0.02	0.01	B.D.L
As	0.02	B.D.L	0.02	B.D.L	B.D.L	B.D.L	B.D.L	B.D.L	0.02	B.D.L	B.D.L	B.D.L	B.D.L	B.D.L	B.D.L	B.D.L
O	-	39.38	39.55	39.78	39.84	39.61	39.70	39.96	39.41	39.40	39.26	39.38	39.18	39.33	39.58	39.77
Total	-	99.19	99.36	100.02	100.04	99.52	99.81	100.18	99.32	99.11	98.37	98.89	98.15	98.90	99.62	99.92

Element (wt.%)	D.L.	147-04	147-04	147-05	147-05	147-05	147-05	042-01	042-01	042-01	042-02	042-02	042-03	042-03	042-03	042-03	042-03
F	0.02	0.66	0.63	0.63	0.71	0.62	0.75	1.84	1.74	1.78	2.01	1.81	1.84	1.72	1.77	1.84	1.80
Cl	0.01	1.70	1.49	1.58	1.53	1.71	1.59	0.88	0.87	0.92	0.78	0.98	0.80	0.84	0.83	0.76	0.90
Ca	0.01	39.28	39.11	38.82	38.58	38.59	38.61	39.18	39.23	39.19	39.44	39.01	38.99	39.26	39.10	39.29	38.76
P	0.01	18.43	18.57	18.60	18.46	18.17	18.41	18.54	18.59	18.43	18.30	18.50	18.40	18.27	18.68	18.27	18.11
Sr	0.03	B.D.L	B.D.L	B.D.L	B.D.L	0.04	B.D.L	B.D.L	B.D.L	B.D.L	B.D.L	B.D.L	B.D.L	B.D.L	B.D.L	B.D.L	B.D.L
La	0.03	B.D.L	B.D.L	B.D.L	0.04	0.03	0.03	B.D.L	B.D.L	0.05	B.D.L	B.D.L	B.D.L	B.D.L	0.04	B.D.L	0.06
Ce	0.02	B.D.L	B.D.L	B.D.L	0.03	B.D.L	B.D.L	0.03	0.03	0.05	B.D.L	0.06	0.04	0.03	B.D.L	B.D.L	0.05
Nd	0.02	B.D.L	0.02	B.D.L	B.D.L	B.D.L	B.D.L	0.04	B.D.L	0.05	B.D.L	0.05	0.02	0.02	B.D.L	0.04	0.03
Si	0.01	B.D.L	B.D.L	0.01	0.01	0.01	0.01	0.03	0.09	0.04	0.04	0.06	0.03	0.03	0.03	0.04	0.03
Mg	0.01	B.D.L	B.D.L	B.D.L	B.D.L	B.D.L	B.D.L	B.D.L	0.03	B.D.L	B.D.L	B.D.L	B.D.L	B.D.L	B.D.L	B.D.L	B.D.L
Al	0.01	B.D.L	B.D.L	B.D.L	B.D.L	B.D.L	B.D.L	B.D.L	0.03	B.D.L	B.D.L	B.D.L	B.D.L	B.D.L	B.D.L	B.D.L	B.D.L
S	0.01	0.01	0.01	0.01	0.01	B.D.L	0.01	0.01	B.D.L	0.02	0.01	0.01	B.D.L	0.07	B.D.L	0.01	0.67
Mn	0.02	0.04	B.D.L	B.D.L	B.D.L	0.08	0.03	0.03	0.04	0.05	0.02	0.03	B.D.L	0.11	0.03	0.07	B.D.L
Na	0.01	B.D.L	0.02	B.D.L	0.01	B.D.L	B.D.L	B.D.L	B.D.L	B.D.L	0.01	B.D.L	B.D.L	B.D.L	B.D.L	B.D.L	B.D.L
As	0.02	B.D.L	0.02	B.D.L	B.D.L	B.D.L	B.D.L	B.D.L	0.02	B.D.L	0.03	0.02	0.03	0.02	B.D.L	B.D.L	B.D.L
O	-	39.52	39.63	39.56	39.29	38.94	39.24	39.66	39.86	39.57	39.48	39.59	39.39	39.46	39.80	39.38	39.92
Total	-	99.69	99.52	99.26	98.70	98.24	98.73	100.28	100.57	100.17	100.18	100.14	99.59	99.89	100.32	99.74	100.34

D.L.: Detection limit; B.D.L: Below detection limit.